A STUDY OF PROPOSED INTERMEDIATES IN THE DEOXOFLUORINATION OF CARBONYL GROUPS BY SF_4

DANIEL STUART
Honours Bachelor of Science, McMaster University, 2015

A Thesis
Submitted to the School of Graduate Studies
of the University of Lethbridge
in Partial Fulfilment of the
Requirements for the Degree

MASTER OF SCIENCE

Department of Chemistry and Biochemistry
University of Lethbridge
LETHBRIDGE, ALBERTA, CANADA

A STUDY OF PROPOSED INTERMEDIATES IN THE DEOXOFLUORINATION OF CARBONYL GROUPS BY SF_4

DANIEL STUART

Date of Defence: May 16th, 2018

Dr. M. Gerken Supervisor	Professor	Ph.D.
Dr. P. W. Dibble Thesis Examination Committee Member	Associate Professor	Ph.D.
Dr. P. Hazendonk Thesis Examination Committee Member	Associate Professor	Ph.D.
Dr. J. Müller External Examiner University of Saskatchewan Saskatoon, Saskatchewan	Professor	Ph.D.
Dr. P. G. Hayes Chair, Thesis Examination Committee	Professor	Ph.D.

Abstract

The $[SF_4{\cdot}O{=}C(CH_3)_2]_2$ and $SF_4{\cdot}[O{=}C(CH_3)_2]_2$ adducts were synthesized and characterized at low temperature (LT) using Raman spectroscopy and, in the case of $[SF_4{\cdot}O{=}C(CH_3)_2]_2$, single-crystal X-ray diffraction. The X-ray crystal structure of $SF_4{\cdot}(O{=}C_{10}H_{14}){\cdot}(HF)$ was obtained, showing F_4S---F−H---$O{=}C_{10}H_{14}$ interactions.

Adducts of $[SF_3]^+$ with acetone, cyclopentanone, and 2-adamantanone were shown by ^{19}F and ^{1}H NMR spectroscopy to exist in solutions below −40 °C. The proposed $[SF_3{\cdot}\{O{=}C(CH_3)_2\}_3]^+$ cation was observed at LT by reacting $[SF_3][AsF_6]$ with excess acetone. Above −40 °C SF_4 formation was observed.

Protonated ketones, $[HO{=}R]^+$ (R = $C(CH_3)_2$, C_5H_8, $C_{10}H_{14}$), and aldehydes, $[H(O{=}CHC_6H_5)_2]^+$ and $[H(O{=}CHCH_3)_x]^+$ (x = 1 or 2), were isolated and characterized in the solid state for the first time. NBO analyses were used to quantify the increase in electrophilicity of the oxonium cations.

The $AsF_5{\cdot}O{=}R$ (R = $C(CH_3)_2$, C_5H_8, $C_{10}H_{14}$) adducts were synthesized and characterized in solution and solid state using LT NMR and Raman spectroscopies, respectively.

Acknowledgments

I would like to thank my supervisor, Dr. Michael Gerken, for his mentorship during my time in his research group. His patience, enthusiasm, and immense knowledge in the field of fluorine chemistry make him an excellent supervisor and inspired me to become a better chemist. Thank you for providing me with the opportunity to work in your lab.

I would like to thank my committee members, Dr. Peter Dibble and Dr. Paul Hazendonk, for their encouragement and insightful comments over the course of my graduate studies.

I would like to thank Dr. Jens Müller for taking time out of his busy schedule to review my thesis and travel to Lethbridge for my defence.

Sincere thank-you goes out to Dr. Stacey D. Wetmore for providing me with the computational resources throughout this thesis, as well as her guidance during the preparation and submission of our published manuscript. I would also like to thank Dr. René T. Boeré for doing an excellent job in teaching me the basics of X-ray crystallography during his course.

Thank you to the members of the Gerken group, Nathan Kostiuk and Douglas Turnbull, for their friendship, assistance in the lab, and many entertaining conversations. A special thanks to Nathan for helping settle into Lethbridge and introducing me to many new friends. I am also thankful for my fellow graduate student peers, Connor and Jackson, for all the amazing days skiing in the mountains.

A heartfelt thanks to all the friends I made throughout the past few years, especially Kathleen, Katelyn, and Chris who have made my time in Lethbridge extra special.

Finally, I would like to thank my family for their endless encouragement, constant love, and support. I am especially thankful for my parents, Pat and Mike, who are the reason I am where I am today. You are always there for me and I am eternally grateful.

Table of Contents

List of Tables

List of Figures

List of Abbreviations

General

r_{vdW}	van der Waals radius
χ	electronegativity
aHF	anhydrous hydrogen fluoride
FEP	copolymer of perfluoroethylene and perfluoropropylene
Kel-F	polychlorotrifluoroethylene
PTFE	polytetrafluoroethylene
ax/eq	axial/equatorial
gem	geminal
IR	infrared
ν	stretch
NMR	Nuclear Magnetic Resonance
o.d.	outer diameter
THF	tetrahydrofuran
RT	room temperature
LT	low temperature
DAST	diethylaminosulfur trifluoride

X-ray Crystallography

a, b, c, α, β, γ	cell parameters
V	volume
λ	wavelength
Z	molecules per unit cell
μ	absorption coefficient
ρ	density
R_1	conventional agreement index
wR_2	weighted agreement index
GooF	goodness of fit

Nuclear Magnetic Resonance

δ	chemical shift
J	scalar coupling constant in Hertz
ppm	parts per million
TMS	tetramethylsilane

Computational Methods

DFT	density functional theory
B3LYP	Becke, 3-parameter, Lee-Yang-Parr
aug-cc-pVTZ	augmented−correlation-consistent−polarized triple-zeta
NBO	natural bond order
NPA	natural population analysis
WBI	Wiberg bond index
HOMO	highest occupied molecular orbital
LUMO	lowest unoccupied molecular orbital

1. Introduction

1.1 Organofluorine Chemistry

Fluorine-containing molecules have found diverse applications in pharmaceutical, agrochemical, and materials chemistry, and as tracers for positron emission tomography.[1] In fact, approximately 30−40% of agrochemicals and 20−25% of pharmaceuticals on the market are estimated to contain fluorine atoms.[1a,2] The addition of fluorine to an organic molecule can drastically alter its chemical properties due to its small size (r_{vdW} = 1.47 Å), high electronegativity (χ = 4.0 on the Pauling scale), strong C−F bond strength (bond dissociation energy of 441 kJ/mol), large dipole moment of C−F bonds (molecular dipole moment of 1.85 D for CH_3F), and its ability to increase the lipophilicity of a molecule .[3] An active area of research includes selective C−F bond formation in organic molecules. The ability to selectively fluorinate a molecule, by means of electrophilic or nucleophilic fluorination, over different functional groups is inherently difficult.[4]

The use of highly oxidizing elemental fluorine (F_2), diluted with nitrogen or helium, was one of the earliest methods used to prepare highly fluorinated organic molecules; however, these reactions are non-selective (see Equation 1.1) and often lead to fragmentation.[5] An important nucleophilic fluorinating agent is hydrogen fluoride (HF), commonly used in the production of chlorofluorocarbons (CFCs) or hydrofluorocarbons (HFCs) (see Equation 1.2).[6] The corrosive and toxic nature of HF, in conjunction with its low boiling point (19.5 °C), makes it difficult to work with under ambient conditions.

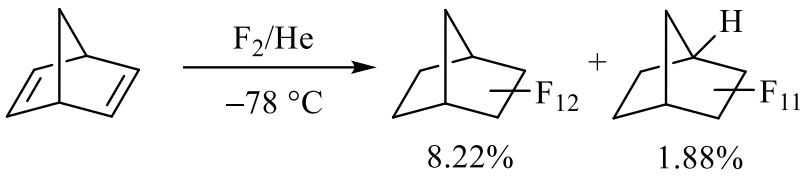

(1.1)

(1.2)

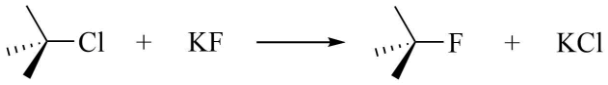

(1.3)

Olah and co-workers developed a stable and less volatile source of anhydrous HF (aHF) using a mixture of 70% HF with 30% pyridine (Olah's reagent) making it easier to handle under ambient conditions. Olah's reagent is a nucleophilic fluorinating agent stable up to 55 °C.[7]

The use of alkali metal fluorides, i.e., KF or CsF, offers a method of providing a $[F]^-$ source that can be used in simple displacement reactions of other halides such as chloride or bromide (see Equation 1.3).[5] These metathesis reactions can sometimes require high temperatures and are selective depending on the substituents of the organic substrate and the solvent used. The larger the cation is, the more isolated the fluoride ion will be, which, consequently, increases its reactivity. Tetraalkyl ammonium salts, such as $[Me_4N][F]$, are alternatives to alkali metal fluorides where the nucleophilicity of the fluoride anion is enhanced by the weakly coordinating quaternary ammonium cation.[8] A challenge associated with the synthesis of these salts is the difficulty obtaining them in the anhydrous form. The nucleophilicity of alkali metal fluorides can be further enhanced by the use of chelating crown ethers, such as 18-crown-6, which encapsulate the cation of alkali metal fluorides leaving an unsaturated "naked" fluoride (see Figure 1.1). This allows nucleophilic substitution of other halides by $[F]^-$ to take place under milder conditions with acceptable yields.[5]

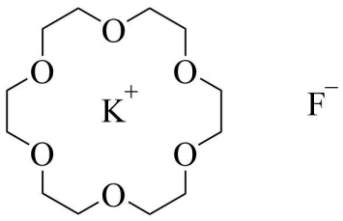

Figure 1.1 Structure of [18]crown-6 chelated to the potassium cation, $[K^+]$, and the isolated fluoride anion, $[F]^-$.

While nucleophilic fluorination is one of the most common methods used to introduce a fluoro-group, other reactions invoke the use of electrophilic fluorinating reagents.[9] These often employ a reagent that formally transfers a "$[F]^+$" and directly converts C−H to C−F bonds. While the use of elemental fluorine is possible for electrophilic fluorination, easier-to-handle compounds have been developed and include perchloryl fluoride ($FClO_3$), xenon difluoride (XeF_2), and trifluoromethyl hypofluorite (CF_3OF).[10] These compounds, however, still pose limitations that have prevented their widespread use including their potential as powerful oxidizing agents or difficulty producing large quantities. An alternative to these sources of fluorine are N^+−F fluorinating agents such as those from *N*-fluoropyridinium salts, including the well known 1-chloromethyl-4-fluoro-1,4-diazoniabicyclo[2.2.2]octane bis(tetrafluoroborate) (Select-fluor™) (Figure 1.2).[9b,11]

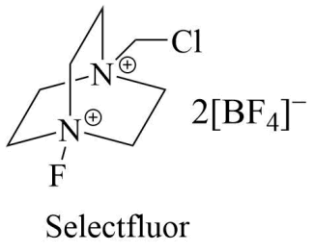

Selectfluor

Figure 1.2 Structure of 1-chloromethyl-4-fluorodiazoniabicyclo[2.2.2]octane bis(tetrafluoroborate), also known as Selectfluor™.

Selectfluor™ is a thermally stable reagent (up to 195 °C) and easy to handle for industrial use.[12] Reactions include the fluorination of toluene with Selectfluor™ in the presence of electron donating groups (Equation 1.4)[13] and electrophilic fluorination of organic substrates in aqueous media (Equation 1.5).[14]

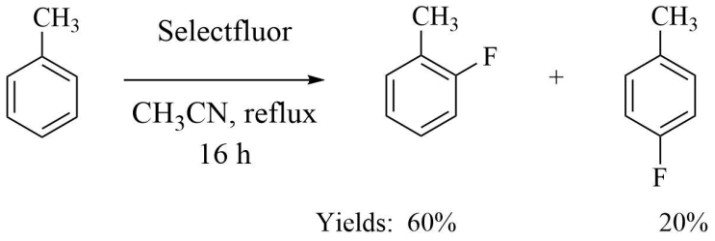

(1.4)

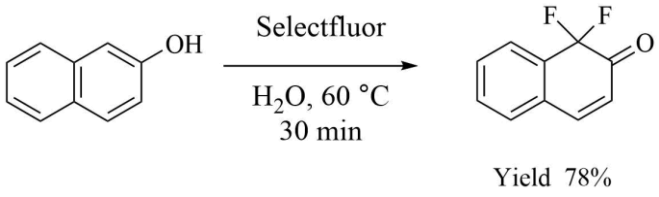

(1.5)

1.1.1 Deoxofluorination Reactions

An effective method of fluorinating organic compounds involves the transformation of alcohols, ketones, and carboxylic acids to −CF, $-CF_2$, and $-CF_3$ groups, respectively, known as deoxofluorination.[15–19] One of the earliest nucleophilic fluorinating reagents used to perform deoxofluorination reactions is sulfur tetrafluoride, SF_4.[15–19] The first reactions which employed SF_4 as a deoxofluorinating reagent involved reacting various ketones with SF_4, and was later expanded to include alcohols.[15] These reactions usually require specialized equipment, high temperatures (>100 °C), high pressures, and anhydrous conditions and have the potential to lead to undesirable by-products. Reaction mechanisms for deoxofluorination reactions of carbonyl groups and hydroxyl groups with SF_4 have been postulated.[18–20] The earliest mechanism proposed by Hasek, Smith, and Engelhardt

(DuPont) involves HF, as a catalyst, polarizing the C=O group allowing for SF_4 to add across the activated carbonyl group giving the alkoxysulfur trifluoride intermediate ($ROSF_3$). This immediately reacts with HF to yield the respective difluoro compound, SOF_2, and HF as products (Scheme 1.1).[15b] The addition of a catalytic amount of Lewis acid, including HF, BF_3, AsF_3, PF_5, or TiF_4, resulted in a large increase in the yield of the desired fluorinated compound.[15c]

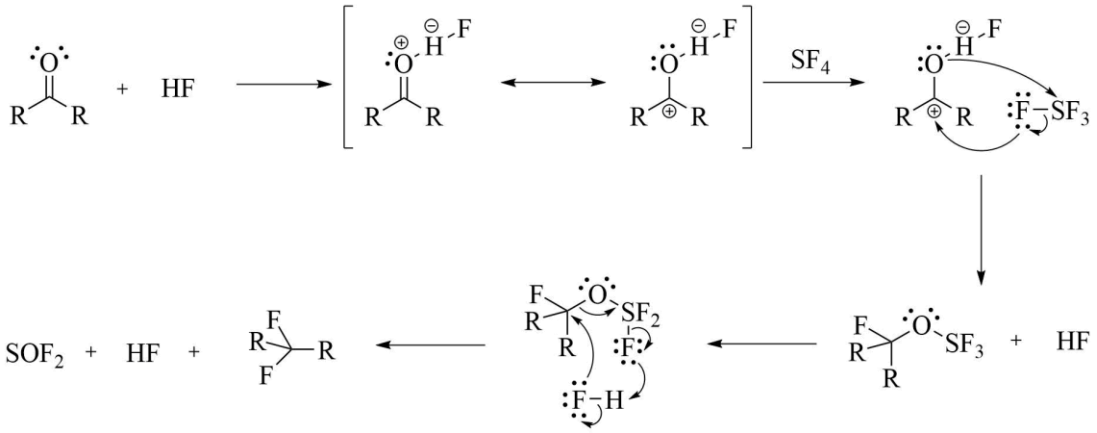

Scheme 1.1 Reaction mechanism for the deoxofluorination of a carbonyl group with SF_4 in the presence of a catalytic amount of HF as proposed by Hasek, Smith, and Engelhardt, (Ref. 15b).

Martin and Kagan carried out reactions of SF_4 with carbonyl-containing steroids and showed the transformation of C=O groups to *gem*-difluorides.[17] It was found that significant amounts of HF rather than catalytic amounts allowed for more controlled fluorination reactions. They suggested that under conditions employing a catalytic amount of Lewis acid the reaction mechanism would follow that proposed by Hasek, Smith, and Engelhardt (Scheme 1.1). However, they also proposed two other possible mechanisms. One involved the formation of an adduct between HF and SF_4 (FH---F−SF_3), in the

presence of excess HF, which then reacts with the carbonyl group to form the $RFCOSF_3$ intermediate (Scheme 1.2).

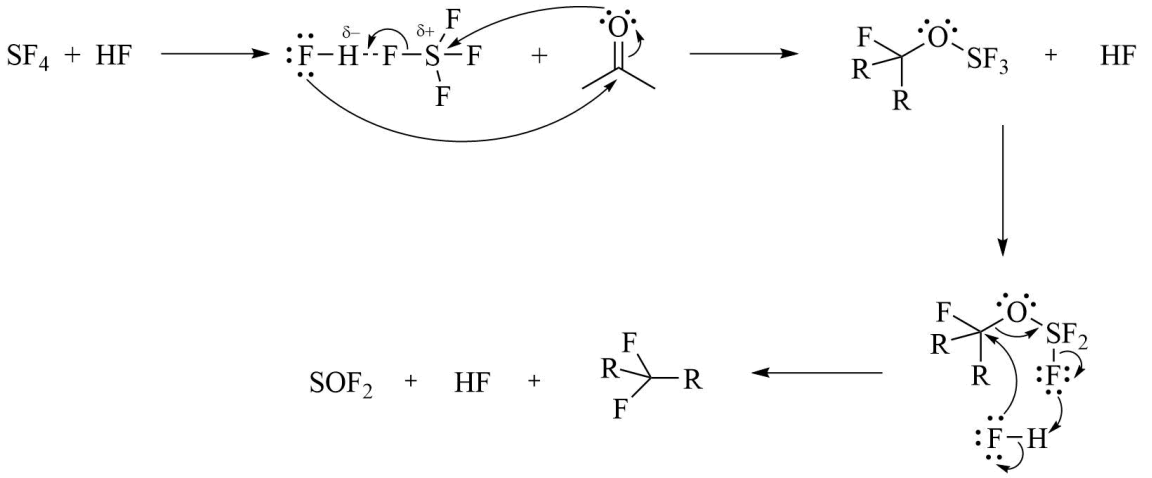

Scheme 1.2 Reaction mechanism for the deoxofluorination of a carbonyl group with SF_4 in the presence of large amounts of HF as proposed by Martin and Kagan (Ref. 17).

Alternatively, they proposed that SF_4 interacts with HF to form an ionic species consisting of $[SF_3]^+$ and $[HF_2]^-$. The oxygen of the carbonyl group then undergoes electrophilic attack by $[SF_3]^+$ followed by donation of a fluoride from $[HF_2]^-$ to the carbon center generating the $RFCOSF_3$ intermediate. In both suggested mechanisms, the $RFCOSF_3$ intermediate is formed which then follows a similar mechanism to that proposed by Hasek, Smith, and Engelhardt.

Dmowski investigated the effect of hydrogen fluoride concentration on the reaction of SF_4 with carboxylic acids and acyl fluorides and found the optimal concentration to be much higher than a catalytic amount, initially proposed by Hasek, Smith, and Engelhardt.[19a] The required amount of HF can be stoichiometric or a large excess to obtain maximum yield of deoxofluorinated product. It was also found that the basicity of the carbonyl group greatly affects the required HF concentration in deoxofluorination

reactions. Highly basic ketones require amounts of HF well above a 1:1 stoichiometry, with respect to the carbonyl compound, because they are more prone towards protonation by HF thereby slowing the deoxofluorination reaction due to a lack of HF in solution. By introducing more electron-withdrawing functional groups to the ketone the basicity is lowered, leaving more HF in solution, and therefore exhibiting a higher reactivity towards SF_4.

With this information, Dmowski proposed a reaction mechanism for the deoxofluorination of ketones with SF_4 similar to the one by Martin and Kagan, whereby the presence of HF induces the dissociation of SF_4 into $[SF_3]^+$ (Equation 1.7), a highly electrophilic cation believed to be the active species responsible for the deoxofluorination reaction.[19] Conductivity measurements had been carried out by Gillespie et al. showing the presence of an equilibrium concentration of $[SF_3]^+$ and $[HF_2]^-$ when SF_4 is dissolved in anhydrous HF with an estimated equilibrium constant of $K = 4(2) \times 10^{-2}$ at 0 °C.[21]

$$SF_4 + HF \rightleftharpoons [SF_3]^+ + [HF_2]^- \qquad (1.7)$$

In an example of deoxofluorination of acyl fluorides, the carbonyl group undergoes electrophilic attack by the $[SF_3]^+$ cation polarizing the C=O bond and forming the resonance-stabilized alkoxysulfur trifluoride cation. It is then suggested that a fluorine atom from the SF_3 substituent acts as a nucleophilic fluoride source and attacks the carbon center followed by elimination of SOF_2 and leaving the fluorocarbenium cation (Scheme 1.3). The highly reactive fluorocarbenium cation reacts with the fluoride source $[HF_2]^-$ to give the resulting fluorinated compound where the carbonyl has been replaced by two fluorine atoms.[19]

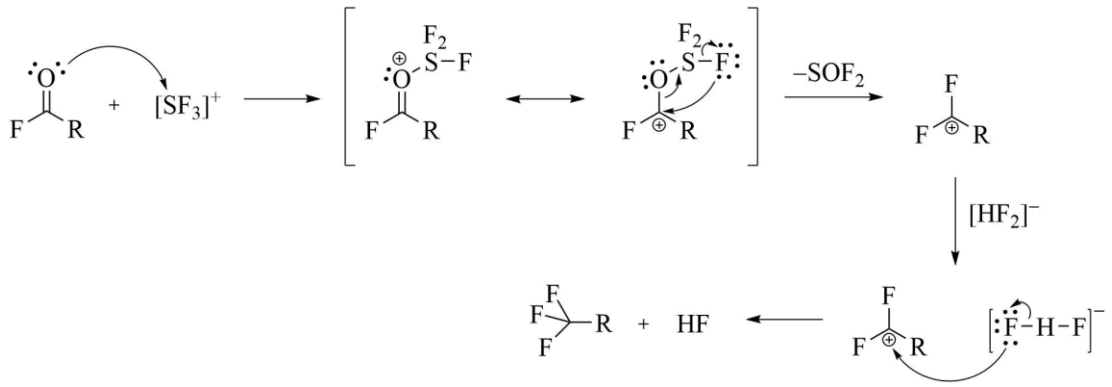

Scheme 1.3 Reaction mechanism for the deoxofluorination reaction of acetyl fluoride with SF_4 in the presence of HF as proposed by Dmowski (Ref. 19).

In reactions of SF_4 with aldehydes, depending on the substituents on the aldehyde, both 1,1- and 1,2-difluoroalkanes were obtained, which is in agreement with the formation of a carbocation that can isomerize to the tertiary carbenium cation (Scheme 1.4) followed by neutralization with fluoride from $[HF_2]^-$. Fluoroethers are known by-products of deoxofluorination reactions as a result of electrophilic attack of the fluorocarbenium ion on a second molecule of the carbonyl compound and subsequent neutralization with fluoride (from $[HF_2]^-$) (see Scheme 1.5).

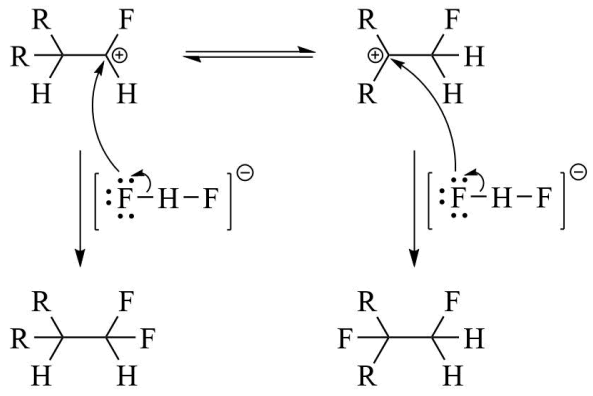

Scheme 1.4 Reaction mechanism showing the reversible isomerization of the fluorocarbenium cation followed by reaction with bifluoride, $[HF_2]^-$, to yield the 1,1-difluoroalkane and 1,2-difluoroalkane as shown by Dmowski (Ref. 19b).

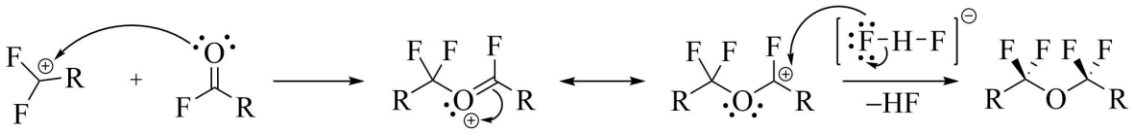

Scheme 1.5 Reaction mechanism for the synthesis of a fluoroether, a by-product in the deoxofluorination mechanism proposed by Dmowski (Ref. 19).

A slightly modified mechanism was proposed by Pustovit and Nazaretian and is shown in Scheme 1.6.[20] Similar to Dmowski's mechanism, $[SF_3]^+$ is invoked (Equation 1.7) to polarize the carbonyl group generating the $[R_2C{-}O{-}SF_3]^+$ cation. This carbocation can undergo nucleophilic attack by fluoride or $[HF_2]^-$ to form the neutral $R_2FC{-}O{-}SF_3$ which, in the presence of HF, is proposed to be in equilibrium with $[R_2FC{-}O{-}SF_2]^+$. In a side reaction, the $[R_2C{-}O{-}SF_3]^+$ cation can also react with another carbonyl compound to form the fluoroethers previously mentioned. Once $[R_2FC{-}O{-}SF_2]^+$ is present in solution, a nucleophile can attack the carbon atom by either an S_N1 or S_N2 reaction, depending on the reaction conditions and substituents present on the cation, eliminating SOF_2 and yielding the fluorinated product.

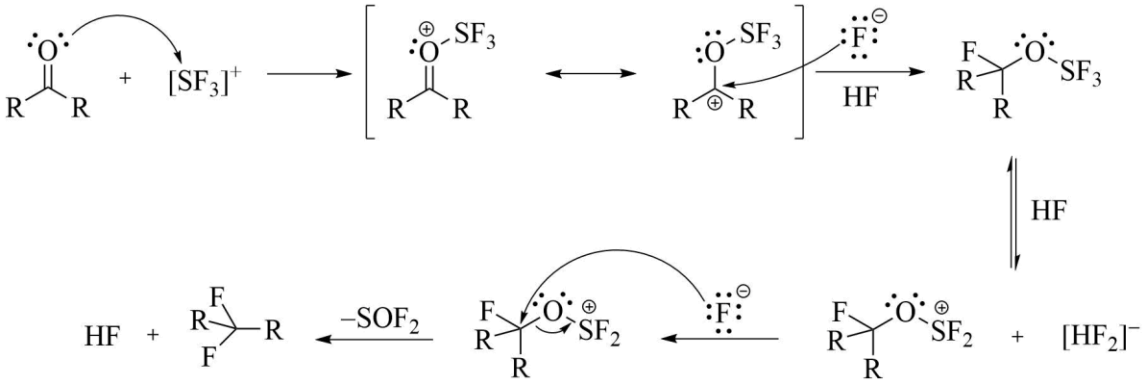

Scheme 1.6 Reaction mechanism for the deoxofluorination of a ketone with SF_4 in HF as proposed by Pustovit and Nazaretian (Ref. 20).

The neutral alkoxysulfur trifluoride intermediate, $ROSF_3$, has been hypothesized to exist; however, the isolation of only a few alkoxysulfur trifluorides has been reported. The reaction of SF_4 with 2-fluoro-2,2-dinitroethanol yielded 2-fluoro-2,2-dinitroethoxysulfur trifluoride (see Equation 1.8), which was solely characterized by ^{19}F NMR spectroscopy (singlet at −109.8 ppm (C−F); multiplet at 62.6 ppm (SF_3)).[18] This species was shown to be readily hydrolyzed by moisture and immiscible in anhydrous HF. The alkoxysulfur trifluoride, an intermediate in each of the previously proposed deoxofluorination mechanisms, likely requires highly electron-withdrawing substituents to be stabilized. The inertness of $(O_2N)_2FC{-}CH_2OSF_3$ towards aHF has been viewed as surprising, since the facile reaction of the $ROSF_3$ intermediate in the presence of HF has been postulated. In later work, the reaction of SF_4 with fluorinated lithium alkoxides resulted in the synthesis of polyfluorinated alkoxysulfur trifluorides (Equation 1.9).[22] A series of polyfluoroalkoxysulfur trifluorides were also been prepared by reaction of α,α,ω-trihydropolyfluoroalkanols with SF_4 in the presence of HF scavengers such as KF or NaF (Equation 1.10).[22] In the absence of the HF scavengers, the deoxofluorination product was exclusively obtained. The reaction of dodecafluoroheptyloxysulfur trifluorides with one equivalent of the Lewis acids HF, BF_3, or SbF_5 at −40 °C in a Freon solution gave the respective dodecafluoroheptyloxydifluorosulfonium salts (Equation 1.11).[22] This cationic alkoxysulfur difluoride species is consistent with the intermediate in the deoxofluorination reaction mechanism proposed by Pustovit and Nazaretian in Scheme 1.6, where the neutral $ROSF_3$ intermediate is in equilibrium with $[ROSF_2]^+$ in the presence of HF.[20]

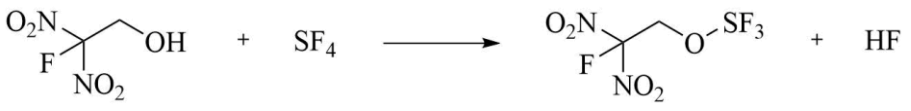

(1.8)

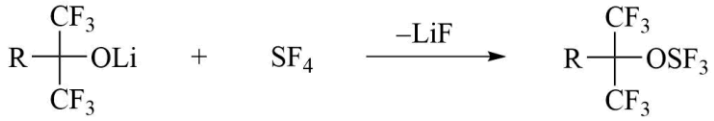

R = H, Me, CF_3, C_2F_5 (1.9)

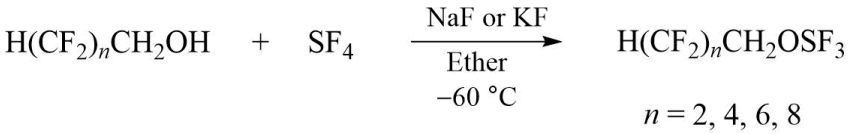

(1.10)

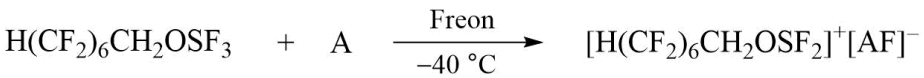

A = HF, BF_3, SbF_5 (1.11)

Over the years, various derivatives of SF_4 have been synthesized which act as more convenient and easier to handle deoxofluorinating reagents compared to SF_4. Diethylaminosulfur trifluoride (DAST) (see Figure 1.3) is used to selectively transform −OH and R_2C=O functional groups to −F and R_2CF_2 under relatively mild conditions.[23] It was later found that DAST decomposes upon warming above 90 °C into SF_4 and the extremely unstable bis(diethylamino)sulfur difluoride which, subsequently, results in detonation (see Equation 1.12).[24]

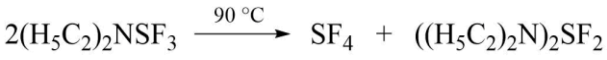

(1.12)

Bis(2-methoxyethyl)aminosulfur trifluoride (Deoxo-Fluor) (see Figure 1.3) was developed as a more thermally stable and safer substitute owing to its conformational rigidity imposed by the alkoxy groups.[25] The fluorination of ketones and aldehydes by Deoxo-Fluor results in the transformation of carbonyl groups to geminal difluorides with relatively good yields (see Equation 1.13). However, both DAST and Deoxo-Fluor are fuming liquids that react

violently with water and thus require a dry atmosphere to perform these reactions. In using these reagents, HF is generated as a by-product which is highly toxic and extremely corrosive.[26]

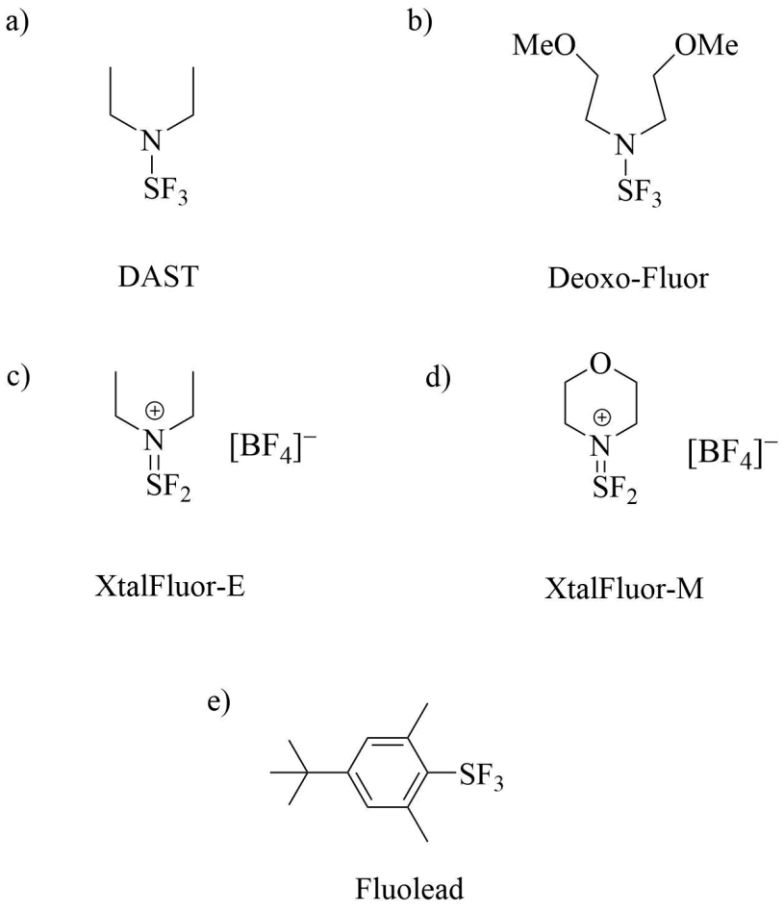

Figure 1.3 Common deoxofluorinating reagents used include: a) Diethylaminosulfur trifluoride (DAST), b) Bis(2-methoxyethyl)aminosulfur trifluoride (Deoxo-Fluor), c) Diethylaminodifluorosulfonium tetrafluoroborate (XtalFluor-E), d) Morpholino-difluorosulfonium tetrafluoroborate (XtalFluor-M), e) 4-*tert*-butyl-2,6-dimethylphenyl-sulfur trifluoride (Fluolead).

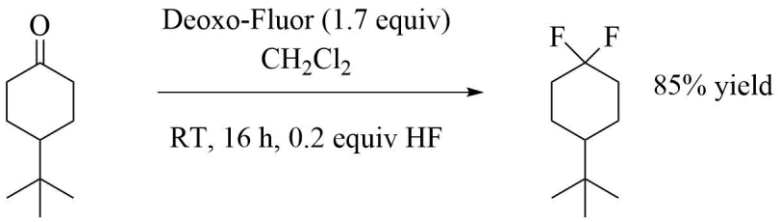

(1.13)

Difficulties associated with handling these reagents (SF_4, DAST, and Deoxo-Fluor) resulted in a push to synthesize deoxofluorinating reagents that are easier and safer to handle and more selective. Diethylaminodifluorosulfonium tetrafluoroborate (XtalFluor-E) and morpholinodifluorosulfonium tetrafluoroborate (XtalFluor-M) are crystalline fluorinating agents (see Figure 1.3) and allow for the formation of C−F bonds from a variety of oxygenated substrates, including aliphatic alcohols, carbonyl compounds, and carboxylic acid derivatives.[27] These reactions require a fluoride source, such as $Et_3N{\cdot}3HF$, to proceed since the direct interaction between (dialkylamino)difluorosulfonium salts with oxygen bases does not contain a nucleophilic fluoride source. Using XtalFluor in reactions with alcohols results in deoxofluorination of the hydroxyl group with very few by-products compared to DAST or DeoxoFluor.[27a] As another alternative, derivatives of arylsulfur trifluorides, including 4-tert-butyl-2,6-dimethylphenylsulfur trifluoride (Fluolead), have been shown to be excellent deoxofluorinating reagents.[28] Fluolead (Figure 1.3) has been shown to be relatively unreactive towards small amounts of water in contrast to DAST and DeoxoFluor.[28c]

1.2 Sulfur Tetrafluoride

Sulfur tetrafluoride is a toxic, corrosive gas at room temperature (RT) with a melting point of −121 °C and boiling point of −38 °C. It is highly reactive with water forming hydrogen fluoride (HF) and thionyl fluoride (SOF_2), and thus must be stored in a high-pressure and corrosion-resistant vessel. Sulfur tetrafluoride is one of several binary covalent fluorides of sulfur (besides SF_2, S_2F_2, S_2F_4, SF_6, and S_2F_{10}), and is a fluorinating agent capable of adding fluorine over various functional groups such as ketones, aldehydes,

carboxylic acids, and alcohols (*vide supra*).[29] Using the pF^- scale developed by Christe and Dixon for Lewis acidity, SF_4 lies between COF_2 (4.99) and XeF_4 (5.71), two relatively mild fluoride-ion acceptors, at a pF^- value of 5.67, corresponding to a fluoride-ion affinity of 56.7 kcal/mol = 237 kJ/mol.[30] Sulfur tetrafluoride is capable of acting as a Lewis acid towards strong fluoride-ion donors such as $[N(CH_3)_4]F$ and CsF to form salts of the $[SF_5]^-$ anion.[31,32] Due to the highly reactive and gaseous nature of SF_4, only recently has the solid-state structure been determined and found to agree with the seesaw geometry determined from gas-phase studies, vibrational spectroscopy, and NMR spectroscopy.[33–40] In the solid state, SF_4 exhibits weak $F_3S{-}F{-}{-}{-}SF_4$ interactions, exclusively involving the more ionic axial fluorine atoms. The ^{19}F NMR spectroscopy shows two chemical resonances as triplets for SF_4 at 90 (F-axial) and 34 ppm (F-equatorial) ($^2J(^{19}F{-}{-}^{19}F)$ = 79 Hz) arising from the chemical inequivalence of the axial and equatorial fluorine ligands at low temperature (LT).

1.2.1 Adducts of SF_4 and Organic Nitrogen and Oxygen Bases

The Lewis acid behaviour of SF_4 towards nitrogen-bases has been well documented in recent years. The first evidence for SF_4 forming an adduct with a nitrogen base came from an early crude tensiometric study suggesting the 1:1 adduct formation with triethylamine and pyridine.[41] An elemental analysis study detected the $SF_4{\cdot}NC_5H_5$ adduct and claimed the existence of the $SF_4{\cdot}2NC_5H_5$, $SF_4{\cdot}4NC_5H_5$, and $SF_4{\cdot}8NC_5H_5$ adducts at −78 °C.[42] A matrix-isolation infrared spectroscopy (IR) study claimed SF_4 to form adducts with NH_3, NC_5H_5, and CH_3CN as evidenced by shifts in the IR bands.[43] However, due to

severe overlap of many of the reactant and product bands, definitive identification was not possible.

The first conclusive evidence for formation of a SF_4·nitrogen-base adduct was the synthesis and characterization of $SF_4 \cdot N(C_2H_5)_3$ by X-ray crystallography, LT Raman spectroscopy and ^{19}F NMR spectroscopy.[44] The X-ray crystal structure contained an S---N distance of 2.3844(19) Å. Other adducts between SF_4 and nitrogen bases including pyridine and pyridine derivatives have been synthesized and characterized in the solid state, each of which are stable towards dissociation below −45 °C.[45] These X-ray crystal structures exhibited weak interactions between the sulfur and nitrogen atoms with S---N distances ranging from 2.141(2)−2.514(2) Å. Shifts in the characteristic Raman bands of SF_4 and nitrogen bases allowed for the donor strengths of each base to be assessed. It was found that the stronger bases showed larger decreases in the equatorial S−F stretching frequency of SF_4.

Studies of these Lewis acid-base adducts between SF_4 and nitrogen-bases showed the adducts to be easily be solvolyzed by HF. The X-ray crystal structures of these solvolysis products showed interesting bonding motifs where the nitrogen bases were protonated and hydrogen-bonded to a fluoride anion which was coordinated to a SF_4 (see Figure 1.4).[46] In another example, a $[HF_2]^-$ anion was shown to accept a hydrogen bond to the protonated nitrogen base as opposed to a fluoride anion.

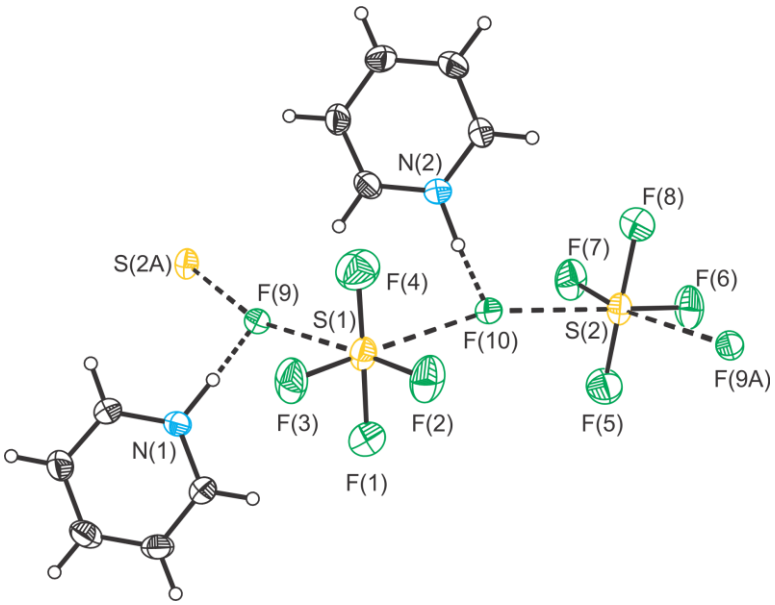

Figure 1.4 Thermal ellipsoid plot of the X-ray crystal structure of $[HNC_5H_5]^+F^-\cdot SF_4$ from Ref. 46. Thermal ellipsoids are set at the 50% probability level. The bridging interaction between the fluoride and SF_4, F_4S---$[F]^-$, has contacts of 2.6826(9) and 2.7739(9) Å. The N(1)H---F(9) distance is 2.4367(13) Å.

Sulfur tetrafluoride has also been shown to form Lewis acid-base adducts with oxygen bases via S---O chalcogen bonding interactions. Early NMR spectroscopy studies proposed SF_4 is not capable of forming adducts with the oxygen-bases tetrahydrofuran (THF) and ethyl acetate since the chemical shift of SF_4 was unaffected.[47] However, LT NMR studies later showed that SF_4 can form adducts with the solvents diethyl ether and THF since there were changes in $\delta(^{19}F)$ and a decrease in $^2J(^{19}F–^{19}F)$ coupling.[48] A matrix-isolation study suggested the 1:1 adduct of SF_4 and acetone existed based on the appearance of two new bands in the IR spectrum at 680, assigned to ν(S−F), and 1706 cm^{-1}, assigned to ν(C=O).[49] Recently, Gerken and co-workers were able to successfully synthesize oxygen-base adducts with SF_4 and characterize them in the solid state.[50] Lewis acid-base adducts of SF_4 with THF, 1,2-dimethoxyethane, and cyclopentanone were synthesized at low temperatures and characterized by X-ray crystallography and Raman spectroscopy. In

addition, caffeine, containing three Lewis basic sites (i.e., one N and two C=O basic groups), was shown to form an adduct with SF_4 through C=O---S interactions (see Figure 1.4).

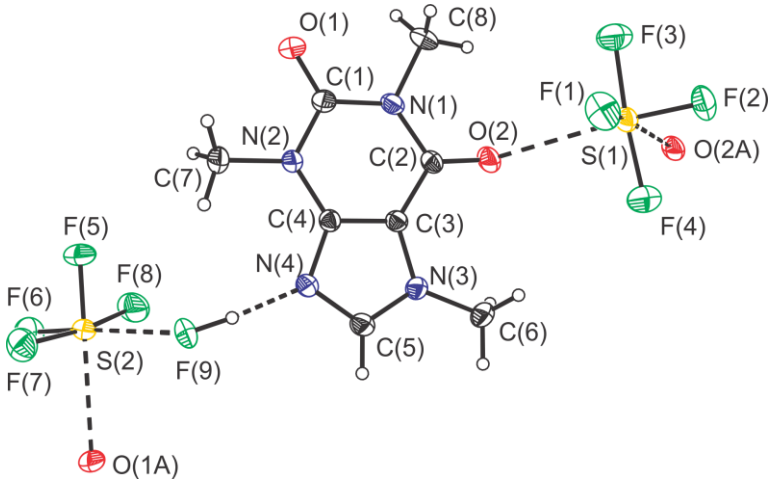

Figure 1.5 Thermal ellipsoid plot of the X-ray crystal structure of $C_8H_{10}N_4O_2 \cdot 2SF_4 \cdot HF$ from Ref. 50. Thermal ellipsoids are set at the 50% probability level. The HF(9) is bridging S(2) of SF_4 (2.7932(15) Å) and the Lewis basic site N(4) of caffeine.

The bonding interactions of this complex, $C_8H_{10}N_4O_2 \cdot 2SF_4 \cdot HF$ (Figure 1.5), showcased SF_4 having a S---F contact with a fluorine atom of HF, which in turn was hydrogen-bonded to the Lewis basic nitrogen site of caffeine. This bonding modality is different from that observed in $[HNC_5H_5]^+F^- \cdot SF_4$ where the nitrogen is protonated by HF.

1.3 The Chemistry of $[SF_3]^+$

SF_4 has been shown to act as a fluoride-ion donor towards strong Lewis acids such as BF_3, PF_5, AsF_5, and SbF_5 to form the respective $[SF_3]^+$ salts (see Equation 1.14).[21,51]

$$SF_4 + MF_5 \longrightarrow [SF_3][MF_6] \quad (M = As, Sb) \tag{1.14}$$

The first report of reactions of SF_4 with Lewis acids was by Bartlett and Robinson where it was suggested that these compounds form a donor-acceptor complex, or an adduct (i.e. $SF_4 \cdot BF_3$, $SF_4 \cdot AsF_5$, $SF_4 \cdot SbF_5$). It was later argued that the $SF_4 \cdot BF_3$ system is not a donor-acceptor complex, but is an ionic species.[52] Infrared spectroscopic measurements of the $SF_4 \cdot BF_3$ adduct were carried out by Seel and Detmer and the presence of a band at 1050 cm^{-1} was assigned to $[BF_4]^-$, and two new bands at 908 and 940 cm^{-1} were assigned to the $[SF_3]^+$ cation.[53] A ^{19}F NMR spectroscopy study of the SF_4/AsF_5 system by Barr and Dunell reported the presence of two distinct resonances with a 1:2 ratio consistent with the formation of the ionic salt $[SF_3][AsF_6]$.[54] Solid-state Raman spectroscopy studies were carried out on the SF_4/MF_5 (M = As and Sb) system and compared to the known $K[AsF_6]$ and $K[SbF_6]$ salts showing bands attributable to the respective anions providing further evidence for an ionic species.[55] Bands associated with the $[SF_3]^+$ in $[SF_3][AsF_6]$ were not confidently assigned until Gillespie et al. confirmed its existence in the solid and solution state by Raman (Table 1.1) and NMR spectroscopies, as well as conductivity measurements.[21] The ^{19}F NMR spectra of $[SF_3][AsF_6]$ and $[SF_3][SbF_6]$ in aHF showed peaks at 30.5 and 27.1 ppm, respectively, attributed to $[SF_3]^+$ while the anions, $[AsF_6]^-$ and $[SbF_6]^-$, were not observed because of exchange of fluoride with the solvent and quadrupole relaxation of the ^{75}As (I = 3/2), ^{121}Sb (I = 5/2), and ^{123}Sb (I = 7/2) nuclei.

Bartlett and coworkers obtained the X-ray crystal structure of $[SF_3][BF_4]$ which crystallized in the *Pnma* space group and showed fluorine bridges between the cation and anion.[56] The sulfur center of $[SF_3]^+$, a cation adopting an approximate C_{3v} symmetry, contained a coordination number of six with three contacts to fluorine atoms of $[BF_4]^-$ (S---F: 2x 2.624(2) and 2.593(3) Å).

Table 1.1 Vibrational frequencies (cm^{-1}) of the $[SF_3][AsF_6]$ salt as reported from reference 21.

Frequency	Assignment
960	ν_1 and ν_3 $[SF_3]^+$
945	
926	
686	ν_1 $[AsF_6]^-$
587	ν_2 $[AsF_6]^-$
563	
530	ν_2 $[SF_3]^+$
411	ν_4 $[SF_3]^+$
379	ν_5 $[AsF_6]^-$

Subsequently, Bartlett prepared the $[SF_3][GeF_5]$ salt by displacement of BF_3 from $[SF_3][BF_4]$ with GeF_4 at −126 °C (Equation 1.15), as well as, the $[SF_3]_2[GeF_6]$ salt by reaction of two equivalents of SF_4 with GeF_4 (see Equation 1.16).[57,58] These compounds were both characterized by Raman spectroscopy, and crystals of $[SF_3]_2[GeF_6]$ were obtained by sublimation at 30−35 °C. The crystal structure of $[SF_3]_2[GeF_6]$ contained a C_{3v}-symmetric cation which exhibits a coordination environment similar to that of $[SF_3][BF_4]$ where the sulfur center has contacts with three fluorine atoms of different $[GeF_6]^{2-}$ anions (2x 2.367(2) and 2.420(1) Å).

$$[SF_3][BF_4] + GeF_4 \longrightarrow [SF_3][GeF_5] + BF_3 \quad (1.15)$$

$$2SF_4 + GeF_4 \longrightarrow [SF_3]_2[GeF_6] \quad (1.16)$$

1.3.1 $[SF_3]^+$·Nitrogen-Base Adducts

The $[SF_3]^+$ cation is highly Lewis acidic and has been found to form adducts with nitrogen bases including pyridine and acetonitrile via S---N bonding interactions. The first report of a Lewis acid-base adduct claimed the formation of $[SF_3{\cdot}NCCH_3]^+$.[59] Fluorine-

19 NMR spectroscopy studies of $[SF_3][AsF_6]$ and CH_3CN in SO_2 at −30 °C showed a change in chemical shift of $[SF_3]^+$ to 17.4 ppm upon addition of CH_3CN compared to $[SF_3]^+$ in SO_2 (30.5 ppm). It was concluded that the 1:1 adduct $[SF_3{\cdot}NCCH_3][AsF_6]$ was formed in solution (Equation 1.17). This study also suggested that an equilibrium exists whereby the $[SF_3{\cdot}NCCH_3][AsF_6]$ salt slowly dissociates into SF_4 and the $AsF_5{\cdot}NCCH_3$ adduct (see Equation 1.18).

$$[SF_3][AsF_6] + NCCH_3 \overset{-30\ ^\circ C}{\rightleftharpoons} [SF_3{\bullet}NCCH_3][AsF_6] \quad (1.17)$$

$$[SF_3{\bullet}NCCH_3][AsF_6] \rightleftharpoons SF_4 + AsF_5{\bullet}NCCH_3 \quad (1.18)$$

Evidence for the $[SF_3{\cdot}(NCCH_3)_2]^+$ and $[SF_3{\cdot}(NC_5H_5)_2]^+$ adducts has been reported based on mass spectrometry studies and ab initio calculations for the reaction enthalpies, bond dissociation energies, and optimized geometries for the adducts.[60–61]

Chaudhary has recently synthesized a variety of $[SF_3]^+$ adducts with nitrogen bases including pyridine, acetonitrile, and phenanthroline.[62] The reactions were carried out at −40 °C in solvents such as CH_3CN, CH_2Cl_2, and SO_2 and characterized by Raman spectroscopy and ^{19}F NMR spectroscopy. The characteristic $\nu_s(SF_3)$ bands were shifted to lower frequencies by upwards of 139 cm^{-1}. The ^{19}F chemical shifts of the $[SF_3{\cdot}(NCCH_3)_2]^+$ and $[SF_3{\cdot}(NC_5H_5)_2]^+$ cations in SO_2 were shifted to lower frequencies, between 18.5 and 16.8 ppm, in comparison to the values for $[SF_3][MF_6]$ (M = As or Sb) in SO_2 (32.9, 31.5 ppm). The X-ray crystal structures of $[SF_3{\cdot}(NCCH_3)_2][MF_6]$, $[SF_3{\cdot}(NC_5H_5)_2][MF_6]$, and $[SF_3{\cdot}(phen)][SbF_6]$ were also obtained (M = As or Sb).

1.4 Goals of Present Research

Selective fluorination of organic molecules is currently a very active area of research and can be highly valuable for industries such as the pharmaceutical and agrochemical fields. Finding compounds which can more easily and selectively fluorinate a carbonyl functional group requires a better understanding of the deoxofluorination reaction mechanism. The primary goal of this thesis is to explore the Lewis acid-base interactions between $[SF_3]^+$, a highly electrophilic cation believed to be the active species in deoxofluorination reactions, and carbonyl bases. One of the proposed intermediates in deoxofluorination reactions is the $[R{-}O{-}SF_3]^+$ cation (R = any alkyl substituent), however, it has yet to be isolated in solution or solid states.[19] Based on previous studies of the $[SF_3{\cdot}(\text{nitrogen-base})_x]^+$ adducts,[62] the $[SF_3{\cdot}(\text{oxygen-base})_x]^+$ (x = 1 or 2) adducts are believed to be stable at low temperatures (< −45 °C), and so the use of LT Raman spectroscopy and ^{19}F and ^{1}H NMR spectroscopy will be used to study these systems in the solution and solid states. In addition, reactions of $[SF_3][AsF_6]$ with ketones and aldehydes in aHF will be carried out at low temperatures in an attempt to shed light on possible intermediates in deoxofluorination reactions.

Sulfur tetrafluoride, a well-known deoxofluorinating agent, has been shown to form Lewis acid-base adducts with ketones.[50] This thesis looks to expand the scope of these reactions to include acetone, the simplest aliphatic ketone, and 2-adamantanone, a bulky polycyclic ketone. Like the $SF_4{\cdot}(O{=}C_5H_8)_2$ adduct previously studied, the reactions between SF_4 and acetone, and SF_4 and 2-adamantanone, will be carried out at low temperatures. X-ray crystallography, together with LT Raman spectroscopy, will be used

to characterize these compounds. Specialized low-temperature mounting techniques will be required when handling these highly temperature and moisture sensitive adducts.

The overall goal of this thesis is to explore the Lewis acid-base interactions between organic carbonyl compounds and Lewis acids such as SF_4 and the $[SF_3][AsF_6]$ salt, as well as, possible side-products present in these reactions. Different solvents and varying temperatures will be used to carry out these reactions. By using low-temperature techniques to synthesize and characterize these compounds, in conjunction with quantum-chemical calculations, insight into the currently speculated mechanisms of deoxofluorination reactions will be explored.

References

[1] (a) Purser, S.; Moore, P. R.; Swallow, S.; Gouverneur, V. *Chem. Soc. Rev.* **2008**, *37*, 320−330. (b) Müller, K; Faeh, C.; Diederch, F. *Science* **2007**, *317*, 1881−1886. (c) Jeschke, P. *ChemBioChem* **2004**, *5*, 570−589. (d) Banerjee, S. *Handbook of Specialty Fluorinated Polymers* Elsevier, 1st edn: Oxford, 2015; Chapter 1−6. (e) Ametamey, S. M.; Honer, M.; Schubiger, P. A. *Chem. Rev.* **2008**, *108*, 1501−1516.

[2] Thayer, A. M. *Chem. Eng. News* **2006**, *84*, 15−24.

[3] (a) Bondi, A. *J. Phys. Chem.* **1964**, *68*, 441−451. (b) O'Hagan, D. *Chem. Soc. Rev.* **2008**, *37*, 308−319.

[4] (a) Neumann, C. N.; Ritter, T. *Angew. Chem Int. Ed.* **2015**, *54*, 3216–3221. (b) Furuya, T.; Kamlet, A. S.; Ritter, T. *Nature* **2012**, *473*, 470–477.

[5] (a) Gerstenberger, M. R. C.; Haas, A. *Angew. Chem. Int. Ed. Eng.* **1981**, *20*, 647–667. (b) Gerhardt, G. E.; Lagow, R. J. *J. Chem. Soc. Perkin Trans. 1* **1981**, 1321−1328.

[6] Banks, R. E.; Smart, B. E.; Tatlow, J. C. *Organofluorine Chemistry: Principles and Commercial Applicatioins* Plenum Press: New York, 1994; Chapter 7.

[7] Olah, G. A.; Welch, J. T.; Vankar, Y. D.; Nojima, M.; Kerekes, I.; Olah, J. A. *J. Org. Chem.* **1979**, *44*, 3872−3881.

[8] Christe, K. O.; Wilson, W. W.; Wilson, R. D.; Bau, R.; Feng, J. A. *J. Am. Chem. Soc.* **1990**, *112*, 7619−7625.

[9] (a) Umemoto, T.; Tomizawa, G. *J. Org. Chem.* **1995**, *60*, 6563−6570. (b) Nyffeler, P. T.; Durón, S. G.; Burkart, M. D.; Vincent, S. P.; Wong, C. H. *Angew. Chem. Int. Ed.* **2004**, *44*, 192−212.

[10] Lal, G. S.; Pez. G. P.; Syvret, R. G. *Chem. Rev.* **1996**, *96*, 1737−1755.

[11] Banks, R. E.; Mohialdin-Khaffaf, S. N.; Lal G. S.; Sharif, I.; Syvret, R. G. *J. Chem. Soc. Chem. Commun.* **1992**, 595−596.

[12] Hart, J. J.; Syvret, R. G. *J. Fluorine Chem.* **1999**, *100*, 157−161.

[13] Banks, R. E. *J. Fluorine Chem.* **1998**, *87*, 1−17.

[14] Stavber, G.; Zupan, M.; Jereb, M.; Stavber, S. *Org. Lett.* **2004**, *6*, 4973−4976.

[15] (a) Smith, W. C. U.S. Patent 2859245, 1958. (b) Hasek, W. R.; Smith, W. C.; Engelhardt, V. A. *J. Am. Chem. Soc.* **1960**, *82*, 543−551. (c) Smith, W. C. *Angew. Chem. Int. Ed.* **1962**, *1*, 467−518.

[16] Wang, C. -L. *J. Org. React*. **1985**, *34*, 319−400.

[17] Martin, D. G.; Kagan, F. *J. Org. Chem.* **1962**, *27*, 3164−3168.

[18] Baum, K. *J. Am. Chem. Soc.* **1969**, *91*, 4594.

[19] (a) Dmowski, W.; Kolinksi, R. *Pol. J. Chem.* **1978**, *52*, 547−559. (b) Dmowski, W. *J. Fluorine Chem.* **1986**, *32*, 255−282.

[20] Nazaretian, V. P.; Pustovit, Y. M. *J. Fluorine Chem.* **1991**, *55*, 29−36 and references therein.

[21] Azeem, M.; Brownstein, M.; Gillespie, R. J. *Can. J. Chem.* **1969**, *47*, 4159−4167.

[22] Pashinnik, V. E. *Russ. J. Org. Chem.* **2000**, *36*, 350−358.

[23] Middleton, W. J. *J. Org. Chem.* **1975**, *40*, 574−578.

[24] Messina, P. A.; Mange, K. C.; Middleton, W. J. *J. Fluorine Chem*. **1989**, *42*, 137−143.

[25] Lal, G. S.; Pez, G. P.; Pesaresi, R. J.; Prozonic, F. M.; Cheng, H. *J. Org. Chem*. **1999**, *71*, 7048−7054.

[26] Yin, J.; Zarkowsky, D. S.; Thomas, D. W.; Zhao, M. M.; Huffman, M. A. *Org. Lett*. **2004**, *6*, 1465−1468.

[27] (a) Beaulieu, F.; Beauregard, L.-P.; Courchesne, G.; Couturier, M.; LaFlamme, F.; L'Heureux, A. *Org. Lett*. **2009**, *11*, 5050−5053. (b) L'Heureux, A.; Beaulieu, F.; Bennett, C.; Bill, D. R.; Clayton, S.; LaFlamme, F.; Mirmehrabi, M.; Tadayon, S.; Tovell, D.; Couturier, M. J. *Org. Chem*. **2010**, *75*, 3401−3411. (c) XtalFluor-E and M are registered trademarks of OmegaChem, Inc.

[28] (a) Umemoto, T.; Xu, Y. U.S. Patent 7265247, 2007. (b) Umemoto, T.; Singh, R. P. U.S. Patent 7381846, 2008. (c) Umemoto, T.; Singh, R. P.; Xu, Y.; Saito, N. *J. Am. Chem. Soc*. **2010**, *132*, 18199−18205. (d) Singh, R. P.; Umemoto, T. *J. Org. Chem*. **2011**, *76*, 3113−3121. (e) Xu, W.; Martinez, H.; Dolbier, W. R., Jr. *J. Fluorine Chem*. **2011**, *132*, 482−488. (f) Fluolead is a trademark of UBE America, Inc.

[29] Seel, F. *Adv. Inorg. Chem. Radiochem.* **1974**, *16*, 297–333.

[30] Christe, K. O.; Dixon, D. A.; McLemore, D.; Wilson, W. W.; Sheehy, J. A.; Boatz, J. A.. *J. Fluorine Chem.* **2000**, *101*, 151–153.

[31] Clark, M.; Kellen-Yuen, C. J.; Robinson, K. D.; Zhang, H.; Yang, Z. Y.; Madappat, K. V.; Fuller, J. W.; Atwood, J. L.; Thrasher, J. S. *Eur. J. Solid State Inorg. Chem.* **1992**, *24*, 809–833.

[32] Bittner, J.; Fuchs, J.; Seppelt, K. *Z. Anorg. Allg. Chem.* **1988**, *557*, 182–190.

[33] Dodd, R. E.; Woodward, L. A.; Roberts, H. L. *Trans Faraday Soc.* **1956**, *52*, 1052−1061.

[34] Raffael, K. D.; Smith, D. M. *J. Mol. Spectrosc.* **2002**, *214*, 21−27.

[35] Raffael, K. D.; Smith, D. M.; Newnham, D. A. *J. Mol. Spectrosc.* **2003**, *218*, 108−113.

[36] Ewing, V. C.; Sutton, L. E. *Trans Faraday Soc.* **1963**, *59*, 1241−1247.

[37] Kimura, K.; Bauer, S. H. *J. Chem. Phys.* **1963**, *39*, 3172−3178.

[38] Spring, C. A.; True, N. S. *J. Am. Chem. Soc.* **1983**, *105*, 7231−7236.

[39] Pavone, M.; Barone, V.; Ciofini, I.; Adamo, C. *J. Chem. Phys.* **2004**, *120*, 9167−9174.

[40] Goettel, J. T.; Kostiuk, N.; Gerken, M. *Angew. Chem. Int. Ed.* **2013**, *52*, 8037–8040.

[41] Muetterties, E. L. *J. Am. Chem. Soc.* **1960**, *82*, 1082−1087.

[42] Padma, D. K. *J. Fluorine Chem.* **1974**, *4*, 441−443.

[43] Sass, C. S.; Ault, B. S. *J. Phys. Chem.* **1985**, *89*, 1002−1006.

[44] Goettel, J. T.; Chaudhary, P.; Hazendonk, P.; Mercier, H. P. A.; Gerken, M. *Chem. Commun.* **2012**, *48*, 9120−9122.

[45] Chaudhary, P.; Goettel, J. T.; Mercier, H. P. A.; Sowlati-Hashjin, S.; Hazendonk, P.; Gerken, M. *Chem. Eur. J.* **2015**, *21*, 6247–6256.

[46] Goettel, J. T.; Kostiuk, N.; Gerken, M. *Inorg. Chem.* **2016**, *55*, 7126−7134.

[47] Muetterties, E. L. U.S. Patent 2,729,663, 1959.

[48] Azeem, M. *Pak. J. Sci. Ind. Res.* **1967**, *10*, 10−12.

[49] Sass, C. S.; Ault, B. S. *J. Phys. Chem.* **1985**, *89*, 1002−1006.

[50] Goettel, J. T.; Gerken, M. *Inorg. Chem.* **2016**, *55*, 12441−12450.

[51] Bartlett, N.; Robinson, P. L. *Chem. Ind. London* **1956**, 1351.

[52] Cotton, F. A.; George, J. W. *J. Inorg. Nucl. Chem.* **1958**, *7*, 397−403.

[53] Seel, F.; Detmer, O. *Z. Anorg. Allg. Chem.* **1959**, *301*, 113−232.

[54] Barr, M. R.; Dunell, B. A. *Can. J. Chem.* **1970**, *48*, 895−903.

[55] Evans, J. A.; Long, D. A. *J. Chem. Soc. A* **1968**, 1688−1694.

[56] Gibler, D. D.; Adams, C. J.; Fischer, M.; Zalkin, A.; Bartlett, N. *Inorg. Chem.* **1972**, *11*, 2325−2329.

[57] Mallouk, T. E.; Bernard, D.; Bartlett, N. *Inorg. Chem*. **1984**, *23*, 3160−3166.

[58] Mallouk, T. E.; Rosenthal, G. L.; Müller, G.; Brusasco, R.; Bartlett, N. *Inorg. Chem*. **1984**, *23*, 3167−3173.

[59] Erhart, M.; Mews, R. *Z. Anorg. Allg. Chem.* **1992**, *615*, 117−122.

[60] Sparrapan R.; Mendes M. A.; Eberlin M. N. *Int. J. Mass Spec*. **1999**, *182/183*, 369−380.

[61] Gozzo, F. C.; Ifa, D. R.; Eberlin, M. N. *J. Org. Chem*. **2000**, *65*, 3920−3925.

[62] Chaudhary, P. PhD Dissertation, University of Lethbridge, 2016.

2. Experimental

CAUTION! Anhydrous HF (aHF) is extremely toxic and corrosive. Exposure can cause severe burns and cause irreparable damage if contact with the skin occurs. It should be handled with extreme care. For the risk and treatments of HF burns the literature should be consulted.[1]

2.1 General Methods

The chemistry presented in this thesis is highly temperature- and moisture-sensitive requiring strictly anhydrous conditions. All reactions were carried out under rigorously dried and inert atmospheres using glass and metal vacuum lines, and a nitrogen-atmosphere dry box (Omni Lab, Vacuum Atmospheres). Nitrogen (99.99%, Praxair) was passed through a column containing anhydrous calcium sulfate (cobalt chloride indicator) and activated 4 Å molecular sieves. Edwards two-stage direct-drive RV8 vacuum pumps were used for the metal and glass vacuum lines, and the antechambers of the glove box. The vacuum on the glass and metal lines was approximately 10^{-3} Torr and 10^{-2} Torr, respectively, and were verified by a mercury McLeod gauge (Labconco).

Pyrex-glass vacuum lines equipped with grease-free 6-mm J. Young glass stopcocks with PTFE (polytetrafluoroethylene) barrels were used to manipulate non-corrosive volatiles which do not react with glass (see Figure 2.1). Heise gauges (model CC, 0-1000 mmHg, beryllium/copper Bourdon tube, Dresser Instruments) were used to measure pressures inside the glass manifold. The final vacuum was monitored by Varian model 801 thermocouple gauges connected to the vacuum lines between the liquid nitrogen traps and the vacuum pumps.

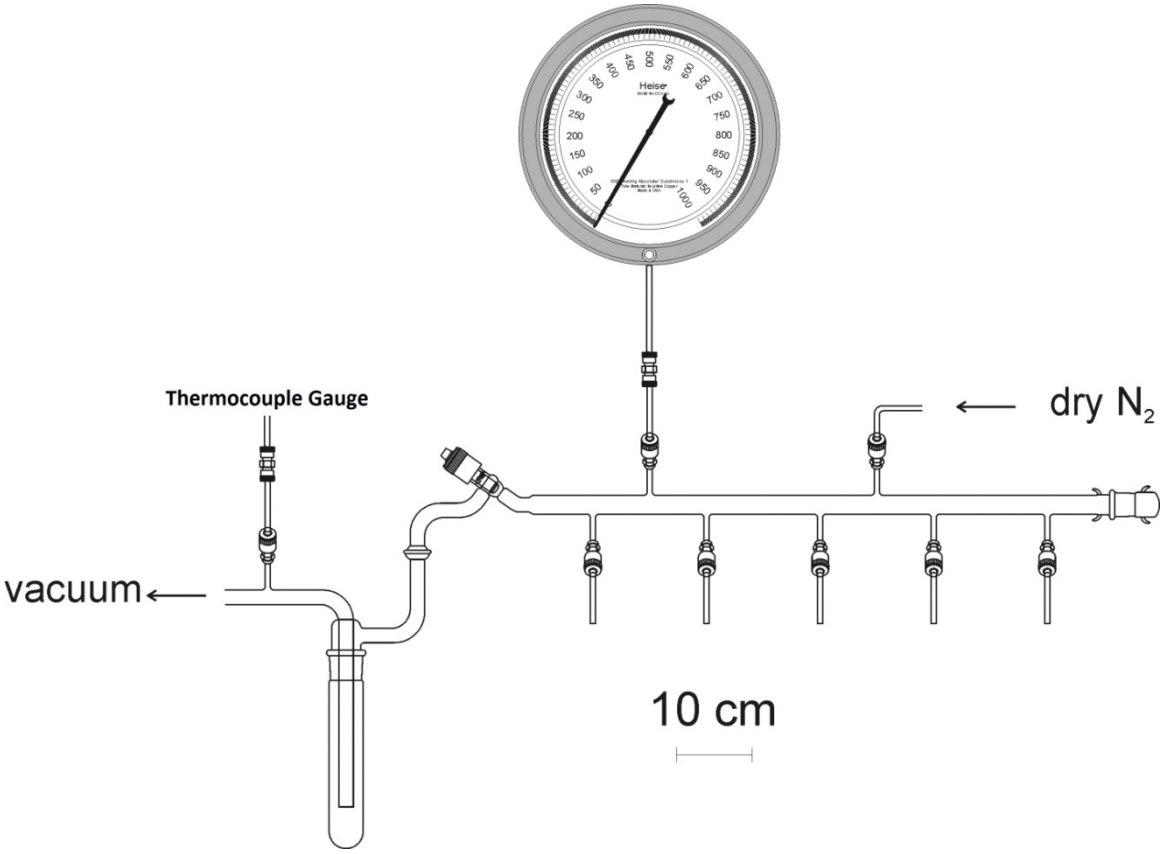

Figure 2.1 Glass vacuum line system equipped with J. Young PTFE/glass stopcocks, a Heise and thermocouple gauge, and vacuum/nitrogen manifolds (Adapted from Jared Nieboer's M.Sc. Thesis, Ref. 2).

Work involving volatile and corrosive fluorides that react with glass (e.g., SF_4) was carried out on a metal vacuum line (see Figure 2.2) constructed primarily from 316 stainless steel and nickel along with 316 stainless steel valves (Autoclave Engineers, Inc.). PTFE tube fitting connectors (Swagelok) were used to connect ¼-in. o.d. FEP (Perfluorinated Ethylene Propylene co-polymer) reactors to the metal line. Three vacuum pumps were connected to the metal line: two pumps for fine vacuum connected to small towers of activated charcoal; and one roughing pump connected to a fluoride/fluorine trap consisting of a stainless-steel cylinder (75-cm length, 17-cm outer diameter) packed with soda lime absorbent (EMD, 4 mesh). The fine vacuum pumps provided high vacuum to each

respective side of the metal line. The roughing vacuum provided a method of removal and disposal of volatile reactive fluorinated compounds (i.e. SF_4 and F_2) for both sides of the metal lines. Pressures were measured using Baratron capacitance manometers (MKS, Type 626A, effective range 0-1000 mmHg) having inert wetted surfaces constructed of Inconel, connected to digital readouts.

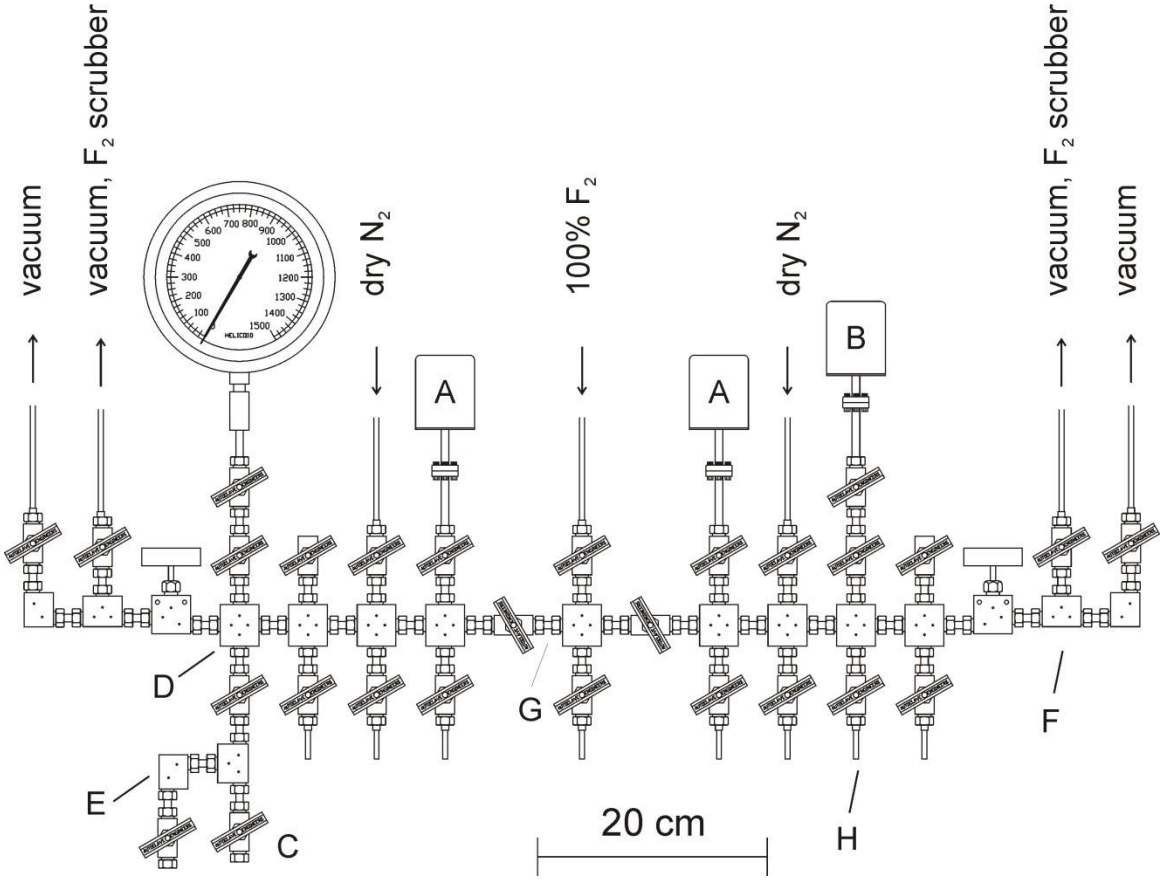

Figure 2.2 Metal vacuum system; (A) MKS type 626A capacitance manometer (0-1000 Torr), (B) MKS Model PDR-5B pressure transducers (0-10 Torr), (C) 3/8-in. stainless- steel high-pressure valves (Autoclave Engineers, 30VM6071), (D) 316 stainless-steel cross (Autoclave Engineers, CX6666), (E) 316 stainless-steel L-piece (Autoclave Engineers, CL6600), (F) 316 stainless steel T-piece (Autoclave engineers, CT6660), (G) 3/8-in o.d., 1/8-in. i.d. nickel connectors, (H) 1/8-in o.d., 1/8-in. i.d. nickel tube. (from Jared Nieboer's M.Sc. thesis, Ref. 2).

Most synthetic work was carried out in reactors constructed from lengths of ¼-in. o.d. FEP tubing which were heat-sealed at one end and heat-flared (45° SAE) at the other. The tubing was connected to Kel-F (chlorotrifluoroethylene polymer) valves, encased in aluminum housings, using brass (45° SAE) flared nuts (Figure 2.3). All vessels were then connected to a glass vacuum line using ¼-in. stainless steel Swagelok Ultratorr unions fitted with Viton elastomer O-rings and were rigorously dried by pumping for a minimum of 6 h under dynamic vacuum. The FEP vessels were then connected to the metal vacuum line and passivated with ca. 1000 Torr of F_2 for ca. 12 h. Passivated vessels were evacuated under dynamic vacuum to remove all volatile impurities and back-filled with dry N_2 (ca. 900 Torr) prior to use. Connections made to a glass vacuum line were dried under dynamic vacuum for several hours. All connections to vacuum lines were made using thick-walled ¼-in. FEP tubing in conjunction with either a ¼-in. Teflon Swagelok connector outfitted with Teflon compression fittings (front and back ferrules), used on the metal line, or ¼-in. stainless steel Swagelok Ultra-Torr connectors outfitted with stainless steel compression fittings and Viton elastomer O-rings, used on the glass lines.

Reactions intended for characterization by NMR spectroscopy were performed in reactors crafted from straightened and sealed 4-mm o.d. FEP tubing that was joined to a short, flared ¼-in. FEP connecting piece. After the contents of the sample were prepared, the 4-mm tube was sealed using a heat gun while the sample was cooled with liquid nitrogen (−196 °C) and placed under dynamic vacuum. This sealed 4-mm tube could then be inserted into a thin-walled 5-mm glass NMR tube before being lowered into the NMR magnet for characterization.

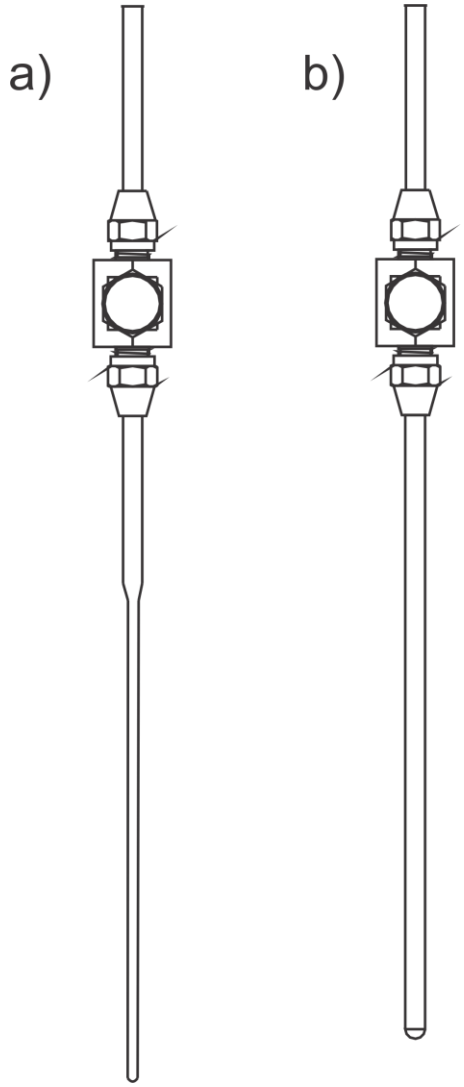

Figure 2.3 Diagrams of (a) a ¼-in. o.d. and (b) 4-mm o.d. FEP reactor fitted with a Kel-F valve. (from Jared Nieboer's M.Sc. thesis, Ref. 2).

2.2 Preparation and Purification of Starting Materials

2.2.1 Sources and Purification of N_2 and F_2

Nitrogen gas (99.99%, Praxair) was dried by passing it through a cartridge of drierite and molecular sieves prior to use. Technical grade fluorine gas (Air Products, >98%) was used without further purification.

2.2.2 Solvent Purification; Anhydrous HF (aHF), SO_2, CH_2Cl_2, and $CFCl_3$

(i) aHF: Anhydrous hydrogen fluoride (Air Products) was stored at room temperature in a nickel storage vessel equipped with a monel (Autoclave Engineers) valve. Hydrogen fluoride was pre-dried with fluorine gas in a ¾-in. o.d. FEP vessel equipped with a stainless-steel valve. The vessel was evacuated and backfilled with approximately 900 Torr of pure fluorine gas. The vessel was agitated periodically for two weeks. After agitating the vessel over a period of two weeks, the HF was vacuum distilled onto potassium hexafluoro-nickelate(IV) in a ¾-in o.d. FEP vessel (see Figure 2.4), equipped with a stainless steel valve, and backfilled with ca. 900 Torr nitrogen. Figure 2.4 shows the distillation setup used to transfer HF from the ¾-in. o.d. FEP vessel to reaction vessels by vacuum distillation on the metal vacuum line through a FEP T-piece FEP connection.

(ii) SO_2: Sulfur dioxide (Matheson Gas Products Canada) was vacuum distilled from a cylinder onto CaH_2 in a dried, glass storage bulb equipped with a Teflon J. Young stopcock.

(iii) CH_2Cl_2: Dichloromethane was dispensed by an MBraun dry solvent system and then vacuum distilled onto freshly activated 4 Å molecular sieves in a dry Pyrex glass bulb fitted with a J. Young PTFE stopcock after being degassed by the freeze-pump-thaw method.

(iv) $CFCl_3$: Trichlorofluoromethane was vacuum distilled onto calcium hydride, and vacuum distilled into a dry, evacuated flask with a J. Young PTFE stopcock.

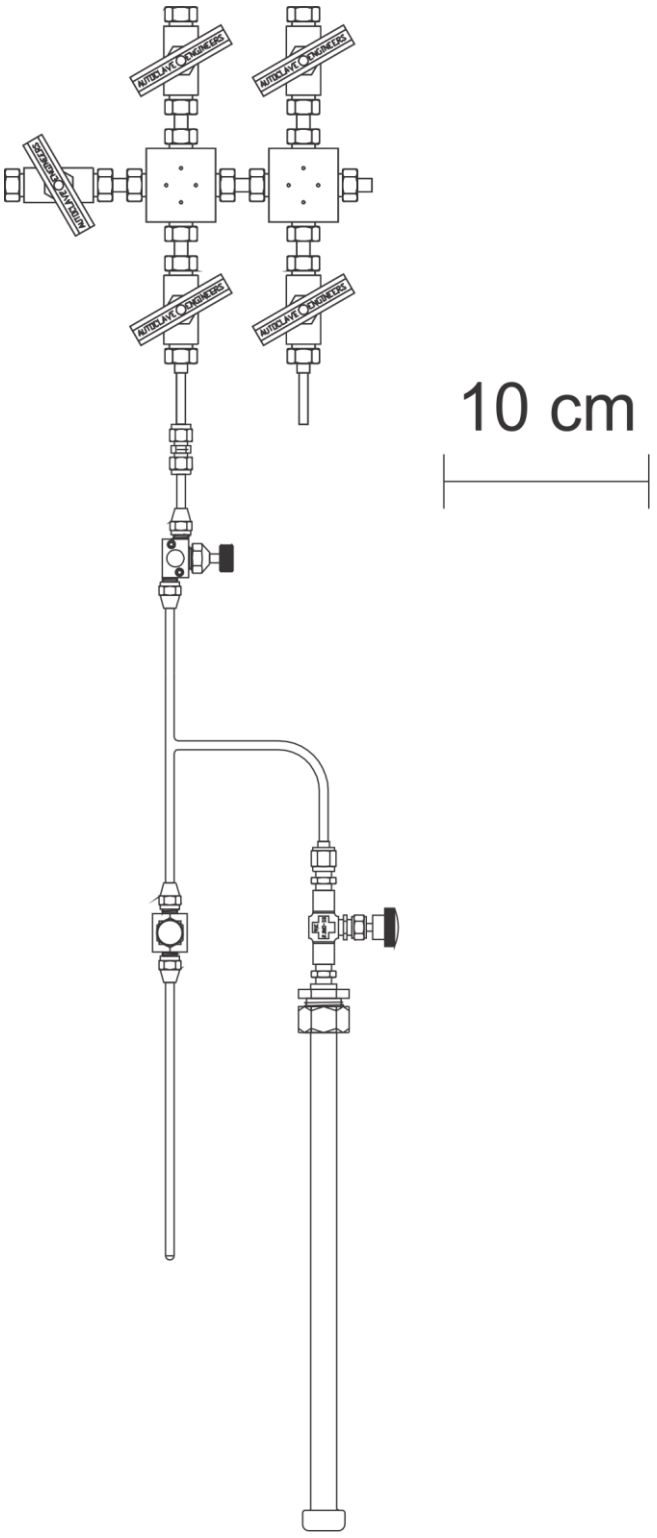

Figure 2.4 A ¾-in. o.d. FEP vessel equipped with a stainless steel valve and a FEP T-piece connection for the distillation of HF into reactors. (from Jared Nieboer's M.Sc. thesis, Ref. 2).

2.2.3 Purification of Oxygen-Bases

(i) Acetone ($O=C(CH_3)_2$): Acetone (Sigma-Aldrich, 99.5%) was stored over B_2O_3 in a dried, glass bulb with a J. Young PTFE stopcock.

(ii) Cyclopentanone ($O=C_5H_8$): Cyclopentanone (BDH/VWR, 99%) was stored in a dry, glass bulb with a J. Young PTFE stopcock and used as is.

(iii) 2-Adamantanone ($O=C_{10}H_{14}$): 2-Adamantanone (Sigma-Aldrich, 99%) was stored in a nitrogen-atmosphere dry box and used as received.

2.2.4 Synthesis and Purification of SF_4, SbF_3 and AsF_5

Sulfur tetrafluoride (Ozark-Mahoning Co.) was purified by passing the gas through a U-trap containing activated charcoal, removing any trace amounts of S_2F_{10} which would interfere with reactions. The SF_4 did contain trace amounts of thionyl fluoride (SOF_2) and sulfur hexafluoride (SF_6), however, these were assumed not to interfere with any chemistry. The SF_4 was stored in a stainless steel cylinder fitted with a stainless steel valve.

Antimony trifluoride, SbF_3 (Ozark Fluorine Specialities), was sublimed under vacuum and transferred into a storage vessel in a nitrogen-atmosphere dry box.

Arsenic pentafluoride, AsF_5, was prepared according to the literature procedure and stored in a nickel reactor with a monel (Autoclave Engineers) valve.[3] AsF_3 was dried over NaF for 24 h to remove any trace amounts of HF which was subsequently transferred to a ¾-in. o.d. FEP reactor and directly fluorinated with an excess of F_2 to yield hydrogen fluoride-free AsF_5.

2.2.5 Synthesis of $[SF_3][AsF_6]$

The $[SF_3][AsF_6]$ salt was prepared according to the literature method.[4] On a steel vacuum line, AsF_5 (a total of 1658 Torr was added inside the metal vacuum line of 0.01953 mL of volume, 1.77 mmol) was vacuum distilled into a ¼-in. o.d. FEP reactor and approximately a 1.6-fold excess of SF_4 (a total of 2737 Torr was added inside the metal vacuum line of 0.01953 mL of volume, 2.92 mmol) was vacuum distilled into the same reactor at −196 °C. The reaction was carried out at −78 °C and then slowly warmed to −38 °C while constantly being agitated to ensure the reaction went to completion. A white powder appeared and the excess SF_4 was removed by pumping on the solid at RT. The purity of the $[SF_3][AsF_6]$ (0.49 g, 1.76 mmol) was confirmed by Raman spectroscopy. This salt was then stored in a nitrogen-atmosphere dry box until further needed.

2.3 Reactions of SF_4 with Ketones

2.3.1 Reaction of SF_4 with 2-Adamantanone

Approximately 0.020 g (0.13 mmol) of 2-adamantanone was transferred into a ¼-in. o.d. FEP reactor in a dry box. Sulfur tetrafluoride (a total of 1624 Torr was added inside the metal vacuum line of 0.01953 mL of volume, 1.74 mmol) was distilled upon the solid at −196 °C on a metal vacuum line. The mixture was warmed to −90 °C where the 2-adamantanone was attempted to be dissolved in the SF_4. At −67 °C the white powder was dissolved by constant agitation and a clear, colourless solution remained. Slow cooling to approximately −75 °C resulted in the formation of a fine suspension. This powder was characterized by Raman spectroscopy at −90 °C, however, no signs of adduct formation were observed as only signals of reactants were detected. The excess SF_4 was pumped off

at −65 °C through a FEP U-trap under dynamic vacuum at −196 °C. However, after removing approximately half of the liquid a white solid appeared on the walls of the reactor. The FEP reactor was back-filled with N_2, redissolved in the SF_4, and cooled to −75 °C where signs of a white solid appeared. The reactor was left in a cryobath at −78 °C for approximately 3 weeks, whereby clear, colourless crystals were formed halfway up the walls of the reactor. Remaining SF_4 was removed under similar conditions described above and the crystals were isolated from the reaction vessel and mounted on the X-ray diffractometer using low-temperature mounting techniques. A single crystal was isolated and shown to be $SF_4 \cdot (O=C_{10}H_{14}) \cdot (HF)$.

2.3.2 Reactions of SF_4 with Acetone

2.3.2.1 Reaction of SF_4 with One Equivalent of Acetone

Acetone (0.077 g, 1.3 mmol) was distilled into a ¼-in. o.d. FEP reactor on a glass vacuum line at −196 °C. The SF_4 (a total of 1366 Torr was added inside the metal vacuum line of 0.01953 mL of volume, 1.46 mmol) was distilled onto the frozen acetone over a metal vacuum line at −196 °C. The reaction of SF_4 with acetone was carried out at −91 °C in an ethanol bath and yielded a clear colourless solution. White blocks began to crystallize by slowly cooling the reaction to −96 °C. The crystals were collected by pumping on the reaction mixture at −100 °C to remove any remaining SF_4 into a FEP U-trap under dynamic vacuum at −196 °C. The crystals were characterized by Raman spectroscopy at −110 °C.

In a second attempt to grow crystals of this reaction, acetone (0.020 g, 0.34 mmol) was reacted with slightly more than one equivalent of SF_4 (0.055 g, 0.51 mmol) at −98 °C where a clear, colourless solution was formed. The sample was slowly cooled to −106 °C

where blocks of clear, colourless crystals were grown. The excess SF_4 was pumped off at −112 °C into a FEP U-trap under dynamic vacuum at −196 °C. The clear, colourless block-like crystals remained and were isolated from the reaction vessel and mounted on the X-ray diffractometer using low-temperature mounting techniques. Handling and growing these crystals proved to be extremely challenging since the crystals would melt upon warming above −106 °C. After attempting to mount multiple crystals, a single crystal was obtained, albeit of poor quality, and unambiguously identified as $[SF_4{\cdot}O{=}C(CH_3)_2]_2$.

2.3.2.2 Reaction of SF_4 with Two Equivalents of Acetone

Sulfur tetrafluoride (0.071 g, 0.66 mmol) was distilled into a ¼-in. o.d. FEP reactor on a metal vacuum line at −196 °C. Approximately 0.1 mL (ca. 1.35 mmol) of acetone was distilled into a glass graduated weighing vessel equipped with a J. Young PTFE stopcock over a glass vacuum line, and subsequently distilled onto the frozen SF_4 at −196 °C. The reaction was performed at −90 °C and yielded a clear colourless solution. It was left at this temperature for 30 min before cooling to −116 °C, however, there were no signs of crystal formation. When the sample was cooled to −120 °C the solution began to freeze into an amorphous solid. The solid was characterized by Raman spectroscopy at −110 °C.

2.4 Reactions of $[SF_3][AsF_6]$ with Ketones in Solutions

All reactions carried out were monitored using ^{19}F and ^{1}H NMR spectroscopy at −80 °C (acetone solvent) or −70 °C (SO_2 solvent). Each respective sample was first melted at −80 °C, in the case where acetone was the solvent, or −70 °C, in the case where SO_2 was the solvent, using an ethanol bath cooled with liquid nitrogen. Once the sample was fully

melted it was placed in the spectrometer which was pre-cooled to either −80 °C (acetone solvent) or −70 °C (SO_2 solvent). Once the data were recorded at this temperature the sample was removed from the spectrometer and immediately placed in a pre-cooled ethanol bath set to the desired temperature where it was allowed to warm for a well-defined period of time. The sample was removed from the bath and immediately placed back in the spectrometer which remained at the set temperature (−80 °C for acetone solutions; −70 °C for SO_2 solutiouns). This process was repeated for each temperature. The internal temperature of the reaction mixture was never precisely known as only the temperature of the ethanol bath was measured.

2.4.1 Reaction of $[SF_3][AsF_6]$ with Acetone

2.4.1.1 Reaction of $[SF_3][AsF_6]$ with Excess Acetone

$[SF_3][AsF_6]$ (0.012 g, 0.043 mmol) was loaded into a 4-mm FEP reactor in a nitrogen-atmosphere dry box. An excess of acetone (ca. 0.3 mL, 4 mmol) was distilled onto the $[SF_3][AsF_6]$ at −196 °C which was then heat sealed. The reaction was slowly warmed to −80 °C where the $[SF_3][AsF_6]$ dissolved in acetone. The contents of the reaction were warmed to variable temperatures for well defined time periods (−80 °C, −60 °C, −40 °C, −20 °C, and RT) and probed using ^{19}F and ^{1}H NMR spectroscopy at −80 °C.

2.4.1.2 Reaction of $[SF_3][AsF_6]$ with Three Equivalents of Acetone

$[SF_3][AsF_6]$ (0.055 g, 0.20 mmol) was loaded into a 4-mm FEP reactor in a nitrogen-atmosphere dry box. The reactor was connected to a glass vacuum line where an excess of SO_2 (ca. 0.5 mL) solvent was distilled onto the $[SF_3][AsF_6]$ and yielding a clear, colourless solution at RT. Approximately three molar equivalents of acetone (0.035 g, 0.61

mmol) were distilled into a glass graduated weighing vessel equipped with a J. Young PTFE stopcock and subsequently distilled onto the $[SF_3][AsF_6]/SO_2$ at −196 °C. The reactor was heat sealed under dynamic vacuum and slowly warmed to −70 °C where acetone was allowed to react with the $[SF_3][AsF_6]$. The contents of the reaction were characterized using ^{19}F and ^{1}H NMR spectroscopy at −70 °C after allowing the reaction to warm to −65 °C, −40 °C, −20 °C, RT for 2 min, and RT for 10 min.

2.4.1.3 Reaction of $[SF_3][AsF_6]$ with Two Equivalents of Acetone

$[SF_3][AsF_6]$ (0.015 g, 0.054 mmol) was loaded into a 4-mm FEP reactor in a nitrogen-atmosphere dry box. The reactor was connected to a glass vacuum line where an excess of SO_2 (ca. 0.4 mL) solvent was distilled onto the $[SF_3][AsF_6]$ giving a clear, colourless solution at RT. Approximately 2.6 molar equivalents of acetone (0.0078 g, 0.14 mmol) was distilled into a glass graduated weighing vessel equipped with a J. Young PTFE stopcock and subsequently distilled onto the $[SF_3][AsF_6]/SO_2$ at −196 °C. The reactor was heat sealed under dynamic vacuum and slowly warmed to −70 °C where the acetone was allowed to react with the $[SF_3][AsF_6]$. The contents of the reaction were characterized using ^{19}F and ^{1}H NMR spectroscopy at −70 °C after allowing to warm to −60 °C, −45 °C, −40 °C, −35 °C, and RT for 5 min.

2.4.1.4 Reaction of $[SF_3][AsF_6]$ with One Equivalent of Acetone

$[SF_3][AsF_6]$ (0.018 g, 0.065 mmol) was loaded into a 4-mm FEP reactor in a nitrogen-atmosphere dry box. The reactor was connected to a glass vacuum line where an excess of SO_2 (ca. 0.4 mL) solvent was distilled onto the $[SF_3][AsF_6]$ and dissolved at RT

to give a clear, colourless solution. Approximately one molar equivalent of acetone (0.0039 g, 0.068 mmol) was distilled into a glass graduated weighing vessel equipped with a J. Young PTFE stopcock and subsequently distilled onto the $[SF_3][AsF_6]/SO_2$ at −196 °C. The reactor was heat sealed under dynamic vacuum and slowly warmed to −70 °C where the acetone was allowed to react with the $[SF_3][AsF_6]$. The contents of the reaction were characterized using ^{19}F and ^{1}H NMR spectroscopy at −70 °C after allowing to warm to −50 °C, −45 °C, −38 °C, −21 °C, −13 °C, and RT for 45 min.

2.4.2 Reaction of $[SF_3][AsF_6]$ with Cyclopentanone

2.4.2.1 Reaction of $[SF_3][AsF_6]$ with Two Equivalents of Cyclopentanone

$[SF_3][AsF_6]$ (0.019 g, 0.068 mmol) was loaded into a 4-mm FEP reactor in a nitrogen-atmosphere dry box. The reactor was connected to a glass vacuum line where an excess of SO_2 (ca. 0.5 mL) solvent was distilled onto the $[SF_3][AsF_6]$ and dissolved at RT to give a clear, colourless solution. Slightly more than two molar equivalents (i.e., 2.2 molar equivalents) of cyclopentanone (0.013 g, 0.15 mmol) was distilled into a glass graduated weighing vessel equipped with a J. Young PTFE stopcock and subsequently distilled onto the $[SF_3][AsF_6]/SO_2$ at −196 °C. The reactor was heat sealed under dynamic vacuum and slowly warmed to −70 °C where cyclopentanone was allowed to react with the $[SF_3][AsF_6]$. The contents of the reaction were characterized using ^{19}F and ^{1}H NMR spectroscopy at −70 °C after allowing to warm to −63 °C, −35 °C, −15 °C, RT for 1 min, RT for 3 min, and RT for 10 min.

2.4.2.2 Reaction of $[SF_3][AsF_6]$ with One Equivalent of Cyclopentanone

$[SF_3][AsF_6]$ (0.016 g, 0.058 mmol) was loaded into a 4-mm FEP reactor in a nitrogen-atmosphere dry box. The reactor was connected to a glass vacuum line where an excess of SO_2 (ca. 0.4 mL) solvent was distilled onto the $[SF_3][AsF_6]$ and dissolved at RT to give a clear, colourless solution. Slightly more than one molar equivalent (i.e. 1.4 molar equivalents) of cyclopentanone (0.007 g, 0.08 mmol) was distilled into a glass graduated weighing vessel equipped with a J. Young PTFE stopcock and subsequently distilled onto the $[SF_3][AsF_6]/SO_2$ at −196 °C. The reactor was heat sealed under dynamic vacuum and slowly warmed to −70 °C where cyclopentanone was allowed to react with the $[SF_3][AsF_6]$. The contents of the reaction were characterized using ^{19}F and ^{1}H NMR spectroscopy at −70 °C after allowing to warm to −70 °C, −45 °C, −21 °C, RT for 2 min, and RT for 70 min.

2.4.3 Reaction of $[SF_3][AsF_6]$ with 2-Adamantanone

2.4.3.1 Reaction of $[SF_3][AsF_6]$ with Two Equivalents of 2-Adamantanone

$[SF_3][AsF_6]$ (0.045 g, 0.16 mmol) was loaded into a 4-mm FEP reactor in a nitrogen-atmosphere dry box. The reactor was connected to a glass vacuum line where an excess of SO_2 (ca. 0.5 mL) solvent was distilled onto the $[SF_3][AsF_6]$ and dissolved at RT to give a clear, colourless solution. Slightly more than two molar equivalents (i.e., 2.3 molar equivalents) of 2-adamantanone (0.0555 g, 0.369 mmol) was loaded into the reactor in the dry box while the sample remained frozen using a metal Dewar filled with dry 4.5-mm copper-plated spheres that had previously been cooled to ca. −140 °C in the glass cryowell (–196 °C) of the dry box. The reactor was quickly brought out of the dry box and connected to a glass vacuum line where the reactor was heat sealed under dynamic vacuum and slowly

warmed to −70 °C where 2-adamantanone was allowed to react with the $[SF_3][AsF_6]$. A white precipitate appeared upon melting and was required to quickly be warmed to −10 °C where it dissolved and was immediately cooled to −40 °C. The contents of the reaction were characterized using ^{19}F and ^{1}H NMR spectroscopy at −40 °C.

^{1}H NMR (ppm from $Si(CH_3)_4$, in SO_2, −40 °C, $\omega_o(^{1}H)$ = 300 MHz)

Major Component: 2.87 (s), 2.45 (s), 2.41 (s), 2.28 (s), 2.24 (sh), 2.19 (s).

Minor Component: 4.20 (s), 4.14 (s), 3.92 (s), 3.59 (s), 3.42 (s), 3.29 (sh), 3.25 (s), 2.96 (sh), 2.71 (s), 2.60 (s), 2.07 (s).

2.4.3.2 Reaction of $[SF_3][AsF_6]$ with One Equivalent of 2-Adamantanone

$[SF_3][AsF_6]$ (0.018 g, 0.065 mmol) was loaded into a 4-mm FEP reactor in a nitrogen-atmosphere dry box. The reactor was connected to a glass vacuum line where an excess of SO_2 (ca. 0.4 mL) solvent was distilled onto the $[SF_3][AsF_6]$ and dissolved at RT to give a clear, colourless solution. Slightly more than one molar equivalent of 2-adamantanone (0.0101 g, 0.0672 mmol) was loaded into the reactor in the dry box while the sample remained frozen using a metal Dewar filled with dry 4.5-mm copper-plated spheres that had previously been cooled to ca. −140 °C in the glass cryowell (–196 °C) of the dry box. The reactor was quickly brought out of the dry box and connected to a glass vacuum line where the reactor was heat sealed under dynamic vacuum and slowly warmed to −70 °C where 2-adamantanone was allowed to react with the $[SF_3][AsF_6]$. The contents of the reaction were characterized using ^{19}F and ^{1}H NMR spectroscopy at −70 °C after allowing to warm to −70 °C, −65 °C, RT for 5 min, and RT for 2 h.

^{1}H NMR (ppm from $Si(CH_3)_4$, in SO_2, −70 °C, $\omega_o(^{1}H)$ = 300 MHz)

Warmed to −70 °C:

Major Component: 3.27 (s), 2.69 (s), 2.65 (s), 2.54 (s), 2.50 (s), 2.45 (s), 2.32 (s).

Minor Component: 4.30 (s), 4.22 (s), 4.00 (s), 3.70 (s), 3.51 (s), 3.37 (s), 3.33 (s), 3.09 (s), br), 3.05 (s, br), 2.99 (s, br), 2.80 (s), 2.25 (s), 2.13 (s), 2.01 (s).

Warmed to RT for 5 min:

Major Component: 3.26 (s), 2.80 (s), 2.75 (s), 2.67 (s), 2.63 (s), 2.58 (s), 2.52 (s), 2.47 (sh), 2.43 (s), 2.42 (sh), 2.34 (s), 2.29 (s), 2.11 (sh), 2.09 (s), 1.97 (s).

Minor Component: 4.25 (s), 3.64 (s, br), 2.99 (sh, br), 2.94 (s), 2.91 (sh, br), 2.25 (s), 2.01 (s).

Warmed to RT for 2 h:

Major Component: 3.01 (s, br), 2.98 (sh), 2.89 (s), 2.85 (s), 2.75 (sh), 2.73 (s), 2.69 (sh), 2.58 (s), 2.53 (s), 2.45 (s), 2.41 (sh), 2.18 (s).

Minor Component: 4.35 (s), 4.27 (s, br), 4.00 (s), 3.73 (sh), 3.69 (s), 3.53 (s), 3.48 (br), 2.37 (sh), 2.34 (sh), 2.28 (s), 2.12 (s), 2.06 (s).

2.5 Synthesis of Protonated Ketones

2.5.1 Synthesis of $[HO{=}C_{10}H_{14}][AsF_6]$

$[SF_3][AsF_6]$ (0.023 g, 0.083 mmol) was loaded into a ¼-in. o.d. FEP reactor inside a nitrogen-atmosphere dry box followed by distillation of ca. 0.2 mL of aHF which dissolved the salt at room temperature. 2-Adamantanone ($O{=}C_{10}H_{14}$) (0.0126 g, 0.0839 mmol) was loaded into the reactor in the dry box while the sample remained frozen using a metal Dewar filled with dry 4.5-mm copper-plated spheres that had previously been cooled to ca. −140 °C in the glass cryowell (–196 °C) of the dry box. The reactor was quickly

brought out of the dry box and left to react at −78 °C at which point a white solid formed. The reactor was allowed to warm to RT where the solid dissolved and a clear, colourless solution remained. Upon cooling to −20 °C white needle-like crystals formed. The reactor was placed under dynamic vacuum at −72 °C to remove the aHF solvent and SF_4 into a FEP U-trap at −196 °C. A single crystal was found and characterized by X-ray crystallography, using low-temperature mounting techniques, and was shown to be $[HO{=}C_{10}H_{14}][AsF_6]$.

2.5.2 Synthesis of $[HO{=}C_{10}H_{14}][SbF_6]$

SbF_3 (0.077 g, 0.43 mmol) was loaded into a ¼-in. o.d. FEP reactor in a nitrogen-atmosphere dry box. Approximately 0.2 mL of aHF was distilled onto the SbF_3 at −196 °C and backfilled with 1000 Torr of F_2. The reactor was continuously agitated at RT allowing for the dissolution of F_2 and the subsequent reaction with SbF_3 to form SbF_5, until no solid SbF_3 was left. The excess fluorine was removed and the reactor filled with 800 Torr of N_2. 2-Adamantanone (0.0712 g, 0.474 mmol) was loaded into the reactor in the dry box while the sample remained frozen using a metal Dewar filled with dry 4.5-mm copper-plated spheres that had previously been cooled to ca. −140 °C in the glass cryowell (–196 °C) of the dry box. The reactor was quickly brought out of the dry box and left to react at −78 °C at which point a white solid formed. The reactor was warmed to RT to dissolve the product, forming a clear, colourless solution, and slowly cooled to 0 °C for ca. 30 min at which point clear, colourless needles crystallized. The excess aHF was removed under dynamic vacuum at −78 °C into a FEP U-trap at −196 °C. These crystals were characterized using Raman spectroscopy at −100 °C.

2.5.3 Synthesis of [HO=C_5H_8][AsF_6]

[SF_3][AsF_6] (0.048 g, 0.17 mmol) was loaded into a ¼-in. o.d. FEP reactor in a nitrogen-atmosphere dry box then dissolved in ca. 0.2 mL of anhydrous HF (aHF) at room temperature (RT). Cyclopentanone (O=C_5H_8) (0.016 g, 0.19 mmol) was distilled into the reactor at −196 °C from a glass graduated weighing vessel with a J. Young PTFE stopcock. The reaction mixture was warmed to −78 °C. A white powder was present which was dissolved by quickly warming to RT and followed by immediately cooling to −69 °C when white needles crystallized. The reactor was further cooled to −78 °C and aHF and SF_4 removed under dynamic vacuum into a FEP U-trap at −196 °C. A single crystal was found and characterized by X-ray crystallography, using low-temperature mounting techniques, and was shown to be [HO=C_5H_8][AsF_6].

2.5.4 Synthesis of [HO=C_5H_8][SbF_6]

SbF_3 (0.054 g, 0.30 mmol) was loaded into a ¼-in. o.d. FEP reactor in a nitrogen-atmosphere dry box. Approximately 0.2 mL of aHF was distilled onto the SbF_3 at −196 °C and backfilled with 1000 Torr of F_2. The reactor was continuously agitated at RT allowing for the dissolution of F_2 and the subsequent reaction with SbF_3 to form SbF_5, until no solid SbF_3 was left. The excess fluorine was removed and the reactor filled with 800 Torr of N_2. Cyclopentanone (O=C_5H_8) (0.028 g, 0.33 mmol) was distilled onto the HF/SbF_5 at −196 °C from a glass graduated weighing vessel with a J. Young PTFE stopcock and allowed to react at −78 °C forming a white solid. The reactor was quickly warmed to RT to dissolve the product, forming a clear, colourless solution, and immediately cooled to −70 °C for ca. 30 min at which point clear, colourless needles crystallized. The excess aHF was removed

under dynamic vacuum at −78 °C into a FEP U-trap at −196 °C. A single-crystal was found and characterized by X-ray crystallography, using low-temperature mounting techniques, and was shown to contain $[HO{=}C_5H_8][SbF_6]$.

2.5.5 Synthesis of $[HO{=}C(CH_3)_2][SbF_6]$

SbF_3 (0.041 g, 0.23 mmol) was loaded into a ¼-in. o.d. FEP reactor in a nitrogen-atmosphere dry box. Approximately 0.2 mL of aHF was distilled onto the SbF_3 at −196 °C and the reactor was filled with 1000 Torr of F_2. The reactor was continuously agitated at RT allowing for the dissolution of F_2 and the subsequent reaction with SbF_3 to form SbF_5, until no solid SbF_3 was left. The excess fluorine was removed and the reactor filled with 800 Torr of N_2. A slight excess of acetone ($O{=}C(CH_3)_2$) (0.016 g, 0.28 mmol) was distilled onto the HF/SbF_5 at −196 °C from a glass graduated weighing vessel with a J. Young PTFE stopcock and allowed to react at −78 °C forming a white solid. The reactor was quickly warmed to RT to dissolve the product, forming a clear, colourless solution, and immediately cooled to −78 °C for ca. 30 min at which point clear, colourless needles crystallized. The excess aHF was removed under dynamic vacuum at −78 °C into a FEP U-trap at −196 °C. A single crystal was found and characterized by X-ray crystallography, using low-temperature mounting techniques, and was shown to be $[HO{=}C(CH_3)_2][SbF_6]$.

2.5.6 Synthesis of $[H\{O{=}C(CH_3)_2\}_2]_3[HO{=}C(CH_3)_2]_3[SbF_6]_5F$

SbF_3 (0.068 g, 0.38 mmol) was loaded into a ¼-in. o.d. FEP reactor in a nitrogen-atmosphere dry box. Approximately 0.2 mL of aHF was distilled onto the SbF_3 at −196 °C and the reactor was filled with 1000 Torr of F_2. The reactor was continuously agitated at

RT allowing for the dissolution of F_2 and the subsequent reaction with SbF_3 to form SbF_5, until no solid SbF_3 was left. The excess fluorine was removed and the reactor filled with 800 Torr of N_2. Two molar equivalents of acetone ($O=C(CH_3)_2$) (0.044 g, 0.76 mmol) were distilled onto the HF/SbF_5 at −196 °C from a glass graduated weighing vessel with a J. Young PTFE stopcock and allowed to react at −78 °C forming a white solid. The reactor was quickly warmed to RT to dissolve the product, forming a clear, colourless solution, and immediately cooled to −60 °C for ca. 5 min at which point clear, colourless needles crystallized. The excess aHF was removed under dynamic vacuum at −75 °C into a FEP U-trap at −196 °C. A single crystal was found and characterized by X-ray crystallography, using low-temperature mounting techniques, and was shown to be $[H\{O=C(CH_3)_2\}_2]_3[HO=C(CH_3)_2]_3[SbF_6]_5F$.

2.6 Synthesis of Protonated Aldehydes

2.6.1 Synthesis of $[H(O=CHC_6H_5)_2][SbF_6]$

SbF_3 (0.044 g, 0.25 mmol) was loaded into a ¼-in. o.d. FEP reactor in a nitrogen-atmosphere dry box. Approximately 0.2 mL of aHF was distilled onto the SbF_3 at −196 °C and the reactor was filled with 1000 Torr of F_2. The reactor was continuously agitated at RT and aHF washed up and down the walls to see the reaction to completion forming SbF_5. The excess fluorine was removed and the reactor filled with 800 Torr of N_2. Benzaldehyde ($O=CHC_6H_5$) (0.024 g, 0.23 mmol) was distilled onto the HF/SbF_5 at −196 °C from a glass graduated weighing vessel with a J. Young PTFE stopcock and allowed to react at −78 °C forming a faint, clear, yellow solution. A white solid formed at which point the reactor was warmed to −60 °C for no more than 10 s to dissolve the product and then cooled to −78 °C.

Pale red, transparent blocks crystallized and excess aHF was removed at −78 °C under dynamic vacuum to a FEP U-trap at −196 °C. These crystals were characterized by Raman spectroscopy at −100 °C. A single crystal was found and characterized by X-ray crystallography, using low-temperature mounting techniques, and was shown to be the hemiprotonated $[H(O{=}CHC_6H_5)_2][SbF_6]$. No signs of the monoprotonated benzaldehyde cation were found.

2.6.2 Synthesis of $[H(O{=}CHCH_3)_2][SbF_6]$ and $[HO{=}CHCH_3][SbF_6]$

SbF_3 (0.042 g, 0.24 mmol) was loaded into a ¼-in. o.d. FEP reactor in a nitrogen-atmosphere dry box. Approximately 0.2 mL of aHF was distilled onto the SbF_3 at −196 °C and the reactor was filled with 1000 Torr of F_2. The reactor was continuously agitated at RT and aHF washed up and down the walls to see the reaction to completion forming SbF_5. Acetaldehyde ($O{=}CHCH_3$) (0.023 g, 0.52 mmol) was distilled onto the HF/SbF_5 at −196 °C from a glass graduated weighing vessel with a J. Young PTFE stopcock and upon warming to −78 °C a clear colourless solution formed with a white powder in the bottom of the reactor. This was easily dissolved by warming to −70 °C and agitating the sample. Crystals were grown by slowly removing aHF at −78 °C under dynamic vacuum and after 3 hours colourless needles appeared. A single crystal was found and characterized by X-ray crystallography, using low-temperature mounting techniques, and was shown to be the hemiprotonated $[H(O{=}CHCH_3)_2][SbF_6]$. No signs of the monoprotonated acetaldehyde were observed.

Following a similar procedure, reaction between acetaldehyde (0.015 g, 0.34 mmol) and SbF_5 (0.27 mmol) was carried out in approximately 0.2 mL of aHF at −75 °C resulting

in a white, crystalline solid. This solid was characterized by Raman spectroscopy at −100 °C. No single crystals suitable for X-ray crystallography were found.

2.7 Synthesis of the Adducts of AsF_5 with Ketones

2.7.1 Synthesis of $AsF_5 \cdot O=C(CH_3)_2$

On a metal vacuum line, AsF_5 (0.046 g, 0.27 mmol) was distilled into a 4-mm FEP reactor at −196 °C. The reactor was connected to a glass vacuum line where an excess of SO_2 (ca. 0.4 mL) was distilled onto the AsF_5 and dissolved at −60 °C to give a clear, colourless solution. Slightly less than one molar equivalent of acetone (0.020 g, 0.24 mmol) was distilled into a glass graduated weighing vessel equipped with a J. Young PTFE stopcock and, subsequently, distilled onto the AsF_5/SO_2 at −196 °C. A clear, colourless solution was present upon warming the reactor to −70 °C. The reactor was heat sealed under dynamic vacuum and the contents of the reaction were characterized using ^{19}F and ^{1}H NMR spectroscopy at −70 °C.

Using the same method, the reaction was also carried out in a ¼-in. o.d. FEP reactor. AsF_5 (0.066 g, 0.39 mmol) was dissolved in SO_2 and acetone (0.025 g, 0.43 mmol) was distilled onto the mixture. The reaction was warmed to −70 °C and a fine, white powder-like suspension crashed out of solution. The solid was dissolved upon agitation and, upon slowly cooling, the white powder reappeared. Crystal growth was attempted by slowly cooling the sample, as well as, slowly removing the SO_2 at −70 °C; however, no evidence for crystal formation appeared. The white solid was characterized by Raman spectroscopy at −100 °C.

2.7.2 Synthesis of $AsF_5 \cdot O=C_5H_8$

A 4-mm FEP reactor was connected to a glass vacuum line where cyclopentanone (0.013 g, 0.15 mmol) was distilled into a glass graduated weighing vessel equipped with a J. Young PTFE stopcock and then into the 4-mm reactor. An excess of CH_2Cl_2 (ca. 0.5 mL) was distilled onto the cyclopentanone and dissolved at RT to give a clear, colourless solution. Approximately one molar equivalent of AsF_5 (total of 145 Torr was added inside the metal vacuum line with a volume of 0.01953 mL, 0.15 mmol) was distilled through a metal vacuum line into the reactor containing cyclopentanone and CH_2Cl_2 at −196 °C. Upon warming the reaction to −79 °C, a fine white powder was suspended in solution. The CH_2Cl_2 was pumped off at −70 °C into a glass U-trap at −196 °C until only a white powder remained. This was characterized by Raman spectroscopy at −100 °C and shown to be $AsF_5 \cdot O=C_5H_8$. An excess of SO_2 was distilled onto the $AsF_5 \cdot O=C_5H_8$ adduct and dissolved at −50 °C. The reactor was heat sealed under dynamic vacuum and the $AsF_5 \cdot O=C_5H_8$ adduct was further characterized using ^{19}F and ^{1}H NMR spectroscopy at −70 °C.

2.7.3 Synthesis of $AsF_5 \cdot O=C_{10}H_{14}$

2-Adamantanone (0.016 g, 0.11 mmol) was loaded into a 4-mm FEP reactor inside a nitrogen-atmosphere dry box followed by distillation of ca. 0.3 mL of SO_2 on a glass vacuum line which easily dissolved at RT. One molar equivalent of AsF_5 (total of 100 Torr was added inside the metal vacuum line with a volume of 0.01953 mL, 0.11 mmol) was distilled through a metal vacuum line into the reactor containing 2-adamantanone and SO_2 at −196 °C. A clear, colourless solution was present upon warming the reactor to −70 °C.

The reactor was heat sealed under dynamic vacuum and the product was characterized using ^{19}F and ^{1}H NMR spectroscopy at −70 °C and found to be the $AsF_5 \cdot O{=}C_{10}H_{14}$ adduct.

Using a similar method, the reaction was also carried out in a ¼-in. o.d. FEP reactor. 2-Adamantanone (0.019 g, 0.13 mmol) was dissolved in CH_2Cl_2 (ca. 0.6 mL) at RT and approximately one equivalent of AsF_5 (total of 140 Torr was added inside the metal vacuum line with volume of 0.01953 mL, 0.15 mmol) was distilled onto the mixture. The reaction was warmed to −80 °C giving a clear, light yellow solution. The CH_2Cl_2 was pumped off at −70 °C into a glass U-trap at −196 °C until a white powder remained. This was characterized by Raman spectroscopy at −100 °C and shown to be $AsF_5 \cdot O{=}C_{10}H_{14}$. Crystal growth was attempted, however, no evidence for crystal formation appeared.

2.8 Single-Crystal X-ray Diffraction

2.8.1 Low-Temperature Crystal Mounting

All samples containing thermally unstable and moisture-sensitive crystals were manipulated using a low-temperature crystal-mounting setup, as shown in Figure 2.5. The FEP sample tubes containing the crystals were cut open and manipulated in an aluminum trough, set to the desired temperature, a under a stream of dry, cold nitrogen produced by passing dry, gaseous nitrogen through a 5 L Dewar of liquid nitrogen. The temperature of the trough was regulated by adjusting the flow rate of nitrogen passing through the Dewar and was monitored using a copper/constantan thermocouple with a digital readout. Single-crystals were isolated and affixed to a cryo-loop bound to a metallic pin which was magnetically mounted to a wand allowing for easy manipulation of the crystals inside the trough. For the crystals obtained in Chapters 3 and 5, the trough was set to −85 °C (with

the exception of $(SF_4 \cdot O{=}C(CH_3)_2)_2$ where the trough was set to −110 °C) and a perfluorinated polyether oil, Fomblin Z-25 (Ausimont Inc.), was used to affix the crystals to the cryo-loop. The metal goniometer tip containing the crystal was transported to the goniometer using liquid-N_2-cooled cryo-tongs.

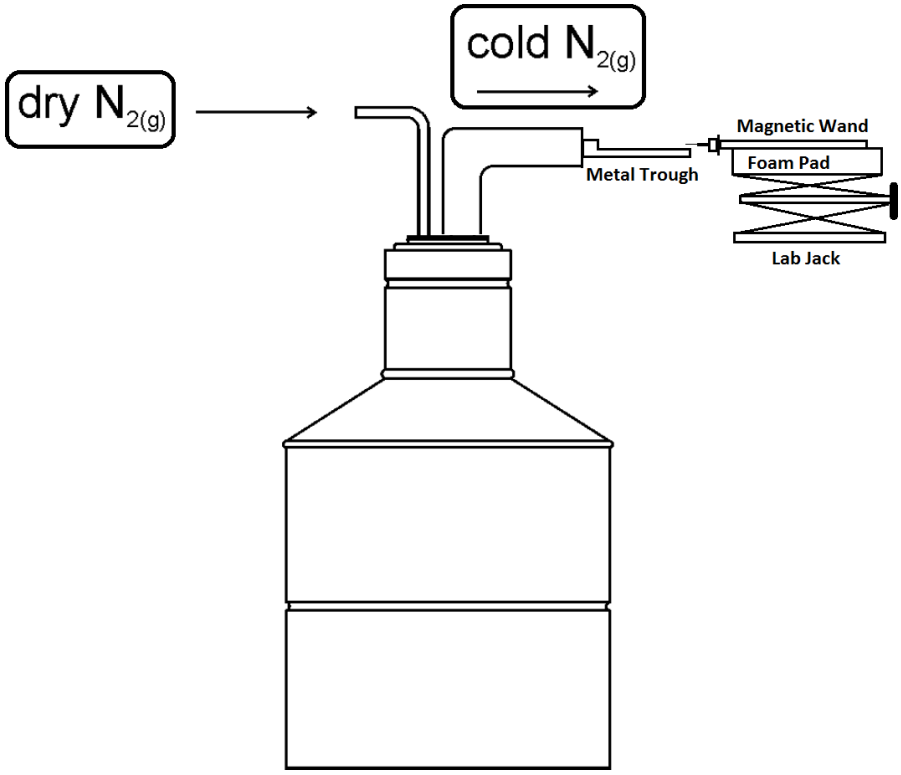

Figure 2.5 Low-temperature crystal-mounting setup, consisting of a 10.5 L Dewar, equipped with a foam stopper, a glass nitrogen inlet, a silvered glass cold nitrogen outlet with an 11 cm long aluminum trough (2 cm o.d.). (Adapted from Jared Nieboer's M.Sc. Thesis, Ref. 2).

2.8.2 Data Collection and Reduction

All crystals were centered on a Rigaku SuperNova diffractometer equipped with a Dectris Pilatus 3R 200K-A hybrid-pixel-array detector, a four-circle κ goniometer, and sealed, graphite-monochromated MoK_α and CuK_α X-ray sources. For

$SF_4 \cdot (O=C_{10}H_{14}) \cdot (HF)$, $(SF_4 \cdot O=C(CH_3)_2)_2$, $[HO=C_{10}H_{14}][AsF_6]$, and $[HO=C_5H_8][AsF_6]$ data were collected using the CuK_α source (λ = 1.54184 Å) at 100 K. For $[HO=C_5H_8][SbF_6]$, $[HO=C(CH_3)_2][SbF_6]$, $[H(O=C(CH_3)_2)_2]_3[HO=C(CH_3)_2]_3[SbF_6]_5F$, $[H(O=CHC_6H_5)_2]$ $[SbF_6]$, and $[H(O=CHCH_3)_2][SbF_6]$ data were collected using the MoK_α source (λ = 0.71073 Å) at 100 K. The data were processed using CrysAlisPro,[5] which applied necessary Lorentz and polarization corrections to the integrated data and scaled the data. A numerical (Gaussian-grid) absorption correction was generated based upon the indexed faces of the crystal.

2.8.3 Structure Solution and Refinement

Atom positions were determined using the intrinsic phasing method (ShelXT)[6] and were refined using least-squares refinement (ShelXL).[7] Structure solution and refinement were performed with the aid of Olex2.[8] Non-hydrogen atoms were refined anisotropically and the extinction coefficient was calculated for the crystal structure. If the error in the extinction coefficient was on the same order of magnitude as the extinction coefficient, it was omitted. Recommended weights for the atoms were determined before hydrogen atoms were introduced using a riding model (HFIX). For the crystal structures reported in Chapter 5 (protonated ketones and aldehydes), protons bound to oxygen were found using the Fourier difference map and their positions freely refined. Both residual values, R_1 based on F and the weighted residual values wR_2 based on F^2, are available in the structure refinement tables along with the goodness of fit (*GooF*). They represent the following equations:

$R_1 = \frac{\sum ||F_{obs}| - |F_{calc}||}{\sum F_{obs}|}$ The conventional R-factor based upon the structure factor.

$wR_2 = \sqrt{\frac{\sum [w(F_{obs}^2 - F_{calc}^2)^2]}{\sum [w(F_{obs}^2)^2]}}$ The weighted R-factor based on the square of the structure factors.

$GooF = \sqrt{\frac{\sum [w(F_{obs}^2 - F_{calc}^2)]}{(n-p)}}$ The *GooF* is based upon intensity where *n* is the number of reflections and *p* is the number of parameters defined.

2.9 Raman Spectroscopy

All Raman spectra were recorded on a Bruker RFS 100 FT Raman spectrometer with a quartz beam splitter, a liquid-nitrogen cooled Ge detector, and R-496 low-temperature accessory. The actual usable Stokes range was from 50 to 3500 cm^{-1}. The 1064 nm line of an Nd:YAG laser was used for excitation of the sample. The Raman spectra were recorded with a spectral resolution of 2 cm^{-1} using laser powers of 150 or 200 mW. The samples were recorded in Pyrex-glass NMR tubes equipped with a J. Young Valve, and 4-mm and ¼-in. o.d. FEP reactors. Spectra were visualized and analyzed using *OPUS 4.2*.[9]

2.10 NMR Spectroscopy

NMR spectra were recorded unlocked on a 300.13 MHz (7.0486 T) Bruker Advance II NMR spectrometer equipped with a BBFO probe which has variable-temperature

capabilities ranging from +150 to −150 °C. *Bruker TopSpin 3.5* was used for data refinement and visualization.[10] The Fluorine-19 NMR spectra were externally referenced to neat $CFCl_3$ at RT. Proton spectra were externally referenced to neat TMS at RT. Shimming on the NMR samples was performed manually on the most intense signal for all samples. All samples were contained in 4-mm FEP tubes that were inserted into 5-mm thin-walled glass NMR tubes. All ^{19}F NMR spectra were first obtained with a spectral window of 603.55 ppm (170.45 kHz) centered at −50 ppm, a default pre-scan delay of 6 μs, and a relaxation delay of 1 s. Afterwards, the spectral window was adjusted to include only the signals of interest. The number of FID data points, acquisition time, and number of scans were optimized for each sample to ensure a good signal-to-noise ratio and digital resolution was obtained. In some cases, specifically for the NMR data presented in Chapter 4, the relaxation delay was increased to upwards of 5 s.

2.11 Computational Details

All quantum-chemical calculations were performed using the Gaussian 09 program package.[11] The X-ray crystal structure was used as a starting geometry, when permitted (i.e., Chapter 5 compounds and the $(SF_4{\cdot}O{=}C(CH_3)_2)_2$ dimer in Chapter 3). Density functional theory (DFT) calculations were carried out to optimize the gas-phase geometries of the $(SF_4{\cdot}O{=}C(CH_3)_2)_2$ dimer (Chapter 3), proposed intermediates in the deoxo-fluorination reaction (Chapter 4), protonated ketones and aldehydes (Chapter 5), and adducts of AsF_5 with ketones (Chapter 6). Specifically, the B3LYP/aug-cc-pVTZ level of theory was chosen for all calculations as it provides reliable structural information. Indeed, the PBE1PBE and B3LYP functionals with the 6-311+G(2df,p) and aug-cc-PVTZ basis

sets result in little to no difference in the geometric parameters for the representative test cases of acetone and protonated acetone (see Tables 2.1 and 2.2).

The energy-minimized geometries were used to calculate B3LYP/aug-cc-pVTZ vibrational frequencies along with the IR and Raman intensities. No scaling factors were used on the calculated vibrational frequencies. The experimental vibrational frequencies were best approximated using the B3LYP functional compared to the PBE1PBE functional (Tables 2.3 and 2.4), which further underscores the reliability of the computational approach used in this thesis. The B3LYP/aug-cc-pVTZ combination resulted in real frequencies for all calculated compounds, with the exception of the $[H(O{=}CHC_6H_5)_2]^+$ (Chapter 5) and $[(CH_3)_2FCOSF_2]^+$ (Chapter 4) cations. These two gas-phase geometries consistently converged to stationary points with a small (-10 cm^{-1} for $[H(O{=}CHC_6H_5)_2]^+$; -13 cm^{-1} for $[(CH_3)_2FCOSF_2]^+$) imaginary frequency using the aug-cc-pVTZ basis set. These frequencies corresponded to the symmetric rocking of the two benzaldehyde molecules ($[H(O{=}CHC_6H_5)_2]^+$) and asymmetric rocking of the fluorocarbenium moiety ($[(CH_3)_2CF]^+$) and SOF_2 moiety of $[(CH_3)_2FCOSF_2]^+$. The cc-pVTZ basis set was used for $[H(O{=}CHC_6H_5)_2]^+$ which resulted in an energy-minimized geometry with all positive frequencies. This approach is justified since B3LYP with both the aug-cc-pVTZ and cc-pVTZ basis sets shows no difference in the optimized geometrical parameters or vibrational frequencies for the test cases of acetone and protonated acetone. Due to the discrepancy with the crystal structure, in the case of $[H(O{=}CHC_6H_5)_2]^+$, hemiprotonated benzaldehyde was further probed by adjusting the starting geometry such that the dihedral angle between the benzene rings was 45°; however, the optimized geometry still resulted in the rings being coplanar. In addition, adjusting the position of the proton in the O−H−O moiety consistently resulted in an asymmetric structure, with different O−H distances. Therefore,

the symmetry observed in the X-ray crystal structure is likely the result of site symmetry in the unit cell.

For the compounds presented in Chapter 5 and Chapter 6, the NBO analyses were performed using the NBO-6.0 program.[12] The GaussView program was used to visualize the vibrational displacements and aid in assignments of the bands, and visualize the molecular orbitals.[13]

Table 2.1 Calculations Comparing Selected Geometric Parameters and Vibrational Frequencies Between the B3LYP and PBE1PBE DFT Functionals with the cc-pVTZ, aug-cc-pVTZ, and 6-311+G(2df,p) Basis Sets for Acetone.

Bond Lengths (Å)						
	exptl [a]	B3LYP/ aug-cc-pVTZ	B3LYP/ cc-pVTZ	B3LYP/ 6-311+G(2df,p)	PBE1PBE/ 6-311+G(2df,p)	PBE1PBE/ aug-cc-pVTZ
O1=C2	1.209(3)	1.210	1.210	1.209	1.206	1.207
C1−C2	1.485(4)	1.514	1.514	1.514	1.506	1.506
C2−C3	1.486(4)	1.514	1.514	1.514	1.506	1.506
Bond Angles (°)						
O1=C2−C1	120.8(2)	121.7	121.7	121.7	121.8	121.8
O1=C2−C3	122.3(3)	121.7	121.7	121.7	121.8	121.8
C1−C2−C3	116.9(2)	116.6	116.5	116.6	116.5	116.4
Vibrational Frequencies (cm^{-1})						
ν(CO)	1709(16)	1782(13)[195]	1792(9)[175]	1786(12)[200]	1824(12)[205]	1820(13)[199]

[a] From Ref 14.

Table 2.2 Calculations Comparing Selected Geometric Parameters and Vibrational Frequencies Between the B3LYP and PBE1PBE DFT Functionals with the cc-pVTZ, aug-cc-pVTZ, and 6-311+G(2df,p) Basis Sets for Protonated Acetone, $[HO{=}C(CH_3)_2]^+$.

Bond Lengths (Å)						
	exptl	B3LYP/ aug-cc-pVTZ	B3LYP/ cc-pVTZ	B3LYP/ 6-311+G(2df,p)	PBE1PBE/ 6-311+G(2df,p)	PBE1PBE/ aug-cc-pVTZ
H1−O1	0.76(4)	0.976	0.976	0.976	0.973	0.973
O1=C2	1.271(3)	1.277	1.277	1.276	1.270	1.272
C1−C2	1.459(4)	1.466	1.466	1.466	1.459	1.460
C2−C3	1.467(3)	1.470	1.470	1.471	1.464	1.464
Bond Angles (°)						
H1−O1=C2	109(3)	115.0	114.4	114.8	114.3	114.1
O1=C2−C1	116.7(2)	115.8	115.8	115.8	115.9	115.9
O1=C2−C3	121.5(2)	121.4	121.4	121.4	121.5	121.4
C1−C2−C3	121.7(2)	122.8	122.8	122.8	122.6	122.6
Vibrational Frequencies (cm^{-1})						
ν(CO)	1593(10)	1588(4)[97]	1591(3)[10]	1590(4)[104]	1623(4)[133]	1619(5)[126]

References

[1] Peters, D.; Miethchen, R. *J. Fluorine Chem.* **1996**, *79*, 161−165.

[2] Neiboer, J. M.Sc. Thesis, University of Lethbridge, 2007.

[3] Emara, A. A. A.; Lehmann, J. F.; Schrobilgen, G. J. *J. Fluorine Chem.* **2005**, *126*, 1373−1376.

[4] Azeem, M.; Brownstein, M.; Gillespie, R. J. *Can. J. Chem*. **1969**, *47*, 4159−4167.

[5] CrysAlisPro. Agilent Technologies, Ltd.: Yarnton, Oxfordshire, England 2014.

[6] Sheldrick, G. M. SHELXT – Integrated Space-Group and Crystal-Structure Determination. *Acta Crystallogr. Sect. A* **2015**, *71*, 3–8.

[7] Sheldrick, G. M. Crystal Structure Refinement with SHELXL. *Acta Crystallogr. Sect. C* **2015**, *71*, 3–8.

[8] O. V. Dolomanov, L. J. Bourhis, R. J. Gildea, J. A. K. Howard, H. Puschmann, OLEX2 : A Complete Structure Solution, Refinement and Analysis Program. *J. Appl. Crystallogr.* **2009**, *42*, 339–341.

[9] *OPUS 4.2*, Bruker Instruments, Inc.: Billerica, Massachusetts, USA.

[10] *TOPSPIN 3.5*, Bruker Instruments, Inc.: Billerica, Massachusetts, USA.

[11] Frisch, M. J.; Trucks, G. W.; Schlegel, H. B.; Scuseria, G. E.; Robb, M. A.; Cheeseman, J.R.; Scalmani, G.; Barone, V.; Mennucci, B.; Petersson, G. A.; Nakatsuji, H.; Caricato, M.; Li, X.; Hratchian, H. P.; Izmaylov, A. F.; Bloino, J.; Zheng, G.; Sonnenberg, J. L.; Hada, M.; Ehara, M.; Toyota, K.; Fukuda, R.; Hasegawa, J.; Ishida, M.; Nakajima, T.; Honda, Y.; Kitao, O.; Nakai, H.; Vreven, T.; Montgomery, J. A., Jr.; Peralta, J. E.; Ogliaro, F.; Bearpark, M.; Heyd, J. J.; Brothers, E.; Kudin, K. N.; Staroverov, V. N.; Kobayashi, R.; Normand, J.; Raghavachari, K.; Rendell, A.; Burant, J. C.; Iyengar, S. S.; Tomasi, J.; Cossi, M.; Rega, N.; Millam, N. J.; Klene, M.; Knox, J. E.; Cross, J. B.; Bakken, V.; Adamo, C.; Jaramillo, J.; Gomperts, R.; Stratmann, R. E.; Yazyev, O.; Austin, A. J.; Cammi, R.; Pomelli, C.; Ochterski, J. W.; Martin, R. L.; Morokuma, K.; Zakrzewski, V. G.; Voth, G. A.; Salvador, P.; Dannenberg, J. J.; Dapprich, S.; Daniels, A.; Farkas, D.; Foresman, J.; Ortiz, J. V.; Cioslowski, J.; Fox, D. J. Gaussian 09, Revision D.01; Gaussian, Inc: Wallingford, CT, 2009.

[12] Glendening, E. D.; Badenhoop, J. K.; Reed, A. E.; Carpenter, J. E.; Bohmann, J. A.; Morales, C. M.; Landis, C. R.; Weinhold, F. NBO 6.0. Theoretical Chemistry Institute, University of Wisconsin: Madison, WI, 2013.

[13] GaussView, version 3.0; Gaussian Inc.: Pittsburgh, PA, 2003.

[14] Allan, D. R.; Clark, S. J.; Ibberson, R. M.; Parsons, S.; Pulham, C. R.; Sawyer, L. *Chem. Commun.* **1999**, 751−752.

3. Lewis Acid-Base Interactions Between SF_4 and Acetone and 2-Adamantanone

3.1 Introduction

Sulfur tetrafluoride is a well-known deoxofluorinating agent used in organic chemistry.[1] In such reaction mixtures, the weak Lewis acid SF_4 can interact with a carbonyl functional group through S---O secondary bonding interactions. Early ^{19}F NMR spectroscopy studies had suggested SF_4 does not form adducts with the oxygen-bases THF and ethyl acetate since the chemical shift of SF_4 was unaffected.[2] However, it was later shown at low temperatures, that SF_4 does form adducts with the solvents diethyl ether and THF as evidenced by changes in $\delta(^{19}F)$ and a decrease in $^2J(^{19}F–^{19}F)$ coupling.[3] Sass and Ault carried out matrix-isolation studies on the 1:1 adduct of SF_4 and acetone and suggested these compounds form weak S---O bonding interactions based on the presence of two new bands in the IR spectrum at 680, assigned to ν(S−F), and 1706 cm^{-1}, assigned to ν(C=O).[4]

These S---O chalcogen bonding modalities have long been postulated to exist, however, isolating such compounds has proven to be challenging. Only recently have Gerken and co-workers managed to successfully synthesize oxygen-base adducts with SF_4 in the solid state.[5] Lewis acid-base adducts of SF_4 and the oxygen-bases THF, 1,2-dimethoxyethane, and cyclopentanone were synthesized at low temperatures and characterized by X-ray crystallography and Raman spectroscopy. Density Functional Theory (DFT) calculations at the B3LYP/aug-cc-pVTZ level of theory were used to determine the optimized gas-phase geometries of these compounds and the calculated vibrational modes were used to aid in the assignments of the Raman bands. In addition, caffeine, containing three Lewis basic sites (i.e., one N and two C=O basic groups), was shown to form an adduct with SF_4 through C=O---S interactions. This complex,

$C_8H_{10}N_4O_2 \cdot 2SF_4 \cdot HF$, also showcased a unique bonding interaction where the sulfur center of SF_4 had an S---F contact with a fluorine atom of HF, which in turn was hydrogen-bonded to the Lewis basic nitrogen site of caffeine.

Studies of the interactions between SF_4 and nitrogen bases found the resulting adducts to be very air and moisture sensitive. The solvolysis reactions by HF of the adduct between SF_4 and pyridine, as well as pyridine derivatives, were studied by X-ray crystallography and Raman spectroscopy.[6] These systems showed unique bonding motifs in the solid state including the F_4S---N and F_4S---(F)---HN interactions.

3.2 Results and Discussion

3.2.1 Synthesis and Properties of $[SF_4 \cdot O=C(CH_3)_2]_2$, $SF_4 \cdot [O=C(CH_3)_2]_2$, and $SF_4 \cdot (O=C_{10}H_{14}) \cdot (HF)$

The previously synthesized $SF_4 \cdot (O=C_5H_8)_2$ is currently the only example of a Lewis acid-base adduct involving a ketone and SF_4 in the solid state.[5] The reactions of acetone, the simplest aliphatic ketone, and 2-adamantanone, a polycyclic ketone, with SF_4 were carried out to further explore the structure and bonding of these Lewis acid-base adducts. Acetone was reacted with slightly more than one equivalent of SF_4, as well as a 2:1 stoichiometric ratio at −90 °C where the two reagents were miscible and formed clear colourless solutions (see Equation 3.1).

$$SF_4 + x\ O=C(CH_3)_2 \xrightarrow{-90\ °C} SF_4 \bullet [O=C(CH_3)_2]_x \quad (x = 1 \text{ or } 2) \tag{3.1}$$

The reaction of SF_4 with one equivalent of acetone yielded white blocks that crystallized by slowly removing any remaining SF_4 under dynamic vacuum at −96 °C. The reaction of SF_4 with two equivalents of acetone was slowly cooled to −116 °C with no signs of crystal

formation. When the sample was cooled to −120 °C the solution began to freeze into an amorphous solid. Both solid samples were characterized by LT Raman spectroscopy. In both reactions, no sign of deoxofluorination of the carbonyl group was observed in the Raman spectrum under these conditions (T < −90 °C).

Crystals of the $[SF_4{\cdot}O{=}C(CH_3)_2]_2$ adduct suitable for single-crystal X-ray diffraction were obtained from a reaction of acetone with 1.5 equivalents of SF_4. This clear, colourless solution was slowly cooled to −106 °C where colourless crystals began to form. The excess SF_4 was removed at −112 °C leaving behind clear white crystals. A single crystal suitable for X-ray crystallography was isolated and shown to be the $[SF_4{\cdot}O{=}C(CH_3)_2]_2$ dimer (see Section 3.2.2).

An excess of SF_4 was added to a known amount of 2-adamantanone at −90 °C, at which temperature the 2-adamantanone was insoluble. The sample was warmed to −67 °C where the white powder dissolved in the SF_4 forming a clear, colourless solution. Upon slowly cooling to −75 °C a white powder began crashing out, which was identified as 2-adamantanone by low-temperature Raman spectroscopy, suggesting that an adduct did not form with SF_4. The sample was concentrated by slowly removing approximately half the SF_4 at −60 °C. The white powder was redissolved in SF_4 and stored in an ethanol bath at −75 °C. After two weeks, clear, colourless crystals were observed above the SF_4 solution. One single crystal was isolated and X-ray crystallography showed this to be $SF_4{\cdot}(O{=}C_{10}H_{14}){\cdot}(HF)$. Raman spectroscopy was not used to characterize this serendipitously obtained crystal.

3.2.2 X-ray Crystallography of $[SF_4{\cdot}O{=}C(CH_3)_2]_2$

The crystallographic parameters and details of data collection for $[SF_4{\cdot}O{=}C(CH_3)_2]_2$ are given in Table 3.1. The bond lengths and bond angles are listed in Table 3.2. Handling and growing these crystals proved to be extremely challenging since the crystals melted above −106 °C. After attempting to mount multiple crystals, a single crystal was obtained, albeit of poor quality, and unambiguously identified as the $[SF_4{\cdot}O{=}C(CH_3)_2]_2$ despite the large R_1 of 7.89%.

Table 3.1 Summary of X-ray Crystal Data and Refinement Results of $[SF_4{\cdot}O{=}C(CH_3)_2]_2$.

Compound	$[SF_4{\cdot}O{=}C(CH_3)_2]_2$
Empirical Formula	$C_3H_6OF_4S$
Formula Weight (g mol^{-1})	166.14
Temperature (^{o}C)	−173
Wavelength (Å)	1.54184
Crystal System	triclinic
Space Group	$P\bar{1}$
a (Å)	7.6967(2)
b (Å)	7.83534(16)
c (Å)	12.7283(2)
α (deg)	83.6926(16)
b (deg)	76.156(2)
γ (deg)	67.391(2)
V ($Å^3$)	687.88(3)
Z	4
μ (mm^{-1})	4.384
ρ_{calcd} (g cm^{-3})	1.604
F(000)	336.0
Crystal Size (mm^3)	0.376 × 0.157 × 0.055
Reflections Collected	87696
Independent Reflections	2515
Data/Restraints/Parameters	2515/0/167
Goodness-of-fit on F^2	1.110
R_1, I ≥2θ(I)	0.0789
wR_2 (F^2)	0.0813

Table 3.2 Experimental and Calculated Bond Lengths (Å) and Angles (°) of $[SF_4 \cdot O{=}C(CH_3)_2]_2$.

Bond Lengths					
	exptl	*calcd*		*exptl*	*calcd*
S(1)---O(1)	2.842(2)	2.955	S(2)---O(1)	2.899(2)	2.998
S(1)---O(2)	2.866(2)	2.923	S(2)---O(2)	2.890(2)	3.041
S(1)−F(1)	1.5411(19)	1.582	S(2)−F(5)	1.547(2)	1.583
S(1)−F(2)	1.5447(19)	1.584	S(2)−F(6)	1.537(2)	1.583
S(1)−F(3)	1.651(2)	1.683	S(2)−F(7)	1.652(3)	1.682
S(1)−F(4)	1.677(2)	1.721	S(2)−F(8)	1.632(3)	1.709
O(1)−C(2)	1.231(4)	1.217	O(2)−C(5)	1.219(4)	1.217
C(1)−C(2)	1.484(5)	1.508	C(4)−C(5)	1.496(5)	1.508
C(2)−C(3)	1.488(5)	1.508	C(5)−C(6)	1.493(5)	1.508
Bond Angles					
F(1)−S(1)−F(2)	99.31(11)	99.01	F(5)−S(2)−F(7)	87.56(16)	86.94
F(1)−S(1)−F(3)	88.32(12)	87.73	F(5)−S(2)−F(8)	87.74(16)	87.54
F(1)−S(1)−F(4)	86.81(12)	86.93	F(5)−S(2)−O(1)	83.50(10)	84.16
F(1)−S(1)−O(1)	175.76(9)	174.78	F(5)−S(2)−O(2)	170.64(12)	167.49
F(1)−S(1)−O(2)	82.46(9)	83.59	F(6)−S(2)−F(5)	99.41(13)	99.46
F(2)−S(1)−F(3)	88.33(12)	87.72	F(6)−S(2)−F(7)	87.36(18)	87.59
F(2)−S(1)−F(4)	86.66(12)	86.90	F(6)−S(2)−F(8)	87.77(17)	87.05
F(2)−S(1)−O(1)	83.34(9)	89.90	F(6)−S(2)−O(1)	169.52(13)	172.12
F(2)−S(1)−O(2)	175.61(10)	175.99	F(6)−S(2)−O(2)	82.59(10)	84.96
F(3)−S(1)−F(4)	172.37(13)	171.74	F(7)−S(2)−O(1)	102.86(13)	99.61
F(3)−S(1)−O(1)	88.45(10)	96.74	F(7)−S(2)−O(2)	101.69(13)	104.41
F(3)−S(1)−O(2)	87.71(10)	95.47	F(8)−S(2)−F(7)	172.60(18)	171.58
F(4)−S(1)−O(1)	96.68(10)	88.91	F(8)−S(2)−O(1)	82.27(12)	86.15
F(4)−S(1)−O(2)	97.47(11)	90.19	F(8)−S(2)−O(2)	83.20(12)	81.58
O(1)−S(1)−O(2)	94.67(7)	93.28	O(2)−S(2)−O(1)	92.96(7)	90.10
C(2)−O(1)−S(1)	133.1(2)	133.42	C(2)−O(1)−S(2)	129.4(2)	132.64
C(5)−O(2)−S(1)	135.7(2)	133.27	C(5)−O(2)−S(2)	127.3(2)	125.20
O(1)−C(2)−C(1)	121.9(3)	121.44	O(2)−C(5)−C(4)	121.1(3)	121.32
O(1)−C(2)−C(3)	121.4(3)	121.61	O(2)−C(5)−C(6)	122.5(3)	121.69
C(1)−C(2)−C(3)	116.6(3)	116.96	C(6)−C(5)−C(4)	116.4(3)	116.99
S(1)−O(1)−S(2)	81.95(6)	83.96	S(1)−O(2)−S(2)	81.69(6)	83.76
Torsion Angles					
S(1)−O(1)−C(2)−C(1)	152.8(2)	170.3	S(2)−O(1)−C(2)−C(1)	31.5(4)	37.9
S(1)−O(1)−C(2)−C(3)	−26.4(5)	−9.8	S(2)−O(1)−C(2)−C(3)	−147.7(3)	−142.3
S(1)−O(2)−C(5)−C(4)	−158.4(2)	−167.5	S(2)−O(2)−C(5)−C(4)	−37.0(4)	−48.7
S(1)−O(2)−C(5)−C(6)	21.2(5)	12.4	S(2)−O(2)−C(5)−C(6)	142.7(3)	131.1

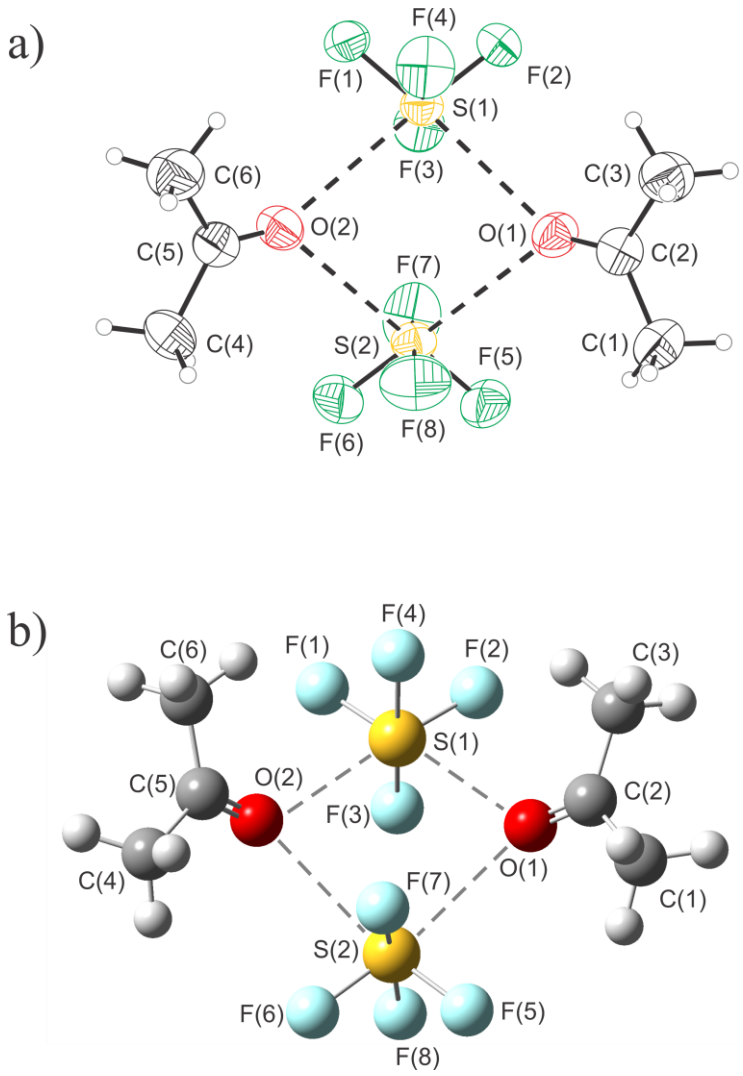

Figure 3.1 a) Thermal ellipsoid plots of $[SF_4 \cdot O{=}C(CH_3)_2]_2$. Thermal ellipsoids are set at the 50% probability level. b) Geometry-optimized gas-phase structure of $[SF_4 \cdot O{=}C(CH_3)_2]_2$ at the B3LYP/aug-cc-pVTZ level of theory.

The $[SF_4 \cdot O{=}C(CH_3)_2]_2$ adduct crystallized in the $P\bar{1}$ space group with two acetone molecules and two SF_4 molecules in the asymmetric unit (Figure 3.1). Each crystallographically unique SF_4 is coordinated by two bridging acetone molecules through S---O dative bonds forming the $[SF_4 \cdot O{=}C(CH_3)_2]_2$ dimer. The two acetone molecules, essentially eclipsed and in a *syn* conformation, form somewhat stronger chalcogen-bonding interactions with the S(1) center (S(1)---O(1) 2.842(2); S(1)---O(2) 2.866(2) Å) compared

to the S(2) center (S(2)---O(1) 2.899(2); S(2)---O(2) 2.890(2) Å) of SF_4. These distances are longer than those reported for previous S(IV)---O adducts, including the $(SF_4{\cdot}THF)_2$ dimer (S---O contacts: 2.7766(17)−2.8022(19) Å), and the $SF_4{\cdot}(O{=}C_5H_8)_2$ adduct (S---O contacts: 2.7952(12) and 2.7880(12) Å).[5] This reflects the weaker Lewis basicity of acetone (BF_3 affinity of 76.03±0.21 kJ/mol) compared to THF (BF_3 affinity of 90.40±0.28 kJ/mol).[7] As observed for other SF_4·oxygen-base adducts, the equatorial S−F bonds (1.537(2)−1.547(2) Å) of each SF_4 are significantly shorter than the axial S−F bonds (1.632(3)−1.677(2) Å). These S−F bond lengths are also indistinguishable from those of SF_4 in the solid state (S−F_{eq} 1.527(4) and 1.535(4); S−F_{ax} 1.647(5) and 1.676(5) Å).[8] The F_{eq}−S−F_{eq} angles of the $(SF_4{\cdot}O{=}C(CH_3)_2)_2$ adduct (99.31(11) and 99.41(13)°) are similar to those of SF_4 in the solid state (101.0(2) and 99.6(3)°) further attesting to the weakness of the Lewis acid-base interactions in the present adduct.[8]

The O(1)−S(1)−O(2) and O(1)−S(2)−O(2) angles of $[SF_4{\cdot}O{=}C(CH_3)_2]_2$ are 94.67(7)° and 92.96(7)°, respectively, which are significantly smaller than those in the $(SF_4{\cdot}THF)_2$ dimer (102.12(6)° and 102.03(5)°). As a result, the S(1)−O(1)−S(2) and S(1)−O(2)−S(2) angles are larger (81.69(6)° and 81.95(6)°), as was also observed in the $(SF_4{\cdot}THF)_2$ dimer (77.49 (5)° and 77.97(4)°).

The C=O bonds in $[SF_4{\cdot}O{=}C(CH_3)_2]_2$ (O(1)−C(2) 1.231(4) and O(2)−C(5) 1.219(4) Å) become slightly elongated compared to free acetone (1.208(3) and 1.209(3) Å) upon adduct formation.[9] This is a result of SF_4 withdrawing electron density from the carbonyl group consequently elongating the bond. However, this effect is not strong enough to significantly affect the C−C bonds of adducted acetone (1.484(4)−1.496(4) Å) compared to free acetone (1.485(4) and 1.486(4) Å).

DFT calculations were carried out on $[SF_4{\cdot}O{=}C(CH_3)_2]_2$ and the gas-phase geometry was optimized using the crystal structure as the starting coordinates. The geometric parameters are shown in Table 3.2. Overall, the calculated bond lengths and bond angles are overestimated compared to the experimental data, largely as a result of the crystal packing in the $[SF_4{\cdot}O{=}C(CH_3)_2]_2$ unit cell. The calculated S---O contacts range from 2.923−3.041 Å. The calculated S−F equatorial bond lengths are shorter than the S−F axial bond lengths of SF_4 observed in the crystal structure. The optimized gas-phase geometry was also calculated for $SF_4{\cdot}[O{=}C(CH_3)_2]_2$, as shown in Figure 3.2, and the bond lengths and bond angles are listed in Table 3.3.

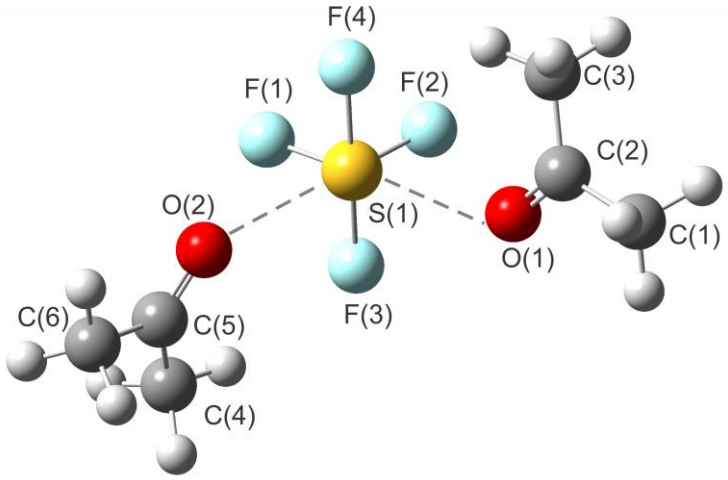

Figure 3.2 Geometry-optimized gas-phase structure of $SF_4{\cdot}[O{=}C(CH_3)_2]_2$ at the B3LYP/aug-cc-pVTZ level of theory.

The $SF_4{\cdot}[O{=}C(CH_3)_2]_2$ adopts a pseudo octahedral geometry about the S(1) center with the acetone molecules staggered in a *syn* conformation. The constraint observed in the O(1)−S(1)−O(2) angle of the $(SF_4{\cdot}O{=}C(CH_3)_2)_2$ dimer (93.28°) is not present in $SF_4{\cdot}[O{=}C(CH_3)_2]_2$ (104.34°) and so, consequently, this calculated angle is larger in the 1:2 adduct. With one less SF_4, the calculated S---O contacts (2.899 Å), while still very weak,

are shorter than the ones of $[SF_4{\cdot}O{=}C(CH_3)_2]_2$. The calculated S−F distances and F−S−F angles of both the 1:1 and 1:2 adducts are essentially the same which reflects the weak Lewis basicity of acetone.

Table 3.3 Calculated Bond Lengths (Å) and Angles (°) of $SF_4{\cdot}[O{=}C(CH_3)_2]_2$.

Bond Lengths			
S(1)---O(1)	2.899	O(1)−C(2)	1.214
S(1)---O(2)	2.899	C(1)−C(2)	1.511
S(1)−F(1)	1.581	C(2)−C(3)	1.510
S(1)−F(2)	1.581	O(2)−C(5)	1.214
S(1)−F(3)	1.707	C(4)−C(5)	1.510
S(1)−F(4)	1.707	C(5)−C(6)	1.511
Bond Angles			
F(1)−S(1)−F(2)	98.39	F(4)−S(1)−O(1)	95.21
F(1)−S(1)−F(3)	87.45	F(4)−S(1)−O(2)	89.74
F(1)−S(1)−F(4)	87.31	O(1)−S(1)−O(2)	104.34
F(1)−S(1)−O(1)	175.96	C(2)−O(1)−S(1)	135.60
F(1)−S(1)−O(2)	78.67	C(5)−O(2)−S(1)	135.66
F(2)−S(1)−F(3)	87.28	O(1)−C(2)−C(1)	121.07
F(2)−S(1)−F(4)	87.44	O(1)−C(2)−C(3)	122.06
F(2)−S(1)−O(1)	78.74	C(1)−C(2)−C(3)	116.87
F(2)−S(1)−O(2)	175.91	O(2)−C(5)−C(4)	122.07
F(3)−S(1)−F(4)	171.95	O(2)−C(5)−C(6)	121.06
F(3)−S(1)−O(1)	89.71	C(6)−C(5)−C(4)	116.86
F(3)−S(1)−O(2)	95.22		
Torsion Angles			
S(1)−O(1)−C(2)−C(1)	173.7	S(1)−O(2)−C(5)−C(4)	−7.2
S(1)−O(1)−C(2)−C(3)	−6.5	S(1)−O(2)−C(5)−C(6)	172.9

3.2.3 Raman Spectroscopy of $[SF_4{\cdot}O{=}C(CH_3)_2]_2$ and $SF_4{\cdot}[O{=}C(CH_3)_2]_2$

The low-temperature Raman spectra of the $[SF_4{\cdot}O{=}C(CH_3)_2]_2$ and $SF_4{\cdot}[O{=}C(CH_3)_2]_2$ adducts were recorded at −110 °C and are depicted in Figure 3.3. Vibrational frequencies of the geometry-optimized compounds were calculated at the B3LYP/aug-cc-pVTZ level of theory and used to aid in the assignments of the Raman bands. The full analysis and assignments of the Raman spectra can be found in the Appendix Table A.1.1. A summary of selected vibrational frequencies is provided in Table 3.4.

Addition of SF_4 to either one or two equivalents of acetone resulted in the formation of the $[SF_4{\cdot}O{=}C(CH_3)_2]_2$ or $SF_4{\cdot}[O{=}C(CH_3)_2]_2$ adduct, respectively, and the subsequent shift in key vibrational frequencies of acetone and SF_4. The C=O stretching frequency of $[SF_4{\cdot}O{=}C(CH_3)_2]_2$ (1699 and 1694 cm^{-1}) and $SF_4{\cdot}[O{=}C(CH_3)_2]_2$ (1702 cm^{-1}) was shifted to a lower frequency compared to free acetone (1709 cm^{-1}). Upon adduct formation, SF_4 withdraws electron density from the C=O bond consequently weakening it which results in a shift to lower frequency. This also results in the strengthening of the C−C bonds which was observed in the Raman spectrum by an increase in the ν_{as} and ν_s (CCC) frequencies of $[SF_4{\cdot}O{=}C(CH_3)_2]_2$ (1236; 798 and 794 cm^{-1}) and $SF_4{\cdot}[O{=}C(CH_3)_2]_2$ (1230; 794 cm^{-1}) relative to acetone (1222; 788 cm^{-1}). The Raman bands of acetone are not greatly shifted, which is in accordance with the observations for other SF_4·oxygen-base adducts. The $SF_4{\cdot}(O{=}C_5H_8)_2$ adduct showed a decrease in the C=O stretching frequency from 1743/1728 cm^{-1}, for cyclopentanone, to 1724/1712 cm^{-1}.[5] The C−C stretches for other SF_4·oxygen-base adducts are also shifted by small amounts and show vibrational coupling.[5]

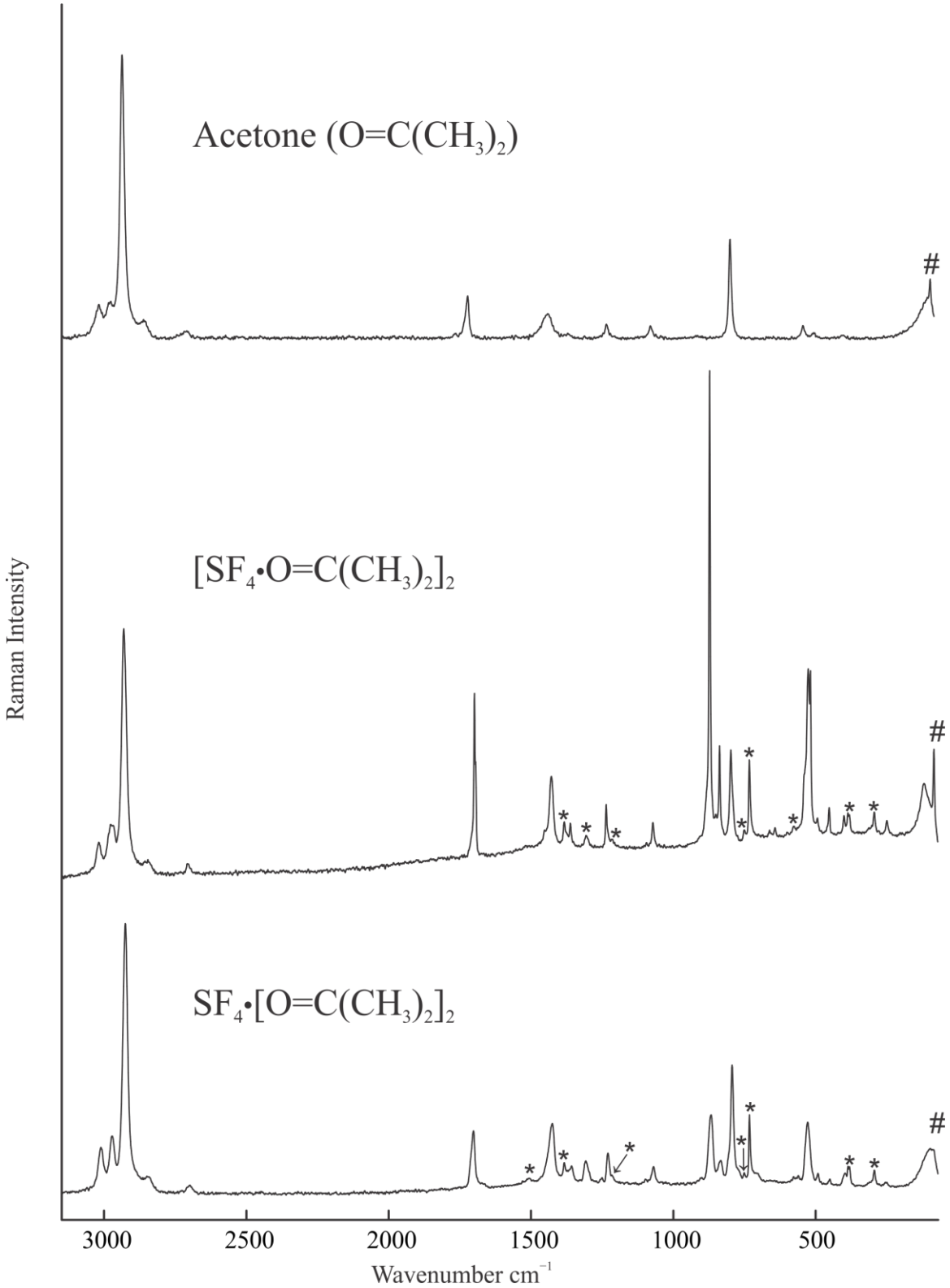

Figure 3.3 Raman spectrum of $O=C(CH_3)_2$, $SF_4 \cdot [O=C(CH_3)_2]_2$ and $[SF_4 \cdot O=C(CH_3)_2]_2$ at −110 °C. Symbols denote bands arising from FEP sample tube (*), and an instrumental artifact (#).

Table 3.4 Observed and Calculated ν(CO), ν(CCC), and Select ν(SF_4) Frequencies (cm^{-1}) of the $SF_4{\cdot}[O{=}C(CH_3)_2]_2$ and $[SF_4{\cdot}O{=}C(CH_3)_2]_2$ Adducts.

SF_4		$O{=}C(CH_3)_2$		$SF_4{\cdot}[O{=}C(CH_3)_2]_2$		$[SF_4{\cdot}O{=}C(CH_3)_2]_2$		Tentative Assignments [a]
exptl [b]	*calcd* [b,c]	*exptl* [d]	*calcd* [e]	*exptl* [b]	*calcd* [e]	*exptl* [a]	*calcd* [e]	
-	-	1709(16)	1782(13)	1702(22)	1770(32) 1766(15)	1699(35) 1694(21)	1759(30) 1753(15)	ν(CO)
-	-	1222(6)	1234(5)	1230(13)	1243(12) 1242(16)	1236(11)	1247(8) 1247(19)	ν_{as}(CCC)
		788(37)	783(16)	805sh 794(45)	788(22) 788(5)	798(20) 794sh	790(15) 790(7)	ν_s(CCC)
892	856(13)	-	-	868(26)	836(95)	880sh 873(100)	828(11) 839(108)	$\nu_s(SF_{2,\,eq})$
867	825(4)	-	-	833(9)	803(18)	850(16) 837(21)	805(2) 797(28)	$\nu_{as}(SF_{2,\,eq})$
730	703(<1)	-	-	n.o.	652(1)	662(2) 643(2)	688(2) 650(2)	$\nu_{as}(SF_{2,\,ax})$
558	535(12)	-	-	528(24)	506(10)	526(36) 519(35)	516(12) 511(4)	$\nu_s(SF_{2,\,ax})$

[a] The abbreviations denote symmetric (s), asymmetric (as), equatorial (eq), axial (ax), stretch (ν), shoulder (sh), and not observed (n.o.). [b] The experimental gas-phase vibrational frequencies and assignments from Ref. 10. [c] The calculated vibrational frequencies and assignments from Ref 10. [d] Raman intensities, in $Å^4\ u^{-1}$, are given in parentheses. [e] DFT calculations at the B3LYP/aug-cc-pVTZ level of theory.

The S−F stretching bands of the adducts are all shifted to lower frequencies upon adduct formation reflecting an increase in ionic character of the S−F bonds in SF_4. The most intense band in the $[SF_4{\cdot}O{=}C(CH_3)_2]_2$ Raman spectrum, at 873 cm^{-1}, is associated with the $\nu_s(SF_{2,eq})$ mode and is significantly shifted to a lower frequency compared to free SF_4 (892 cm^{-1}). As well, the $\nu_s(SF_{2,ax})$ mode is dramatically lowered to 526/519 cm^{-1} compared to free SF_4 (558 cm^{-1}). Many of the S−F bands in the $[SF_4{\cdot}O{=}C(CH_3)_2]_2$ Raman spectrum show splitting into two bands which can be associated with vibrational coupling of the two SF_4 moieties in the $[SF_4{\cdot}O{=}C(CH_3)_2]_2$ dimer. These splittings were also

predicted in the calculated vibrational frequencies for the gas-phase optimized geometry. Similar shifts to lower frequencies in the $\nu_s(SF_{2,eq})$ and $\nu_s(SF_{2,ax})$ modes were also detected in $SF_4 \cdot [O=C(CH_3)_2]_2$ Raman spectrum (868; 528 cm^{-1}).

3.2.4 X-ray Crystallography of $SF_4 \cdot (O=C_{10}H_{14}) \cdot (HF)$

The crystallographic parameters and details of data collection for $SF_4 \cdot (O=C_{10}H_{14}) \cdot (HF)$ are given in Table 3.5. The bond lengths and bond angles are listed in Table 3.6. The data showed a completeness of 88% to 136.388° as a result of the twinned nature of the crystal.

The $SF_4 \cdot (O=C_{10}H_{14}) \cdot (HF)$ crystallized in the $P3_2$ space group and contains chains of alternating SF_4, $O=C_{10}H_{14}$, and HF molecules (Figure 3.4). Each SF_4 has one S---O chalcogen bond to an oxygen atom, (S(1)---O(2) 2.969(4); S(2)---O(3) 2.973(4); S(3)---O(1) 3.060(4) Å) from 2-adamantanone, and a second S---F chalcogen bond to a fluorine atom of HF (S(1)---F(1) 2.784(4); S(2)---F(6) 2.835(3); S(3)---F(11) 2.728(4) Å), which in turn is hydrogen-bonded to an oxygen atom of 2-adamantanone (O(1)---F(1) 2.462(5); O(2)---F(6) 2.489(5); O(3)---F(11) 2.469(4) Å). Previous crystal structures of $(SF_4 \cdot O=C(CH_3)_2)_2$ and $SF_4 \cdot (O=C_5H_8)_2$ have contained S---O chalcogen bonds between SF_4 and a ketone ranging from 2.842(2)−2.899(2) Å and 2.7952(12)−2.7880(12) Å, respectively.[5] The S---O chalcogen bonding interactions in $SF_4 \cdot (O=C_{10}H_{14}) \cdot (HF)$ are even weaker but still smaller than the sum of the van der Waals radii (3.32 Å).[11] This O---(HF)---S secondary bonding interaction is the first example where HF is bridging a sulfur atom of SF_4 to an oxygen atom of a ketone. The crystal structure of $C_8H_{10}N_4O_2 \cdot 2SF_4 \cdot HF$ showed HF hydrogen-bonded to a Lewis basic nitrogen atom of caffeine with an N---(HF)---S

linkage. In this structure caffeine forms an adduct with SF_4 through similarly weak C=O---S chalcogen bonding interactions (up to 2.9954(18) Å).[5]

Table 3.5 Summary of X-ray Crystal Data and Refinement Results of $SF_4 \cdot (O=C_{10}H_{14}) \cdot (HF)$.

Compound	$SF_4 \cdot (O=C_{10}H_{14}) \cdot (HF)$
Empirical Formula	$C_{10}H_{15}OF_5S$
Formula Weight (g mol^{-1})	278.32
Temperature (^oC)	−173
Wavelength (Å)	1.54184
Crystal System	trigonal
Space Group	$P3_2$
a (Å)	16.26538(14)
b (Å)	16.26538(14)
c (Å)	11.89644(13)
α (deg)	90
b (deg)	90
γ (deg)	120
V ($Å^3$)	2725.69(5)
Z	9
μ (mm^{-1})	2.999
ρ_{calcd} (g cm^{-3})	1.573
F(000)	1340.0
Crystal Size (mm^3)	0.400 × 0.325 × 0.189
Reflections Collected	17181
Independent Reflections	5860
Data/Restraints/Parameters	5860/1/469
Goodness-of-fit on F^2	1.055
R_1, I ≥2θ(I)	0.0314
wR_2 (F^2)	0.0812

Table 3.6 Experimental Bond Lengths (Å) and Angles (°) of $SF_4 \cdot (O=C_{10}H_{14}) \cdot (HF)$.

Bond Lengths			
O(1)---F(1)	2.462(5)	C(26)−C(27)	1.538(7)
O(2)---F(6)	2.489(5)	C(27)−C(30)	1.536(8)
O(3)---F(11)	2.469(4)	C(28)−C(30)	1.543(7)
S(1)---O(2)	2.969(4)	C(29)−C(30)	1.532(7)
S(2)---O(3)	2.973(4)	O(2)−C(11)	1.229(6)
$S(3)^1$---O(1)	3.060(4)	C(11)−C(12)	1.487(7)
S(1)---F(1)	2.784(4)	C(11)−C(19)	1.505(7)
S(1)−F(2)	1.545(3)	C(12)−C(13)	1.546(7)
S(1)−F(3)	1.559(3)	C(12)−C(17)	1.548(7)
S(1)−F(4)	1.653(4)	C(13)−C(14)	1.537(7)
S(1)−F(5)	1.651(3)	C(14)−C(15)	1.534(7)
S(2)---F(6)	2.835(3)	C(14)−C(20)	1.545(8)
S(2)−F(7)	1.638(4)	C(15)−C(16)	1.529(7)
S(2)−F(8)	1.661(4)	C(16)−C(17)	1.528(8)
S(2)−F(9)	1.539(3)	C(16)−C(18)	1.535(8)
S(2)−F(10)	1.550(3)	C(18)−C(19)	1.551(6)
S(3)---F(11)	2.728(4)	C(19)−C(20)	1.536(7)
S(3)−F(12)	1.546(4)	O(1)−C(1)	1.241(6)
S(3)−F(13)	1.538(4)	C(1)−C(2)	1.497(6)
S(3)−F(14)	1.669(4)	C(1)−C(8)	1.507(7)
S(3)−F(15)	1.647(4)	C(2)−C(3)	1.542(7)
O(3)−C(21)	1.232(6)	C(2)−C(10)	1.534(7)
C(21)−C(22)	1.507(7)	C(3)−C(4)	1.532(8)
C(21)−C(26)	1.501(7)	C(4)−C(5)	1.533(7)
C(22)−C(23)	1.558(7)	C(4)−C(9)	1.522(7)
C(22)−C(28)	1.534(7)	C(5)−C(6)	1.548(7)
C(23)−C(24)	1.523(7)	C(6)−C(7)	1.530(7)
C(24)−C(25)	1.530(7)	C(6)−C(10)	1.523(7)
C(24)−C(29)	1.519(8)	C(7)−C(8)	1.566(7)
C(25)−C(26)	1.567(7)	C(8)−C(9)	1.534(7)
Bond Angles			
F(2)−S(1)−F(3)	97.98(18)	C(27)−C(26)−C(21)	108.0(4)
F(2)−S(1)−F(4)	87.7(2)	C(27)−C(26)−C(25)	108.4(4)
F(2)−S(1)−F(5)	87.1(2)	C(30)−C(27)−C(26)	110.5(4)
F(2)−S(1)−F(1)	71.67(15)	C(30)−C(28)−C(22)	110.3(4)
F(2)−S(1)−O(2)	170.79(17)	C(30)−C(29)−C(24)	110.2(4)
F(3)−S(1)−F(4)	87.5(2)	C(28)−C(30)−C(27)	108.0(4)
F(3)−S(1)−F(5)	87.4(2)	C(29)−C(30)−C(27)	109.1(4)
F(3)−S(1)−F(1)	167.18(16)	C(29)−C(30)−C(28)	110.2(4)
F(3)−S(1)−O(2)	75.92(15)	O(1)−F(1)−S(1)	118.60(15)
F(4)−S(1)−F(1)	99.35(16)	C(11)−O(2)−S(1)	123.9(3)
F(4)−S(1)−O(2)	85.22(16)	O(2)−C(11)−C(12)	124.0(5)
F(5)−S(1)−F(4)	172.1(2)	C(19)−C(11)−O(2)	122.1(5)
F(5)−S(1)−F(1)	84.59(16)	C(19)−C(11)−C(12)	114.0(4)
F(5)−S(1)−O(2)	99.39(15)	C(13)−C(12)−C(11)	108.2(4)
F(1)−S(1)−O(2)	115.26(11)	C(17)−C(12)−C(11)	108.6(4)
F(7)−S(2)−F(8)	172.4(2)	C(17)−C(12)−C(13)	108.6(4)
F(7)−S(2)−F(6)	82.95(15)	C(14)−C(13)−C(12)	110.2(4)
F(7)−S(2)−O(3)	99.40(15)	C(15)−C(14)−C(13)	109.9(4)
F(8)−S(2)−F(6)	101.12(17)	C(20)−C(14)−C(13)	108.3(4)
F(8)−S(2)−O(3)	84.42(16)	C(20)−C(14)−C(15)	109.6(4)
F(9)−S(2)−F(7)	87.7(2)	C(16)−C(15)−C(14)	109.2(4)

F(9)−S(2)−F(8)	87.7(2)	C(17)−C(16)−C(15)	110.5(5)
F(9)−S(2)−F(10)	99.01(18)	C(18)−C(16)−C(15)	110.3(5)
F(9)−S(2)−F(6)	70.49(14)	C(18)−C(16)−C(17)	109.1(4)
F(9)−S(2)−O(3)	169.22(17)	C(16)−C(17)−C(12)	109.3(4)
F(10)−S(2)−F(7)	87.3(2)	C(19)−C(18)−C(16)	109.1(4)
F(10)−S(2)−F(8)	87.5(2)	C(18)−C(19)−C(11)	107.5(4)
F(10)−S(2)−F(6)	165.90(16)	C(20)−C(19)−C(11)	108.5(4)
F(10)−S(2)−O(3)	73.39(14)	C(20)−C(19)−C(18)	109.7(4)
F(6)−S(2)−O(3)	118.24(11)	C(19)−C(20)−C(14)	109.7(4)
F(12)−S(3)−F(14)	87.0(3)	F(1)−O(1)−S(3)[1]	95.54(14)
F(12)−S(3)−F(15)	88.2(3)	C(1)−O(1)−S(3)[1]	124.0(3)
F(12)−S(3)−F(11)	80.14(17)	C(1)−O(1)−F(1)	128.7(3)
F(13)−S(3)−F(12)	99.6(2)	C(2)−C(1)−O(1)	124.4(4)
F(13)−S(3)−F(14)	87.4(3)	C(8)−C(1)−O(1)	121.5(4)
F(13)−S(3)−F(15)	87.6(3)	C(8)−C(1)−C(2)	114.1(4)
F(13)−S(3)−F(11)	178.2(2)	C(3)−C(2)−C(1)	107.8(4)
F(14)−S(3)−F(11)	90.85(19)	C(10)−C(2)−C(1)	107.6(4)
F(15)−S(3)−F(14)	172.4(2)	C(10)−C(2)−C(3)	109.7(4)
F(15)−S(3)−F(11)	94.15(18)	C(4)−C(3)−C(2)	110.3(4)
C(21)−O(3)−S(2)	128.1(3)	C(5)−C(4)−C(3)	109.1(4)
C(22)−C(21)−O(3)	123.7(4)	C(9)−C(4)−C(3)	108.3(4)
C(26)−C(21)−O(3)	121.8(5)	C(9)−C(4)−C(5)	110.2(4)
C(26)−C(21)−C(22)	114.4(4)	C(6)−C(5)−C(4)	109.8(4)
C(23)−C(22)−C(21)	107.6(4)	C(7)−C(6)−C(5)	109.5(4)
C(28)−C(22)−C(21)	107.2(4)	C(10)−C(6)−C(5)	109.8(4)
C(28)−C(22)−C(23)	109.6(4)	C(10)−C(6)−C(7)	109.5(4)
C(25)−C(24)−C(23)	110.2(4)	C(8)−C(7)−C(6)	108.8(4)
C(29)−C(21)−C(22)	108.5(4)	C(7)−C(8)−C(1)	107.4(4)
C(29)−C(24)−C(23)	110.7(4)	C(9)−C(8)−C(1)	107.6(4)
C(29)−C(24)−C(25)	109.6(5)	C(9)−C(8)−C(7)	110.1(4)
C(26)−C(25)−C(24)	109.9(4)	C(8)−C(9)−C(4)	110.6(4)
C(25)−C(26)−C(21)	107.6(4)	C(6)−C(10)−C(2)	110.1(4)

[1] 1−y, +x−y, −1/3+z

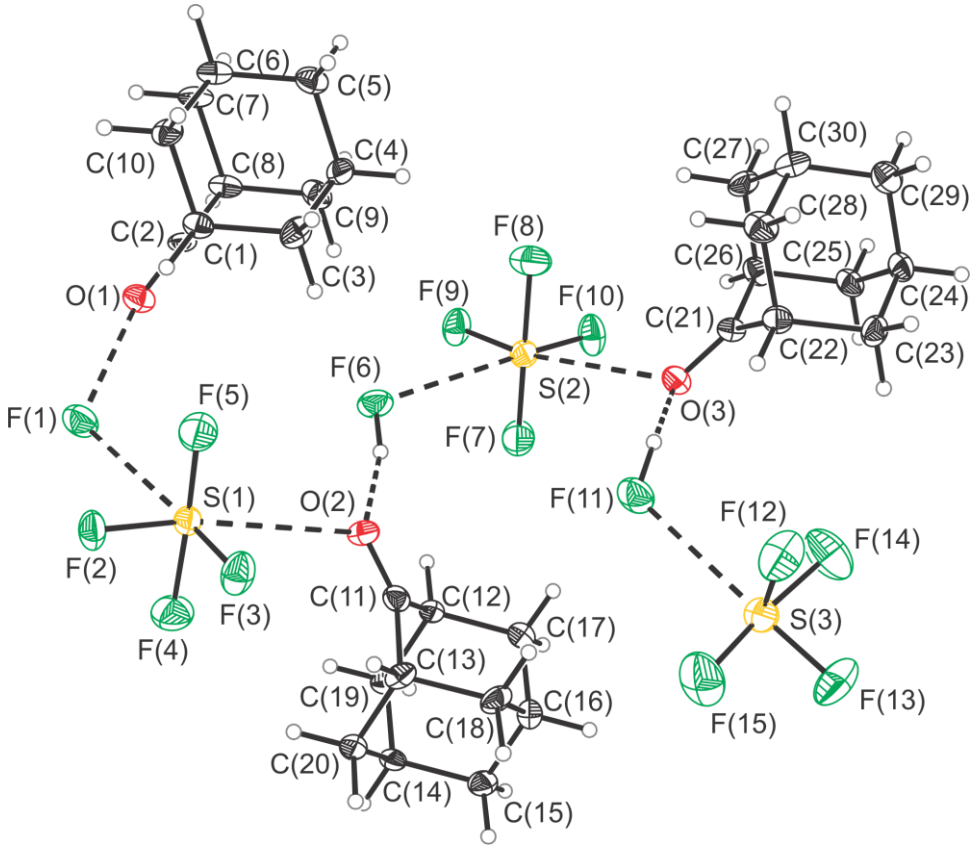

Figure 3.4 Thermal ellipsoid plots of $SF_4 \cdot (O=C_{10}H_{14}) \cdot (HF)$. Thermal ellipsoids are set at the 50% probability level.

The C=O bond of each 2-adamantanone are slightly elongated in $SF_4 \cdot (O=C_{10}H_{14}) \cdot (HF)$ (O(1)=C(1) 1.241(6); O(2)=C(11) 1.229(6); O(3)=C(21) 1.232(6) Å) compared to non-adducted 2-adamantanone (1.215(3) Å).[12] This is a result of weakly Lewis acidic SF_4 withdrawing electron density from the carbonyl bond upon adduct formation, typical of SF_4·oxygen-base adducts. Previous adducts of SF_4 with pyridine, and its derivatives, by solvolysis with HF, included the protonation of the nitrogen base which, in turn, resulted in the formation of F_4S---(F)---HN interactions.[13] This is not the case for the crystal structure of $SF_4 \cdot (O=C_{10}H_{14}) \cdot (HF)$ as two of the three protons were found in the electron difference map bonded to a fluorine atom forming HF as opposed to protonation

of the oxygen of the carbonyl group. In contrast to pyridine, the carbonyl group is not basic enough to be protonated under these conditions.[6] If the C=O group was protonated by HF, the C=O bond length would be even more elongated, as was previously observed for the oxonium cation $[HO{=}C_{10}H_{14}]^+$ (1.274(2) Å) in the solid state.[14] Deoxofluorination reactions of ketones with SF_4 typically require at least a catalytic amount of HF in order to generate, what is believed to be the active species, $[SF_3]^+$ and $[HF_2]^-$. The reaction mixture of SF_4, HF, and 2-adamantanone should result in the deoxofluorination of the carbonyl group to a $-CF_2$ group under more severe reaction conditions. The crystal structure of $SF_4{\cdot}(O{=}C_{10}H_{14}){\cdot}(HF)$ illustrates the interactions between these three molecules prior to the possible deoxofluorination of 2-adamantanone. It shows the weakening of the C=O bond as a result of the F−H---O=C interaction. The presence of a F−H---FSF_3 linkage is not present, despite the assumption that the first step of a deoxofluorination reaction is the generation of $[SF_3]^+$ and $[HF_2]^-$.

3.3 Summary and Conclusions

The Lewis acid-base adduct between SF_4 and acetone, the simplest aliphatic ketone, has long been sought-after and has now finally been synthesized and characterized in the solid state. The $SF_4{\cdot}[O{=}C(CH_3)_2]_2$ and $[SF_4{\cdot}(O{=}C(CH_3)_2]_2$ adducts were both characterized by Raman spectroscopy which showed shifts in characteristic bands associated with the acetone molecules. The C=O stretch decreased by 7 and 10 cm^{-1} for $SF_4{\cdot}[O{=}C(CH_3)_2]_2$ and $[SF_4{\cdot}(O{=}C(CH_3)_2]_2$, respectively. These small changes in frequency are a result of the weak interactions between SF_4 and acetone. The symmetric and asymmetric stretches of the SF_2 moieties in SF_4 showed significant decreases as well. The most notable is the symmetric

(SF_2)-equatorial stretch which decreased by 24 cm^{-1} for $SF_4 \cdot [O=C(CH_3)_2]_2$ and 19 cm^{-1} for $[SF_4 \cdot (O=C(CH_3)_2]_2$. A single crystal of the thermally unstable $(SF_4 \cdot (O=C(CH_3)_2)_2$ was successfully isolated and the X-ray crystal structure confirmed the weak interactions between acetone and SF_4 with S---O distances ranging from 2.842(2)−2.899(2) Å. DFT calculations of the gas-phase optimized geometry of the $[SF_4 \cdot (O=C(CH_3)_2]_2$ dimer typically overestimate the bond lengths and bond angles which was attributed $[SF_4 \cdot (O=C(CH_3)_2]_2$ being in the gas phase as opposed to the solid state where crystal packing likely resulted in more constrained geometric parameters.

The crystal structure of $SF_4 \cdot (O=C_{10}H_{14}) \cdot (HF)$ shows a new bonding modality where HF bridges a ketone and SF_4 via O---(HF)---S secondary bonding interactions creating a chained packing arrangement. Also present were weak S---O chalcogen bonding interactions with distances of 2.969(3)−3.060(4) Å. This F−H---O=C interaction is in contrast to a F−H---FSF_3 interaction which would lead to the proposed intermediate $[SF_3]^+$ in deoxofluorination reactions. This X-ray crystal structure could shed light onto the reaction mechanism of deoxofluorination reactions involving SF_4. However, in solution the interactions between all species are dynamic and this structure may not represent the relevant interactions for the actual reaction pathway.

References

[1] (a) Dmowski, W. Introduction of Fluorine Using Sulfur Tetrafluoride and Analogues in Organo-Fluorine Compounds, *Houben-Weyl, Methods of Organic Chemistry*; Baasner, B.; Hagemann, H.; Tatlow, J. C.; Eds.; Thieme: Stuttgart, Germany, 2000; Vol. E10a, pp 321−431. (b) Smith, W. C. *Angew. Chem. Int. Ed.* **1962**, *1*, 467−518.

[2] Muetterties, E. L. U.S. Patent 2,729,663, 1959.

[3] Azeem, M. *Pak. J. Sci. Ind. Res.* **1967**, *10*, 10−12.

[4] Sass, C. S.; Ault, B. S. *J. Phys. Chem.* **1985**, *89*, 1002−1006.

[5] Goettel, J. T.; Gerken, M *Inorg. Chem.* **2016**, *55*, 12441−12450.

[6] Goettel, J. T.; Kostiuk, N.; Gerken, M. *Inorg. Chem.* **2016**, *55*, 7126−7134.

[7] Laurence, C.; Gal, J.-F. *Lewis Basicity and Affinity Scales: Data and Measurement*; John Wiley & Sons: Chichester, 2010; Chapter 3.

[8] Goettel, J. T.; Kostiuk, N.; Gerken, M. *Angew. Chem. Int. Ed.* **2013**, *52*, 8037−8040.

[9] Allan, D. R.; Clark, S. J.; Ibberson, R. M.; Parsons, S.; Pulham, C. R.; Sawyer, L. *Chem. Commun.* **1999**, 751−752.

[10] Christe, K. O.; Zhang, X.; Sheehy, J. A.; Bau, R. *J. Am. Chem. Soc.* **2001**, *123*, 6338−6348.

[11] Bondi, A. *J. Phys. Chem.* **1964**, *68*, 441−451.

[12] Amoureux, J. P.; Bee, M. *J. Phys. C.* **1980**, *13*, 3577−3583.

[13] Chaudhary, P.; Goettel, J. T.; Mercier, H. P.; Sowlati-Hashjin, S.; Hazendonk, P.; Gerken, M. *Chem. Eur. J.* **2015**, *21*, 6247−6256.

[14] Stuart, D.; Wetmore, S. D.; Gerken, M. *Angew. Chem. Int. Ed.* **2017**, *56*, 16380−16384.

4. Lewis Acid-Base Adducts of $[SF_3]^+$ with Ketones

4.1 Introduction

Deoxofluorination reactions are commonly used in organic chemistry as a means of transforming either an alcohol, ketone, or carboxylic acid to a −CF, $-CF_2$, or $-CF_3$ group, respectively.[1–4] The archetypical deoxofluorinating reagents is sulfur tetrafluoride, SF_4.[2] The reaction mechanism for deoxofluorination reactions with SF_4 is speculated to include a reactive species responsible for polarizing the C=O bond, consequently allowing for a nucleophilic fluoride source to attack the carbon center and generate the desired C−F bond. Mechanisms for deoxofluorination have been proposed (see Chapter 1, Section 1.1.1). One proposed intermediate for this mechanism is the $[SF_3]^+$ cation adducted to a carbonyl group. Another is the neutral alkoxysulfur trifluoride, $ROSF_3$, however, there are only a few reports of such a species existing.[5,6]

4.2 Results and Discussion

4.2.1 Synthesis of $[SF_3][AsF_6]$ with the Ketones Acetone, Cyclopentanone, and 2-Adamantanone

In an effort to synthesize adducts of $[SF_3]^+$ with ketones, the $[SF_3][AsF_6]$ salt was reacted with approximately one or two molar equivalents of cyclopentanone and 2-adamantanone. In the case of acetone, 1−3 equivalents were used, as well as, an excess of acetone (i.e., as the solvent). Sulfur dioxide (m.p. = −72 °C) was chosen as the solvent for the stoichiometric reactions as both the ketones and $[SF_3][AsF_6]$ were highly soluble in it resulting in solutions even at low temperatures. As the only exception, the reaction of $[SF_3]^+$ with two equivalents of 2-adamantanone resulted in precipitation of a white solid at −70

°C. The $[SF_3]^+$ cation does not react with SO_2 making it an ideal polar solvent. The solubility of $[SF_3][AsF_6]$ was tested in other solvents including CH_2Cl_2, $CFCl_3$, and SO_2ClF, however, it was found to be insoluble. Attempts to carry out these reactions in anhydrous HF resulted in the generation of a superacidic solution where protonation of the ketones was observed as opposed to adduct formation (see Chapter 5 for these results). Solvents containing a nitrogen base (i.e. pyridine and acetonitrile) were avoided since their higher basicity would result in the formation of $[SF_3{\cdot}(N\text{-base})_2]^+$ adducts, as previously shown.[7]

Reactions of $[SF_3][AsF_6]$ with acetone, cyclopentanone, and 2-adamantanone were carried out in SO_2 starting at −70 °C (Equation 4.1) and were allowed to gradually warm to higher temperatures (up to RT) for controlled periods of time while using ^{19}F and ^{1}H NMR spectroscopy at −70 °C to monitor the progress of the reaction. When two equivalents of 2-adamantanone were reacted with $[SF_3][AsF_6]$ in SO_2 at −70 °C, an insoluble white solid was present and required the reaction mixture to be warmed to −40 °C to dissolve the unidentified product. Due to the challenges associated with working on a small scale (< 40 mg of $[SF_3][AsF_6]$), volumes of the ketones, acetone and cyclopentanone, were measured to the nearest 0.01 mL or 0.001 g and only approximate ratios were be obtained. The $[SF_3{\cdot}(O\text{-base})_x][AsF_6]$ (x = 1−3) adducts were attempted to be characterized in the solid state using LT Raman spectroscopy, but removal of SO_2 under dynamic vacuum consistently resulted in either dark brown or purple powders that could not be identified due to large fluorescence in the Raman spectrum. These adducts were also highly sensitive to temperature and moisture in SO_2 solutions resulting in dark red or orange solutions when warmed to RT. In some instances, when the reaction was not carefully controlled and kept at −70 °C, small dark orange spots would appear on the top of the ¼-in. o.d. FEP reactors.

These unidentified decomposition products were a result of parts of the reactor being at RT. When these came in contact with the bulk sample, an immediate colour change of the sample from colourless to dark orange appeared indicating the decomposition of the $[SF_3 \cdot (O\text{-base})_x]^+$ adduct.

$$[SF_3][AsF_6] \; + \; x\, O{=}R \xrightarrow{SO_2} [SF_3 \bullet (O{=}R)_x][AsF_6] \qquad (x = 1, 2)$$
$$R = C(CH_3)_2,\ C_5H_8,\ C_{10}H_{14} \tag{4.1}$$

4.2.2 $[SF_3][AsF_6]$ in Excess Acetone

The reaction of $[SF_3][AsF_6]$ with excess acetone, i.e., acetone as the solvent, was carried out at −80 °C (m.p. of acetone = −94.7 °C), and allowed to warm up for carefully controlled periods of time. The ^{19}F NMR spectra are depicted in Figure 4.1 and the chemical shifts and coupling constants listed in Table 4.1. Upon melting the mixture of acetone and $[SF_3][AsF_6]$ at −80 °C, a clear and colourless solution formed. The ^{19}F NMR spectrum (Figure 4.1) contained resonances at 18.43 ppm, tentatively assigned to the $[SF_3 \cdot \{O{=}C(CH_3)_2\}_3]^+$ adduct cation, and −63.94 ppm, associated with the $[AsF_6]^-$ anion (Equation 4.2). The chemical shift of $[SF_3]^+$ in SO_2 appears at 32.91 ppm as a singlet and the $[AsF_6]^-$ resonance of $[SF_3][AsF_6]$ in SO_2 solvent is a broad singlet at –58.53 ppm. Upon dissolving this salt in acetone, a Lewis basic solvent, the chemical shift of $[SF_3]^+$ decreases in frequency to 18.43 ppm due to the donation of electron density from the oxygen of acetone to sulfur. This leads to the S−F bonds being slightly more ionic which results in a significant decrease in the chemical shift. Evidence for the coordination of three acetone molecules to $[SF_3]^+$ is also detected by the shape of the ^{19}F resonance for $[AsF_6]^-$ which appears as a sharp equal-intensity quartet. The sulfur center of $[SF_3]^+$ has three additional

contacts with the anions in solid $[SF_3][AsF_6]$ and $[SF_3][SbF_6]$ resulting in a coordination number of 6.[7] Only with strong bases, such as pyridine, has sulfur of $[SF_3]^+$ been observed to accept only 2 dative bonds forming the $[SF_3(NC_5H_5)_2]^+$ cation.[7] The observation of a sharp quartet with a $^1J(^{75}As–^{19}F)$ = 934 Hz is a consequence of a negligible electric field gradient about ^{75}As (I = 3/2, 100%), causing slow quadrupolar relaxation. This indicates the anion is perfectly isolated adopting an octahedral geometry with no contacts to the cation.

$$[SF_3][AsF_6] \; + \; 3\ O{=}C(CH_3)_2 \xrightarrow[\text{Acetone}]{-80\ ^\circ C} [SF_3{\bullet}\{O{=}C(CH_3)_2\}_3][AsF_6] \qquad (4.2)$$

While no changes were observed when the reaction was warmed to −60 °C, at −40 °C the solution turned an orange/brown colour. The ^{19}F resonance for the $[SF_3{\cdot}\{O{=}C(CH_3)_2\}_3]^+$ cation (18.42 ppm) was no longer present and, instead, two new resonances at 76.88 (F_{ax} of SF_4) and 30.16 ppm (F_{eq} of SF_4) appeared due to the formation of SF_4, with scalar $^2J(^{19}F–^{19}F)$ coupling of 68.6 Hz between the equatorial and axial fluorine atoms. The $[SF_3{\cdot}\{O{=}C(CH_3)_2\}_3][AsF_6]$ compound seems to undergo a dismutation reaction presumably forming the elusive and highly reactive $[SF_2{\cdot}\{O{=}C(CH_3)_2\}_3][AsF_6]_2$ compound in addition to SF_4 (Equation 4.3). The proposed dismutation reaction is supported by the observed integration of 1.9:2.0:10.3 for the axial and equatorial fluorine environments of SF_4 and $[AsF_6]^-$ after warming the reaction mixture to −40 °C. However, the $[SF_2{\cdot}\{O{=}C(CH_3)_2\}_3]^{2+}$ cation is expected to be highly reactive, i.e., strongly oxidizing, and likely reacts with acetone to form a radical cation which would account for the intense dark purple colour of the solution.

$$2\ [SF_3{\bullet}\{O{=}C(CH_3)_2\}_3][AsF_6] \longrightarrow [SF_2{\bullet}\{O{=}C(CH_3)_2\}_3][AsF_6]_2 \; + \; SF_4 \qquad (4.3)$$

Table 4.1 Selected ^{19}F chemical shifts (δ) at −80 °C for the reaction of $[SF_3][AsF_6]$ with excess acetone.

Compound	Chemical Shift (ppm) [a]	$^2J(^{19}F–^{19}F)$ (Hz)	$^1J(^{19}F–^{75}As)$ (Hz)
Reaction at −80 °C for 1 min			
SOF_2	69.12 (s)	--	--
$[SF_3{\cdot}\{O{=}C(CH_3)_2\}_3]^+$	18.43 (s)	--	--
$[AsF_6]^-$	–63.94 (q)	--	934
Reaction at −60 °C for 5 min			
SOF_2	69.10 (s)	--	--
$[SF_3{\cdot}\{O{=}C(CH_3)_2\}_3]^+$	18.42 (s)	--	--
$[AsF_6]^-$	–63.94 (q)	--	934
Reaction at −40 °C for 10 min			
SF_4	76.88 (F_{ax}, t) 30.16 (F_{eq}, t) [b]	68.6	--
SOF_2	69.08 (s)	--	--
$[AsF_6]^-$	−63.85 (q)	--	931
HF	−180.86 (s, br)	--	--
Reaction at −20 °C for 10 min			
SF_4	76.94 (F_{ax}, t) 30.19 (F_{eq}, t) [b]	68.6	--
SOF_2	69.12 (s) [c]	--	--
$[AsF_6]^-$	−63.82 (q)	--	931
HF	−180.84 (s, br)	--	--
Reaction at RT for 1 min			
SOF_2	69.10 (s) [c]	--	--
$[AsF_6]^-$	−63.82 (q)	--	931
HF	−180.84 (s, br)	--	--

[a] Abbreviations: (s) singlet; (t) triplet; (q) quartet; (ax) axial; (eq) equatorial; (br) broad.
[b] $\Delta\delta(^{34}S–^{32}S)$ = 0.065 ppm. [c] $^1\Delta^{19}F(^{34/32}S)$ = 0.057 ppm.

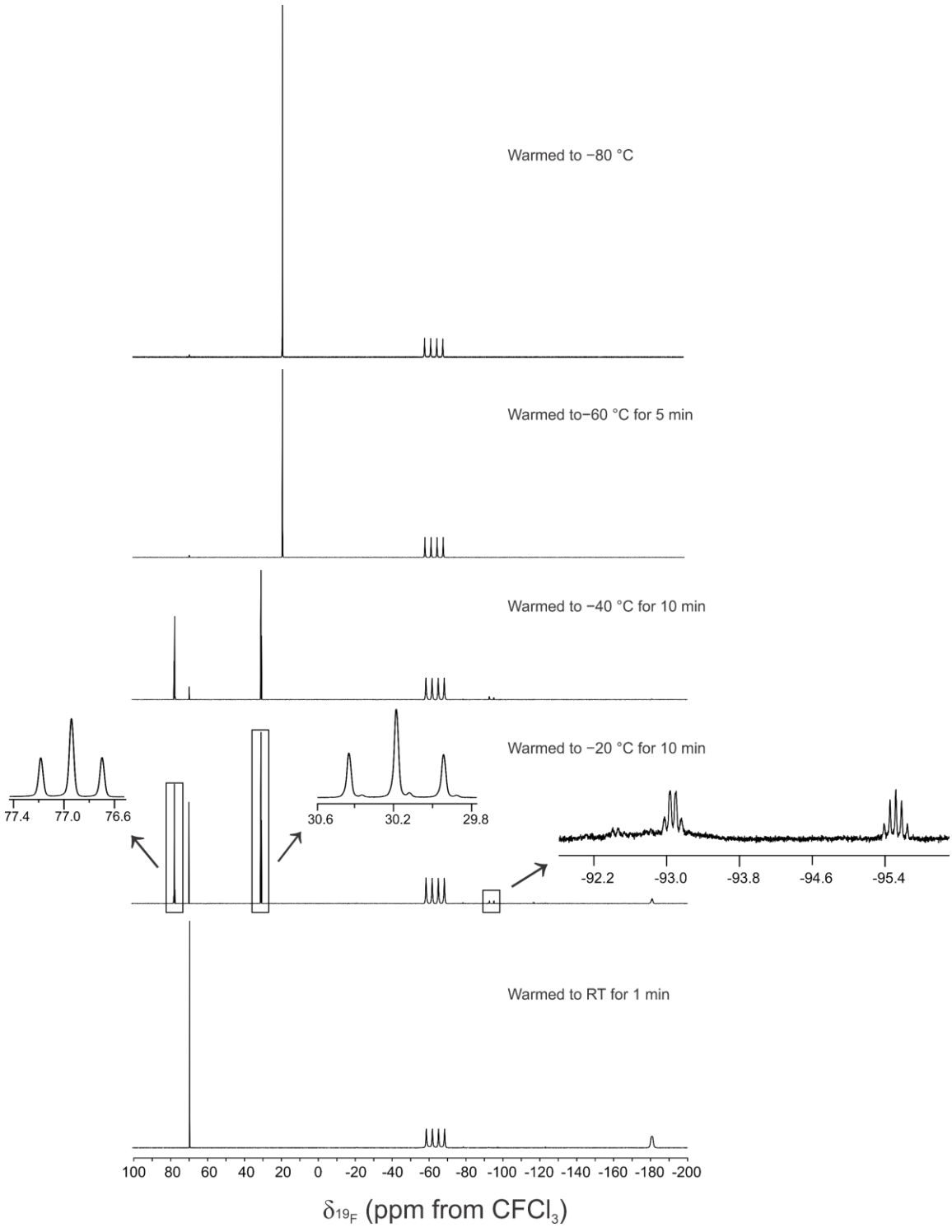

Figure 4.1 ^{19}F NMR spectrum (282.40 MHz) of $[SF_3][AsF_6]$ dissolved in excess acetone at −80 °C. Reaction warmed from −80 °C to RT. Externally referenced to $CFCl_3$ at RT.

After warming to −20 °C for 10 min, SOF_2 and HF were observed, by-products of deoxofluorination, as well as some weak resonances at −93.1 (quartet; J = 17.6 Hz) and −95.5 ppm (septet; J = 18.2 Hz). The assignments of a septet multiplicity is based on the relative intensities of the observed central five transitions (expected: 1:6:15:20:15:6:1 for septet; 1:4:6:4:1 for quintet) which provides an excellent fit to the experimentally observed relative intensities. These two multiplets contain coupling constants in the range characteristic of $^3J(^{19}F–^1H)$ (fluorocarbenium cation ($[(CH_3)_2CF]^+$: $^3J(^{19}F–^1H)$ = 26 Hz; $\delta(^{19}F)$ = 182 ppm; $\delta(^1H)$ = 3.9 ppm; difluoropropane $CF_2(CH_3)_2$: $^3J(^{19}F–^1H)$ = 19 Hz; $\delta(^{19}F)$ = −81.5 ppm; $\delta(^1H)$ = 1.37 ppm).[8] The resonances assigned to SF_4 (76.94 and 30.19 ppm) appear as sharp triplets, however, they are shifted to lower frequencies compared to when SF_4 is dissolved in SO_2 (85.9 and 34.1 ppm) (Table 4.2) where two broad singlets are observed (Figure 4.2). Acetone forms chalcogen bonding interactions with SF_4 donating electron density from the oxygen of the carbonyl group to the sulfur along the equatorial plane (see Chapter 3 for results pertaining to the solid-state interactions of SF_4 and acetone). This results in larger shifts of the resonances of the F-axial ligands of SF_4 ($\Delta\delta$ = 9.0 ppm), making the bonds slightly more ionic, compared to the change in chemical shift of the F-equatorial ligands ($\Delta\delta$ = 3.9 ppm). This was confirmed by mixing SF_4 with excess acetone (i.e., the solvent) which showed two sharp triplet ^{19}F resonances at 77.80 and 30.53 ppm (Figure 4.3) even after warming to RT for 1 h. The two triplets were observed in the presence of HF, which usually facilitates rapid exchange between the axial and equatorial fluorine environments, even at low temperatures. This is an indication that SF_4, in the presence of excess acetone, is not the reactive species responsible for deoxofluorination or any decomposition products.

Table 4.2 ^{19}F chemical shifts (δ) of SF_4 in SO_2 and acetone, as well as a mixture of SF_4 with $[SF_3][AsF_6]$ in SO_2 at −70 °C.

Compounds	Solvent	δ of SF_4 or $[SF_3]^+$ (ppm) [a]	$^2J(^{19}F–^{19}F)$ (Hz)	δ of $[AsF_6]^-$ (ppm)
SF_4	SO_2	85.9 (F_{ax}, s, br) 34.1 (F_{eq}, s, br)	--	--
SF_4	Acetone	77.80 (F_{ax}, t) 30.53 (F_{eq}, t) [b]	69.3	--
SF_4 + Acetone [c]	SO_2	86.48 (F_{ax}, t) 33.32 (F_{eq}, t) [d]	75.9	--
$[SF_3][AsF_6]$	SO_2	32.91 (s)	--	−57.31 (s, br)
$[SF_3][AsF_6]$ + SF_4 [c]	SO_2	44.8 (s)	--	−56.11 (s)

[a] Abbreviations: (s) singlet; (t) triplet; (ax) axial; (eq) equatorial; (br) broad.
[b] $^1\Delta^{19}F(^{34/32}S)$ = 0.066 ppm. [c] Mixed in a 1:1 ratio. [d] $^1\Delta^{19}F(^{34/32}S)$ = 0.069 ppm.

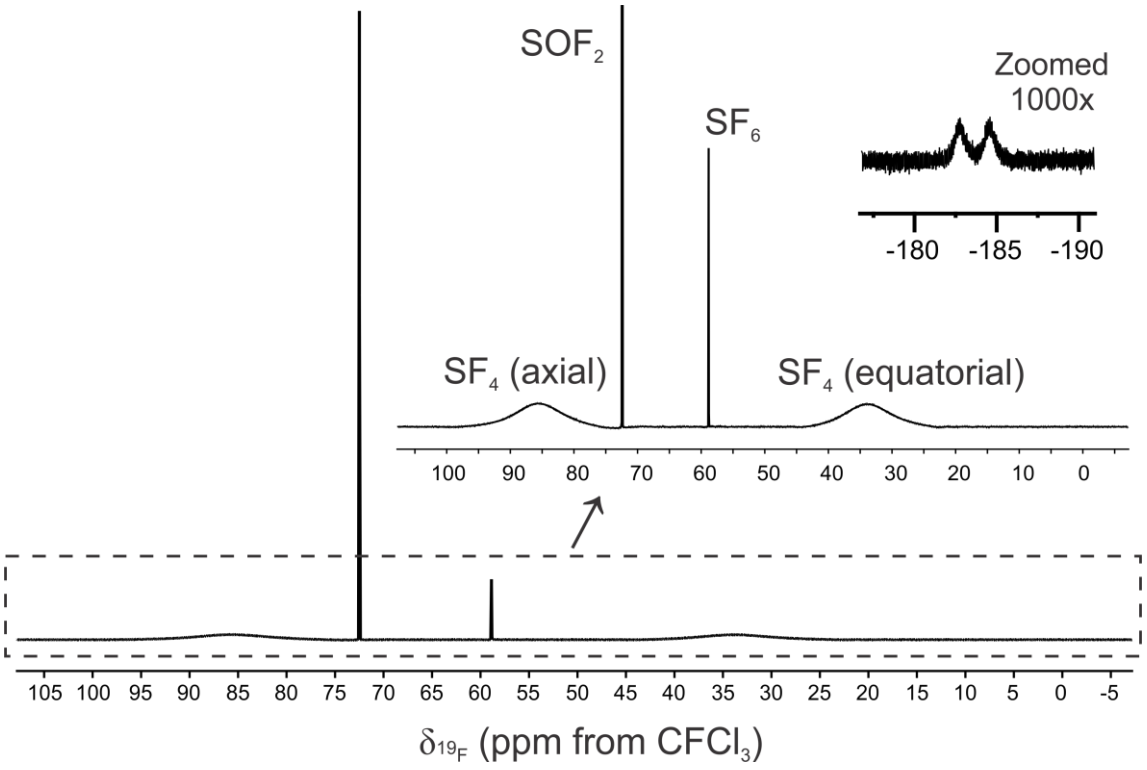

Figure 4.2 ^{19}F NMR spectrum (282.40 MHz) of SF_4 in SO_2 at −70 °C. Externally referenced to $CFCl_3$ at RT.

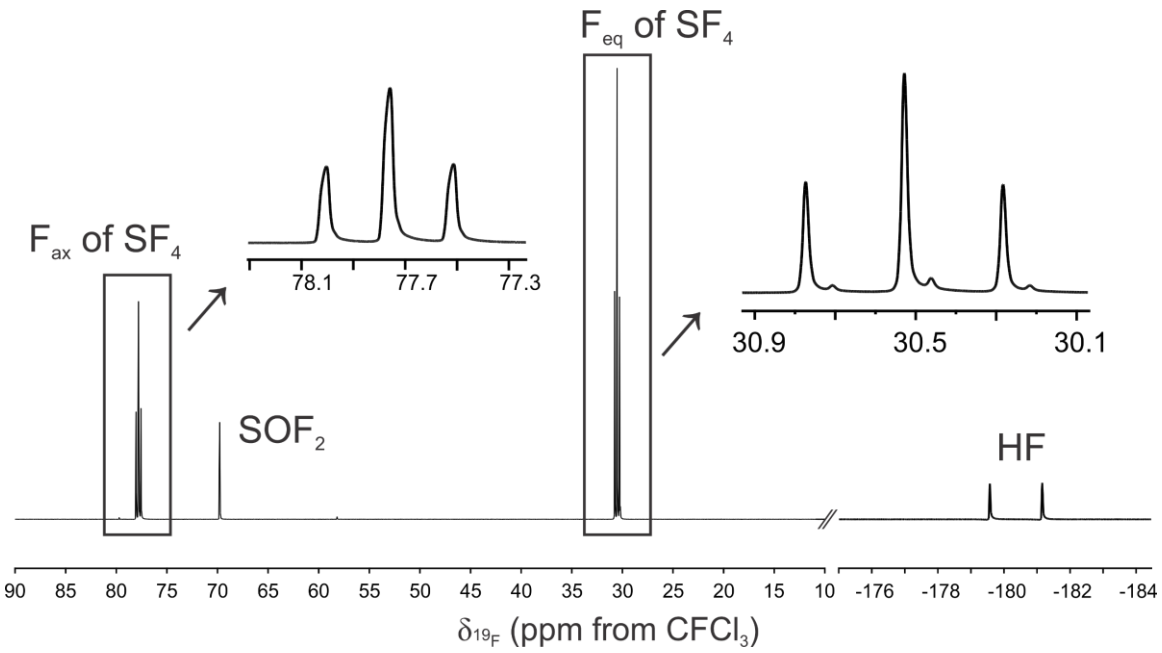

Figure 4.3 ^{19}F NMR spectrum (282.40 MHz) of SF_4 in excess acetone at −70 °C. Sample was warmed to RT for 1 h. Externally referenced to $CFCl_3$ at RT.

After the reaction was brought to RT for 1 min, no SF_4 remained. The only resonances observed were SOF_2, two equivalents of $[AsF_6]^-$, and four equivalents HF with integration ratios of 2.0:12.0:4.4 indicating complete deoxofluorination of acetone, with respect to the SF_4 generated via the dismutation (Equation 4.3). The nature of the cation in solution could not be identified as it is likely a radical cation which will not be observable by NMR spectroscopy. A potential radical cationic deoxofluorination product decomposed to generate HF as four equivalents of HF accounts for all fluorines, besides those of SOF_2; two from the SF_4 reacting to yield SOF_2, and two from the proposed $[SF_2]^{2+}$ species. The origin of the hydrogens in HF are likely the methyl groups of acetone as stoichiometric amounts of HF via hydrolysis from moisture contamination can be excluded. The fate of the sulfur from $[SF_2]^{2+}$ is also not understood.

Proton NMR spectroscopy was used to characterize the reaction contents, however, since acetone was used as the solvent, only a singlet resonance was observed at 2.01 ppm. The strong colour change to dark orange/brown is likely a result of either the paramagnetic reaction product or fast chemical exchange between acetone solvent and adducted acetone.

4.2.3 $[SF_3][AsF_6]$ and Three Equivalents of Acetone in SO_2

The reaction involving three molar equivalents of acetone with $[SF_3][AsF_6]$ in SO_2 resulted in clear, colourless solutions upon melting at −70 °C. The ^{19}F NMR spectra are depicted in Figure 4.4 and the chemical shifts and coupling constants are listed in Table 4.3.

Table 4.3 Selected ^{19}F chemical shifts (δ) at −70 °C for the reaction of $[SF_3][AsF_6]$ with three molar equivalents of acetone in SO_2.

Compound	Chemical Shift (ppm) [a]	$^2J(^{19}F–^{19}F)$ (Hz)	$^1J(^{19}F–^{75}As)$ (Hz)
Reaction at −65 °C for 2 min [b]			
SOF_2	72.59 (s) [c]	--	--
$[SF_3{\cdot}O{=}C(CH_3)_2]^+$	26.7 (s, br)	--	--
$[SF_3{\cdot}\{O{=}C(CH_3)_2\}_2]^+$	22.7 (s, br)	--	--
$[AsF_6]^-$	–57.0 [d]	--	Not resolved [d]
Reaction at −40 °C for 3 min [b]			
SF_4	87 (s, br)	--	--
SOF_2	72.57 (s) [c]	--	--
$[SF_3{\cdot}\{O{=}C(CH_3)_2\}_2]^+$	28.4 (s); 24 (sh)	--	--
$[AsF_6]^-$	–57.1 [d]	--	Not resolved [d]
Reaction at −20 °C for 3 min [b]			
SF_4	86.35 (F_{ax}, t) 33.26 (F_{eq}, t)	75.2	--
SOF_2	72.59 (s) [c]	--	--
$SF_4/[SF_3]^+$	45.9 (s)	--	--
$[AsF_6]^-$	–57.3 [d]	--	Not resolved [d]
Reaction at RT for 2 min [b]			
SF_4	86.40 (F_{ax}, t) 33.30 (F_{eq}, t)	--	--
SOF_2	72.61 (s) [c]	--	--
$SF_4/[SF_3]^+$	56.49 (s)	--	--
$[AsF_6]^-$	−57.7 [d]	--	Not resolved [d]
Reaction at RT for 10 min [b]			
SF_4	86.5 (F_{ax}, t) 33.3 (F_{eq}, t)	76.1	--
SOF_2	72.59 (s) [c]	--	--
$SF_4/[SF_3]^+$	58.96 (s)	--	--
$[AsF_6]^-$	−57.0 [d]	--	Not resolved [d]
$(CH_3)_2CF_2$	−79.40 (sept) [e]	--	--

[a] Abbreviations: (s) singlet; (t) triplet; (sept) septet; (sh) shoulder; (ax) is axial; (eq) equatorial. [b] Unidentified impurity at −16 ppm. [c] $^1\Delta^{19}F(^{34/32}S) = 0.060$ ppm. [d] Quadrupolar broadened. [e] $^3J(^{19}F–^1H) = 18.9$ Hz.

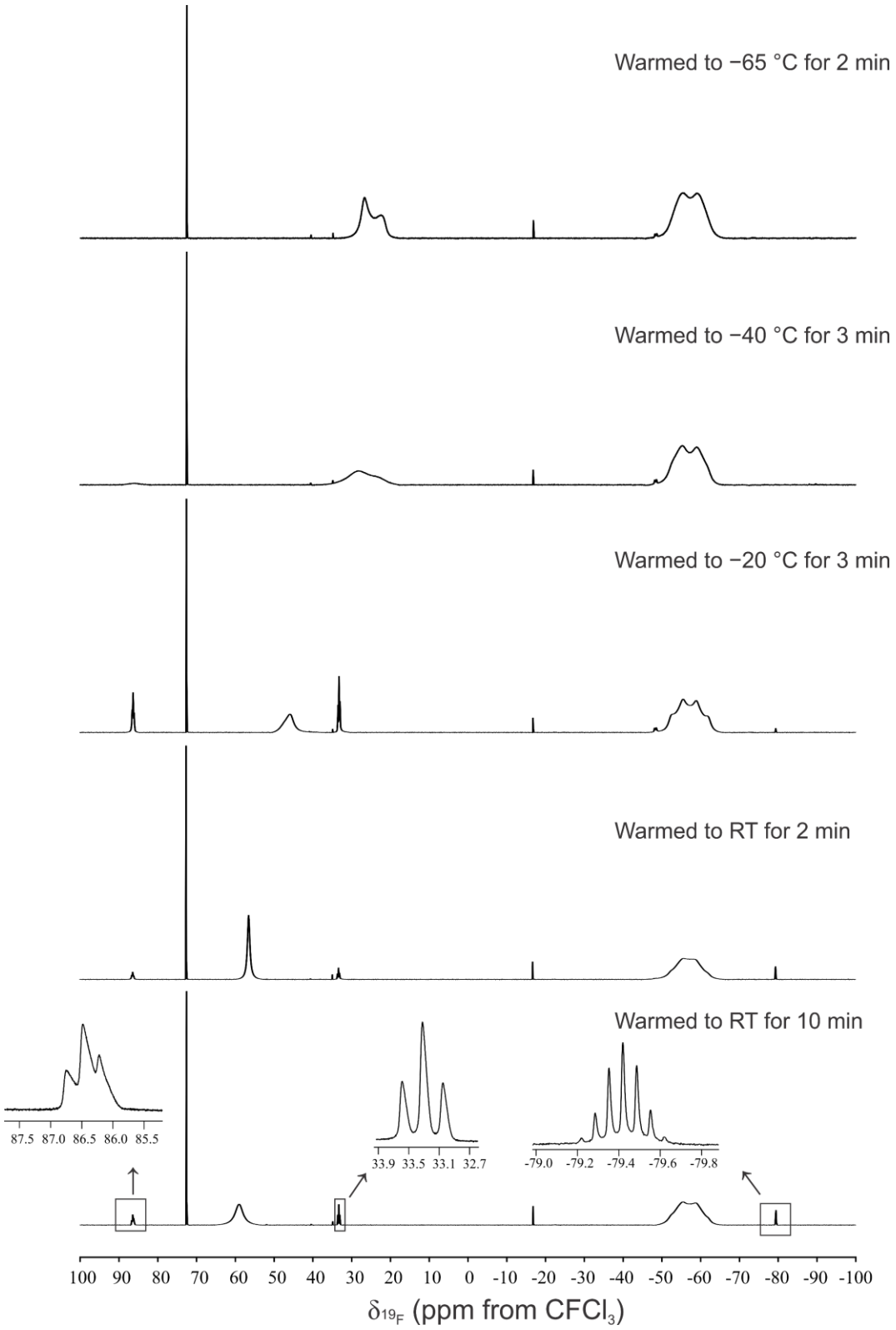

Figure 4.4 ^{19}F NMR spectra (282.40 MHz) showing the progress of the reaction of $[SF_3][AsF_6]$ with three molar equivalents of acetone in SO_2 at −70 °C. All spectra were externally referenced to $CFCl_3$ at RT.

Once the reaction was warmed to −20 °C, two resonances of SF_4 were observed as triplets (86.35 and 33.26 ppm) with scalar $^2J(^{19}F–^{19}F)$ coupling of 75.2 Hz, as well as a broad resonance at 45.9 ppm. The observation of the triplets may suggest SF_4 is weakly interacting with acetone preventing exchange of the fluorine environments. When SF_4 was dissolved in SO_2, broad singlets were observed at 85.9 (F_{ax}) and 34.1 ppm (F_{eq}), whereas, when SF_4 was dissolved in excess acetone, sharp triplet resonances at 77.70 (F_{ax}) and 30.53 ppm (F_{eq}) were detected (Table 4.2). When SF_4 was reacted with acetone in SO_2, in a 1:1 molar ratio, sharp triplet resonances were observed at 86.48 (F_{ax}) and 33.32 ppm (F_{eq}). Rapid exchange of the fluorine environments was most likely prevented through weak interactions with the Lewis base acetone, thus allowing the observation of the triplets as opposed to broad singlets. The broad resonance at 45.9 ppm, in the ^{19}F NMR spectrum of the reaction, was likely associated with the presence of SF_4 whose fluorine environments rapidly exchange with those of $[SF_3]^+$. This was confirmed by dissolving $[SF_3][AsF_6]$ in SO_2 and adding SF_4 (approximate 1:1 molar ratio) which gave only one broad singlet at 44.8 ppm in the ^{19}F NMR spectrum recorded at −70 °C as a consequence of fast exchange between the fluorine environments of $[SF_3]^+$ and SF_4 (refer to Table 4.2). A very weak doublet was observed at 48.3 ppm from the dissociation of $[SF_3][AsF_6]$ into SF_4 and $AsF_5{\cdot}O{=}C(CH_3)_2$ (refer to Chapter 6 for results regarding adducts of AsF_5 with ketones).

At RT, the reaction turned a dark, deep red colour. The SF_4 triplet resonances were slightly diminished and a broad singlet appeared at 56.5 ppm, attributed to rapidly exchanging SF_4 and $[SF_3]^+$ with an increased contribution from SF_4. Leaving the reaction at RT for 10 min resulted in this resonance (59.0 ppm) slightly decreasing in relative intensity with respect to $[AsF_6]^-$ going from an integration of 2.4:6.0 to 1.9:6.0. This was followed by the appearance of a septet at −79.40 ppm, albeit in small quantities, associated

with 2,2-difluoropropane (reported $\delta(^{19}F)$ of −81.5 ppm),[8] a product of the deoxofluorination of acetone.

The progress of this reaction was also characterized using ^{1}H NMR spectroscopy at −70 °C (Figure 4.5), however, because of the complexity of this reaction, little information was obtained from the ^{1}H NMR spectra. At −63 °C the proton NMR spectrum showed three different acetone singlet resonances: $[SF_3{\cdot}O{=}C(CH_3)_2]^+$ (2.74 ppm), $[SF_3{\cdot}\{O{=}C(CH_3)_2\}_2]^+$ (2.58 ppm), and free acetone (2.55 ppm) (acetone in SO_2 appears at 2.53 ppm). This is consistent with the ^{19}F NMR spectrum, which showed both the 1:1 (26.74 ppm) and 1:2 (22.66 ppm) adducts of $[SF_3]^+$ with acetone. Upon warming to RT for 10 min, no free acetone remained, and the main resonance was observed at 3.00 ppm along with a small amount (< 1%) of 2,2-difluoropropane (1.82 ppm).

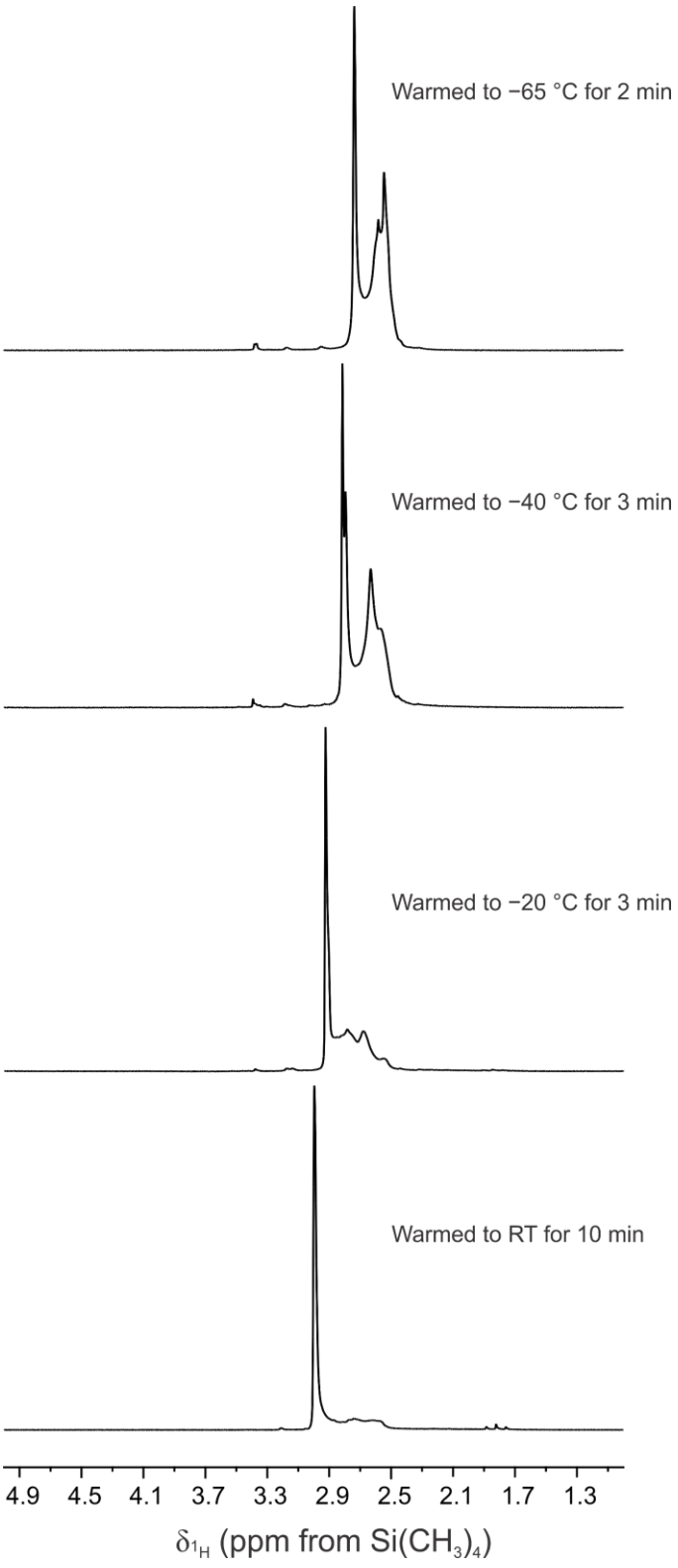

Figure 4.5 ^{1}H NMR spectra (300.13 MHz) showing the progress of the reaction of $[SF_3][AsF_6]$ with three equivalents of acetone at −70 °C in SO_2. Spectra were externally referenced to $Si(CH_3)_4$ at RT.

4.2.4 $[SF_3][AsF_6]$ and 2.5 Equivalents of Acetone in SO_2

The reaction of 2.5 molar equivalents of acetone with $[SF_3][AsF_6]$ in SO_2 resulted in a clear, colourless solution upon melting at −70 °C. The ^{19}F NMR spectra are depicted in Figure 4.6 and the chemical shifts and coupling constants are listed in Table 4.4. At −60 °C, a ^{19}F resonance appeared as a singlet at 21.26 ppm (Figure 4.5) which was assigned to the $[SF_3{\cdot}\{O{=}C(CH_3)_2\}_2]^+$ cation. An additional weaker, broad peak at 28.5 ppm was assigned to the $[SF_3{\cdot}O{=}C(CH_3)_2]^+$ adduct, which is present likely as a result of insufficient mixing. The $[AsF_6]^-$ anion has a ^{19}F resonance at –56.5 ppm, however, unlike when the reaction was performed in excess acetone, the electric field gradient about ^{75}As in these adducts causes quadrupolar relaxation of the ^{75}As (I = 3/2, 100%) nucleus such that the $^1J(^{19}F–^{75}As)$ coupling is partially quadrupolar collapsed. The $[AsF_6]^-$ anion can share one contact with the $[SF_3{\cdot}\{O{=}C(CH_3)_2\}_2]^+$ cation giving the sulfur of $[SF_3]^+$ a coordination number of 6.

The colour began to change upon warming to −45 °C to a clear, faint red solution. The $[SF_3{\cdot}\{O{=}C(CH_3)_2\}_2]^+$ cation was still present in solution at this temperature, however, an unidentified shoulder peak appeared at 21.9 ppm. Warming to −40 °C resulted in a resonance at 22.12 ppm with no shoulder peak. This may be the result of small amounts of SF_4 forming leading to exchange of the fluorine environments and a subsequent increase in the chemical shift. When the sample was warmed to −35 °C, the solution turned a dark orange/brown colour and the ^{19}F NMR spectrum showed the presence of two broad singlets at 86.5 (F_{ax}) and 33.1 ppm (F_{eq}) from the formation of SF_4, and some remaining $[SF_3{\cdot}\{O{=}C(CH_3)_2\}_2]^+$ cation (22.1 ppm). A dismutation reaction occurs where two

equivalents of $[SF_3{\cdot}\{O{=}C(CH_3)_2\}_2][AsF_6]$ yields SF_4 and presumably $[SF_2{\cdot}\{O{=}C(CH_3)_2\}_2][AsF_6]_2$ (Equation 4.4).

$$2\ [SF_3{\bullet}\{O{=}C(CH_3)_2\}_2][AsF_6] \longrightarrow [SF_2{\bullet}\{O{=}C(CH_3)_2\}_2][AsF_6]_2 + SF_4 \quad (4.4)$$

Table 4.4 Selected ^{19}F chemical shifts (δ) at −70 °C for the reaction of $[SF_3][AsF_6]$ with 2.5 molar equivalents of acetone in SO_2.

Compound	Chemical Shift (ppm) [a]	$^2J(^{19}F–^{19}F)$ (Hz)	$^1J(^{19}F–^{75}As)$ (Hz)
Reaction at −60 °C for 2 min			
SOF_2	72.95 (s)	--	--
$[SF_3{\cdot}O{=}C(CH_3)_2]^+$	28.5 (s, br, sh)	--	--
$[SF_3{\cdot}\{O{=}C(CH_3)_2\}_2]^+$	21.26 (s)	--	--
$[AsF_6]^-$	–56.5 [b]	--	Not resolved [b]
Reaction at −45 °C for 2 min			
SOF_2	72.96 (s)	--	--
$[SF_3{\cdot}\{O{=}C(CH_3)_2\}_2]^+$	21.70 (s); 21.9 (sh)	--	--
$[AsF_6]^-$	–56.5 [b]	--	Not resolved [b]
Reaction at −40 °C for 2 min			
SOF_2	72.96 (s)	--	--
$[SF_3{\cdot}\{O{=}C(CH_3)_2\}_2]^+$	22.12 (s)	--	--
$[AsF_6]^-$	–56.5 [b]	--	Not resolved [b]
Reaction at −35 °C for 5 min			
SF_4	86.5 (F_{ax}, s) 33.1 (F_{eq}, s)	--	--
SOF_2	72.73 (s)	--	--
$[SF_3{\cdot}\{O{=}C(CH_3)_2\}_2]^+$	22.1 (s)	--	--
$[AsF_6]^-$	−56.8 [b]	--	Not resolved [b]
Reaction at RT for 5 min			
SF_4	86.80 (F_{ax}, t) 33.64 (F_{eq}, t)	76.1	--
SOF_2	72.90 (s)	--	--
$[AsF_6]^-$	−56.7 [b]	--	Not resolved [b]
HF	−158.8 (s)	--	--

[a] Abbreviations: (s) singlet; (t) triplet; (sh) shoulder; (ax) axial; (eq) equatorial; (br) broad. [b] Quadrupolar broadened.

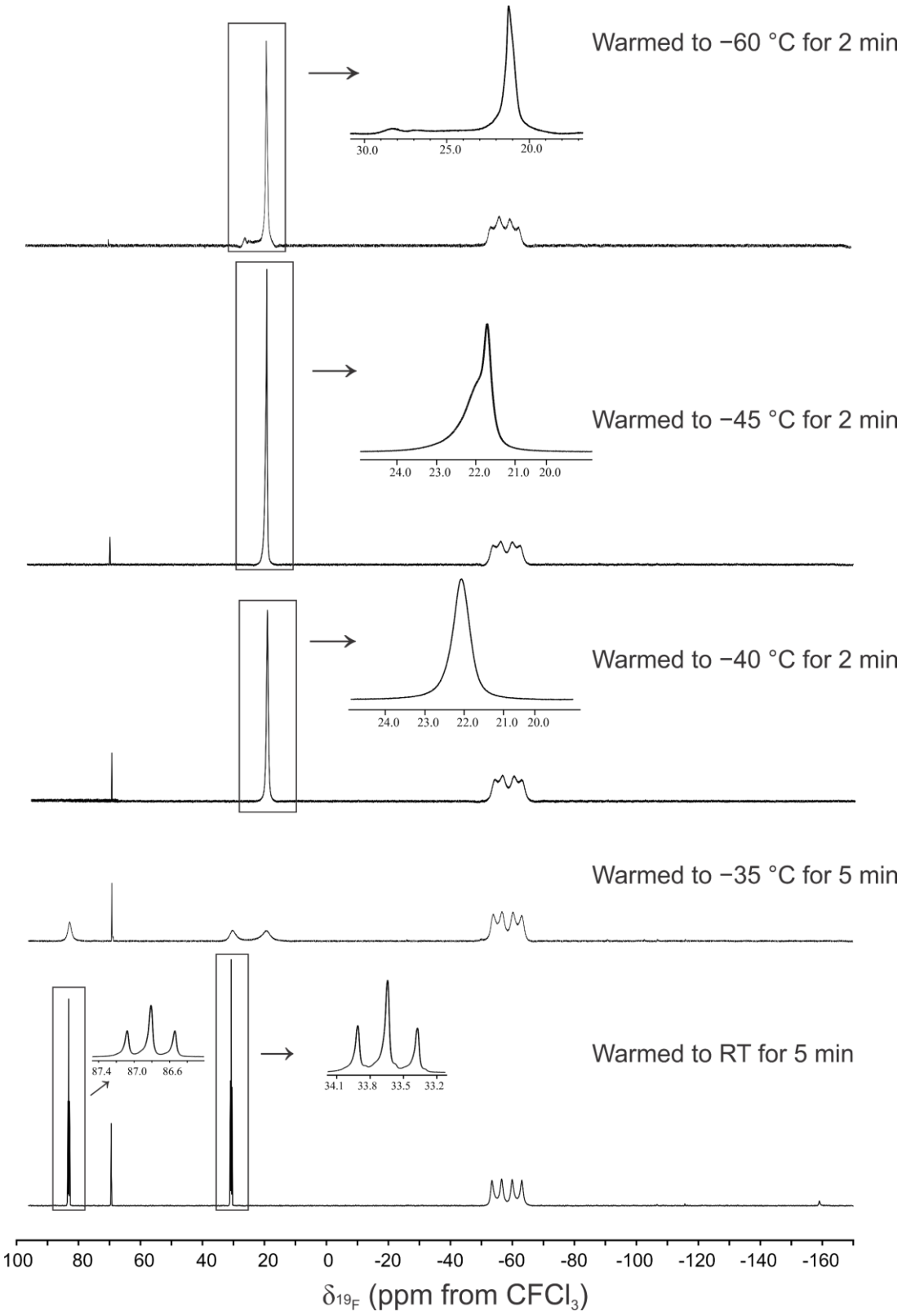

Figure 4.6 ^{19}F NMR spectra (282.40 MHz) showing the progress of the reaction of $[SF_3][AsF_6]$ with 2.5 molar equivalents of acetone in SO_2 at −70 °C. All spectra were externally referenced to $CFCl_3$ at RT.

The dark orange/brown solution remained when warmed to RT. After 5 min at RT, the SF_4 signals became two sharp triplet ^{19}F resonances at 86.80 (F_{ax}) and 33.64 ppm (F_{eq}) with $^2J(^{19}F–^{19}F)$ coupling of 76.1 Hz. A small amount of HF was detected at −158.8 ppm as a singlet, but otherwise no deoxofluorination products, such as 2,2-difluoropropane, were observed upon warming the reaction to RT. While ^1H NMR spectroscopy was acquired, no additional information was obtained. The singlet resonance in the ^1H NMR spectrum was the only signal observed which gradually shifted to higher frequencies upon warming the reaction (2.49 ppm at −56 °C; 2.80 ppm at −35 °C; 2.97 at RT for 5 min). The single resonance indicates fast chemical exchange. The increasing chemical shift over time likely resulted from an increase in the concentration of strongly adducted acetone or the unidentified paramagnetic species interacting with acetone.

4.2.5 $[SF_3][AsF_6]$ and One Equivalent of Acetone in SO_2

The reaction between $[SF_3][AsF_6]$ and one equivalent of acetone in SO_2 gave unexpected results. Upon melting at −70 °C, a clear, colourless solution was formed. The ^{19}F NMR spectra are depicted in Figure 4.7 and the chemical shifts and coupling constants are listed in Table 4.5.

Table 4.5 Selected ^{19}F chemical shifts (δ) at −70 °C for the reaction of $[SF_3][AsF_6]$ with one molar equivalent of acetone in SO_2.

Compound	Chemical Shift (ppm) [a]	$^2J(^{19}F–^{19}F)$ (Hz)	$^1J(^{19}F–^{75}As)$ (Hz)
Reaction at −50 °C for 5 min			
SOF_2	72.75 (s)	--	--
$[SF_3]^+$	30.17 (s)	--	--
$[SF_3{\cdot}O{=}C(CH_3)_2]^+$	29.8 (sh)	--	--
$[SF_3{\cdot}\{O{=}C(CH_3)_2\}_2]^+$	21.62 (s)	--	--
$[AsF_6]^-$	–56.0 [b]	--	Not resolved [b]
Reaction at −45 °C for 5 min			
SF_4	87 (s, br)	--	--
SOF_2	72.91 (s)	--	--
$[SF_3{\cdot}O{=}C(CH_3)_2]^+$	29.34 (s)	--	--
$[SF_3{\cdot}\{O{=}C(CH_3)_2\}_2]^+$	23.48 (s)	--	--
$[AsF_6]^-$	–56.6 [b]	--	Not resolved [b]
Reaction at −38 °C for 5 min			
SF_4	86.7 (F_{ax}, s) 32.3 (F_{eq}, sh, br)	--	--
SOF_2	72.88 (s)	--	--
$[SF_3{\cdot}\{O{=}C(CH_3)_2\}_2]^+$	24.7 (s, br)	--	--
$AsF_5{\cdot}O{=}C(CH_3)_2$	−47.9 (d)	124	--
$[AsF_6]^-$	–56.6 [b]	--	Not resolved [b]
Reaction at −21 °C for 3 min [c]			
SOF_2	72.90 (s)	--	--
$SF_4/[SF_3]^+$	55.03 (s)	--	--
$AsF_5{\cdot}O{=}C(CH_3)_2$	−47.9 (d)	124	--
$[AsF_6]^-$	–56.4 [b]	--	Not resolved [b]
Reaction at −13 °C for 3 min			
SOF_2	72.90 (s) [d]	--	--
$SF_4/[SF_3]^+$	56.86 (s)	--	--
$AsF_5{\cdot}O{=}C(CH_3)_2$	−47.9 (d)	124	--
$[AsF_6]^-$	–56.6 [b]	--	Not resolved [b]
$CF_2(CH_3)_2$	−79.0 (m)	--	--
Reaction at RT for 45 min			
SF_4	87 (s, br) 34 (s, br)	--	--
SOF_2	72.74 (s) [d]	--	--
$[AsF_6]^-$	–56.6 [b]	--	Not resolved [b]
$CF_2(CH_3)_2$	−79.2 (sept) [e]	--	--

[a] Abbreviations: (s) singlet; (sept) septet; (m) multiplet; (ax) axial; (eq) equatorial; (sh) shoulder; (br) broad. [b] Quadrupolar broadened. [c] Sample contained two phases due to difficulty mixing. [d] $^1\Delta^{19}F(^{34/32}S)$ = 0.06 ppm. [e] $^3J(^{19}F–^1H)$ = 18.9 Hz, yield ca. 3%.

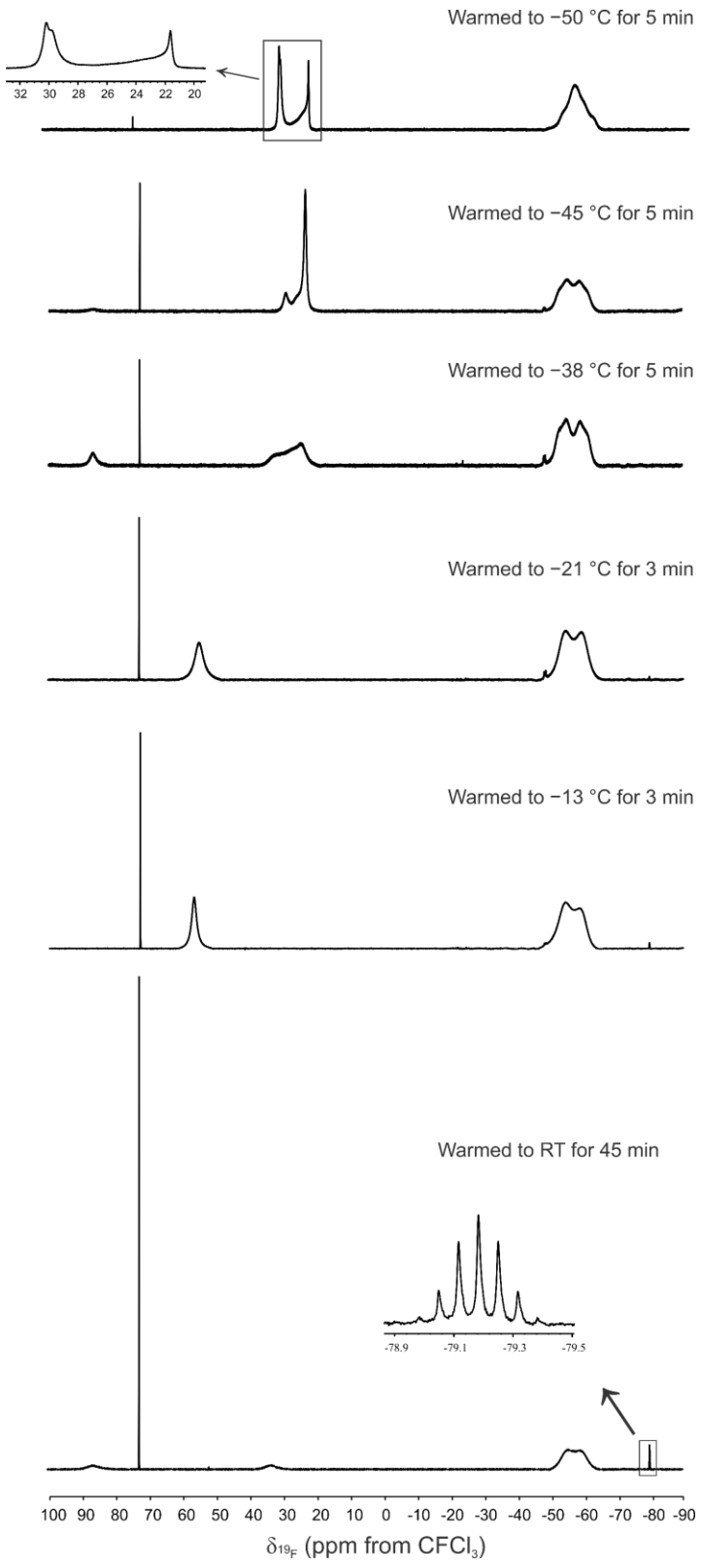

Figure 4.7 ^{19}F NMR spectra (282.40 MHz) showing the progress of the reaction of $[SF_3][AsF_6]$ with acetone in SO_2 at −70 °C in a 1:1 molar ratio. All spectra were externally referenced to $CFCl_3$ at RT.

At −50 °C, three different $[SF_3]^+$ species were present: free $[SF_3]^+$ (30.17 ppm), $[SF_3{\cdot}O{=}C(CH_3)_2]^+$ (shoulder at 29.8 ppm), and $[SF_3{\cdot}\{O{=}C(CH_3)_2\}_2]^+$ (21.62 ppm). The likely cause of multiple $[SF_3]^+$-species is a result of the difficulties in sufficiently mixing the solution to give a homogeneous mixture while maintaining a stable low temperature. The $[AsF_6]^-$ anion appeared at −56.0 ppm as a quadrupolar collapsed multiplet where no $^1J(^{19}F{-}^{75}As)$ coupling was observed (Figure 4.7). At −45 °C the $[SF_3]^+$ cation was presumably adducted to two acetone molecules (23.48 ppm), however, a broad singlet at 29.3 ppm suggested that a small amount of the 1:1 adduct is also present in solution. A very weak, broad ^{19}F resonance characteristic of the axial fluorine atoms in SF_4 was detected at 87 ppm. When the reaction was warmed to −38 °C, the sample began turning to a dark red colour and the broad singlet ^{19}F resonances at 86.7 and 32.3 ppm indicated the formation of SF_4. Interestingly, a doublet at −47.9 ppm was also observed indicative of the formation of $AsF_5{\cdot}O{=}C(CH_3)_2$ due to the equilibrium between $[SF_3][AsF_6]$ and SF_4/AsF_5 (Equation 4.5), induced by the presence of one equivalent of acetone and strong F_3S^+---$FAsF_5^-$ interactions (see Chapter 6 for results regarding adducts of ketones with AsF_5).

$$[SF_3{\bullet}O{=}R][AsF_6] \rightleftharpoons SF_4 + AsF_5{\bullet}O{=}R \quad (R = C(CH_3)_2,\ C_5H_8,\ C_{10}H_{14}) \tag{4.5}$$

Unlike the reaction with two equivalents of acetone, or excess acetone, warming to higher temperatures (−21 and −13 °C) resulted in observation of SF_4 as a broad singlet at 55.03 ppm (56.86 at −13 °C) as a result of exchanges with $[SF_3]^+$, similar to the one exhibited in the reaction with three equivalents of acetone, as well as a small amount of the $AsF_5{\cdot}O{=}C(CH_3)_2$ adduct (−47.9 ppm). At −13 °C, the integration ratio between SOF_2 (72.90 ppm), the $SF_4/[SF_3]^+$ resonance (56.86 ppm), and $[AsF_6]^-$ (−56.6 ppm), gave a

0.2:4.0:14.2 ratio (or 0.1:2.0:7.1). The integration of 0.2 for SOF_2 suggests that deoxofluorination of the carbonyl group had not occurred to any significant extent.

Warming the sample to RT for 45 min resulted in weak broad singlets at 87 and 34 ppm from SF_4, as well as a septet at −79.2 ppm with a scalar $^3J(^{19}F–^1H)$ coupling of 18.9 Hz. The ^1H NMR spectrum (Figure 4.8) of the reaction at this temperature contained an intense singlet at 3.14 ppm, associated with acetone, and a less intense triplet resonance at 1.93 ppm ($^3J(^{19}F–^1H)$ = 18.9 Hz), likely from 2,2-difluoropropane ($\delta(^1H)$ = 1.37 ppm; $^3J(^{19}F–^1H)$ = 19 Hz).[8] The ^1H NMR spectrum of a solution of acetone in SO_2 at −70 °C shows a singlet at 2.53 ppm; the acetone signal in the sample warmed to RT is now shifted to a higher frequency (3.14 ppm) indicating electron density has been removed from the CH_3 groups, possibly through adducted acetone.

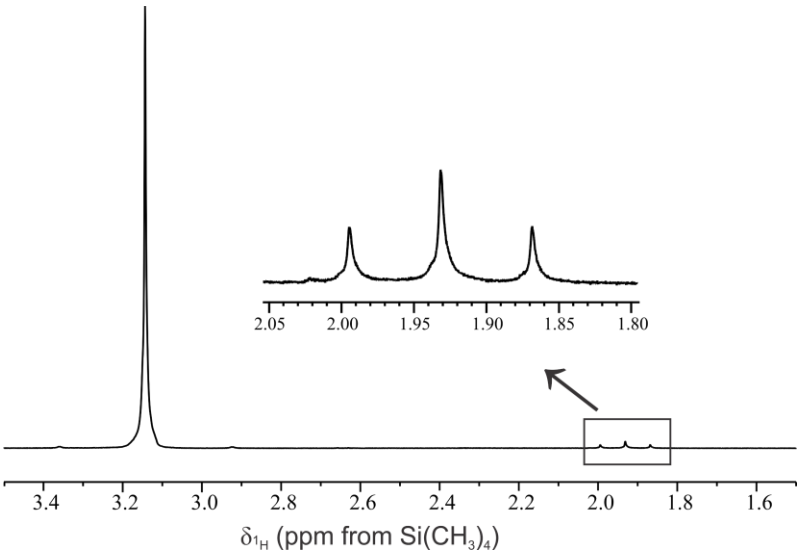

Figure 4.8 ^1H NMR spectrum (300.13 MHz) at −70 °C showing the reaction of $[SF_3][AsF_6]$ with acetone in SO_2 in a 1:1 molar ratio after having been warmed to RT for 45 min. Externally referenced to $Si(CH_3)_4$ at RT.

4.2.6 $[SF_3][AsF_6]$ and Two Equivalents of Cyclopentanone in SO_2

Reacting $[SF_3][AsF_6]$ with 2.2 molar equivalents of cyclopentanone in SO_2 at −70 °C resulted in a clear colourless solution. The ^{19}F NMR spectra are depicted in Figure 4.9 and the chemical shifts and coupling constants are listed in Table 4.6.

Table 4.6 Selected ^{19}F chemical shifts (δ) at −70 °C for the reaction of $[SF_3][AsF_6]$ with 2.2 molar equivalents of cyclopentanone in SO_2.

Compound	Chemical Shift (ppm) [a]	$^2J(^{19}F–^{19}F)$ (Hz)	$^1J(^{19}F–^{75}As)$ (Hz)
Reaction at −63 °C for 1 min [b]			
SOF_2	72.67 (s)	--	--
$[SF_3{\cdot}(O{=}C_5H_8)_2]^+$	25.04 (s)	--	--
$[AsF_6]^-$	–56.9 [c]	--	Not resolved [c]
Reaction at −35 °C for 15 min [b]			
SF_4	86.4 (F_{ax}, s)	--	--
SOF_2	72.64 (s)	--	--
$[SF_3{\cdot}(O{=}C_5H_8)_2]^+$	25.47 (s)	--	--
$[AsF_6]^-$	–56.9 [c]	--	Not resolved [c]
Reaction at −15 °C for 4 min [b]			
SF_4	86.7 (F_{ax}, s, br) 32.6 (F_{eq}, br, sh)	--	--
SOF_2	72.63 (s)	--	--
$[SF_3{\cdot}(O{=}C_5H_8)_2]^+$	26.13 (s)	--	--
$[AsF_6]^-$	–56.9 [c]	--	Not resolved [c]
Reaction at RT for 1 min [b]			
SF_4	86.4 (F_{ax}, s, br)	--	--
SOF_2	72.72 (s) [d]	--	--
$[SF_3{\cdot}(O{=}C(CH_3)_2)_2]^+$	28.7 (s, br)	--	--
$[AsF_6]^-$	−56.9 [c]	--	Not resolved [c]
Reaction at RT for 3 min [b]			
SOF_2	72.72 (s) [d]	--	--
$SF_4/[SF_3]^+$	58.6 (s, br)	--	--
$AsF_5{\cdot}O{=}C_5H_8$	−50.9 (d)	123	--
$[AsF_6]^-$	−56.9 [c]	--	Not resolved [c]
Reaction at RT for 10 min [b]			
SOF_2	72.71 (s) [d]	--	--
$[AsF_6]^-$	−56.8 [c]	--	Not resolved [c]

[a] Abbreviations: (s) singlet; (d) doublet; (ax) axial; (eq) equatorial; (sh) shoulder
[b] Unidentified resonance at −17 ppm, likely an impurity. [c] Quadrupolar broadened.
[d] $^1\Delta^{19}F(^{34/32}S)$ = 0.061 ppm.

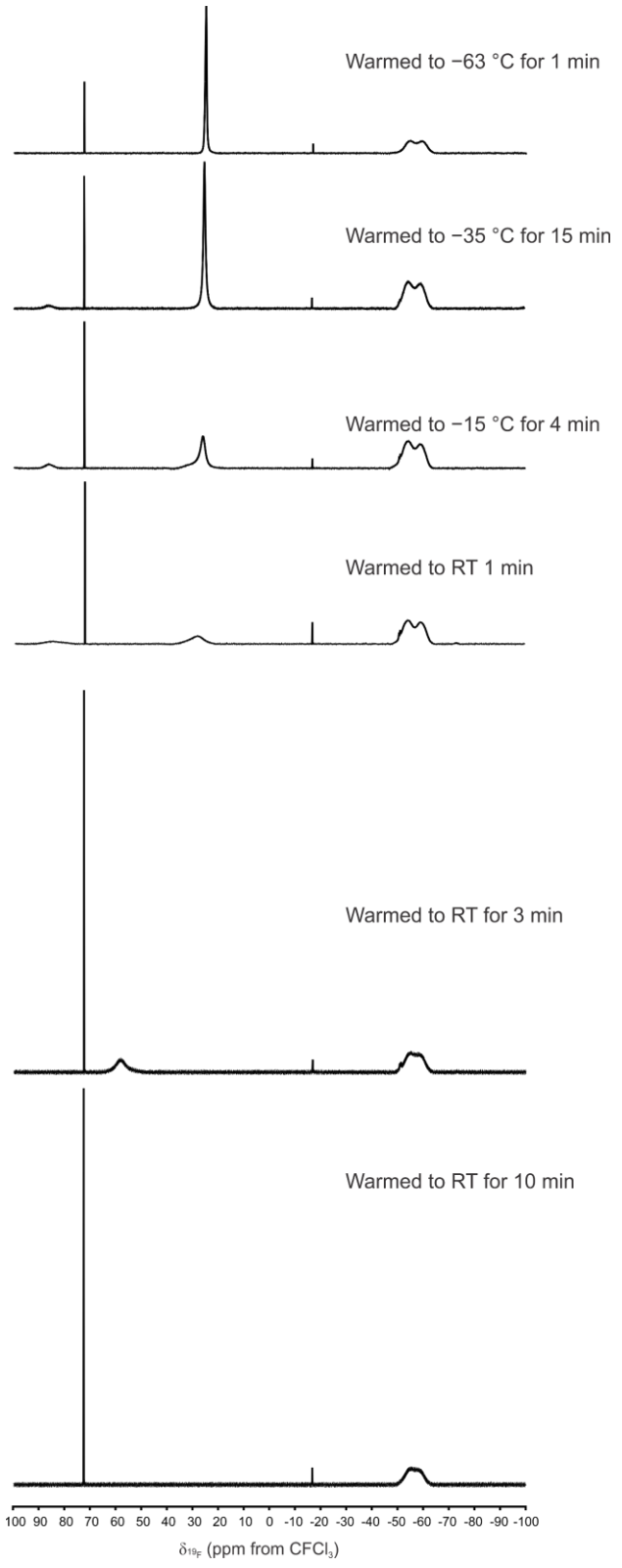

Figure 4.9 ^{19}F NMR spectra (282.40 MHz) showing the progress of the reaction of $[SF_3][AsF_6]$ with 2.2 molar equivalents of cyclopentanone in SO_2 at −70 °C. All spectra were externally referenced to $CFCl_3$ at RT.

When the reaction was first warmed to −63 °C, the 1:2 adduct between $[SF_3]^+$ and cyclopentanone was formed (25.04 ppm). At −35 °C the solution turned a clear orange colour and the ^{19}F NMR spectrum showed the $[SF_3{\cdot}(O{=}C_5H_8)_2]^+$ cation (25.47 ppm) to be stable, as well as a weak broad resonance at 86.4 ppm revealing the formation of SF_4. Unlike the acetone system, the $[SF_3{\cdot}(O{=}C_5H_8)_2]^+$ adduct (26.13 ppm) was still detected in solution at −15 °C. The chemical shift increased slightly due to chemical exchange of the fluorine atoms with those from some of the SF_4. The decrease in the intensity of the signal was accompanied by an increase in the amount of non-exchanging SF_4 (86.7 and 32.6 ppm). Three different ^{19}F NMR spectra were collected at −70 °C after leaving the reaction at RT for different lengths of time. After the first minute, the sample turned a dark red colour and the concentration of the 1:2 adduct (28.7 ppm) in solution had significantly decreased. After 3 min, a new resonance appeared at 58.6 ppm resulting from exchange between the fluorine environments of SF_4 and $[SF_3]^+$. The weak resonance at −50.9 ppm is associated with a small concentration of the $AsF_5{\cdot}O{=}C_5H_8$ adduct resulting from the dissociation of $[SF_3][AsF_6]$ into SF_4 and AsF_5 (refer to Equation 4.5). After 10 min at RT, the only resonances remaining were the $[AsF_6]^-$ (−56.8 ppm) and SOF_2 (72.71 ppm). No signs of deoxofluorination products were detected (i.e., 1,1-difluorocyclopentane), however, going from 1 min to 10 min at RT resulted in an increase in the amount of SOF_2 (integration SOF_2:$[AsF_6]^-$ at RT for 1 min, 0.3:12; RT for 10 min, 0.6:12) suggesting some kind of deoxofluorination occurred. It is possible the cationic species in this system is a radical which would not be observed in the NMR spectrum and could account for the solution becoming a dark red colour.

The ^1H NMR spectra were also recorded for the SO_2 solutions at −70 °C and are depicted in Figure 4.10 with the chemical shifts listed in Table 4.7. A gradual increase in

the chemical shift was observed upon warming the reaction from −63 °C to RT. Unadducted cyclopentanone in SO_2 at −70 °C gives rise to two resonances at 2.40 and 2.16 ppm. The adducted cyclopentanone, in a 1:2 ratio, gave rise to two resonances at 2.80 and 2.32 ppm at −63 °C. Only one set of signals were observed due to the fast exchange of the adducted and non-adducted cyclopentanone. The increase in frequency from non-adducted cyclopentanone was a consequence of the highly Lewis acidic $[SF_3]^+$ withdrawing electron density from the C=O group and, subsequently, the 5-membered carbon ring of cyclopentanone. Once the reaction was at RT for 5 min the resonances were shifted to even higher frequencies (3.18 and 2.49 ppm) possibly resulting from the interaction with a paramagnetic species or fast chemical exchange of a strongly adducted cyclopentanone.

Table 4.7 ^1H chemical shifts (δ) at −70 °C for the reaction of $[SF_3][AsF_6]$ with 2.2 molar equivalents of cyclopentanone in SO_2 (referenced to $Si(CH_3)_4$ at RT).

Reaction Temperature (°C)	Chemical Shift (ppm)
−63	2.80, 2.32
−35	2.81, 2.30
−15	2.90, 2.35
RT for 1 min	3.06, 2.44
RT for 5 min	3.18, 2.49

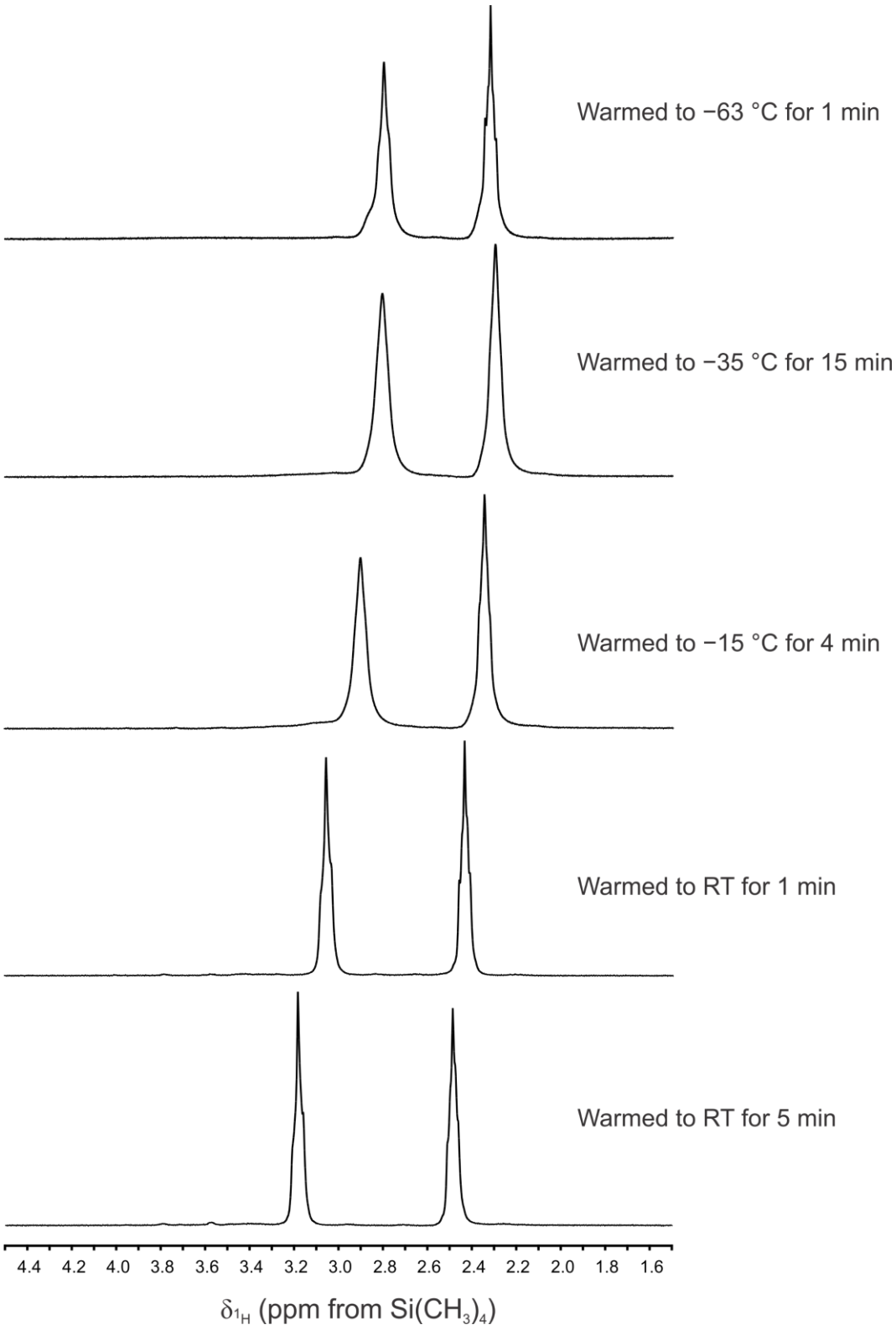

Figure 4.10 ^{1}H NMR spectra (300.13 MHz) showing the progress of the reaction of $[SF_3][AsF_6]$ with 2.2 molar equivalents of cyclopentanone in SO_2 at −70 °C. All spectra were externally referenced to $Si(CH_3)_4$ at RT.

4.2.7 $[SF_3][AsF_6]$ and One Equivalent of Cyclopentanone in SO_2

The reaction of $[SF_3][AsF_6]$ with 1.4 molar equivalent of cyclopentanone in SO_2 at −70 °C resulted in a clear colourless solution. The ^{19}F NMR spectra are depicted in Figure 4.11 and the chemical shifts and coupling constants are listed in Table 4.8. At this temperature, the 1:1 adduct between $[SF_3]^+$ and cyclopentanone was formed (31.59 ppm) which is somewhat lower in frequency to $[SF_3][AsF_6]$ in SO_2 (32.91 ppm). The resonance of $[AsF_6]^-$ (−56.6 ppm) was observed as a quadrupolar collapsed broad singlet due to the relatively large electric flied gradient about the ^{75}As nucleus (I = 3/2, 100%) compared to the 1:2 adduct where some $^1J(^{19}F–^{75}As)$ coupling could be detected (signals were overlapping and no information could be obtained). The fluorine ligands of $[AsF_6]^-$ likely share upwards of two contacts with the sulfur of $[SF_3]^+$, which can have a coordination number of 6, resulting in a distorted octahedral geometry and a broad singlet that is quadrupolar collapsed.

Table 4.8 Selected ^{19}F chemical shifts (δ) at −70 °C for the reaction of $[SF_3][AsF_6]$ with 1.4 molar equivalent of cyclopentanone in SO_2.

Compound	Chemical Shift (ppm) [a]	$^2J(^{19}F–^{19}F)$ (Hz)
Reaction at −70 °C for 1 min		
SOF_2	72.78 (s) [b]	--
$[SF_3{\cdot}O{=}C_5H_8]^+$	31.59 (s)	--
$[AsF_6]^-$	–56.6 [c]	--
Reaction at −45 °C for 5 min		
SOF_2	72.76 (s) [b]	--
$[SF_3{\cdot}O{=}C_5H_8]^+$	32.46 (s)	--
$AsF_5{\cdot}O{=}C_5H_8$	−50.80 (d)	122
$[AsF_6]^-$	–56.4 [c]	--
Reaction at −21 °C for 7 min		
SOF_2	72.76 (s) [b]	--
$[SF_3]^+/SF_4$	37.78 (s)	--
$AsF_5{\cdot}O{=}C_5H_8$	−50.80 (d) −73.17 (quin)	128 125
$[AsF_6]^-$	–56.5 [c]	--
Reaction at RT for 2 min		
SOF_2	72.78 (s) [b]	--
$[SF_3]^+/SF_4$	41.67 (s)	--
$AsF_5{\cdot}O{=}C_5H_8$	−50.80 (d) −73.16 (quin)	125
$[AsF_6]^-$	–56.4 [c]	--
Reaction at RT for 70 min		
SOF_2	72.78 (s) [b]	--
$[SF_3]^+/SF_4$	46.42 (s)	--
$[AsF_6]^-$	–56.4 [c]	--

[a] Abbreviations: (s) singlet; (d) doublet; (quin) quintet; (ax) axial; (eq) equatorial.
[b] $^1\Delta^{19}F(^{34/32}S)$ = 0.061 ppm. [c] Quadrupolar broadened, no $^1J(^{75}As–^{19}F)$ coupling observed.

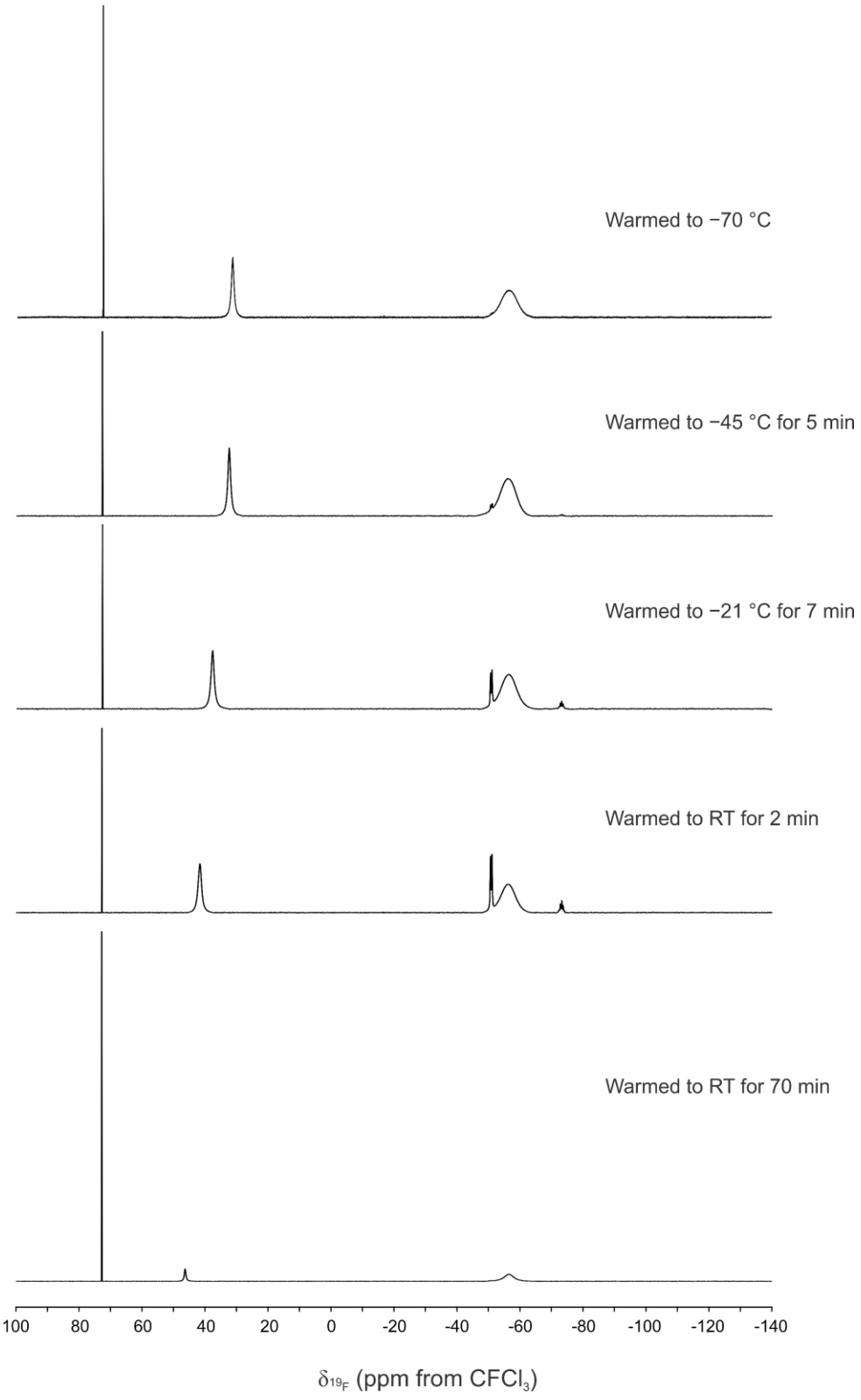

Figure 4.11 ^{19}F NMR spectra (282.40 MHz) showing the progress of the reaction of $[SF_3][AsF_6]$ with 1.4 molar equivalents of cyclopentanone in SO_2 at −70 °C. All spectra were externally referenced to $CFCl_3$ at RT.

Upon warming this reaction to −45 °C, a pale red solution formed. The $[SF_3{\cdot}O{=}C_5H_8]^+$ resonance was slightly shifted to 32.46 ppm, likely due to exchange with some SF_4 being formed, and the $AsF_5{\cdot}O{=}C_5H_8$ adduct was detected as a doublet resonance at −50.80 ppm (F_{eq}). At −21 °C the solution remained a pale red colour. The doublet resonance of $AsF_5{\cdot}O{=}C_5H_8$ increased in intensity and the corresponding quintet was also detected (F_{ax} at −73.17 ppm; $^2J(^{19}F{-}^{19}F)$ = 125 Hz). When the reaction was allowed to warm to RT for 2 min, the clear pale red coloured solution remained and more of the $AsF_5{\cdot}O{=}C_5H_8$ adduct was formed. The $[SF_3][AsF_6]$ salt undergoes an equilibrium reaction to form SF_4 and AsF_5 in the presence of one equivalent of cyclopentanone (see Equation 4.5), similar to the 1:1 adduct of $[SF_3]^+$ and acetone (refer to Section 4.2.5). At these higher temperatures, and upon forming the $AsF_5{\cdot}O{=}C_5H_8$ adduct, more SF_4 is made which forms a second equilibrium involving the dissociation of $[SF_3{\cdot}O{=}C_5H_8]^+$ to free $[SF_3]^+$. As the reaction was warmed to higher temperatures, the concentration of SF_4 increased and, therefore, less $[SF_3]^+$ is in solution resulting in the resonances being shifted to higher frequencies (37.78 ppm at −21 °C and 41.67 ppm at RT for 2 min). Rapid exchange of the fluorine environments of $[SF_3]^+$ and SF_4 results from the open coordination sites around $[SF_3]^+$ leading to a broadened signal. Based on the integration ratios between AsF_5 and $[AsF_6]^-$, three equivalents of $[AsF_6]^-$ were present for every one equivalent of AsF_5. Leaving this reaction for 70 min at RT resulted in a deep, dark red coloured solution where nearly all $AsF_5{\cdot}O{=}C_5H_8$ had dissociated and only the resonances for the $[SF_3]^+/SF_4$ equilibrium (46.42 ppm), $[AsF_6]^-$ anion (−56.4 ppm), and a significantly increased amount of SOF_2 (72.78 ppm) remained with an integration ratio of 3.8:12.0:2.0. The disappearance of the $AsF_5{\cdot}O{=}C_5H_8$ adduct and increase in SOF_2 suggests $AsF_5{\cdot}O{=}C_5H_8$ may be involved in deoxofluorination, as previously stated by Smith et al.[9]

The ^{1}H NMR spectra were collected at −70 °C and are shown in Figure 4.12 and the chemical shifts are listed in Table 4.9. The resonance of the $[SF_3{\cdot}O{=}C_5H_8]^+$ cation (3.12 and 2.49 ppm) at −70 °C showed no significant change until the reaction was warmed to −21 °C, and subsequently RT for 2 min, where the $AsF_5{\cdot}O{=}C_5H_8$ was detected at 3.49, 3.40, and 2.57 ppm. The presence of only two signals at −70 °C is a result of fast exchange between adducted and non-adducted cyclopentanone with $[SF_3]^+$. The $AsF_5{\cdot}O{=}C_5H_8$ adduct is not undergoing fast exchange and appears as separate signals at 3.49, 3.40, and 2.57 ppm after being at RT for 2 min. Leaving the reaction at RT for 70 min resulted in the chemical shifts moving to higher frequencies (3.61, 2.66 ppm) and the appearance of a signal at 14.69 ppm, characteristic of the $[HO{=}C_5H_8]^+$ cation. The relative integrations of the resonances at 14.69, 3.61, and 2.66 ppm were 1.0:4.0:4.3, suggesting that all of the cyclopentanone was protonated. The origin of the proton is currently not understood; quantitative hydrolysis of SF_4 from accidental water is highly unlikely. No deoxofluorination products (i.e., 1,1-difluorocyclopentane) were observed in the ^{19}F or ^{1}H NMR spectra.

Table 4.9 ^{1}H chemical shifts (δ) at −70 °C for the reaction of $[SF_3][AsF_6]$ with 1.4 molar equivalents of cyclopentanone in SO_2 (referenced to $Si(CH_3)_4$ at RT).

Compound	Reaction Temperature (°C)	Chemical Shift (ppm)
$[SF_3{\cdot}O{=}C_5H_8]^+$	−70	3.12, 2.49
$[SF_3{\cdot}O{=}C_5H_8]^+$	−45	3.11, 2.48
$[SF_3{\cdot}O{=}C_5H_8]^+/SF_4{\cdot}O{=}C_5H_8$	−21	3.13, 2.49
$AsF_5{\cdot}O{=}C_5H_8$		3.49, 3.40, 2.57
$[SF_3{\cdot}O{=}C_5H_8]^+/SF_4{\cdot}O{=}C_5H_8$	RT for 2 min	3.16, 2.50
$AsF_5{\cdot}O{=}C_5H_8$		3.49, 3.40, 2.57
$[SF_3{\cdot}O{=}C_5H_8]^+$	RT for 70 min	14.69,[a] 3.61, 2.66

[a] Resulting from the formation of $[HO{=}C_5H_8]^+$ (Integration of 1.0:4.0:4.3)

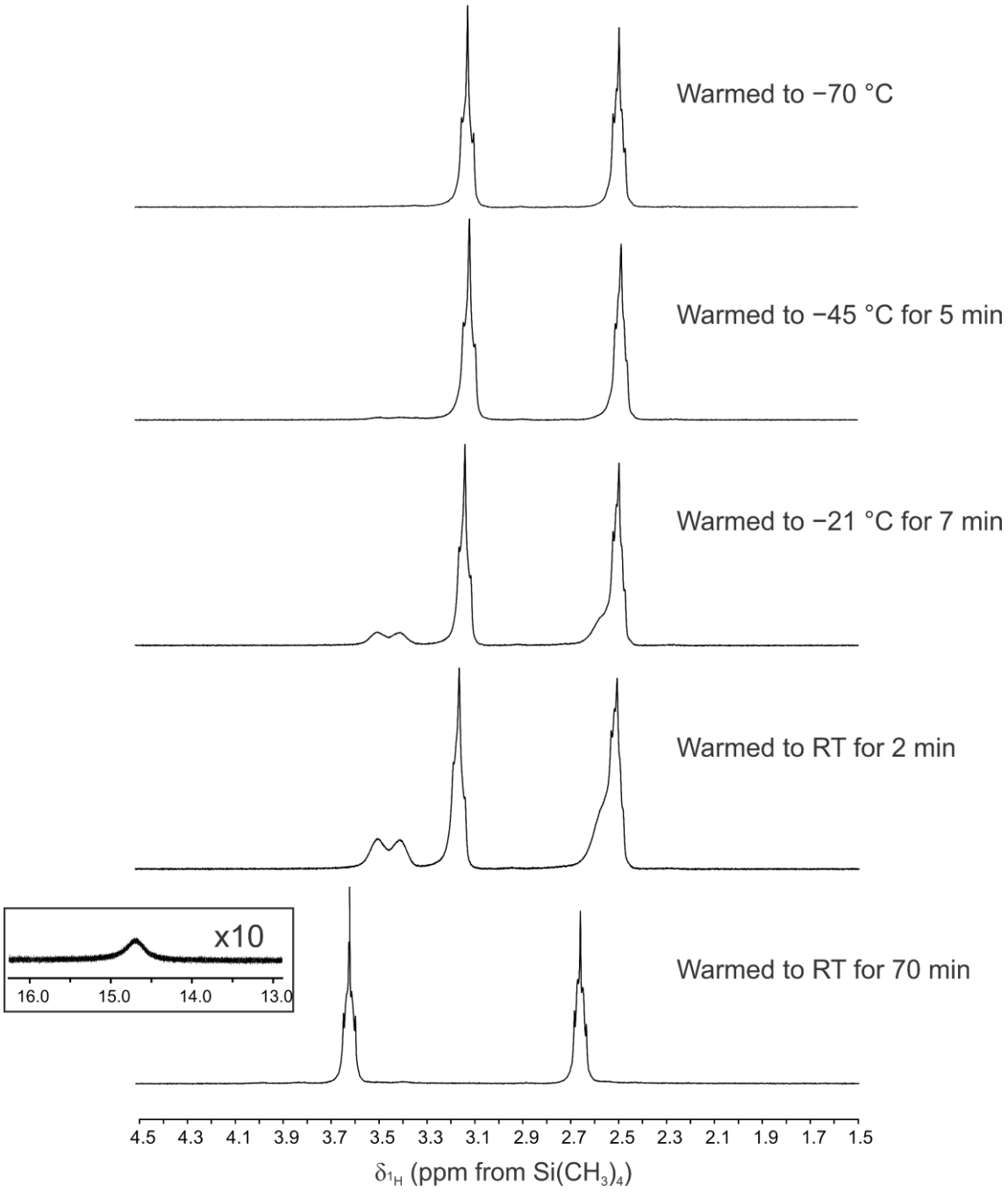

Figure 4.12 ^{1}H NMR spectra (300.13 MHz) showing the progress of the reaction of $[SF_3][AsF_6]$ with cyclopentanone in SO_2 at −70 °C in a 1:1.4 molar ratio. All spectra were externally referenced to $Si(CH_3)_4$ at RT.

4.2.8 $[SF_3][AsF_6]$ and Two Equivalents of 2-Adamantanone in SO_2

The reaction of $[SF_3][AsF_6]$ with two molar equivalents of 2-adamantanone in SO_2 was carried out at −70 °C and resulted in the precipitation of a white powder. In a separate reaction, attempts to characterize the white precipitate were made by removing the SO_2 under dynamic vacuum at −60 °C, however, a light brown powder remained which was unidentifiable by Raman spectroscopy due to large fluorescence. The insolubility of the powder in SO_2 at low temperatures required the NMR sample to be quickly warmed to −10 °C (ca. 1 min) until the reaction product dissolved resulting in a clear yellow solution. In doing so, gas formation was observed and presumed to be SF_4. This was confirmed after collecting the ^{19}F NMR spectrum at −40 °C (Figure 4.13) where broad singlet resonances at 87.3 and 31.8 ppm were detected characteristic of SF_4 (Table 4.10). While ^{1}H NMR spectroscopy was also acquired, the spectra provided little information in determining the exact nature of the products of this reaction as a result many overlapping signals of 2-adamantanone (Figure 4.14). The presence of the smaller set of signals from 4.20 to 3.15 ppm might be an indication that a small amount of adamantyl cation was formed, although no evidence for the 2-fluoroadamantyl cation was observed in the ^{19}F NMR spectra.

Table 4.10 Selected ^{19}F chemical shifts (δ) at −40 °C for the reaction of $[SF_3][AsF_6]$ with two molar equivalents of 2-adamantanone in SO_2.

Compound	Chemical Shift (ppm) [a]	$^2J(^{19}F–^{19}F)$ (Hz)
Reaction at −10 °C for 1 min		
SF_4	87.3 (F_{ax}, s, br) 31.8 (F_{eq}, sh)	--
SOF_2	73.32 (s) [b]	--
$[SF_3{\cdot}(O{=}C_{10}H_{14})_2]^+$	25.6 (s, br)	--
$AsF_5{\cdot}O{=}C_{10}H_{14}$	−47.0 (d) −73.0 (quin)	127
$[AsF_6]^-$	–57.6 [c]	--
$C_{10}H_{14}F_2$	−98.58 (s) [d]	--

[a] Abbreviations: (s) singlet; (d) doublet; (quin) quintet; (ax) axial; (eq) equatorial; (sh) shoulder; (br) broad. Unidentified impurity at −17 ppm.
[b] $^1\Delta^{19}F(^{34/32}S)$ = 0.060 ppm. [c] $^1J(^{19}F–^{75}As)$ not resolved, quadrupolar collapsed.
[d] $^1J(^{19}F–^{13}C)$ = 268 Hz.

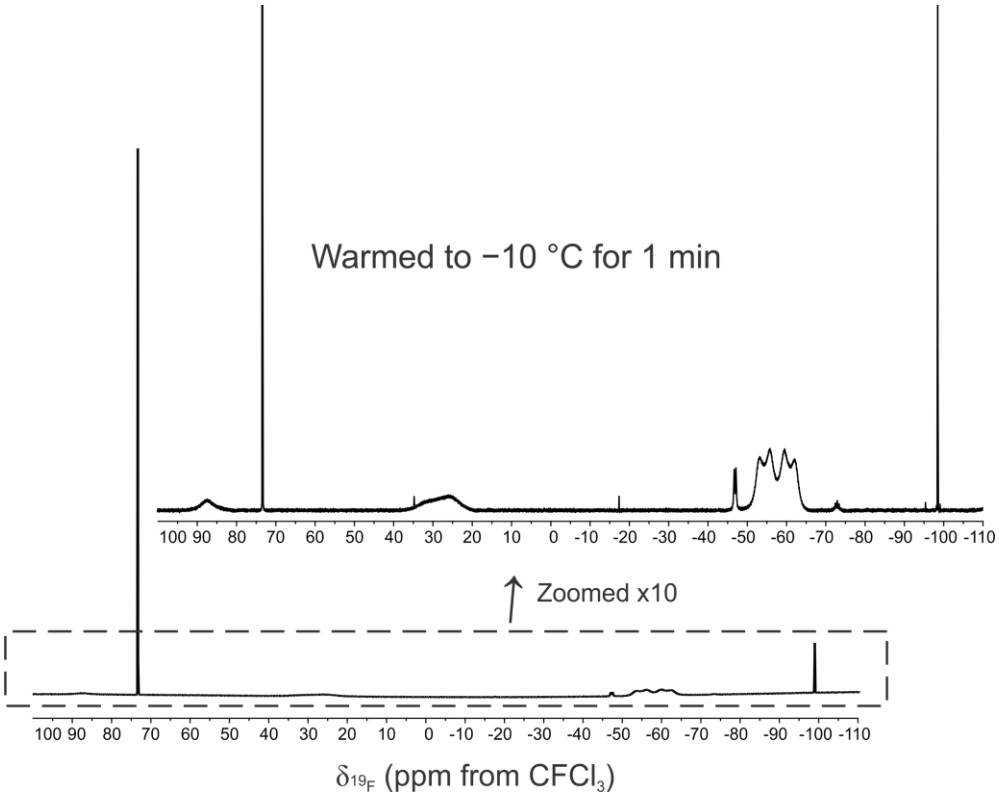

Figure 4.13 ^{19}F NMR spectrum (282.40 MHz) showing the reaction of $[SF_3][AsF_6]$ with two molar equivalents of 2-adamantanone in SO_2 at −40 °C. The reaction was briefly warmed to −10 °C to dissolve the product. Externally referenced to $CFCl_3$ at RT.

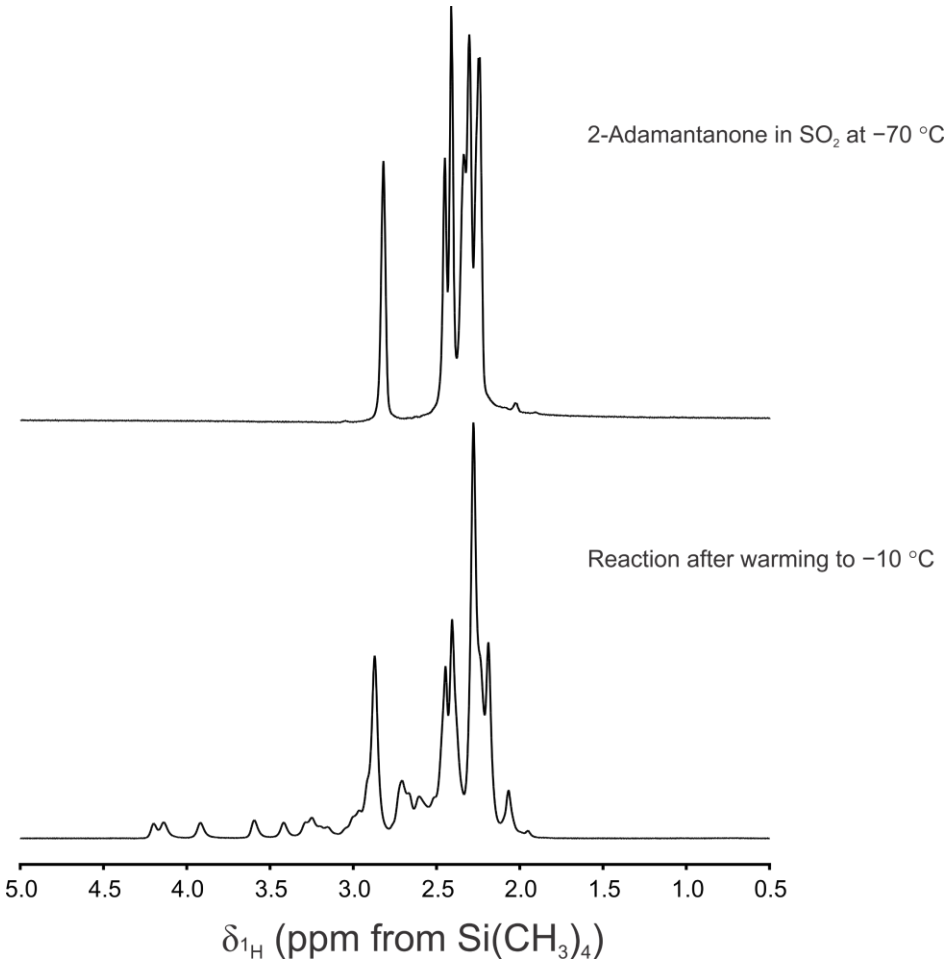

Figure 4.14 ^{1}H NMR spectra (300.13 MHz) showing the reaction of $[SF_3][AsF_6]$ with 2 equivalents of 2-adamantanone in SO_2 at −40 °C after having been warmed to −10 °C compared to 2-adamantanone in SO_2 at −70 °C. Externally referenced to $Si(CH_3)_4$ at RT.

The doublet (−47.0 ppm) and quintet (−73.0 ppm) resonances (Figure 4.13) associated with the $AsF_5{\cdot}O{=}C_{10}H_{14}$ adduct were also detected in the ^{19}F NMR spectrum after warming to −10 °C. Based on the reactions of $[SF_3][AsF_6]$ with cyclopentanone and acetone, the use of two equivalents of Lewis base should result in only negligible concentrations of the $AsF_5{\cdot}O{=}R$ adduct, however, using two equivalents of 2-adamantanone resulted in the formation of significant amounts of $AsF_5{\cdot}O{=}C_{10}H_{14}$.

The broad singlet at 25.6 ppm was attributed to the $[SF_3{\cdot}(O{=}C_{10}H_{14})_2]^+$ cation (Figure 4.13) and the $[AsF_6]^-$ anion was observed at −57.6 ppm as a partially quadrupolar

collapsed multiplet suggesting some cation-anion interactions. The deoxofluorination products 2,2-difluoroadamantane (−98.58 ppm) and SOF_2 (73.32 ppm) were detected with an integration ratio of 0.3:1.0.

4.2.9 $[SF_3][AsF_6]$ and One Equivalent of 2-Adamantanone in SO_2

Unlike the reaction of $[SF_3][AsF_6]$ with two equivalents of 2-adamantanone in SO_2, the use of a 1:1 molar ratio did not produce any solubility challenges at −70 °C and resulted in a clear colourless solution upon reaction. All reaction products were characterized at −70 °C in SO_2 using ^{19}F NMR spectroscopy. While ^{1}H NMR spectra were acquired, the spectra proved to be quite complex and did not provide any additional information in determining the products of this reaction. The ^{19}F NMR spectra are depicted in Figure 4.15 and the chemical shifts and coupling constants are listed in Table 4.11.

Upon melting at −70 °C, a broad singlet resonance at 31 ppm was observed associated with the $[SF_3{\cdot}O{=}C_{10}H_{14}]^+$ adduct, as well as, a broad quadrupolar collapsed singlet at −57 ppm associated with the $[AsF_6]^-$ anion. Immediately upon warming the reaction, the $[SF_3{\cdot}O{=}C_{10}H_{14}]^+$ adduct began to dissociate into free SF_4 and $AsF_5{\cdot}O{=}C_{10}H_{14}$ (Equation 4.5) as demonstrated by the appearance of a doublet at −46.6 ppm and a quintet at −71.4 ppm. This adduct increased in concentration upon warming to −40 °C, which resulted in a clear, light yellow solution. This was accompanied by a shift in the broad $[SF_3]^+$ resonance to 37 ppm due to the formation of SF_4 in solution which rapidly exchanges with $[SF_3]^+$, as seen for the acetone and cyclopentanone systems. Additional resonances at −94.60 and −98.82 ppm were detected as singlets; the resonance at −98.82 ppm is likely associated with the deoxofluorination of 2-adamantanone to 2,2-difluoroadamantane.[10]

Table 4.11 Selected ^{19}F chemical shifts (δ) at −70 °C for the reaction of $[SF_3][AsF_6]$ with one molar equivalent of 2-adamantanone in SO_2.

Compound	Chemical Shift (ppm) [a]	$^2J(^{19}F–^{19}F)$ (Hz)
Reaction at −70 °C for 1 min [b]		
SOF_2	72.74 (s) [c]	--
$[SF_3{\cdot}O{=}C_{10}H_{14}]^+$	31 (s, br)	--
$AsF_5{\cdot}O{=}C_{10}H_{14}$	−46.6 (d) −71.4 (quin)	130.31 Not resolved
$[AsF_6]^-$	−57.0 [d]	--
$C_{10}H_{14}F_2$	−98.78 (s)	--
Reaction at −40 °C for 8 min [b]		
SOF_2	72.70 (s) [c]	--
$[SF_3]^+/SF_4$	37 (s, br)	--
$AsF_5{\cdot}O{=}C_5H_8$	−46.65 (d) −71.49 (quin)	125.33 128.84
$[AsF_6]^-$	−57.0 [d]	--
$C_{10}H_{14}F_2$	−94.60 (s) −98.82 (s)	--
Reaction at RT for 5 min [b]		
SOF_2	72.70 (s) [c]	--
$[SF_3]^+/SF_4$	46 (s, br)	--
$AsF_5{\cdot}O{=}C_5H_8$	−46.66 (d) −71.53 (quin)	124.35 126.22
$[AsF_6]^-$	−56.4 [d]	--
$C_{10}H_{14}F_2$	−94.62 (s) −98.81 (s)	--
Reaction at RT for 2 h [b]		
SOF_2	72.80 (s) [c]	--
$[SF_3]^+$	31.76 (s)	--
$AsF_5{\cdot}O{=}C_5H_8$	−46.54 (d) −71.43 (quin)	124.02 126.22
$[AsF_6]^-$	−56.0 [d]	--
$C_{10}H_{14}F_2$	−94.54 (s) −98.71 (s)	--
$C_{10}H_{14}F_2$	−97.14 (d) −104.81 (d)	230

[a] Abbreviations: (s) singlet; (d) doublet; (quin) quintet; (ax) axial; (eq) equatorial; (br) broad. [b] Unidentified singlet resonance at −16.6 ppm.
[c] $^1\Delta^{19}F(^{34/32}S)$ = 0.060 ppm. [d] $^1J(^{19}F–^{75}As)$ not resolved, quadrupolar collapsed.

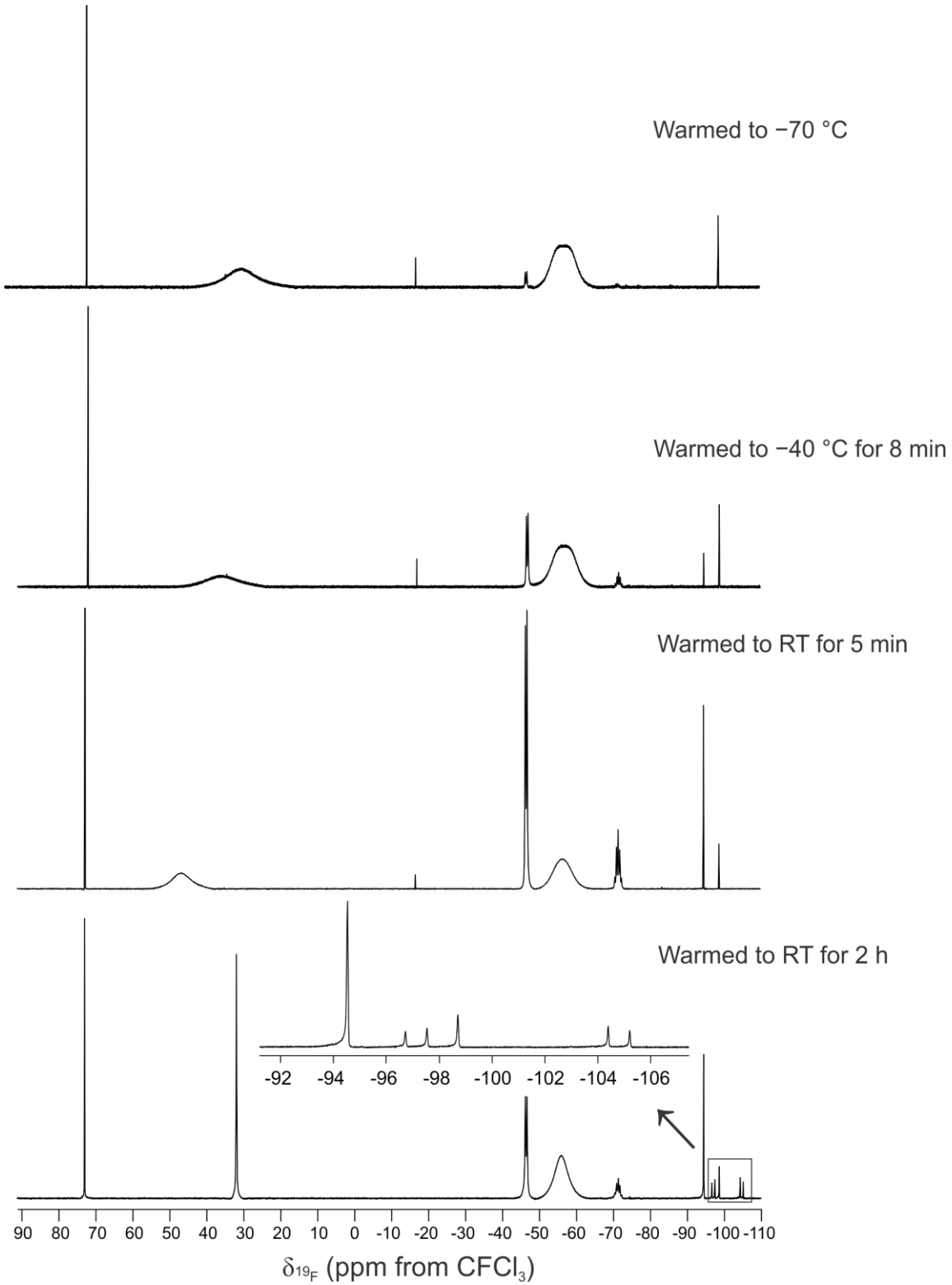

Figure 4.15 ^{19}F NMR spectra (282.40 MHz) showing the progress of the reaction of $[SF_3][AsF_6]$ with 2-adamantanone in SO_2 at −70 °C in a 1:1 molar ratio. All spectra were externally referenced to $CFCl_3$ at RT.

Warming the reaction to RT for 5 min resulted in a large increase in intensity of the $AsF_5{\cdot}O{=}C_{10}H_{14}$ resonances and an increase in the chemical shift of the $[SF_3]^+/SF_4$ resonance (46 ppm), indicating the increased concentration of SF_4. The singlet at −94.62 ppm increased in intensity, which may have resulted from fluorination of the adamantane ring by SF_4. The $AsF_5{\cdot}O{=}C_{10}H_{14}$ adduct remained relatively stable even after leaving the reaction at RT for 2 h, however, no SF_4 remained and only a sharp singlet resonance at 31.76 ppm associated with free $[SF_3]^+$ was present. The SF_4 presumably reacted with the adamantane ring to yield more of the fluorinated adamantane product. When warmed to RT for 5 min the largest amount of $AsF_5{\cdot}O{=}C_{10}H_{14}$ adduct was generated, relative to the $[AsF_6]^-$; for every one $[AsF_6]^-$, one equivalent of $AsF_5{\cdot}O{=}C_{10}H_{14}$ was formed as detected by the characteristic doublet (F_{eq}: −46.66 ppm) and quintet (F_{ax}: −71.53 ppm) resonances in the ^{19}F NMR spectrum. The relative integrations after 2 h at RT were 3.0:12.0:3.5:1.0 for $[SF_3]^+$, $[AsF_6]^-$, and the doublet (F_{eq}) and quintet (F_{ax}) resonances of $AsF_5{\cdot}O{=}C_{10}H_{14}$, respectively. For every one $AsF_5{\cdot}O{=}C_{10}H_{14}$ present, two $[AsF_6]^-$ anions exist and for every one SOF_2 generated, 4 molar equivalents of the $AsF_5{\cdot}O{=}C_{10}H_{14}$ adduct are present (integration of 2.0:14.1:4.1 for SOF_2:$AsF_5{\cdot}O{=}C_{10}H_{14}$). The resonance attributed to 2,2-difluoroadamantane (−98.71 ppm) decreased in intensity and an AB pattern centered around −97.14 and −104.81 ppm with a J = 230 Hz was observed, which is common for geminal $^2J(^{19}F{-}^{19}F)$ coupling. This suggests that the adamantane ring was broken up as 2-fluoroadamantane (−173 ppm), 1-fluoroadamantane (−128 ppm), and 2-fluoroadamantane cation, $[C_{10}H_{14}F]^+$ (120 ppm), products were not observed.[10] Generating approximately 4 equivalents of SOF_2 yielded 1 equivalent of 2,2-difluoroadamantane, approximately two equivalents of the unknown difluoro-species at −97.14 and −104.81 ppm, and

approximately 5 equivalents of the unidentified species at −94.54 ppm (relative integration of 7.5:9.6:2.5:2.0:2.4).

4.2.10 Computational Studies of Possible Deoxofluorination Intermediates

Density functional theory (DFT) calculations were carried out on the following five proposed potential intermediates of the deoxofluorination reaction of acetone: $[SF_3{\cdot}O{=}C(CH_3)_2]^+$, $[SF_3{\cdot}\{O{=}C(CH_3)_2\}_2]^+$, $[SF_3{\cdot}\{O{=}C(CH_3)_2\}_3]^+$, $(CH_3)_2FCOSF_3$, and $[(CH_3)_2FCOSF_2]^+$. The gas-phase geometries of these compounds were optimized using the B3LYP/aug-cc-pVTZ level of theory and are shown in Figure 4.16. A summary of selected geometric parameters is given in Table 4.12.

Table 4.12 Selected Calculated Bond Lengths (Å) of $[SF_3{\cdot}O{=}C(CH_3)_2]^+$, $[SF_3{\cdot}\{O{=}C(CH_3)_2\}_2]^+$, $[SF_3{\cdot}\{O{=}C(CH_3)_2\}_3]^+$, $(CH_3)_2FCOSF_3$, and $[(CH_3)_2FCOSF_2]^+$.

Compound	S−O	C−O	S−F	C−F
$[SF_3{\cdot}O{=}C(CH_3)_2]^+$	2.157	C(2)−O(1) 1.242	S(1)−F(1) 1.581 S(1)−F(2) 1.539 S(1)−F(3) 1.549	--
$[SF_3{\cdot}\{O{=}C(CH_3)_2\}_2]^+$	S(1)−O(1) 2.299 S(1)−O(2) 2.300	C(2)−O(1) 1.233 C(5)−O(2) 1.233	S(1)−F(1) 1.559 S(1)−F(2) 1.581 S(1)−F(3) 1.581	--
$[SF_3{\cdot}\{O{=}C(CH_3)_2\}_3]^+$	S(1)−O(1) 2.478 S(1)−O(2) 2.504 S(1)−O(3) 2.359	C(2)−O(1) 1.226 C(5)−O(2) 1.226 C(8)−O(3) 1.229	S(1)−F(1) 1.588 S(1)−F(2) 1.564 S(1)−F(3) 1.567	--
$(CH_3)_2FCOSF_3$	1.726	1.413	S(1)−F(1) 1.588 S(1)−F(2) 1.721 S(1)−F(3) 1.575	1.410
$[(CH_3)_2FCOSF_2]^+$	1.451	C(2)−O(1) 2.542	S(1)−F(1) 1.600 S(1)−F(2) 1.602	1.279

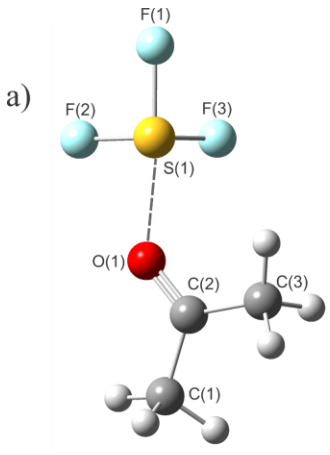

E = −2.338278 x10^6 kJ/mol

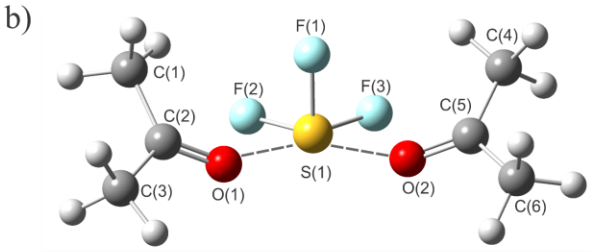

E = −2.846152 x10^6 kJ/mol

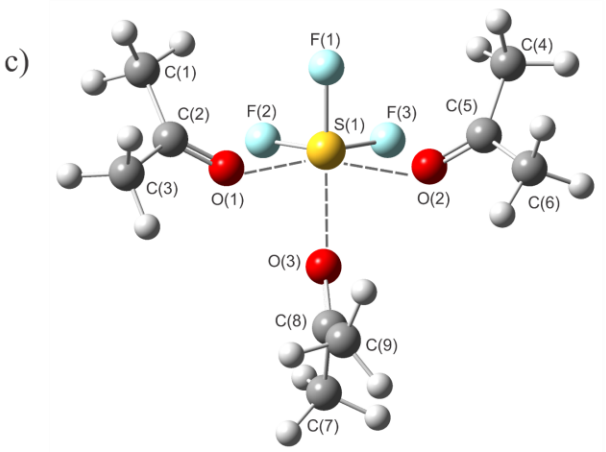

E = −3.352919 x10^6 kJ/mol

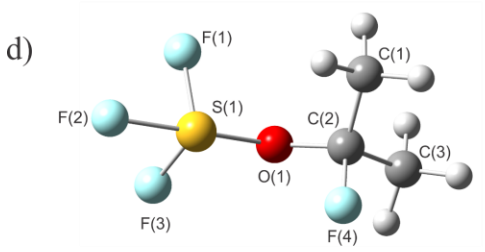

E = −2.601204 x10^6 kJ/mol

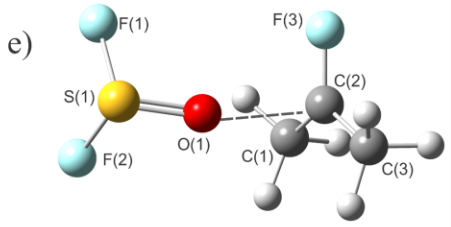

E = −2.338331 x10^6 kJ/mol

Figure 4.16 Optimized gas-phase geometries and energies of possible intermediates in the deoxofluorination reaction: a) $[SF_3{\cdot}O{=}C(CH_3)_2]^+$, b) $[SF_3{\cdot}\{O{=}C(CH_3)_2\}_2]^+$, c) $[SF_3{\cdot}\{O{=}C(CH_3)_2\}_3]^+$, d) $(CH_3)_2FCOSF_3$, and e) $[(CH_3)_2FCOSF_2]^+$.

It was first suggested by Dmowski that the $[SF_3{\cdot}O{=}C(CH_3)_2]^+$ cation is the first intermediate in the deoxofluorination reaction mechanism and responsible for polarizing the C=O bond of acetone (see Chapter 1 for more details). The NMR spectroscopy studies described in Section 4.2.2−4.2.5 showed the ability of $[SF_3]^+$ to form adducts with acetone when reacted in 1:1, 1:2 and 1:3 ratios in SO_2 at low-temperatures (< −40 °C). In the case where excess acetone was reacted with $[SF_3]^+$, the $[SF_3{\cdot}\{O{=}C(CH_3)_2\}_3]^+$ cation was proposed to exist, which did not form in the case where three equivalents of acetone were used. The calculated S−O bond lengths of the $[SF_3{\cdot}O{=}C(CH_3)_2]^+$ (2.157 Å), $[SF_3{\cdot}\{O{=}C(CH_3)_2\}_2]^+$ (2.299 and 2.300 Å), and $[SF_3{\cdot}\{O{=}C(CH_3)_2\}_3]^+$ (2.359−2.504 Å) cations increase as more acetone molecules are added to the coordination sphere of the sulfur in $[SF_3]^+$. Consequently, the $[SF_3]^+$ cation will not polarize the C=O bond to as large of an extent resulting in shorter C=O bond lengths as more acetones are added (C−O bond lengths: acetone 1.210 Å; $[SF_3{\cdot}O{=}C(CH_3)_2]^+$ 1.242 Å; $[SF_3{\cdot}\{O{=}C(CH_3)_2\}_2]^+$ 1.233 Å; and $[SF_3{\cdot}\{O{=}C(CH_3)_2\}_3]^+$ 1.226−1.229 Å). In the $[SF_3{\cdot}O{=}C(CH_3)_2]^+$ cation, the acetone coordinates to the sulfur via the axial position (F(1)−S(1)−O(1) 173.3°) and the lone pair on sulfur occupies the equatorial position of the trigonal bipyramidal geometry. The $[SF_3{\cdot}\{O{=}C(CH_3)_2\}_2]^+$ cation adopts a square pyramidal geometry with the two acetone molecules coordinating to the sulfur in the equatorial positions (F(3)−S(1)−O(1) 179.40°; F(2)−S(1)−O(2) 179.62°). Lastly, the gas-phase geometry of $[SF_3{\cdot}\{O{=}C(CH_3)_2\}_3]^+$ is octahedral with three equatorial acetone ligands coordinating trans to a S−F bond (F(3)−S(1)−O(1) 178.33°; F(2)−S(1)−O(2) 178.59°; F(1)−S(1)−O(3) 170.93°).

Based on the deoxofluorination reaction mechanism proposed by Pustovit and Nazaretian, the $[SF_3{\cdot}O{=}C(CH_3)_2]^+$ cation undergoes nucleophilic attack at the carbon center by a fluoride source to generate the neutral $(CH_3)_2FCOSF_3$. The optimized gas-phase

geometry of this species was calculated, along with the $[(CH_3)_2FCOSF_2]^+$ cation which is proposed to be in equilibrium with $(CH_3)_2FCOSF_3$ in the presence of HF. The $(CH_3)_2FCOSF_3$ compound contained S−O (1.726 Å) and C−O (1.413 Å) single bonds and the C(2) center adopted a tetrahedral geometry (O(1)−C(2)−F(4) 107.52°). The $[(CH_3)_2FCOSF_2]^+$ cation optimized to SOF_2 and $[(CH_3)_2CF]^+$ with a weak O(1)−C(2) interaction of 2.542 Å ($\sum r_{vdW}$ = 3.22 Å). The optimized structure showed the $[(CH_3)_2CF]^+$ moiety to be nearly planar with a sum of angles about the central carbon of 359.36° deviating only slightly from 360° for a trigonal planar geometry. This strongly supports the proposed mechanism by Pustovit and Nazaretian, which states that $[(CH_3)_2FCOSF_2]^+$ readily loses SOF_2 and allows for nucleophilic attack by a fluoride source (i.e., $[HF_2]^-$) yielding 2,2-difluoropropane.

The HOMO and LUMO energies of the $[SF_3{\cdot}O{=}C(CH_3)_2]^+$, $[SF_3{\cdot}\{O{=}C(CH_3)_2\}_2]^+$, and $[SF_3{\cdot}\{O{=}C(CH_3)_2\}_3]^+$ cations were calculated and are listed in Table 4.13. The LUMO energies decreased as more acetone molecules were added around $[SF_3]^+$ ($[SF_3{\cdot}O{=}C(CH_3)_2]^+$ −732 kJ/mol; $[SF_3{\cdot}(O{=}C(CH_3)_2)_2]^+$ −613 kJ/mol; and $[SF_3{\cdot}\{O{=}C(CH_3)_2\}_3]^+$ −500 kJ/mol) compared to neutral acetone (−18 kJ/mol). The $[SF_3]^+$ cation is highly Lewis acidic and reacts readily with ketones, as shown by NMR spectroscopy and the observed colour changes of the reactions, even at low temperatures (*vide supra*). The low energy of the LUMO makes the carbon of the carbonyl group much more readily available towards nucleophilic attack. These values can be compared to the calculated LUMO energies of the oxonium cations $[HO{=}C(CH_3)_2]^+$ (−189 kJ/mol) and $[H\{O{=}C(CH_3)_2\}_2]^+$ (−596 kJ/mol) (presented in Chapter 5) which are much more thermally stable even at RT, in the case of $[HO{=}C(CH_3)_2]^+$.

Table 4.13 Calculated Energies (kJ/mol) of the HOMO and LUMO for $[SF_3{\cdot}\{O{=}C(CH_3)_2\}_x]^+$ (x = 1−3) and Protonated Ketones $[H\{O{=}C(CH_3)_2\}_x]^+$ (x = 1, 2).

Compound	HOMO Energy	LUMO Energy
$O{=}C(CH_3)_2$	−162	−18
$[HO{=}C(CH_3)_2]^+$	−376	−189
$[H\{O{=}C(CH_3)_2\}_2]^+$	−1203	−596
$[SF_3{\cdot}\{O{=}C(CH_3)_2\}_3]^+$	−1035	−500
$[SF_3{\cdot}\{O{=}C(CH_3)_2\}_2]^+$	−1126	−613
$[SF_3{\cdot}O{=}C(CH_3)_2]^+$	−1271	−732

4.3 Summary and Conclusions

A detailed study of the reactions between $[SF_3][AsF_6]$ and the ketones, acetone, cyclopentanone, and 2-adamantanone, has been carried out using ^{19}F and ^{1}H NMR spectroscopy at low temperatures. The 1:1 and 1:2 adducts of $[SF_3]^+$ with the ketones, acetone, cyclopentanone, and 2-adamantanone, have been observed at low temperatures in SO_2 for the first time by NMR spectroscopy. The reaction of $[SF_3][AsF_6]$ with an excess of acetone (i.e., as the solvent) at −80 °C resulted in a decrease in the $\delta(^{19}F)$ from 32.91 to 18.43 ppm attributed to the formation of the 1:3 adduct, $[SF_3{\cdot}\{O{=}C(CH_3)_2\}_3]^+$. DFT calculations were used to optimize the gas-phase geometry of these adducts and structural parameters were reported. As well, the geometries of the proposed intermediates of deoxofluorination, $(CH_3)_2FCOSF_3$ and $[(CH_3)_2FCOSF_2]^+$, were optimized in the gas phase. For each of the reactions performed, gradually warming to −40 °C resulted in a colour change to a dark red or orange/brown and the appearance of SF_4 in the ^{19}F NMR spectrum. This was attributed to the presumed dismutation reaction of two equivalents of $[SF_3][AsF_6]$ to SF_4 and $[SF_2{\cdot}(O{=}R)_x][AsF_6]$ (R = $C(CH_3)_2$, C_5H_8, $C_{10}H_{14}$; x = 1−3). The proposed $[SF_2]^{2+}$

product has not been observed and is likely too oxidatively reactive to be stabilized in these solutions.

The reactions between $[SF_3][AsF_6]$ and ketone in a 1:1 ratio consistently gave the $AsF_5{\cdot}O{=}R$ adduct (R = $C(CH_3)_2$, C_5H_8, $C_{10}H_{14}$) as a by-product. This was likely due to the strong F_3S---$FAsF_5$ interactions and insufficient concentration of the carbonyl compound to shield $[SF_3]^+$ from interacting with the anion. The reaction with 2-adamantanone, when warmed to RT for 5 min, gave the largest amount of $AsF_5{\cdot}O{=}C_{10}H_{14}$ adduct relative to the $[AsF_6]^-$ anion as detected by the characteristic doublet (F_{eq}: −46.66 ppm) and quintet (F_{ax}: −71.53 ppm) resonances in the ^{19}F NMR spectrum.

Despite the lack of F^- present, required for conversion of a C=O group to a $-CF_2$ group, some reactions yielded the deoxofluorination product (i.e., the difluoro species) in very small amounts. Upon warming these reactions to RT, dark coloured solutions were generated, attributed to the existence of a radical cation, which could not be detected via NMR spectroscopy. The radical cation was possibly generated from the reaction of the ketone with the highly reactive and elusive $[SF_2]^{2+}$ species.

References

[1] Smith, W. C. U.S. Patent 2859245, 1958.

[2] Hasek, W. R.; Smith, W. C.; Engelhardt, V. A. *J. Am. Chem. Soc.* **1960**, *82*, 543−551.

[3] Smith, W. C. *Angew. Chem. Int. Ed.* **1962**, *1*, 467−518.

[4] Wang, C. -L. *J. Org. React*. **1985**, *34*, 319−400.

[5] Baum, K. *J. Am. Chem. Soc.* **1969**, *91*, 4594.

[6] Pashinnik, V. E. *Russ. J. Org. Chem.* **2000**, *36*, 350−358.

[7] Chaudhary, P. PhD Dissertation, University of Lethbridge, 2016.

[8] Olah G. A; Chambers, R. D.; Comisarow, M. B. *J. Am. Chem. Soc.* **1967**, 89, 1268−1269.

[9] Hasek, W. R.; Smith, W. C.; Engelhardt, V. A. *J. Am. Chem. Soc.* **1960**, *82*, 543−551.

[10] Hara, S.; Aoyama, M. *Synthesis* **2008**, *16*, 2510−2512.

5. Solid-State Structure of Protonated Ketones and Aldehydes in Superacidic Media

(Based on publication: Stuart, D.; Wetmore, S. D.; Gerken, M. *Angew. Chem. Int. Ed.* **2017**, *56*, 16380−16384)

5.1 Introduction

Protonated ketones and aldehydes are key intermediates in many organic reactions. Ground-breaking work by Gillespie and Olah proved by NMR spectroscopy that these cationic intermediates can be stabilized in superacidic solutions at low temperatures (LT).[1] Olah studied the protonation of a suite of organic molecules with varying functional groups including ketones, aldehydes, alcohols, ethers, thiols, and carboxylic acids.[1a] The use of superacidic media, such as HSO_3F-SbF_5 ("magic acid") or HF/SbF_5, provide proton sources for the organic intermediates and stablize these protonated compounds. One of the first ketones to be studied by ^1H NMR spectroscopy was the conjugate acid of acetone, with a pKa of −7.3, giving rise to a ^1H resonance of the $C{=}OH^+$ group at 14.45 ppm.[1b] Two resonance structures can be written for protonated ketones and aldehydes: the oxonium and hydroxycarbenium cation structures (Scheme 5.1). Strong evidence for the oxonium structure being favoured has been obtained by the highly deshielded ^1H resonances between 13 and 15 ppm,[1c-e] as well as by the observation of the *E*- and *Z*-stereoisomers of protonated aldehydes and unsymmetrically substituted ketones.[1d,e]

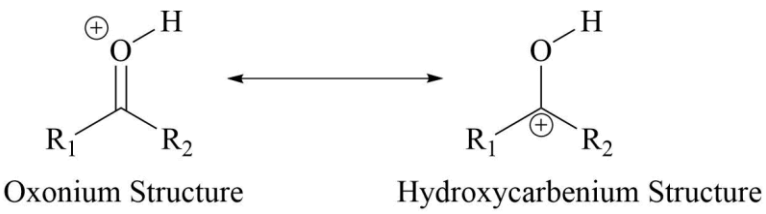

Scheme 5.1 Resonance structures for protonated ketones.

A small number of protonated ketones have been studied in the solid state. Structural studies of monoprotonated ketones are limited to a group of cyclopropylcarbinyl derivatives which were part of investigations of the stabilization of a positive charge by cylcopropyl groups and in homoaromatic systems (Figure 5.1).[2] In one attempt to isolate the 2-hydroxyhomotropylium benzannelated cation, the X-ray crystal structure showcased a hemiprotonated cation consisting of two hydrogen-bridged ketones.[3]

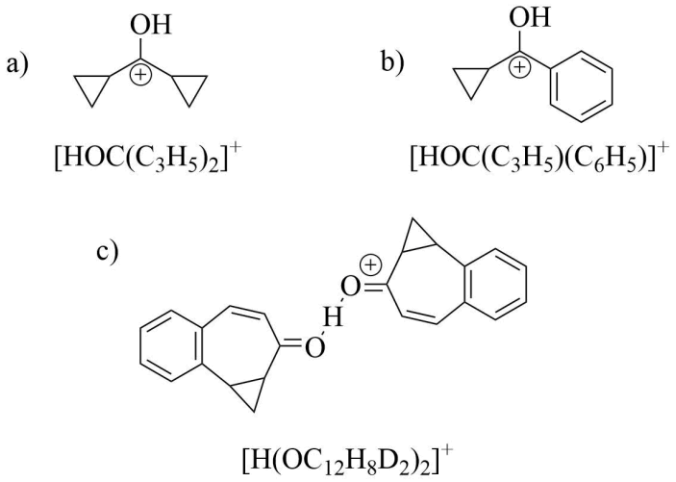

Figure 5.1 Structures of the previous protonated cyclopropylcarbinyl derivatives studied.

In a study involving the isolation of solvated protons in organic oxygen-donor solvents, the X-ray crystal structure of hemiprotonated benzophenone was determined.[4] Computational studies using the B3LYP/6-31++G(d,p) level of theory have been carried out on the carbonyl bases $R_2C{=}O$ (R = F, H, CH_3), investigating the changes in bond lengths and vibrational frequencies upon protonation.[5] It was predicted that a dramatic decrease of up to 232 cm^{-1} in the ν(CO) stretching frequency and increase in the C=O bond distances occured once the carbonyl group was protonated. Semi-empirical studies in conjunction with mass spectrometric measurements have been used to study the geometric properties and stability of protonated acetone clusters.[6]

Currently, no solid-state studies of protonated aldehydes have been reported. Infrared photodissociation spectroscopy along with calculations at the B3LYP/6-311++G(2df,2pd) level of theory were used to probe protonated benzaldehyde.[7] Excited state and optimized geometry calculations showed the lowest-energy configuration to be the *E*-configuration.[8] Mass spectrometry studies, along with gas-phase calculations, have suggested that formaldehyde and acetaldehyde form hydrogen-bridged dimers, $(RCHO)_2H^+$ (R = H or CH_3).[9] Attempts to synthesize protonated formaldehyde in the solid state have been unsuccessful and instead a $[H_2C{=}O{-}CH_2OH]^+$ salt was obtained and characterized by X-ray crystallography and IR and Raman spectroscopies (Equation 5.1).[10]

$$O{=}CH_2 + MF_5 + HF \xrightarrow{\text{aHF}} [H_2COCH_2OH][MF_6] \quad (M = As, Sb) \qquad (5.1)$$

5.2 Results and Discussion

5.2.1 Synthesis and Properties of Protonated 2-Adamantanone, Cyclopentanone, Acetone, Benzaldehyde, and Acetaldehyde

While investigating the reaction mechanism of deoxofluorination reactions between ketones and the highly Lewis acidic $[SF_3]^+$ cation, an equimolar reaction between the $[SF_3][AsF_6]$ salt and 2-adamantanone ($O{=}C_{10}H_{14}$) in anhydrous hydrogen fluoride (aHF) resulted in protonation of the carbonyl group and the synthesis of the $[AsF_6]^-$ salt of $[HO{=}C_{10}H_{14}]^+$. The protonation of the ketone can be explained by the superacidic nature of the $[SF_3][AsF_6]$/aHF system (Equation 5.2). In excess aHF, formation of SF_4 and $[H_2F][AsF_6]$, a proton source, were formed in solution. Upon isolating the product, the SF_4 produced was easily removed under dynamic vacuum.

$$[SF_3][AsF_6] + 2\,HF \rightleftharpoons SF_4 + [H_2F][AsF_6] \quad (5.2)$$

In targeted reactions, salts of the protonated ketones, [2-adamantanone ($O{=}C_{10}H_{14}$), cyclopentanone ($O{=}C_5H_8$), acetone ($O{=}C(CH_3)_2$)] and protonated aldehydes, [benzaldehyde ($O{=}CHC_6H_5$), acetaldehyde ($O{=}CHCH_3$)] were isolated using stoichiometric amounts of either $[SF_3][AsF_6]$ or SbF_5 in aHF. Reactions using AsF_5 were attempted, but led to inaccurate stoichiometric ratios, which resulted in reduced stability of the product, likely due to oxidation of the organic substrate by excess AsF_5.

Reactions of $[SF_3][AsF_6]$ with $O{=}C_{10}H_{14}$ and $O{=}C_5H_8$ in aHF at −78 °C yielded the hexafluoroarsenate salts of $[HO{=}C_{10}H_{14}]^+$ and $[HO{=}C_5H_8]^+$, respectively (Equation 5.3). Reaction occured instantaneously upon melting, producing white powders that dissolved at 0 °C. Crystals of $[HO{=}C_{10}H_{14}][AsF_6]$ and $[HO{=}C_5H_8][AsF_6]$ were grown at −20 and −78 °C, respectively. The salt of $[HO{=}C_{10}H_{14}]^+$ was stable at room-temperature (RT) for 20 min before turning pale yellow, whereas $[HO{=}C_5H_8][AsF_6]$ was more stable and remained a white powder for upwards of 1 h. The bands in the LT Raman spectra showed no change in frequency; however, increasing fluorescence was observed in the spectral baseline the longer the sample was left at RT.

$$[SF_3][AsF_6] + O{=}R + HF \xrightarrow{aHF} [HO{=}R][AsF_6] + SF_4 \quad (R = C_{10}H_{14}, C_5H_8) \quad (5.3)$$

Hexafluoroantimonate salts can be obtained via the reaction of ketones with one molar equivalent of SbF_5 in aHF. Stoichiometric amounts of SbF_5 can be prepared from the reaction of a known amount of solid SbF_3 with elemental fluorine in aHF (Equation 5.4). Subsequent addition of equimolar quantities of 2-adamantanone, cyclopentanone, and acetone resulted in immediate reactions at −78 °C producing white powders of

$[HO{=}C_{10}H_{14}][SbF_6]$, $[HO{=}C_5H_8][SbF_6]$, and $[HO{=}C(CH_3)_2][SbF_6]$, respectively, according to reaction equation 5.5. The $[HO{=}C(CH_3)_2][SbF_6]$ salt proved to be the most stable among those studied, lasting 24 h at RT before LT Raman spectroscopy showed some fluoresence in the baseline.

$$SbF_3 + F_2 \xrightarrow{aHF} SbF_5 \tag{5.4}$$

$$SbF_5 + O{=}R + HF \xrightarrow{aHF} [HO{=}R][SbF_6] \quad (R = C_{10}H_{14}, C_5H_8, C(CH_3)_2) \tag{5.5}$$

By reacting two equivalents of acetone with SbF_5 in aHF at −78 °C, it was believed the $[H\{O{=}C(CH_3)_2\}_2][SbF_6]$ salt could be synthesized. This reaction produced a white solid which was then dissolved by quickly bringing the sample to RT so that the solid dissolved. Clear, colourless blocks crystallized at −60 °C over a period of ca. 30 min. Instead of pure $[H\{O{=}C(CH_3)_2\}_2][SbF_6]$, X-ray crystallography showed several of these crystals to be $[H\{O{=}C(CH_3)_2\}_2]_3[HO{=}C(CH_3)_2]_3[SbF_6]_5F$, likely due to the actual stoichiometry being slightly less than 1:2. Several crystals were mounted and shown to have the same unit cell, however, the structure of the bulk sample was not determined. The stability of this salt was not tested.

The reaction of benzaldehyde ($O{=}CHC_6H_5$) with SbF_5 in aHF yielded the $[SbF_6]^-$ salt of hemiprotonated, hydrogen-bridged dimeric $[H(O{=}CHC_6H_5)_2]^+$, even when a one molar equivalent of SbF_5 was used (Equation 5.6). The sample was warmed to −60 °C to dissolve the solid, and pale red, transparent blocks crystallized at −78 °C. No evidence for the monoprotonated $[H(O{=}CHC_6H_5)_2]^+$ cation was obtained by Raman spectroscopy or X-ray crystallography. Reacting acetaldehyde ($O{=}CHCH_3$) with SbF_5 in 2:1 and 1:1 molar

ratios, resulted in the synthesis of the $[SbF_6]^-$ salts of $[H(O{=}CHCH_3)_2]^+$ and $[HO{=}CHCH_3]^+$, respectively (Equation 5.6 and 5.7). The three salts, $[H(O{=}CHC_6H_5)_2][SbF_6]$, $[H(O{=}CHCH_3)_2][SbF_6]$, and $[HO{=}CHCH_3][SbF_6]$, were isolated as white powders and characterized by Raman spectroscopy at low temperature proving to be unstable, decomposing upon warming to RT. The $[H(O{=}CHCH_3)_2][SbF_6]$ salt was only obtained in admixture with $[HO{=}CHCH_3][SbF_6]$. The white powder produced easily dissolved at −70 °C and colourless needles crystallized at −78 °C. No single crystals suitable for X-ray crystallography were found.

$$SbF_5 + 2\ O{=}CH(R) + HF \xrightarrow{aHF} [H(O{=}CHR)_2][SbF_6] \quad (R = C_6H_5, CH_3) \tag{5.6}$$

$$SbF_5 + O{=}CH(CH_3) + HF \xrightarrow{aHF} [HO{=}CH(CH_3)][SbF_6] \tag{5.7}$$

5.2.2 X-ray Crystallography of Protonated Ketones

The crystallographic parameters and details for the protonated ketone salts $[HO{=}C_{10}H_{14}][AsF_6]$, $[HO{=}C_5H_8][AsF_6]$, $[HO{=}C_5H_8][SbF_6]$, $[HO{=}C(CH_3)_2][SbF_6]$, and $[H\{O{=}C(CH_3)_2\}_2]_3[HO{=}C(CH_3)_2]_3[SbF_6]_5F$ are provided in Table 5.1. A summary of selected experimental and calculated bond lengths are listed in Table 5.2. A full list of experimental and calculated bond lengths and bond angles of the protonated ketones can be found in Appendix Tables A.2.1−A.2.6.

Table 5.1 Summary of X-ray Crystal Data and Refinement Results for Protonated Ketones Derived From 2-Adamantanone, Cyclopentanone, and Acetone.

Compounds	$[HO{=}C_{10}H_{14}][AsF_6]$	$[HO{=}C_5H_8][AsF_6]$	$[HO{=}C_5H_8][SbF_6]$	$[HO{=}C(CH_3)_2][SbF_6]$	$[H\{O{=}C(CH_3)_2\}_2]_3[HO{=}C(CH_3)_2]_3[SbF_6]_5F$
Empirical Formula	$C_{10}H_{15}OAsF_6$	$C_5H_9OAsF_6$	$C_5H_9OSbF_6$	$C_3H_7OSbF_6$	$C_{27}H_{54}O_9F_{31}Sb_5$
Formula Weight (g mol^{-1})	340.14	274.04	320.87	294.84	1720.45
Temperature (^{o}C)	–173	–173	–173	–173	–173
Wavelength (Å)	1.54184	1.54184	0.71073	0.71073	0.71073
Crystal System	monoclinic	monoclinic	monoclinic	triclinic	triclinic
Space Group	$P2_1/n$	$P2_1/c$	$P2_1/c$	$P\bar{1}$	$P2_1/n$
a (Å)	6.71420(10)	8.24930(10)	10.3244(2)	7.7094(2)	18.3950(3)
b (Å)	9.01740(10)	9.87020(10)	8.3210(2)	8.9984(2)	16.6616(3)
c (Å)	19.7057(2)	11.4762(2)	10.6795(2)	12.0138(2)	18.8869(3)
α (deg)	90	90	90	71.622(2)	90
b (deg)	95.1790(10)	110.687(2)	96.264(2)	80.430(2)	90.7690(10)
γ (deg)	90	90	90	89.353(2)	90
V (Å^3)	1188.20(3)	874.17(2)	911.99(3)	779.16(3)	5788.13(7)
Z	4	4	4	4	4
μ (mm^{-1})	4.542	11.931	3.081	3.594	2.442
ρ_{calcd} (g cm^{-3})	1.901	4.164	2.33	2.513	1.974
F(000)	680	1072	604	552	3288.0
Crystal Size (mm^3)	0.16 × 0.108 × 0.078	0.206 × 0.137 × 0.097	0.345 × 0.231 × 0.156	0.437 × 0.147 × 0.099	0.18 × 0.156 × 0.114
Reflections Collected	26439	16402	22907	17633	139690
Independent Reflections	2430	1900	2084	3557	13257
Data/Restraints/Parameters	2430/0/168	1900/0/123	2084/0/123	3557/0/215	13257/0/691
Goodness-of-fit on F^2	1.059	1.097	1.076	1.042	1.022
R_1, $I \geq 2\theta(I)$[a]	0.0232	0.0302	0.0139	0.0218	0.0282
wR_2 (F^2)[b]	0.0570	0.0747	0.0334	0.0515	0.0598
CCDC	1577976	1577974	1577979	1577975	N/A

Table 5.2 Selected Experimental and Calculated Bond Lengths (Å) of Oxonium Cations $[HO{=}C_{10}H_{14}]^+$, $[HO{=}C_5H_8]^+$, and $[HO{=}C(CH_3)_2]^+$ as well as the Parent Ketones $O{=}C_{10}H_{14}$, $O{=}C_5H_8$, and $O{=}C(CH_3)_2$.

	$O{=}C_{10}H_{14}$		$[HO{=}C_{10}H_{14}]^+$	
	exptl [b]	*calcd* [e]	*exptl*	*calcd* [e]
C=O	1.215(3)	1.213	1.274(2)	1.285
$C_{C=O}{-}C_{cis}$ [a]	1.5176(16)	1.524	1.469(2)	1.468
$C_{C=O}{-}C_{trans}$ [a]	1.5176(16)	1.524	1.472(2)	1.464
O---F			2.6233(16)	
	$O{=}C_5H_8$		$[HO{=}C_5H_8]^+$	
	exptl [c]	*calcd* [e]	*exptl* $[AsF_6]^-$; $[SbF_6]^-$	*calcd* [e]
C=O	1.2109(15) 1.2148(15)	1.205	1.266(3); 1.267(2)	1.275
$C_{C=O}{-}C_{cis}$ [a]	1.5078(18) 1.5103(14)	1.528	1.473(3); 1.481(2)	1.476
$C_{C=O}{-}C_{trans}$ [a]	1.5111(15) 1.5103(14)	1.528	1.469(3); 1.477(2)	1.470
O---F			2.560(3); 2.6043(16)	
	$O{=}C(CH_3)_2$		$[HO{=}C(CH_3)_2]^+$	
	exptl [d]	*calcd* [e]	*exptl*	*calcd* [e]
C=O	1.208(3) 1.209(3)	1.210	1.271(3) O(1)−C(2) 1.273(3) O(2)−C(5)	1.277
$C_{C=O}{-}C_{cis}$ [a]	1.478(4) 1.485(4)	1.514	1.467(3) C(2)−C(3) 1.469(4) C(5)−C(6)	1.470
$C_{C=O}{-}C_{trans}$ [a]	1.485(4) 1.486(4)	1.514	1.459(4) C(1)−C(2) 1.464(4) C(4)−C(5)	1.466
O---F			2.597(2) 2.619(2)	

[a] Refers to the carbon *cis* or *trans* to the proton on the oxygen. [b] from Ref. 11; [c] from Ref. 12; [d] from Ref. 13; [e] DFT calculations at the B3LYP/aug-cc-pVTZ level of theory.

Crystals of $[HO{=}C_{10}H_{14}][AsF_6]$, $[HO{=}C_5H_8][AsF_6]$, $[HO{=}C_5H_8][SbF_6]$, and $[HO{=}C(CH_3)_2][SbF_6]$ were grown from aHF. The crystal structures of these salts (Figures 5.2−5.4) clearly show the protonation of 2-adamantanone, cyclopentanone, and acetone. As a result of protonation of the carbonyl group, the X-ray crystal structures show an increase in the C=O bond lengths ($[HO{=}C_{10}H_{14}]^+$ 1.274(2) Å; $[HO{=}C_5H_8]^+$ 1.266(3);

$[HO{=}C(CH_3)_2]^+$ 1.271(3) and 1.273(3) Å) compared to their respective parent ketones ($O{=}C_{10}H_{14}$ 1.215(3) Å;[10] $O{=}C_5H_8$ 1.21909(15) Å;[11] $O{=}C(CH_3)_2$ 1.208(3) Å[12]) (Table 5.2). The C=O bond lengths of the protonated compounds, however, remain significantly shorter than the typical C−O single bond in an alcohol (1.432(13) Å).[13] As confirmed by DFT calculations at the B3LYP/aug-cc-pVTZ level of theory (Table 5.2), a significant decrease in the $C_{C=O}$–C bond lengths is observed for the protonated ketones ($C_{C=O}$–C_{cis}: $[HO{=}C_{10}H_{14}]^+$ 1.469(2) Å; $[HO{=}C_5H_8]^+$ 1.473(3) Å; $[HO{=}C(CH_3)_2]^+$ 1.467(3) Å) relative to the parent compounds ($O{=}C_{10}H_{14}$ 1.5176(16) Å;[10] $O{=}C_5H_8$ 1.5078(18) Å;[11] $O{=}C(CH_3)_2$ 1.478(4) Å).[12] Whereas slightly longer $C_{C=O}$–C_{cis} bonds are calculated than for the $C_{C=O}$–C_{trans} bonds, the experimental $C_{C=O}$–C bond distances in each protonated ketone are the same within 3σ.

The oxonium cations $[HO{=}C_{10}H_{14}]^+$ and $[HO{=}C_5H_8]^+$ in the $[AsF_6]^-$ salts exhibit strong hydrogen bonds to a F atom of the $[AsF_6]^-$ anion. The O---F distance in $[HO{=}C_{10}H_{14}]^+$ (O---F(1) 2.6233(16) Å) is larger than $[HO{=}C_5H_{18}]^+$ (O---F(1) 2.560(3) Å), however, both are comparable to previously reported hydrogen bonds in protonated cyclopropylcarbinyl derivates (O---F 2.557(6) and 2.601(6) Å).[2d] These hydrogen bonds result in an elongation of the As−F(1) distance and an ensuing distortion of the idealized octahedral geometry of the anion. The $[HO{=}C_5H_8][AsF_6]$ and $[HO{=}C_5H_8][SbF_6]$ salts are isostructural with cation $[HO{=}C_5H_{18}]^+$ in both salts exhibiting no difference in the C=O bond length (1.267(2) Å). The $[AsF_6]^-$ salt, however, forms stronger hydrogen-bonding interactions (O---F(1) 2.560(3) Å) than in the $[SbF_6]^-$ salt (O---F(1) 2.6043(16) Å).

Unlike $[HO{=}C_{10}H_{14}]^+$ and $[HO{=}C_5H_8]^+$, the X-ray crystal structure of $[HO{=}C(CH_3)_2][SbF_6]$ crystallized in the $P\bar{1}$ space group with two crystallographically unique cations and three different anion environments in the unit cell. One of the three

$[SbF_6]^-$ anions does not have any significant contacts with the oxonium cation, whereas the other two anions accept one or two hydrogen-bonds from $[HO{=}C(CH_3)_2]^+$ cations.

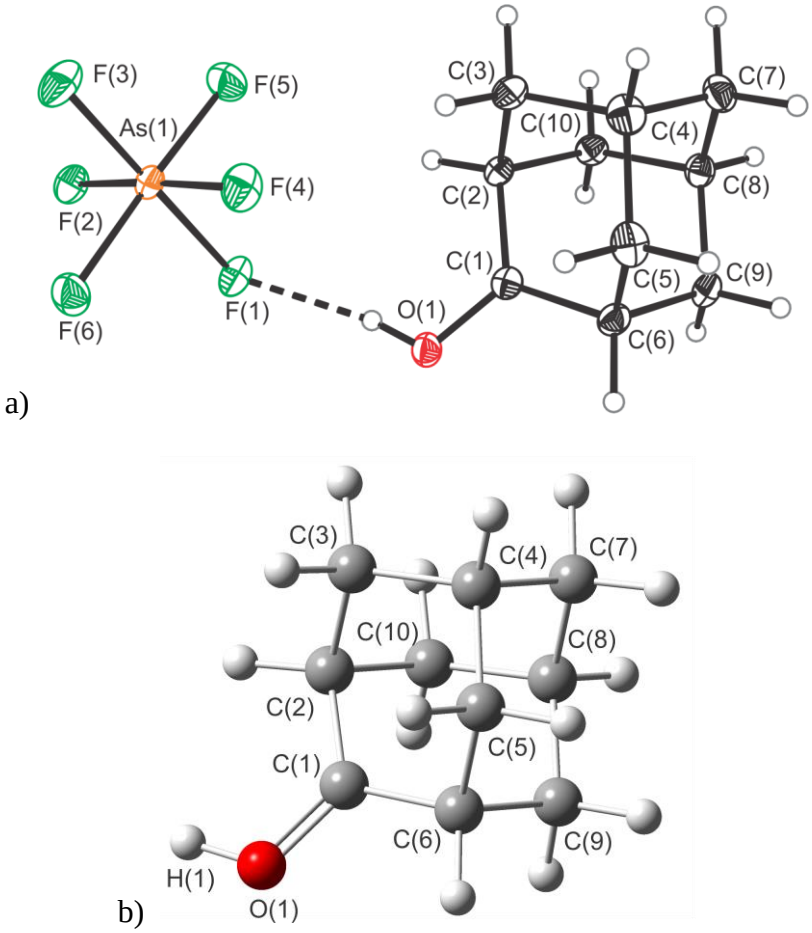

Figure 5.2 a) Thermal ellipsoid plot of $[HO{=}C_{10}H_{14}][AsF_6]$. Thermal ellipsoids are set at the 50% probability level. b) Geometry-optimized gas-phase structure of $[HO{=}C_{10}H_{14}]^+$ at the B3LYP/aug-cc-pVTZ level of theory.

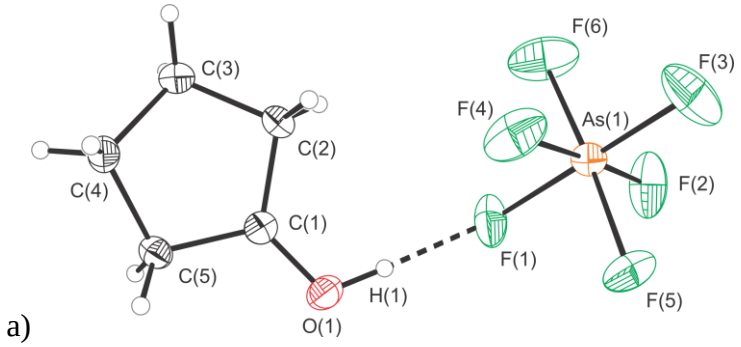

a)

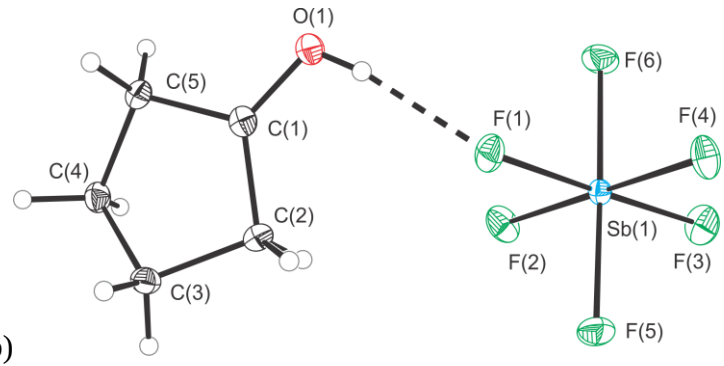

b)

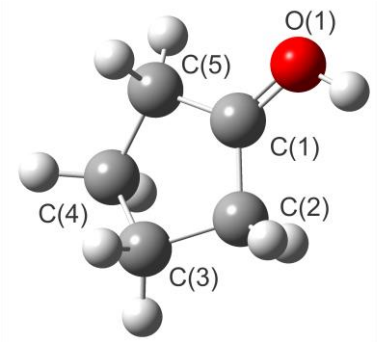

c)

Figure 5.3 Thermal ellipsoid plots of a) $[HO{=}C_5H_8][AsF_6]$, and b) $[HO{=}C_5H_8][SbF_6]$. Thermal ellipsoids are set at the 50% probability level. c) Geometry-optimized gas-phase structure of $[HO{=}C_5H_8]^+$ at the B3LYP/aug-cc-pVTZ level of theory.

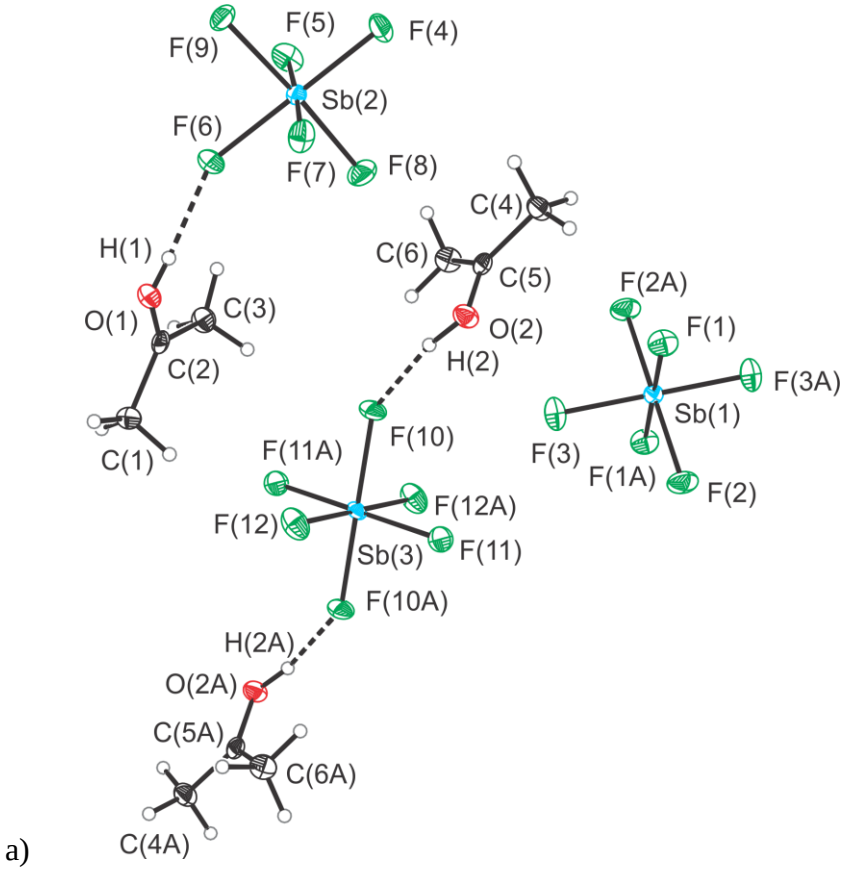

a)

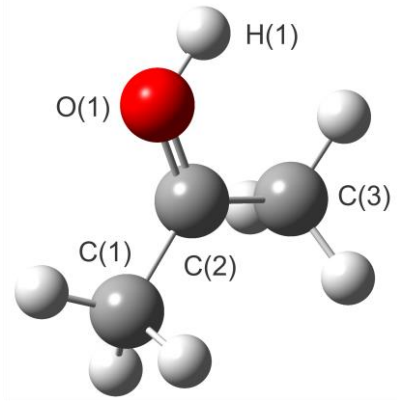

b)

Figure 5.4 Thermal ellipsoid plots of $[HO{=}C(CH_3)_2][SbF_6]$. Thermal ellipsoids are set at the 50% probability level. b) Geometry-optimized gas-phase structure of $[HO{=}C(CH_3)_2]^+$ at the B3LYP/aug-cc-pVTZ level of theory.

Crystals of $[H\{O{=}C(CH_3)_2\}_2]_3[HO{=}C(CH_3)_2]_3[SbF_6]_5F$ were grown from aHF at −60 °C and crystallized in the $P2_1/n$ space group. The asymmetric unit consists of three protonated acetone cations, three hemiprotonated acetone cations, five $[SbF_6]^-$ anions, and a fluoride anion (Figure 5.5). The $[HO{=}C(CH_3)_2]^+$ cations are each hydrogen-bonded to the fluoride anion in the centre of the asymmetric unit (O---F 2.462(3), 2.444(3), 2.443(3) Å) (see Figure 5.6). As expected, the C=O bond distances of the three $[HO{=}C(CH_3)_2]^+$ cations are longer (1.259(4), 1.255(4), 1.253(4) Å) and the C−C bonds are shorter relative to neutral acetone (Table 5.3). However, these C=O bond distances are significantly shorter than the aforementioned monoprotonated ketones by upwards of 0.021 Å. This is a result of the hydrogen bonds being stronger than those present in $[HO{=}C_{10}H_{14}][AsF_6]$, $[HO{=}C_5H_8][AsF_6]$, $[HO{=}C_5H_8][SbF_6]$, and $[HO{=}C(CH_3)_2][SbF_6]$ causing the elongation of the C=O bond to be less drastic.

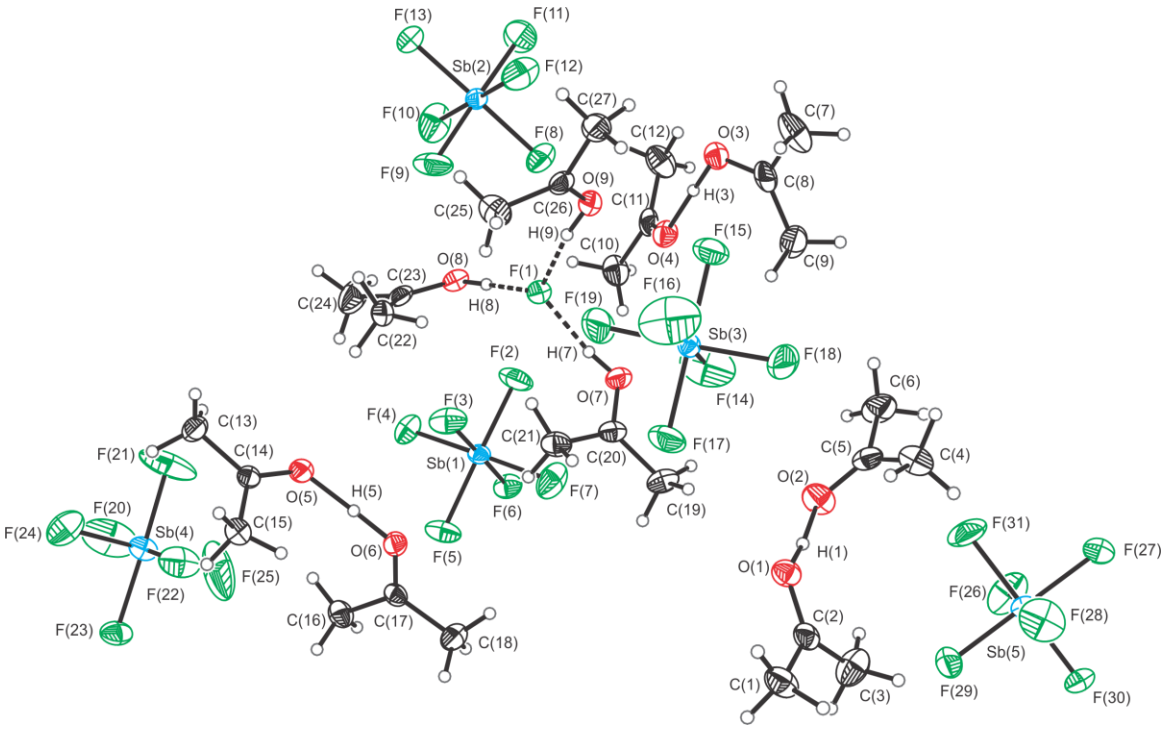

Figure 5.5 Thermal ellipsoid plots of the asymmetric unit $[H\{O{=}C(CH_3)_2\}_2]_3$ $[HO{=}C(CH_3)_2]_3[SbF_6]_5F$. Thermal ellipsoids are set at the 50% probability level.

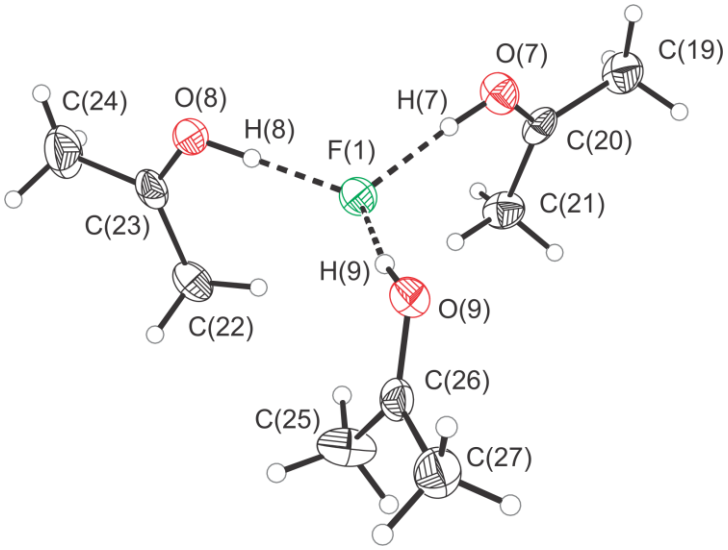

Figure 5.6 Thermal ellipsoid plots of the $[HO=C(CH_3)_2]_3F$ unit in the $[H\{O=C(CH_3)_2\}_2]_3[HO=C(CH_3)_2]_3[SbF_6]_5F$ salt. Thermal ellipsoids are set at the 50% probability level.

a)

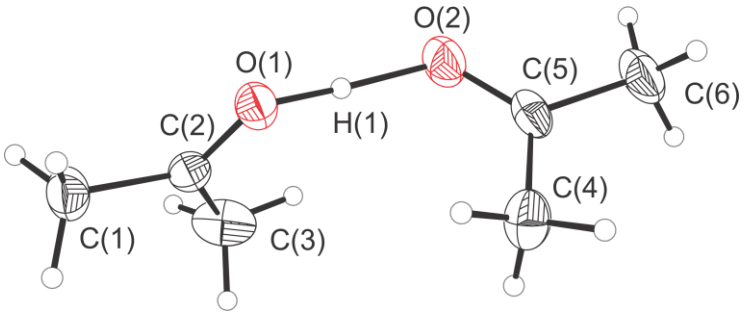

b)

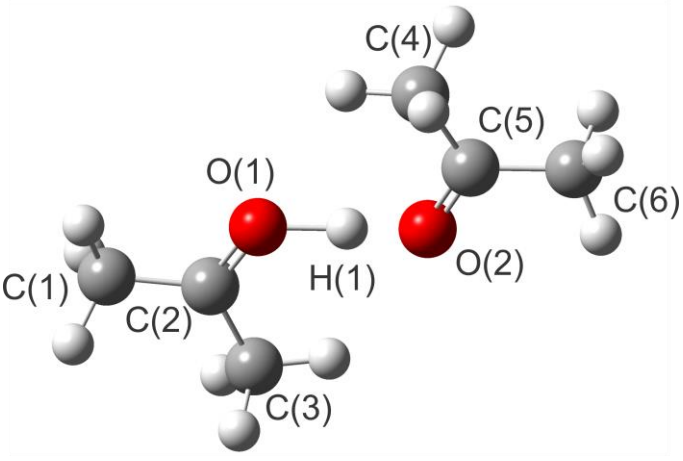

Figure 5.7 Thermal ellipsoid plots of one of three $[H\{O=C(CH_3)_2\}_2]^+$ cations in the $[H\{O=C(CH_3)_2\}_2]_3[HO=C(CH_3)_2]_3[SbF_6]_5F$ salt. Thermal ellipsoids are set at the 50% probability level.

Table 5.3 Selected Experimental and Calculated Bond Lengths (Å) of Oxonium Cations $[H\{O=C(CH_3)_2\}_2]^+$ and $[HO=C(CH_3)_2]^+$ in the $[H\{O=C(CH_3)_2\}_2]_3[HO=C(CH_3)_2]_3[SbF_6]_5F$ salt.

	$[HO=C(CH_3)_2]^+$		$[H\{O=C(CH_3)_2\}_2]^+$	
	exptl	*calcd* [b]	*exptl*	*calcd* [b]
C=O	1.259(4) O(7)=C(20) 1.255(4) O(8)=C(23) 1.253(4) O(9)=C(26)	1.277	1.236(4)−1.243(4)	1.250 1.242
$C_{C=O}-C_{cis}$ [a]	1.465(5)−1.474(5)	1.470	1.472(6)−1.486(4)	1.486 1.491
$C_{C=O}-C_{trans}$ [a]	1.468(5)−1.479(5)	1.466	1.477(5)−1.487(5)	1.482 1.487
O−H	0.84(5) O(7)−H(7) 0.91(5) O(8)−H(8) 0.89(6) O(9)−H(9)	0.98	1.13(7), 1.33(7) 1.04(6), 1.40(6) 1.09(6), 1.37(6)	1.15, 1.27
O---F(1)	2.462(3) O(7)---F(1) 2.444(3) O(8)---F(1) 2.443(3) O(9)---F(1)	--	--	--
O---O	--	--	2.450(3) O(1)---O(2) 2.437(3) O(3)---O(4) 2.450(3) O(5)---O(6)	2.423

[a] Refers to the carbon *cis* or *trans* to the proton on the oxygen; [b] DFT calculations at the B3LYP/aug-cc-pVTZ level of theory.

The three hemiprotonated acetone cations, $[H\{O=C(CH_3)_2\}_2]^+$, show two acetone molecules bridged by a proton and, unlike the monoprotonated species, have no contacts with the anions (Figure 5.7). The C=O bond distances for each species are the same within 3σ. Upon hemiprotonation, the C=O bond distances become elongated and C−C bonds contracted (Table 5.3). The calculated C=O distances of the optimized geometry for the gas-phase structure (1.250 and 1.242 Å) fall within, or just outside, the range of experimental data for the three $[H\{O=C(CH_3)_2\}_2]^+$ cations (1.236(4)−1.243(4) Å). The O−H−O moieties are asymmetric and have O---O distances (2.450(3), 2.437(3), 2.450(3) Å) comparable to the previously synthesized $[H(benzophenone)_2]^+$ (O---O 2.470(3) Å).[4] This asymmetric O−H−O bridge is replicated in the calculated structure. The calculated

O−H distances (1.15 and 1.27 Å) are slightly larger than the experimental distances likely due to packing effects in the solid state.

5.2.3 X-ray Crystallography of Hemiprotonated Aldehydes

The crystallographic paramters and details for hemiprotonated aldehydes $[H(O{=}CHC_6H_5)_2][SbF_6]$ and $[H(O{=}CHCH_3)_2][SbF_6]$ are provided in Table 5.4. A summary of selected experimental and calculated bond lengths are listed in Table 5.5. A full list experimental and calculated bond lengths and bond angles of the protonated aldehydes can be found in Appendix Tables A.2.8−A.2.11.

Table 5.4 Summary of X-ray Crystal Data and Refinement Results for Hemiprotonated Aldehydes Derived from Benzaldehyde and Acetaldehyde.

Compound	$[H(O{=}CHC_6H_5)_2][SbF_6]$	$[H(O{=}CHCH_3)_2][SbF_6]$
Empirical Formula	$C_{14}H_{13}O_2SbF_6$	$C_4H_9O_2SbF_6$
Formula Weight (g mol^{-1})	448.99	324.86
Temperature (^{o}C)	–173	–173
Wavelength (Å)	0.71073	0.71073
Crystal System	monoclinic	triclinic
Space Group	$P2_1/c$	$P\bar{1}$
a (Å)	9.2348(3)	5.5396(3)
b (Å)	10.6507(3)	8.0496(3)
c (Å)	8.2117(3)	11.6215(3)
α (deg)	90	71.882(3)
b (deg)	95.646(3)	81.277(3)
γ (deg)	90	71.389(4)
V ($Å^3$)	803.76(5)	465.98(4)
Z	2	2
μ (mm^{-1})	1.782	3.024
ρ_{calcd} (g cm^{-3})	1.855	2.315
F(000)	436	308
Crystal Size (mm^3)	0.245 × 0.162 × 0.155	0.253 × 0.182 × 0.164
Reflections Collected	19295	10877
Independent Reflections	1770	2048
Data/Restraints/Parameters	1770/0/107	2048/0/124
Goodness-of-fit on F^2	1.081	1.071
R_1, $I \geq 2\theta(I)^a$	0.0302	0.0160
wR_2 $(F^2)^b$	0.0815	0.0372
CCDC	1577978	1577977

Table 5.5 Selected Experimental and Calculated Bond Lengths (Å) of Oxonium Cations $[H(O{=}CHC_6H_5)_2]^+$ and $[H(O{=}CHCH_3)_2]^+$, as well as the Parent Aldehydes Benzaldehyde and Acetaldehyde.

	$O{=}CHC_6H_5$		$[H(O{=}CHC_6H_5)_2][SbF_6]$	
	exptl [a]	*calcd* [c]	*exptl*	*calcd* [c]
C=O	1.20936	1.208	1.248(3)	1.256, 1.246
C −C	1.47768	1.478	1.441(4)	1.423, 1.433
O−H	--	--	1.213(3)	1.140, 1.276
O---O	--	--	2.425(4)	2.415
	$O{=}CHCH_3$		$[H(O{=}CHCH_3)_2][SbF_6]$	
	exptl [b]	*calcd* [d]	*exptl*	*calcd* [d]
C=O	1.208(3)	1.205	1.239(2) C(2)−O(1) 1.232(2) C(3)−O(2)	1.240 1.233
C −C	1.514(5)	1.501	1.457(3) C(2)−C(1) 1.471(3) C(3)−C(4)	1.464 1.472
O−H	--	--	0.88(4), 1.58(4)	1.167, 1.253
O---O	--	--	2.4449(19)	2.419

[a] from Ref. 16; [b] from Ref. 17; [c] DFT calculations at the B3LYP/cc-pVTZ level of theory. [d] DFT calculations at the B3LYP/aug-cc-pVTZ level of theory.

The X-ray crystal structures of the $[SbF_6]^-$ salts of hemiprotonated aldehydes $[H(O{=}CHC_6H_5)_2][SbF_6]$ and $[H(O{=}CHCH_3)_2][SbF_6]$ reveal the hydrogen-bridged dimeric nature of the oxonium cations, which contrasts that of the monoprotonated ketones discussed in Section 5.2.2. Hydrogen-bridged dimeric cations were previously observed by X-ray crystallography for benzannelated 2-hydroxyhomotropylium[3] and $[H(O{=}CPh_2)_2]^+$ cations,[4] as well as for acetone, according to IR spectroscopy.[15] The cations $[H(O{=}CHC_6H_5)_2]^+$ and $[H(O{=}CHCH_3)_2]^+$ are isolated, having no contacts with the anions in the unit cell. In the X-ray crystal structure of $[H(O{=}CHC_6H_5)_2][SbF_6]$ (Figure 5.8), the $[H(O{=}CHC_6H_5)_2]^+$ cation is comprised of two symmetry-related hydrogen-bridged benzaldehyde molecules (O(1)−H(1) 1.213(3) Å, O(1)---O(1A) 2.425(4) Å). The previously synthesized $[H(O{=}CPh_2)_2]^+$ cation shows a similar O---O distance (2.470(3) Å)

to $[H(O{=}CHC_6H_5)_2]^+$, however, the O−H−O moiety is asymmetric in the crystal structure.[4] Upon hemiprotonation of benzaldehyde, the C=O bond distance increases ($[H(O{=}CHC_6H_5)_2]^+$ 1.248(3) Å; $O{=}CHC_6H_5$ 1.212(3) Å) and the $C_{C=O}$–C bond length decreases ($[H(O{=}CHC_6H_5)_2]^+$ 1.441(4) Å) when compared to the reported gas-phase electron diffraction data for $O{=}CHC_6H_5$ (1.479(4) Å) (Table 5.5).[16]

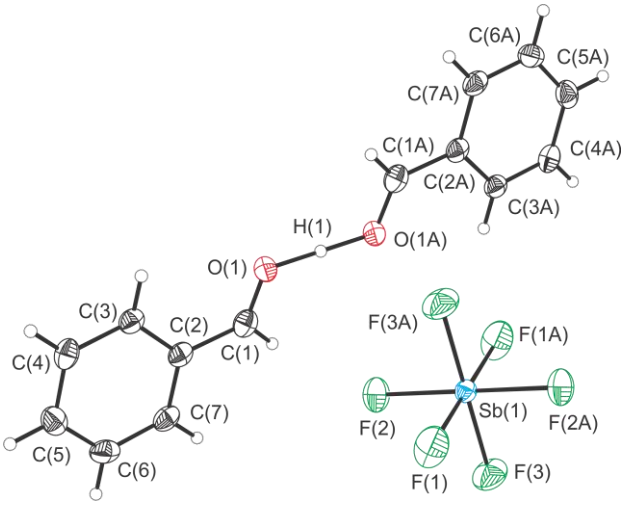

a)

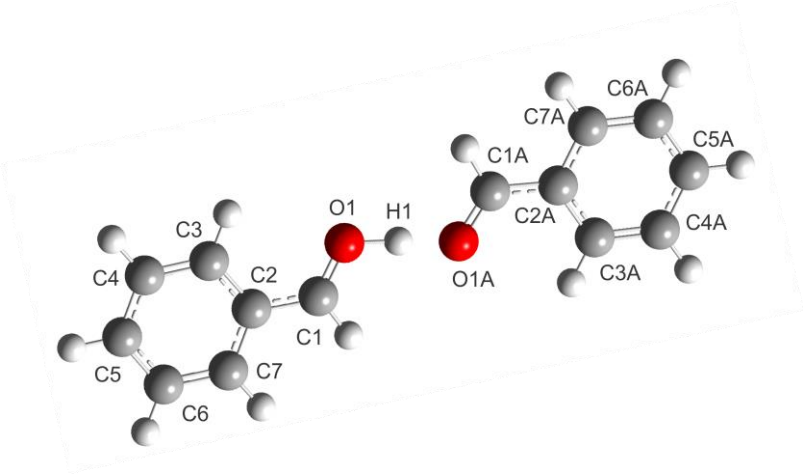

b)

Figure 5.8 a) Thermal ellipsoid plots of $[H(O{=}CHC_6H_5)_2][SbF_6]$. Thermal ellipsoids are set at the 50% probability level. b) Geometry-optimized gas-phase structure of $[H(O{=}CHC_6H_5)_2]^+$ at the B3LYP/cc-pVTZ level of theory.

Geometry optimization at the B3LYP/cc-pVTZ level of theory reproduced the planar geometry of $[H(O{=}CHC_6H_5)_2]^+$ and the *E*-configuration of the C=O−H moiety; the hydrogen-bridge is shown to be asymmetric in the gas phase, whereas the symmetric hydrogen bridge in the crystal structure is imposed by crystallographic symmetry. The calculated C=O bond distances (1.256 and 1.246 Å) compare well with the experimental value for $[H(O{=}CHC_6H_5)_2]^+$, whereas the C−C bond distances are underestimated by the calculations (by up to 0.018 Å), likely due to packing effects in the solid state.

The crystal structure of $[H(O{=}CHCH_3)_2][SbF_6]$ (Figure 5.9) contains a protonated acetaldehyde in the *Z*-configuration that is hydrogen-bonded to a second acetaldehyde molecule in an *E*-configuration. DFT calculations at the B3LYP/aug-cc-pVTZ level of theory showed the configuration of the lowest-energy gas-phase geometry of $[H(O{=}CHCH_3)_2]^+$ to be the reverse, suggesting packing effects influence the configuration in the solid state. The *Z*-geometry of the oxonium cation $[HO{=}CHCH_3]^+$ was calculated to be only 3 kJ/mol higher in energy than *E*-$[HO{=}CHCH_3]^+$ (see Figure 5.10).

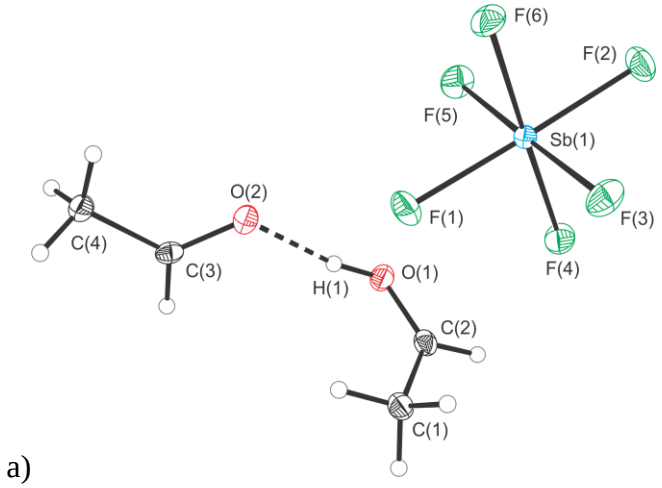

a)

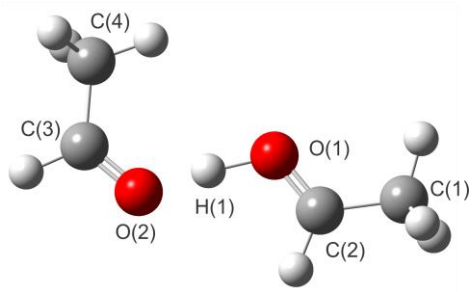

b)

Figure 5.9 a) Thermal ellipsoid plots of $[H(O{=}CHCH_3)_2][SbF_6]$. Thermal ellipsoids are set at the 50% probability level. b) Geometry-optimized gas-phase structure of $[H(O{=}CHCH_3)_2]^+$ at the B3LYP/aug-cc-pVTZ level of theory.

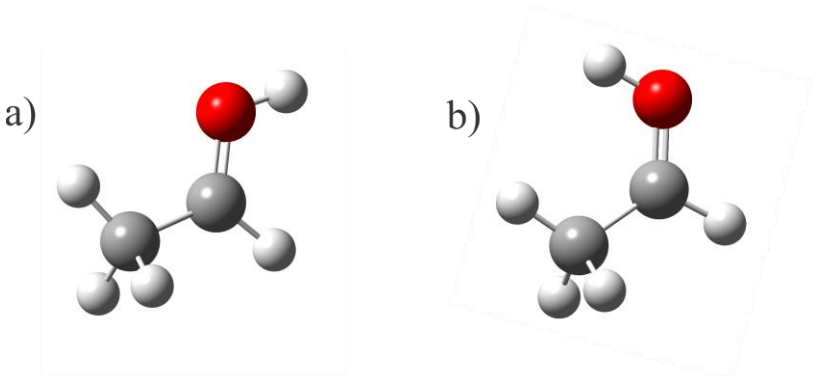

Figure 5.10 Protonated acetaldehyde, $[HO{=}CHCH_3]^+$, energies in the a) *E*-configuration, E = −404 862 kJ/mol, and b) *Z*-configuration, E = −404 859 kJ/mol. Calculations done at the B3LYP/aug-cc-pVTZ level of theory.

The hydrogen-bond in $[H(O{=}CHCH_3)_2]^+$ (O(1)---O(2) 2.4449(19) Å) is asymmetric, similar to the hydrogen-bridge observed in $[H(O{=}C(CH_3)_2)_2]^+$ (O(1)---O(2) 2.450(3) Å). However, this contrasts with the symmetric hydrogen-bridge in $[H(O{=}CHC_6H_5)_2]^+$ (2.425(4) Å) where the O---O distance is smaller and thus results in a significantly stronger bridging interaction in. Similar to the previous protonated ketones and aldehydes, the C=O bond distance decreases ($[H(O{=}CHCH_3)_2]^+$ C(2)−O(1) 1.239(2) Å; $O{=}CHCH_3$ 1.208(3) Å) and the $C_{C=O}$−C bond increases ($[H(O{=}CHCH_3)_2]^+$ C(2)−C(1) 1.457(3) Å; $O{=}CHCH_3$ 1.514(5) Å) upon protonation (Table 5.5) when compared to a previous electron diffraction study of acetaldehyde.[17] Interestingly, the second acetaldehyde in the asymmetric unit appears to be almost equally affected by the hydrogen-bridge. The small difference in C=O bond lengths in the two acetaldehyde moieties is reproduced by the geometry optimization.

5.2.4 Raman Spectroscopy of Protonated 2-Adamantanone, Cyclopentanone, Acetone, Benzaldehyde, and Acetaldehyde

The low-temperature Raman spectra of the protonated ketone and aldehyde salts (excluding $[H\{O{=}C(CH_3)_2\}_2]_3[HO{=}C(CH_3)_2]_3[SbF_6]_5F$) were recorded at −100 °C and are depicted in Figures 5.11−5.15. Vibrational frequencies of the geometry-optimized cations were calculated and used to aid in the assignments of the Raman bands. The full analysis and assignments of the Raman spectra can be found in Appendix Tables A.2.12−A.2.17.

Table 5.6 Observed and Calculated ν(CO) Frequencies (cm^{-1}) for Protonated Ketones and Aldehydes, as well as their Parent Compounds.

Compounds	exptl [a]	calcd [b]
$O=C_{10}H_{14}$	1719(13)	1779(17)[280]
$[HO=C_{10}H_{14}]^+$	1564(11)	1555(8)[184]
$O=C_5H_8$	1743(16) 1727(23)	1806(15)[264]
$[HO=C_5H_8]^+$	1605(16)	1591(9)[211]
$O=C(CH_3)_2$	1751(3) 1709(16)	1782(13)[195]
$[HO=C(CH_3)_2]^+$	1593(10) [c]	1588(4)[97]
$O=CHC_6H_5$	1698(46)	1767(113)[287] *[d]*
$[H(O=CHC_6H_5)_2]^+$	1639(66)	1712(11)[23], *[d]* 1678(125)[61] *[d]*
$O=CHCH_3$	1732sh 1712(33)	1805(13)[197]
$[H(O=CHCH_3)_2]^+$	1665(15) 1629(18)	1740(7)[117] 1715(15)[51]
$[HO=CHCH_3]^+$	1604(18)	1644(7)[137]

[a] Raman intensities, in $Å^4\,u^{-1}$, are given in parentheses. [b] DFT calculations at the B3LYP/aug-cc-pVTZ level of theory. Unscaled Raman intensities, in $Å^4\,u^{-1}$, are given in parentheses; infrared intensities, in km mol^{-1}, are given in square brackets; [c] Previous LT-IR study from Ref. 15 shows ν(CO) 1590 cm^{-1}; [d] DFT calculations at the B3LYP/cc-pVTZ level of theory.

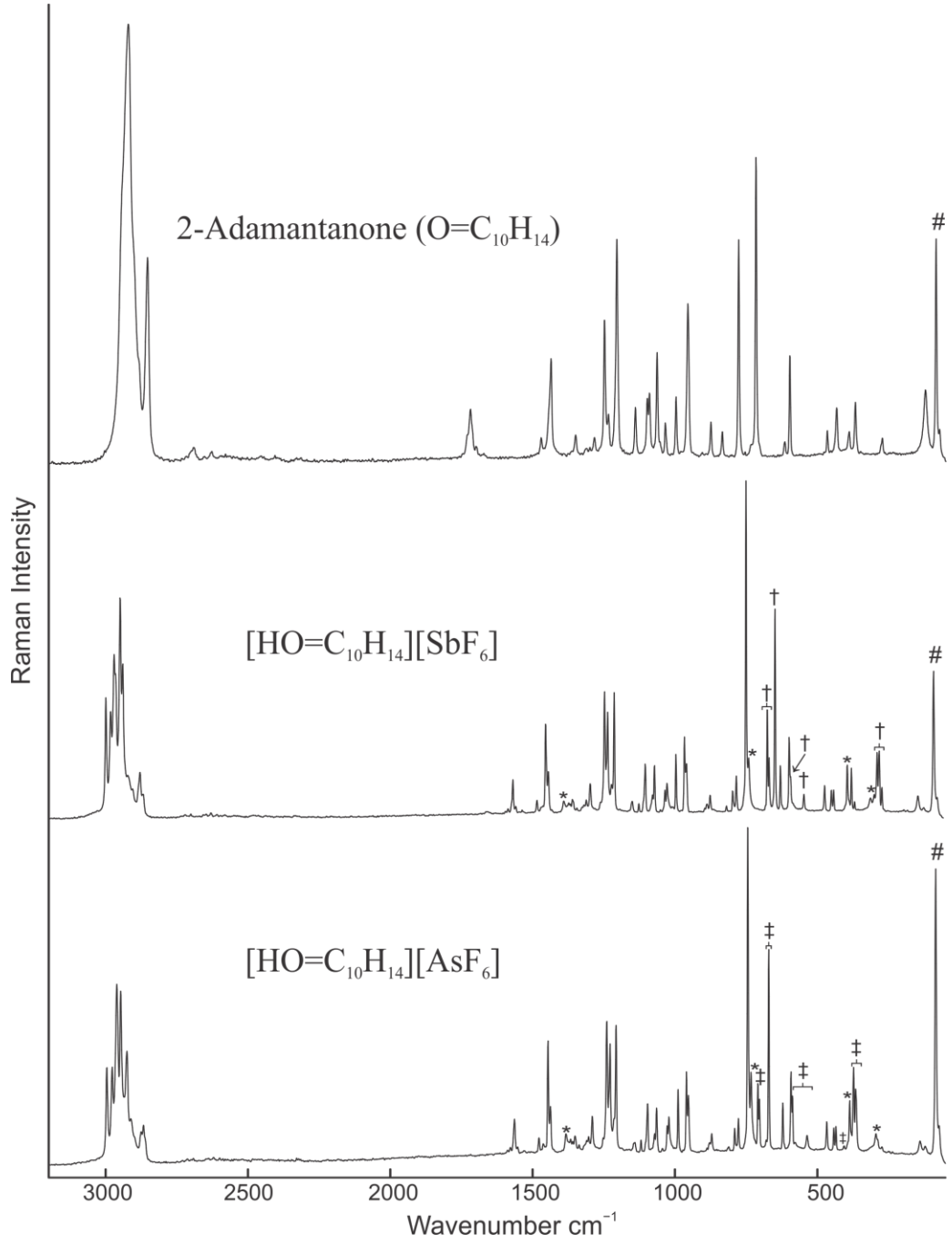

Figure 5.11 Raman spectrum of $O=C_{10}H_{14}$, $[HO=C_{10}H_{14}][SbF_6]$, and $[HO=C_{10}H_{14}][AsF_6]$ at −100 °C. Symbols denote bands arising from FEP sample tube (*), an instrumental artifact (#), $[SbF_6]^-$ vibrations (†), and $[AsF_6]^-$ vibrations (‡).

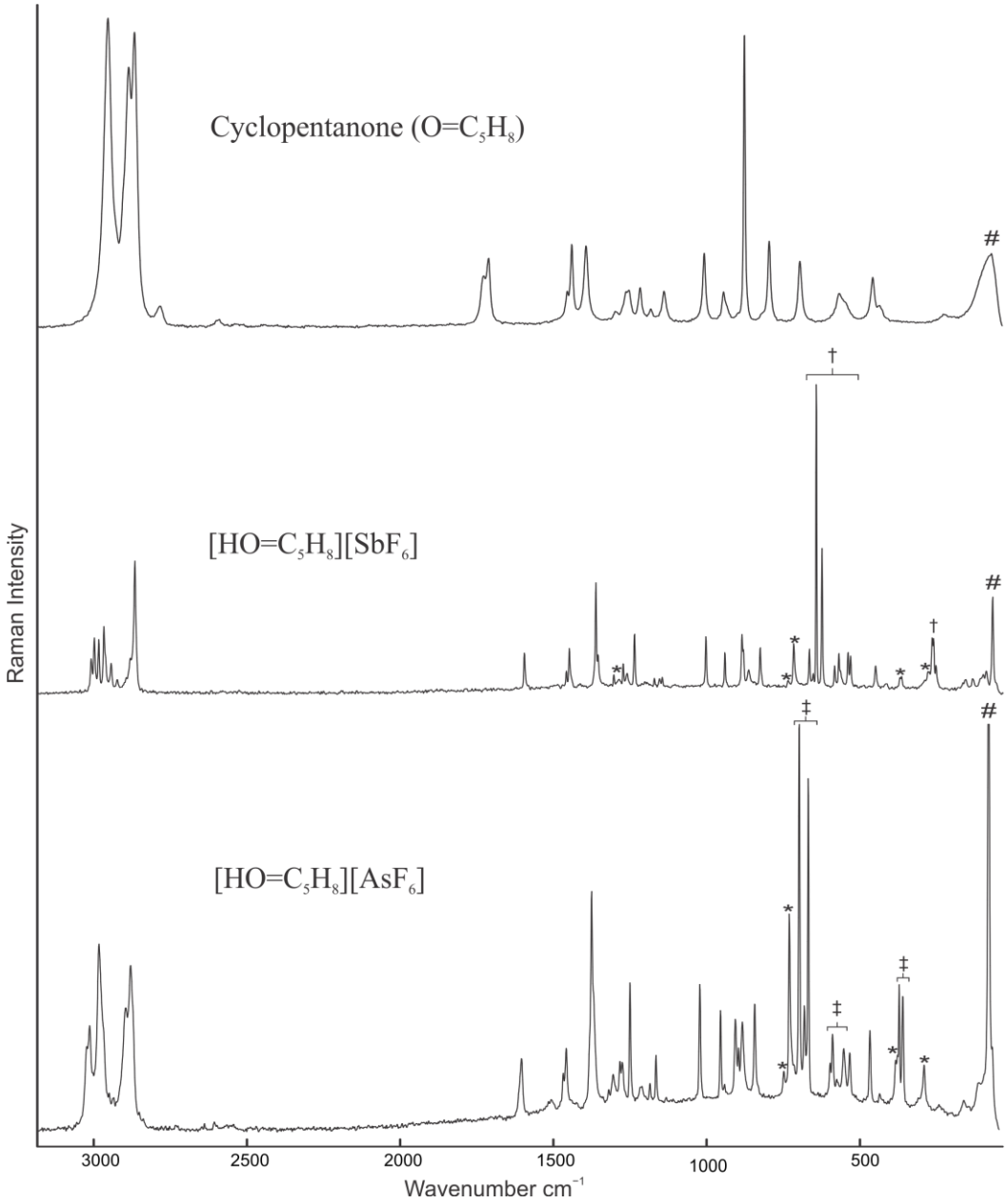

Figure 5.12 Raman spectrum of $O=C_5H_8$, $[HO=C_5H_8][SbF_6]$, and $[HxO=C_5H_8][AsF_6]$ at −100 °C. Symbols denote bands arising from FEP sample tube (*), an instrumental artifact (#), $[SbF_6]^-$ vibrations (†), and $[AsF_6]^-$ vibrations (‡).

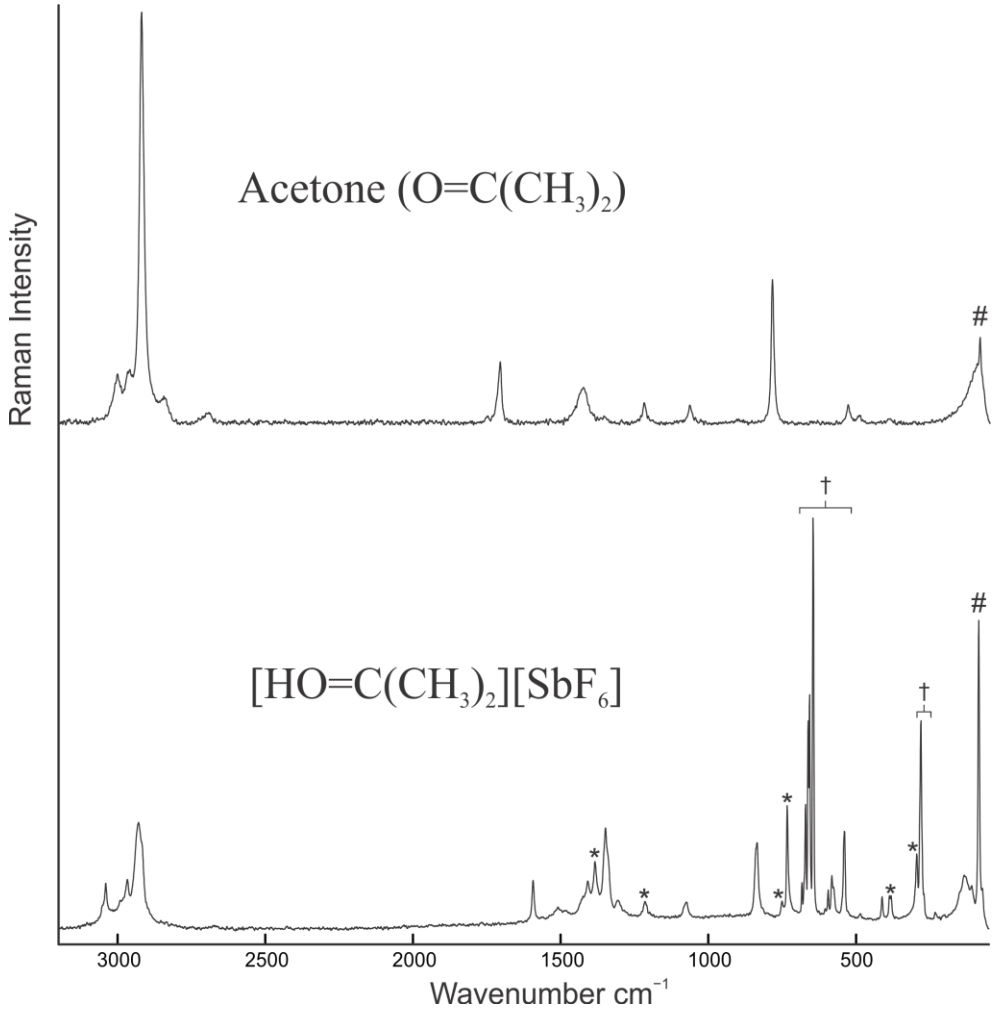

Figure 5.13 Raman spectrum of $O=C(CH_3)_2$ and $[HO=C(CH_3)_2][SbF_6]$ at −100 °C. Symbols denote bands arising from FEP sample tube (*), an instrumental artifact (#), and $[SbF_6]^-$ vibrations (†).

Protonation of the ketones and aldehydes was accompanied by a dramatic decrease in the characteristic C=O stretching frequency. A comparison of the ν(CO) stretching frequencies can be found in Table 5.6. For monoprotonated ketones $[HO=C_{10}H_{14}]^+$, $[HO=C_5H_8]^+$, and $[HO=C(CH_3)_2]^+$, the C=O stretching frequencies decreased between 116 and 155 cm^{-1} relative to the neutral parent compounds, which was in agreement with a previous LT-IR study of $[HO=C(CH_3)_2][SbF_6]$.[15] This reflects a weakening of the C=O

bond. DFT calculations at the B3LYP/aug-cc-pVTZ level of theory overestimated the decrease in the C=O stretching frequencies upon protonation (194 to 224 cm^{-1}), consistent with the absence of H-bonding in the computed gas-phase structures. Due to the high degree of splitting and coupling of the bands in the Raman spectra, trends in the ν(CCC) stretching region could not easily be determined. With the aid of DFT calculations, the ν(CCC) stretching frequency and ring breathing modes of the ketones increased upon protonation. There was an increase in the ν(CCC) stretching frequency of acetone from 788 cm^{-1} to 835 cm^{-1} upon protonating the carbonyl group. The ring breathing modes of 2-adamantanone, 717 cm^{-1}, and cyclopentanone, 811 cm^{-1}, increased upon protonating the carbonyl group to 743 and 898 cm^{-1}, respectively. This increase in frequency complimented the decrease in bond lengths of the *cis* and *trans* C−C bonds and subsequent increase in bond strength.

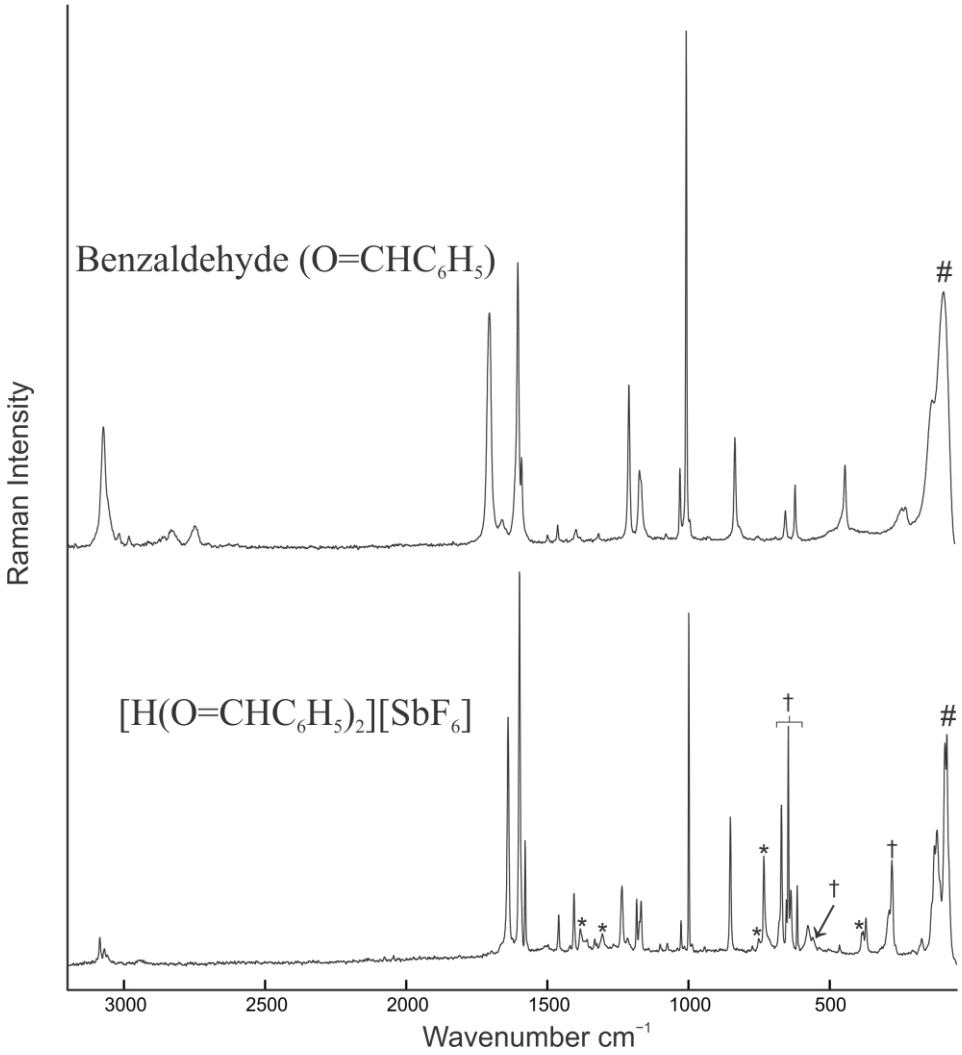

Figure 5.14 Raman spectrum of $O{=}CHC_6H_5$ and $[H(O{=}CHC_6H_5)_2][SbF_6]$ at −100 °C. Symbols denote bands arising from FEP sample tube (*), an instrumental artifact (#), and $[SbF_6]^-$ vibrations (†).

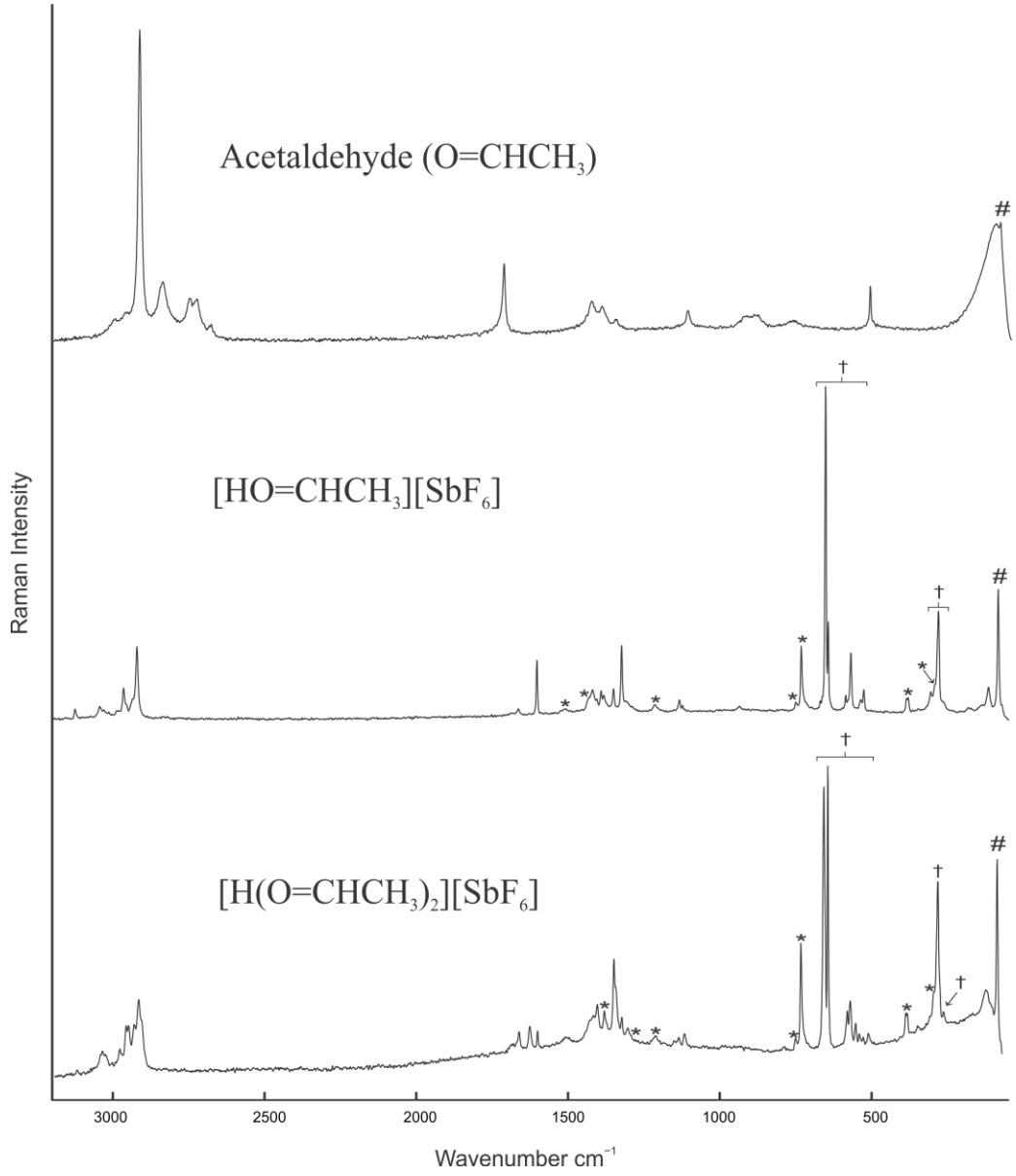

Figure 5.15 Raman spectrum of $O{=}CHCH_3$, $[HO{=}CHCH_3][SbF_6]$, and $[H(O{=}CHCH_3)_2][SbF_6]$ at −100 °C. Symbols denote bands arising from FEP sample tube (*), an instrumental artifact (#), and $[SbF_6]^-$ vibrations (†).

Unlike the protonated ketones, the C=O stretching frequency of $[H(O{=}CHC_6H_5)_2][SbF_6]$ (1639 cm^{-1}) only decreased by 59 cm^{-1} relative to $O{=}CHC_6H_5$. The Raman spectrum of $[H(O{=}CHCH_3)_2][SbF_6]$ showed two C=O stretching frequencies (1665 and 1629 cm^{-1}), which were associated with the protonated and hydrogen-bond

accepting acetaldehyde moieties, respectively, as observed in the crystal structure of $[H(O{=}CHCH_3)_2][SbF_6]$. The decrease in the C=O stretching frequency by up to 83 cm^{-1} indicates a decrease in the bond strength similar to the protonated ketones. As expected, the decrease in C=O stretching frequency was more dramatic for the monoprotonated acetaldehyde cation, $[HO{=}CHCH_3]^+$ (108 cm^{-1}), since there are no bonding interactions with a second acetaldehyde. While it is expected that the ring modes of hemiprotonated benzaldehyde and C−C stretches of acetaldehyde increased, this could not be confidently confirmed due to the high degree of coupling and splitting of the Raman bands.

5.2.5 Computational Results

Density functional theory (DFT) calculations at the B3LYP/aug-cc-pVTZ level of theory were carried out on the protonated cations previously discussed along with their parent compounds. This level of theory was chosen as it provides reliable structural information (see Chapter 2, Section 2.11 for method validation). Vibrational frequencies along with IR and Raman intensities were calculated. The DFT-optimized gas-phase geometries of the oxonium cations as well as their parent ketones, generally show excellent agreement with the experimental values (*vide supra*).

Natural bond order (NBO) analyses were carried out to investigate the bonding in these protonated ketones and aldehydes (Appendix Tables A.2.18−A.2.22). A summary of the NBO analysis is found in Table 5.7. For acetone, the Natural Population Analysis (NPA) charge on the carbonyl carbon increased from 0.59 to 0.73 when protonated, while the charge on oxygen did not change appreciably. When protonated, the C=O bond order in acetone decreased from 1.83 to 1.39, reflecting the significant weakening of the bond,

which is paralleled by the increase in C=O bond length and lowering of the C=O stretching frequency. The NPA charges of the hemiprotonated acetone cation (0.70 and 0.68) were slightly lower on the carbon of the carbonyl compared with $[HO=C(CH_3)_2]^+$. The bond order of $[H\{O=C(CH_3)_2\}_2]^+$ (1.53 and 1.58) is in between $[HO=C(CH_3)_2]^+$ and the parent compound, consistent with its slightly shorter C=O bond length. Similar trends were found for the monoprotonated cyclopentanone and 2-adamantanone systems. Protonation of cyclopentanone and 2-adamantanone resulted in an increase of the NPA charge on the carbon of the C=O group from 0.60 to 0.74 and 0.61 to 0.74, respectively. The bond order of C=O decreased from 1.84 to 1.39 for cyclopentanone and 1.83 to 1.35 for 2-adamantanone, very similar to acetone.

NBO analyses for $O=CHCH_3$, $[HO=CHCH_3]^+$, and $[H(O=CHCH_3)_2]^+$ showed the expected decrease in the C=O bond order from $O=CHCH_3$ (1.88) to protonated acetaldehyde, $[HO=CHCH_3]^+$ (1.47), with that of hemiprotonated $[H(O=CHCH_3)_2]^+$ being intermediate (1.61 and 1.65). Similarly, hemiprotonation of benzaldehyde decreased the C=O bond order from 1.82 to 1.48 and 1.54 in $[H(O=CHC_6H_5)_2]^+$. The NPA charge on the carbon of the carbonyl in acetaldehyde is 0.44 and increased to 0.53 and 0.54 in $[H(O=CHCH_3)_2]^+$ and 0.57 in $[HO=CHCH_3]^+$. The NPA charge of this carbon in the benzaldehyde system did not show as large of a difference upon hemiprotonation ($O=CHC_6H_5$ 0.41; $[H(O=CHC_6H_5)_2]^+$ 0.45 and 0.45). This may be a result of the ability of the conjugated benzene rings to delocalize the positive charge upon formation of the hemiprotonated benzaldehyde dimer cation.

Table 5.7 Selected NPA Charges, Valences and Wiberg Bond Indices of the Oxonium Cations and their Parent Compounds.

	NPA Charges (Valences [a])	NPA Charges (Valences [a])	Wiberg Bond Indices
	O	C	CO
$O{=}C_{10}H_{14}$	−0.56 (2.04)	0.61 (3.87)	1.83
$[HO{=}C_{10}H_{14}]^+$	−0.54 (2.21)	0.74 (3.72)	1.35
$O{=}C_5H_8$	−0.54 (2.06)	0.60 (3.87)	1.84
$[HO{=}C_5H_8]^+$	−0.52 (2.23)	0.74 (3.71)	1.39
$O{=}C(CH_3)_2$	−0.55 (2.04)	0.59 (3.87)	1.83
$[HO{=}C(CH_3)_2]^+$	−0.52 (2.23)	0.73 (3.71)	1.39
$[H\{O{=}C(CH_3)_2\}_2]^+$	−0.57 (2.18) −0.59 (2.13)	0.70 (3.76) 0.68 (3.77)	1.53 1.58
$O{=}CHC_6H_5$	−0.52 (2.06)	0.41 (3.85)	1.82
$[H(O{=}CHC_6H_5)_2]^+$	−0.56 (2.17) −0.57 (2.11)	0.45 (3.77) 0.45 (3.78)	1.48 1.54
$O{=}CHCH_3$	−0.52 (2.06)	0.44 (3.83)	1.88
$[HO{=}CHCH_3]^+$	−0.49 (2.26)	0.57 (3.61)	1.47
$[H(O{=}CHCH_3)_2]^+$	−0.52 (2.20) −0.55 (2.17)	0.54 (3.84) 0.53 (3.70)	1.61 1.65

[a] Sum of the Wiberg Bond Indices per atom.

Formation of these protonated ketones and aldehydes affected the shape and energy of the molecular orbitals (see Appendix Figures A.2.1−A.2.8). Using acetone as a representative example for the protonated ketones, Figure 5.14 shows the HOMO and LUMO of acetone and protonated acetone, and their corresponding energies. The energy of the LUMO was dramatically lowered from −18 kJ/mol to −189 kJ/mol, and even lower to −596 kJ/mol for hemiprotonated acetone, making the carbonyl more accessible for nucleophilic attack upon protonation (Table 5.8). This reflects the increased reactivity of protonated carbonyl compounds as proposed intermediates in acid-catalyzed reactions.

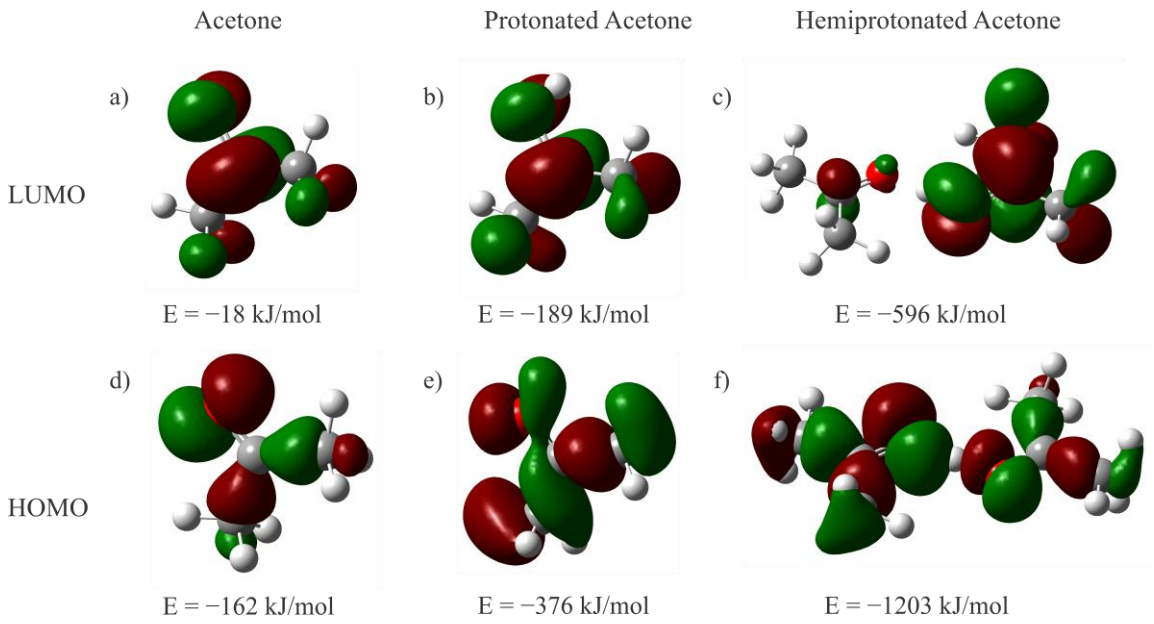

Figure 5.16 Molecular orbtials of acetone, protonated acetone, and hemiprotonated acetone. a) LUMO of acetone with E = −18 kJ/mol; b) LUMO of protonated acetone with E = −189 kJ/mol; c) LUMO of hemiprotonated acetone with E = −596 kJ/mol; d) HOMO of acetone with E = −162 kJ/mol; e) HOMO of protonated acetone with E = −376 kJ/mol; f) HOMO of hemiprotonated acetone with E = −1203 kJ/mol.

Table 5.8 Calculated Energies (kJ/mol) of the HOMO and LUMO for the Protonated Ketones, $[HO{=}C_{10}H_{14}]^+$, $[HO{=}C_5H_8]^+$, $[HO{=}C(CH_3)_2]^+$, and $[H\{O{=}C(CH_3)_2\}_2]^+$.

Compound	HOMO Energy	LUMO Energy
$O{=}C_{10}H_{14}$	−151	−13
$[HO{=}C_{10}H_{14}]^+$	−286	−163
$O{=}C_5H_8$	−157	−20
$[HO{=}C_5H_8]^+$	−323	−182
$O{=}C(CH_3)_2$	−162	−18
$[HO{=}C(CH_3)_2]^+$	−376	−189
$[H\{O{=}C(CH_3)_2\}_2]^+$	−1203	−596

A substantial decrease in the energy of the HOMO was also observed from −162 kJ/mol to −376 kJ/mol, and −1203 kJ/mol for hemiprotonated acetone, reducing the accessibility to electrophilic attack upon forming the O−H bond. A similar drop in energy of the LUMO and HOMO was observed for $[HO{=}C_{10}H_{14}]^+$ and $[HO{=}C_5H_8]^+$ cations (Table 5.8).

Table 5.9 Calculated Energies (kJ/mol) of the HOMO and LUMO for the Protonated Aldehydes, $[H(O{=}CHC_6H_5)_2]^+$, $[H(O{=}CHCH_3)_2]^+$, and $[HO{=}CHCH_3]^+$.

Compound	HOMO Energy	LUMO Energy
$O{=}CHC_6H_5$	−697	−196
$[H(O{=}CHC_6H_5)_2]^+$	−1021	−621
$O{=}CHCH_3$	−216	−157
$[HO{=}CHCH_3]^+$	−382	−201
$[H(O{=}CHCH_3)_2]^+$	−1270	−664

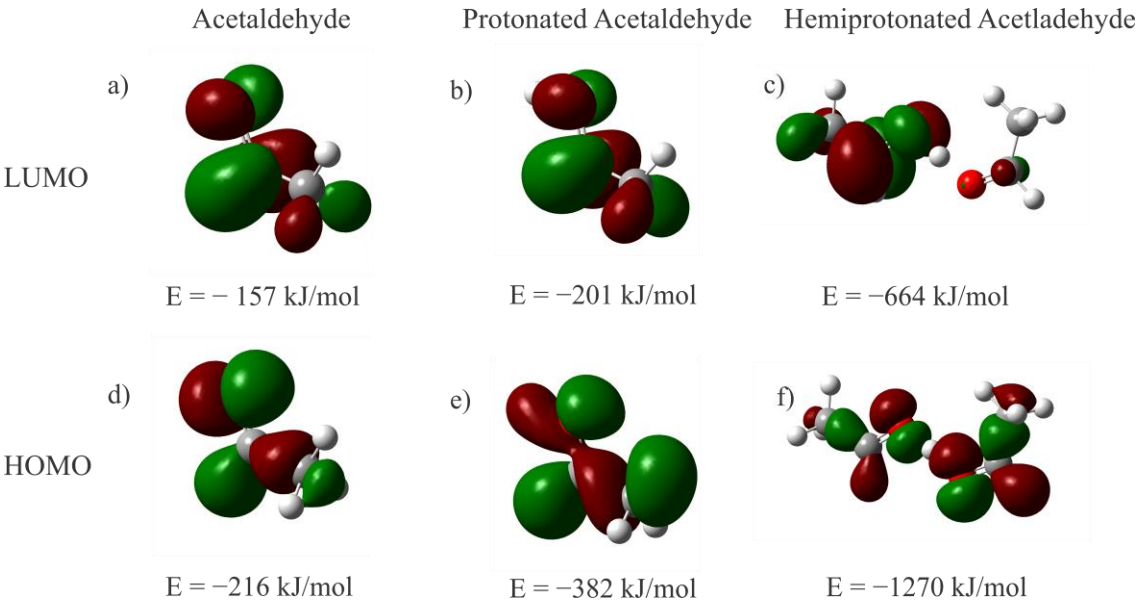

Figure 5.17 Molecular orbtials of acetaldehyde and protonated acetaldehyde. a) LUMO of acetaldehyde with E = −157 kJ/mol; b) LUMO of protonated acetaldehyde with E = −201 kJ/mol; c) LUMO of hemiprotonated acetaldehyde with E = −664 kJ/mol; d) HOMO of acetaldehyde with E = −216 kJ/mol; e) HOMO of protonated acetaldehyde with E = −382 kJ/mol; f) HOMO of hemiprotonated acetaldehyde with E = −1270 kJ/mol.

The HOMO and LUMO of acetaldehyde, protonated acetaldehyde, and hemiprotonated acetaldehyde are shown in Figure 5.14. The decrease in energy between the LUMO of acetaldehyde and protonated acetaldehyde, $[HO{=}CHCH_3]^+$, was 44 kJ/mol (Table 5.9). This change in energy was not as large when compared to the protonation of acetone where the energy difference was 171 kJ/mol. The two methyl groups in acetone

provide more steric hinderance making it less prone towards nucleophilic attack compared to acetaldehyde. This results in acetone being less reactive in acid-catalyzed reactions compared to acetaldehyde. The energy of the LUMO of hemiprotonated acetaldehyde, $[H(O{=}CHCH_3)_2]^+$ (−664 kJ/mol) was even lower compared to the monoprotonated compound (−201 kJ/mol). Despite the NPA charge of the carbon of the carbonyl group for $[H(O{=}CHCH_3)_2]^+$ being slightly lower than $[HO{=}CHCH_3]^+$ (Table 5.7), the lower LUMO energy suggests the reactivity of $[H(O{=}CHCH_3)_2]^+$ is much higher than $[HO{=}CHCH_3]^+$. Hemiprotonation of benzaldehyde also led to a large decrease in the energy of the HOMO (by 324 kJ/mol) and LUMO (by 425 kJ/mol), as expected from the previous two hemiprotonated cations.

5.3 Summary and Conclusions

In conclusion, the cations presented in this study are the first examples of representative protonated ketones and aldehydes to be isolated and structurally characterized in the solid state. Salts of $[HO{=}C_{10}H_{14}][AsF_6]$, $[HO{=}C_5H_8][AsF_6]$, $[HO{=}C_5H_8][SbF_6]$ and $[HO{=}C(CH_3)_2][SbF_6]$ were found to be stable at RT and characterized by Raman spectroscopy and single-crystal X-ray diffraction. X-ray crystallography has shown the $[HO{=}C_{10}H_{14}]^+$, $[HO{=}C_5H_8]^+$, and $[HO{=}C(CH_3)_2]^+$ cations to contain hydrogen bonds with their respective anions aiding in their thermal stability at RT. This is especially the case for the $[HO{=}C(CH_3)_2][SbF_6]$ salt which was stable for 1 h before signs of decomposition were observed by Raman spectroscopy. The protonation of these ketones resulted in an increase in the C=O bonds and decrease in the *cis* and *trans* C−C bonds relative to their parent compounds.

The X-ray crystal structure of hemiprotonated acetone was obtained for the first time. The complex salt of $[H\{O=C(CH_3)_2\}_2]_3[HO=C(CH_3)_2]_3[SbF_6]_5F$ showed two different cation environments: the isolated $[H(O=C(CH_3)_2)_2]^+$ cations and the $[HO=C(CH_3)_2]^+$ cations having hydrogen bonding interactions with a lone fluoride anion. The crystal structure revealed $[H\{O=C(CH_3)_2\}_2]^+$ to be a hydrogen-bridged dimer-like cation where the O−H−O moiety is asymmetric with O---O distances of 2.437(3) and 2.450(3) Å.

The protonated aldehydes, $[H(O=CHC_6H_5)_2]^+$, $[H(O=CHCH_3)_2]^+$, and $[HO=CHCH_3]^+$ were isolated for the first time and, unlike the monoprotonated ketones, proved to be much more temperature-sensitive, rapidly decomposing at RT. In the case of benzaldehyde, even using one molar equivalent of aldehyde versus SbF_5 resulted in the synthesis of the hemiprotonated benzaldehyde dimer. The $[H(O=CHCH_3)_2][SbF_6]$ salt could only be obtained in admixture with $[HO=CHCH_3][SbF_6]$. The crystal structure of $[H(O=CHCH_3)_2]^+$ showed a similar asymmetric hydrogen bridge to the hemiprotonated acetone with a distance of 2.4449(19) Å.

The presented experimental and computational results provide key data about a class of intermediates that are ubiquitous in acid-catalysed organic reaction mechanisms. As expected, protonation significantly increases the electrophilicity of the carbonyl carbon, as reflected by bond elongation, significant decrease in the ν(CO) stretching frequencies, as well as calculated charges, bond orders, and LUMO energies.

References

[1] (a) Olah, G. A.; White, A. M.; O'Brien, D. H. *Chem. Rev.* **1970**, *70*, 561−591. (b) Birchall, T.; Gillespie, R. J. *Can. J. Chem.* **1965**, *43*, 1045−1051. (c) Olah, G. A.; Calin, M. *J. Am. Chem. Soc.* **1968**, *90*, 938−943. (d) Olah, G. A.; O'Brien, D. H.; Calin, M. *J. Am. Chem. Soc.* **1967**, *89*, 3582−3586. (e) Olah, G. A.; O'Brien, D. H.; Calin, M. *J. Am. Chem. Soc.* **1967**, *89*, 3586−3590. (f) Olah, G. A.; Liang, G.; Mateescu, G. D. *J. Org. Chem.* **1974**, *39*, 3750−3754. (g) Olah, G. A.; Halpern, Y.; Mo, Y. K.; Liang, G. *J. Am. Chem. Soc.* **1972**, *94*, 3554−3561.

[2] (a) Childs, R. F.; Varadarajan, A.; Lock, C. J. L.; Faggiani, R.; Fyfe, C. A.; Wasylishen, R. E. *J. Am. Chem. Soc.* **1982**, *104*, 2452−2456. (b) Childs, R. F.; Faggiani, R.; Lock, C. J. L.; Mahendran, M.; Zweep, S. D. *J. Am. Chem. Soc.* **1986**, *108*, 1692−1693. (c) Chadda, S. K.; Childs, R. F.; Faggiani, R.; Lock, C. J. L. *J. Am. Chem. Soc.* **1986**, *108*, 1694−1695. (d) Childs, R. F.; Kostyk, M. D.; Lock, C. J. L.; Mahendran, M. *J. Am. Chem. Soc.* **1990**, *112*, 8912−8920.

[3] Childs, R. F.; Faggiani, R.; Lock, C. J. L.; Varadarajan, A. *Acta Crystallogr. Sect. C* **1984**, *40*, 1291−1294.

[4] Stasko, D.; Hoffmann, S. P.; Kim, K. C.; Fackler, N. L. P.; Larsen, A. S.; Drovetskaya, T.; Tham, F. S.; Reed, C. A.; Rickard, C. E. F.; Boyd, P. D. W.; Stoyanov, E. S. *J. Am. Chem. Soc.*, **2002**, *124*, 13869−13876.

[5] Chandra, A. K.; Nguyen, M. T.; Zeegers-Huyskens, T. *Chem. Phys.* **2000**, *255*, 149−163.

[6] (a) Aviyente, V.; Vernali, T. *J. Mol. Struc. (Theochem)* **1992**, *277*, 285−292. (b) Aviyente, V.; Iraqi, M.; Peres, T.; Lifshitz, C. *J. Am. Soc. Mass Spectrom.* **1991**, *2*, 113−119.

[7] Chakraborty, S.; Patzer, A.; Dopfer, O. *J. Chem. Phys.* **2010**, *133*, 044307/ 1−044307/12.

[8] Alata, I.; Omidyan, R.; Dedonder-Lardeux, C.; Broquier, M.; Jouvet, C. *Phys. Chem. Chem. Phys.* **2009**, *11*, 11479−11486.

[9] (a) Hagler, A. T.; Karpas, Z.; Klein, F. S. *J. Am. Chem. Soc.* **1979**, *101*, 2191−2196. (b) Tzeng, W. B.; Wei, S.; Castleman Jr., A. W. *Chem. Phys. Lett.* **1990**, *168*, 30−36.

[10] Minkwitz, R.; Schneider, S.; Preut, H. *Angew. Chem. Int. Ed.* **1998**, *37*, 494−496.

[11] Amoureux, J. P.; Bee, M. *J. Phys. C.* **1980**, *13*, 3577−3583.

[12] Yufit, D. S.; Howard, J. A. K. *Acta. Crystallogr. Sect. C* **2011**, *67*, 104−106.

[13] Allan, D. R.; Clark, S. J.; Ibberson, R. M.; Parsons, S.; Pulham, C. R.; Sawyer, L. *Chem. Commun.* **1999**, 751−752.

[14] Allen, F. H.; Kennard, O.; Watson, D. G.; Brammer, L.; Orpen, A. G.; Taylor, R. in *International Tables for Crystallography, Vol.* C (Eds.: A. J. C. Wilson), Kluwer Academic, Dordrecht, **2006**, pp. 685–706.

[15] Huong, P. V.; Noel, G. *Spectrochim. Acta, Part A*, **1976**, *32A*, 831–835.

[16] Kato, C.; Konaka, S.; Iijima, T.; Kimura, M. *Bull. Chem. Soc. Jpn.* **1969**, *42*, 2148−2158.

[17] Borisenko, K. B.; Bock, C. W.; Hargittai, I. *J. Phys. Chem.* **1996**, *100*, 7426−7434.

[18] Smith, J. G. *Organic Chemistry*, 3rd ed.; The McGraw-Hill Companies: New York, 2011.

6. Lewis Acid-Base Adducts of Ketones with AsF_5

6.1 Introduction

Lewis acids are commonly used, mostly as catalysts, in a variety of organic chemistry reactions including Friedel-Crafts (Equation 6.1), Diels-Alder (Equation 6.2), Hosomi-Sakurai (Equation 6.3), and Mukaiyama aldol reactions (Equation 6.4).[1]

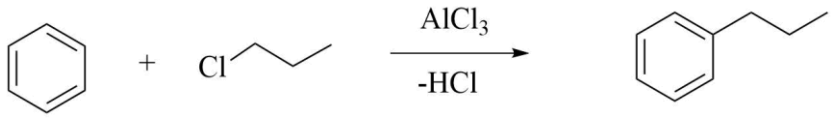

(6.1)

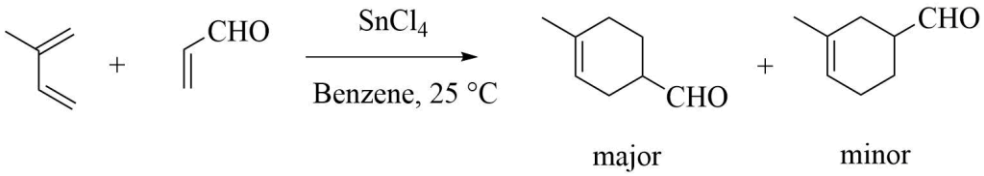

(6.2)

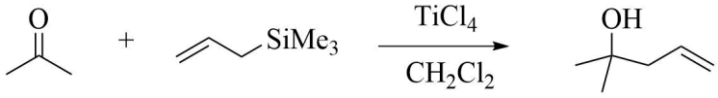

(6.3)

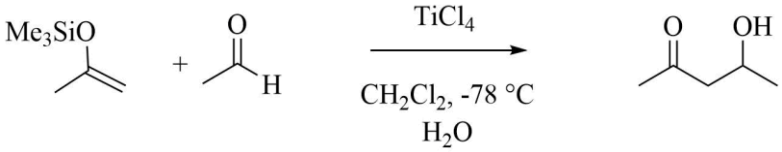

(6.4)

Lewis acid reagents used in organic chemistry include the readily available $AlCl_3$, $TiCl_4$, BF_3, and $SnCl_4$.[2] The mechanism involves the binding of the Lewis acid to a Lewis basic substrate, for example a ketone or aldehyde, which is accompanied by withdrawal of electron density from the functional group, such as the C=O group. This lowers the energy of the LUMO making the carbon center more readily accessible for nucleophilic attack.[3] The reaction mechanism of the Hosomi-Sakurai reaction is shown as an example in Scheme

6.1 where the Lewis acid $TiCl_4$ activates the electrophile allowing for allylation by allyltrimethylsilane.[4]

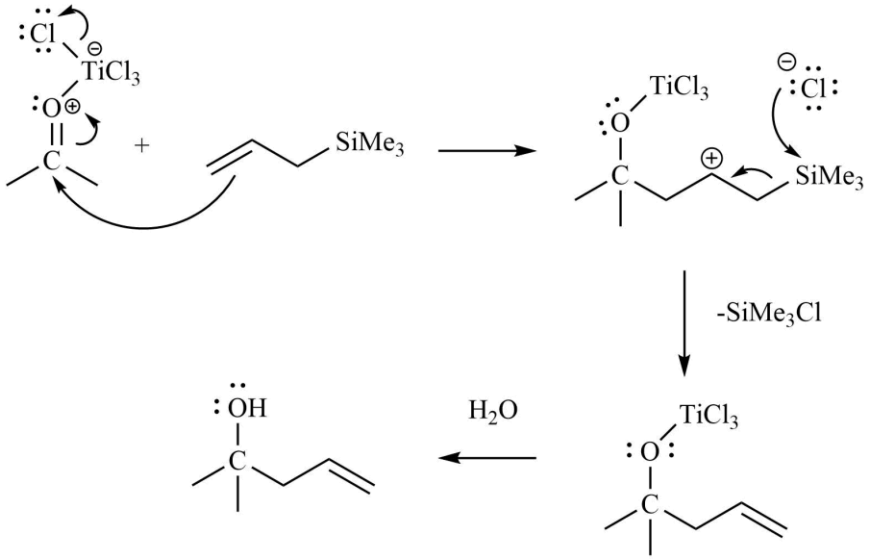

Scheme 6.1 The reaction mechanism of a Hosomi-Sakurai reaction activated by the Lewis acid $TiCl_4$.

Early IR spectroscopy studies of the $AlCl_3{\cdot}O{=}CCl_2$ adduct showed a decrease of 173 cm^{-1} in the C=O stretching frequency upon adduct formation, which is indicative of an oxygen-bridged coordination complex as opposed to the formation of the ionic structure $[ClCO][AlCl_4]$.[5] The relatively low Lewis basicity of neutral, organic oxygen bases results in a low stability of the adduct, and, in the case of $AlCl_3{\cdot}O{=}CCl_2$, full dissociation occurred under ambient conditions.[5,6] Only a few X-ray crystallography studies have been carried out on main-group Lewis acid-base adducts with carbonyl compounds.[7] One crystal structure shows the $BF_3{\cdot}$benzaldehyde adduct with a B---O interaction of 1.59 Å in an *E*-configuration (Figure 6.1).[3] Semi-empirical MNDO (Modified Neglect of Diatomic Overlap) calculations of the $BF_3{\cdot}O{=}CHCH_3$ adduct also showed the *E*-configuration to be more favourable over the *Z*-configuration by 7.5 kJ/mol.[3] A ^{13}C NMR spectroscopy study

of Lewis acid-base adducts between BF_3 and various aliphatic ketones, such as acetone and cyclopentanone, showed the ^{13}C resonances of the α-carbons to shift to higher frequencies by 24.3 and 26.2 ppm, respectively.[8] A crystallographic study of 1:1 $AlCl_3$·tetramethylurea showed the existence of an Al---O interaction with an Al−O distance of 1.78 Å and an Al−O−C angle of 132.5°.[9]

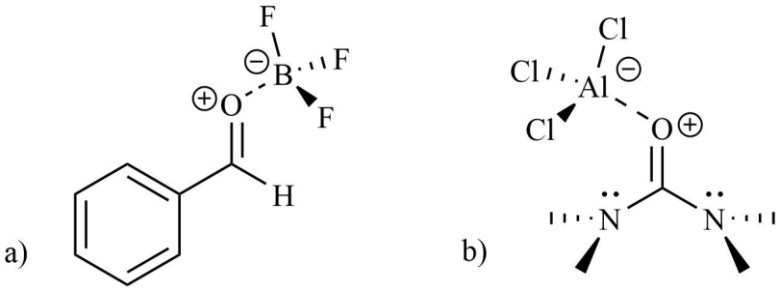

Figure 6.1 Structures of (a) the *E*-configuration of the adduct between BF_3 and benzaldehyde and (b) the adduct between $AlCl_3$ and tetramethylurea.

The 1:1 adducts of $O{=}CCl_2$, O=CClF, and $O{=}CF_2$ with the strong Lewis acids, AsF_5 and SbF_5, were synthesized and also found to dissociate at ambient temperature.[6] Vibrational and multinuclear NMR spectroscopies were used to characterize these Lewis acid-base adducts at low temperatures. Upon adduct formation, the ν(CO) stretching frequencies significantly decreased by upwards of 240 cm^{-1} ($O{=}CCl_2$) and 199 cm^{-1} (O=CClF). Geometries were optimized in the gas-phase at the B3LYP/SBK+(d) level of theory and the calculated energies were used to determine the relative stability amongst the carbonyl halide adducts with AsF_5 and SbF_5. The $SbF_5{\cdot}O{=}CCl_2$ adduct was determined to be the most stable. Passmore and co-workers were able to synthesize the 1:1 adduct of $O{=}CF_2$ with AsF_5 and SbF_5 in both the liquid and solid states.[10] Low-temperature Raman spectroscopy showed a decrease of 118 and 136 cm^{-1} in the C=O stretching frequency upon

formation of the oxygen-bridged adducts $AsF_5 \cdot O{=}CF_2$ and $SbF_5 \cdot O{=}CF_2$, respectively, compared to their respective free ketones. Dissociation occurred upon warming to RT, however, in all cases the reactions were found to be reversible.

Matrix-isolation studies have shown ketones, including acetone, cyclopentanone, and adamantanone, to form complexes with SbF_5. Vibrational spectroscopy, complimented with semi-empirical and *ab initio* calculations, showed decreases in the characteristic C=O stretching frequencies.[11] Adducts of dimethyl ether and dimethyl peroxide with AsF_5 were synthesized in the solid state and characterized by Raman spectroscopy.[12] Only the stability of $AsF_5 \cdot CH_3OOCH_3$ was reported and decomposition occurred at −30 °C.

A series of 1:1 S=O---MF_5 (M = As, Sb) coordination complexes have been studied by Raman and NMR spectroscopy including adducts of SO_2, SOF_2, and SO_2F_2.[10] The $\nu(SO)/\nu_s(SO)$ frequencies decreased by values ranging from 26 cm^{-1} ($AsF_5 \cdot SO_2F_2$) to 141 cm^{-1} ($SbF_5 \cdot SOF_2$). Minkwitz et al. synthesized the $MF_5 \cdot O{=}SClCH_3$ (M = As, Sb) adducts by reaction of $O{=}SClCH_3$ with MF_5 in aHF at −70 °C (Equation 6.5).[13] These compounds were found to be stable towards dissociation below −20 °C and were characterized by Raman and ^1H and ^{13}C NMR spectroscopy. This same study also reported the X-ray crystal structure of $SbCl_5 \cdot O{=}SClCH_3$ which was obtained by reaction of $SbCl_5$ with $O{=}SClCH_3$. Despite using a superacidic medium, HF/MF_5, protonation of the S=O bond was reportedly not observed.

$$O{=}SClCH_3 \; + \; MF_5 \xrightarrow{\text{aHF}} MF_5 \bullet O{=}SClCH_3 \qquad (M = As, Sb) \tag{6.5}$$

The interaction of strong Lewis acids, such as AsF_5 and SbF_5, with weak Lewis bases, such as oxygen containing molecules, has been relatively unexplored. One of the first oxygen-base adducts to AsF_5 to be synthesized was $AsF_5 \cdot O(CH_3)_2$ and was

characterized by ^{1}H and ^{19}F NMR spectroscopy.[14] Two ^{19}F resonances at −86 (axial fluorine atom) and −61 ppm (equatorial fluorine atoms on As) were observed as a result of the adopted octahedral geometry about As upon formation of the $AsF_5 \cdot O(CH_3)_2$ adduct. Due to the quadrupole relaxation of the arsenic nucleus, the fluorine resonance lines were broadened to the point where no fluorine-fluorine spin coupling was observed. However, the quadrupolar relaxation of ^{75}As was not rapid enough to cause complete self-decoupling that would result in sharp ^{19}F signals. Since $N(CH_3)_3$ is a stronger base than $O(CH_3)_2$, the electric field gradient about ^{75}As in $AsF_5 \cdot N(CH_3)_3$ is smaller and quadrupolar relaxation is slower. As a consequence, equal-intensity quartet splitting of the resonances at −74.8 and −67.4 ppm were observed in the ^{19}F NMR spectrum arising from $^{1}J(^{75}As–^{19}F)$ coupling of 840 and 1048 Hz, respectively. Doublet (−67.4 ppm) and quintet (−74.8 ppm) splittings arising from the $^{2}J(^{19}F–^{19}F)$ coupling of 120 Hz were also discerned.

6.2 Results and Discussion

6.2.1 Synthesis and Properties of Lewis Acid-Base Adducts of Acetone, Cyclopentanone, and 2-Adamantanone with AsF_5

During the studies of Lewis acid-base interactions between $[SF_3][AsF_6]$ and ketones (see Chapter 4), one of the decomposition products observed in the ^{19}F NMR spectra upon warming above −40 °C was a 1:1 adduct between the neutral ketone and AsF_5 (Equation 6.6).

$$[SF_3 \bullet O{=}R][AsF_6] \longrightarrow SF_4 + AsF_5 \bullet O{=}R \quad (R = C(CH_3)_2,\ C_5H_8,\ C_{10}H_{14}) \qquad (6.6)$$

As before, the ketones chosen for this study were acetone, an aliphatic compound, cyclopentanone, a monocyclic compound, and 2-adamantanone, a polycyclic compound (Figure 6.2).

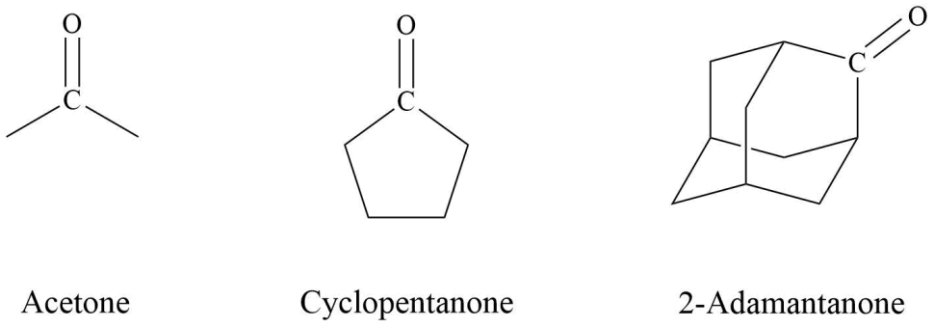

Acetone Cyclopentanone 2-Adamantanone

Figure 6.2 Structures of the ketones used to form adducts with AsF_5.

Targeted reactions were performed where a known amount of acetone, cyclopentanone, or 2-adamantanone was dissolved in SO_2 at RT. A stoichiometric amount of AsF_5 was added to the solution and the reactions were allowed to proceed at −78 °C. Dichloromethane was also a suitable solvent for reactions with 2-adamantanone and cyclopentanone. Using CH_2Cl_2 resulted in instantaneous reactions forming an insoluble fine, white powder, while using SO_2 resulted in a clear, colourless solution. Removing the solvent at −78 °C yielded white powders identified by LT Raman spectroscopy as the 1:1 adducts of $AsF_5 \cdot O{=}R$ (Equation 6.7). Crystal growth of these adducts from SO_2 and CH_2Cl_2 was unsuccessful.

$$O{=}R + AsF_5 \xrightarrow{SO_2 \text{ or } CH_2Cl_2} AsF_5 \bullet O{=}R \quad (R = C(CH_3)_2,\ C_5H_8,\ C_{10}H_{14}) \tag{6.7}$$

Upon warming the solid $AsF_5 \cdot O{=}C(CH_3)_2$ adduct to RT, the sample quickly decomposed into a dark yellow powder unidentifiable by Raman spectroscopy due to

significant fluorescence. The $AsF_5{\cdot}O{=}C_5H_8$ and $AsF_5{\cdot}O{=}C_{10}H_{14}$ adducts were stable at RT for roughly 1 h before the samples began turning light brown in colour. While LT Raman spectroscopy showed fluorescence in the baseline, some Raman bands attributable to the adducts were still observed. After two days the $AsF_5{\cdot}O{=}C_5H_8$ and $AsF_5{\cdot}O{=}C_{10}H_{14}$ adducts were of grey colour and unidentifiable by Raman spectroscopy due to a large fluorescence.

These adducts were also characterized in solution using ^{1}H and ^{19}F NMR spectroscopy at −70 °C in SO_2 and were found to be stable at RT in solution, even after 40 min. A colour change was observed for the $AsF_5{\cdot}O{=}C(CH_3)_2$ adduct in SO_2 to yellow, most likely as a result of some acetone undergoing redox chemistry due to the presence of excess AsF_5 in solution. The $AsF_5{\cdot}O{=}C_5H_8$, and $AsF_5{\cdot}O{=}C_{10}H_{14}$ compounds were stable and did not show any colour change upon warming to RT.

6.2.2 Raman Spectroscopy

The Raman spectra of $AsF_5{\cdot}O{=}C(CH_3)_2$, $AsF_5{\cdot}O{=}C_5H_8$, and $AsF_5{\cdot}O{=}C_{10}H_{14}$ were recorded at −100 °C and are depicted in Figures 6.3−6.5. Vibrational frequencies of the geometry-optimized compounds were calculated and used to aid in the assignments of the Raman bands. The complete list of experimental and calculated vibrational bands can be found in Appendix Tables A.3.4−A.3.6.

Table 6.1 Observed and Calculated ν(CO) Frequencies (cm^{-1}) for $AsF_5 \cdot O=C(CH_3)_2$, $AsF_5 \cdot O=C_5H_8$, and $AsF_5 \cdot O=C_{10}H_{14}$, as well as their Free Ketones.

Compounds	exptl [a]	calcd [b]
$O=C(CH_3)_2$	1751(3) 1709(16)	1782(13)[195]
$AsF_5 \cdot O=C(CH_3)_2$	1592(2)	1683(5)[344]
$SbF_5 \cdot O=C(CH_3)_2$	1590 [d]	--
$O=C_5H_8$	1743(16) 1727(23)	1806(15)[264]
$AsF_5 \cdot O=C_5H_8$	1620(6) 1604(2)	1706(4)[422][c]
$SbF_5 \cdot O=C_5H_8$	1610 [d]	--
$O=C_{10}H_{14}$	1719(13)	1779(17)[280]
$AsF_5 \cdot O=C_{10}H_{14}$	1577(6) 1568(9) 1553(3)	1668(7)[513][c]
$SbF_5 \cdot O=C_{10}H_{14}$	1550 [d]	--

[a] Raman intensities are given in parentheses. [b] DFT calculations at the B3LYP/aug-cc-pVTZ level of theory. Unscaled Raman intensities are given in parentheses; infrared intensities are given in square brackets; [c] DFT calculations at the B3LYP/cc-pVTZ level of theory. [d] matrix-isolation study from reference 11.

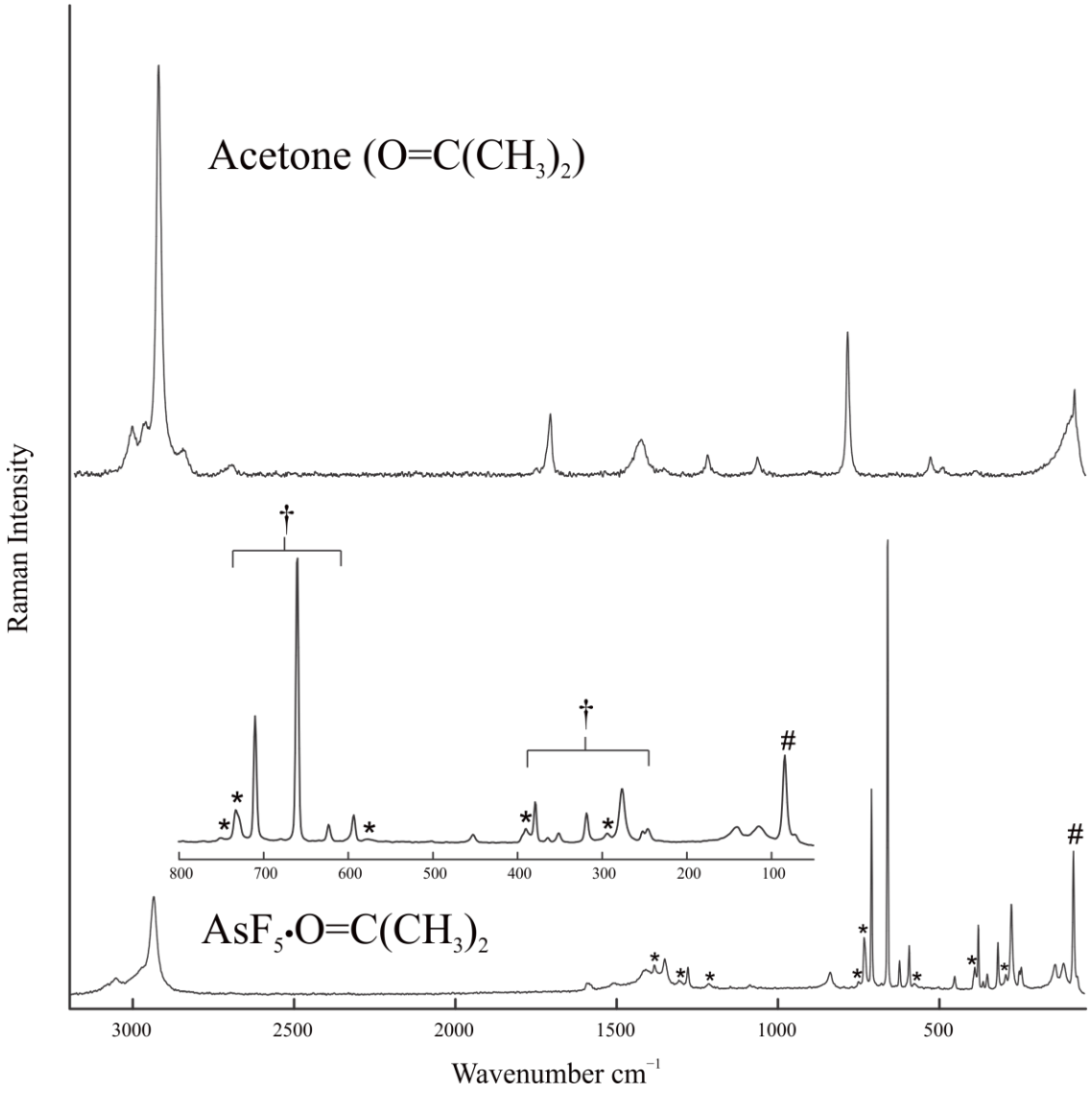

Figure 6.3 Raman spectrum of $O=C(CH_3)_2$ and $AsF_5 \cdot O=C(CH_3)_2$ at −100 °C. Symbols denote bands arising from FEP sample tube (*), an instrumental artifact (#), and the AsF_5 vibrations (†).

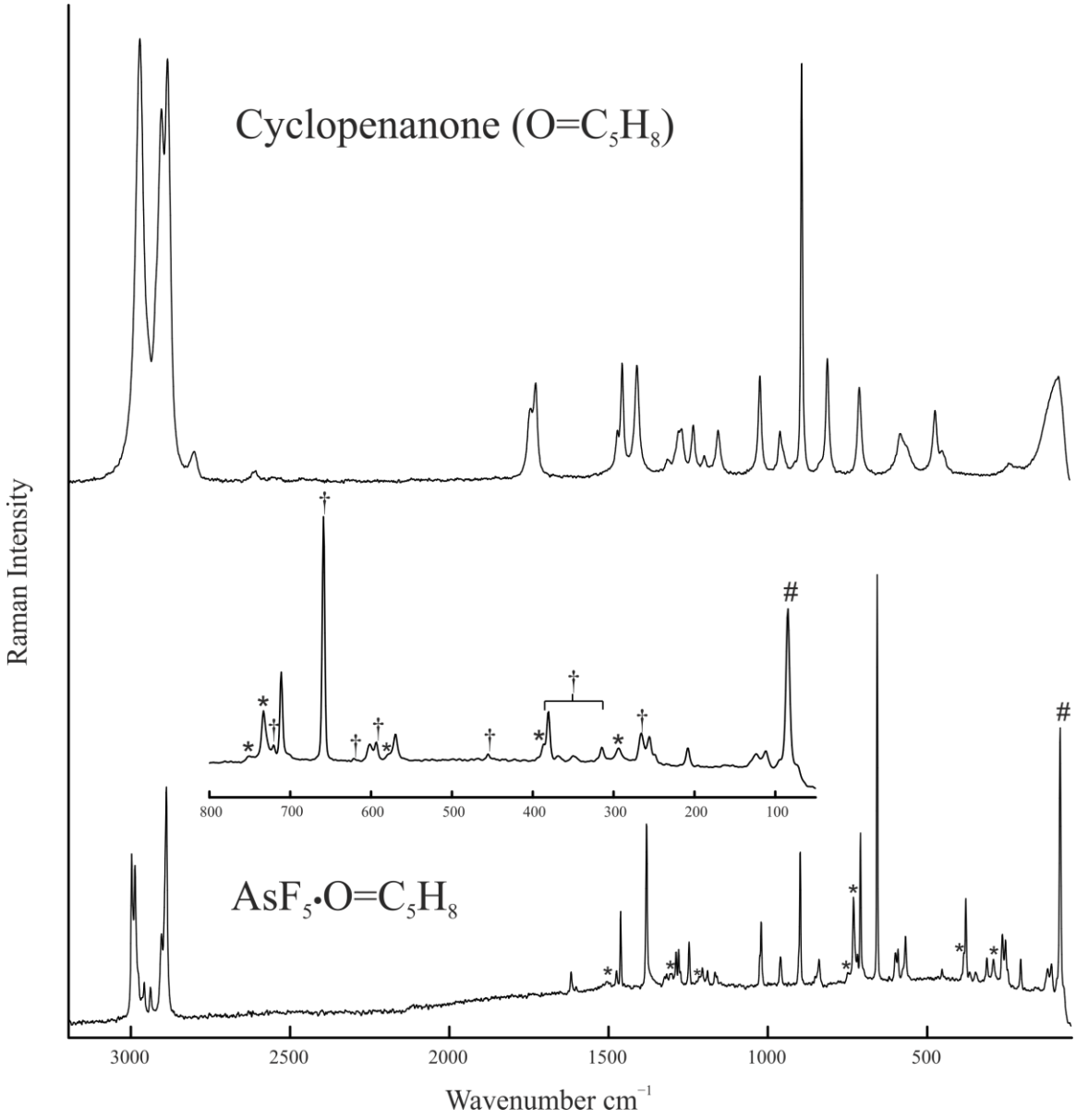

Figure 6.4 Raman spectrum of $O=C_5H_8$ and $AsF_5 \cdot O=C_5H_8$ at −100 °C. Symbols denote bands arising from FEP sample tube (*), an instrumental artifact (#), and the AsF_5 vibrations (†).

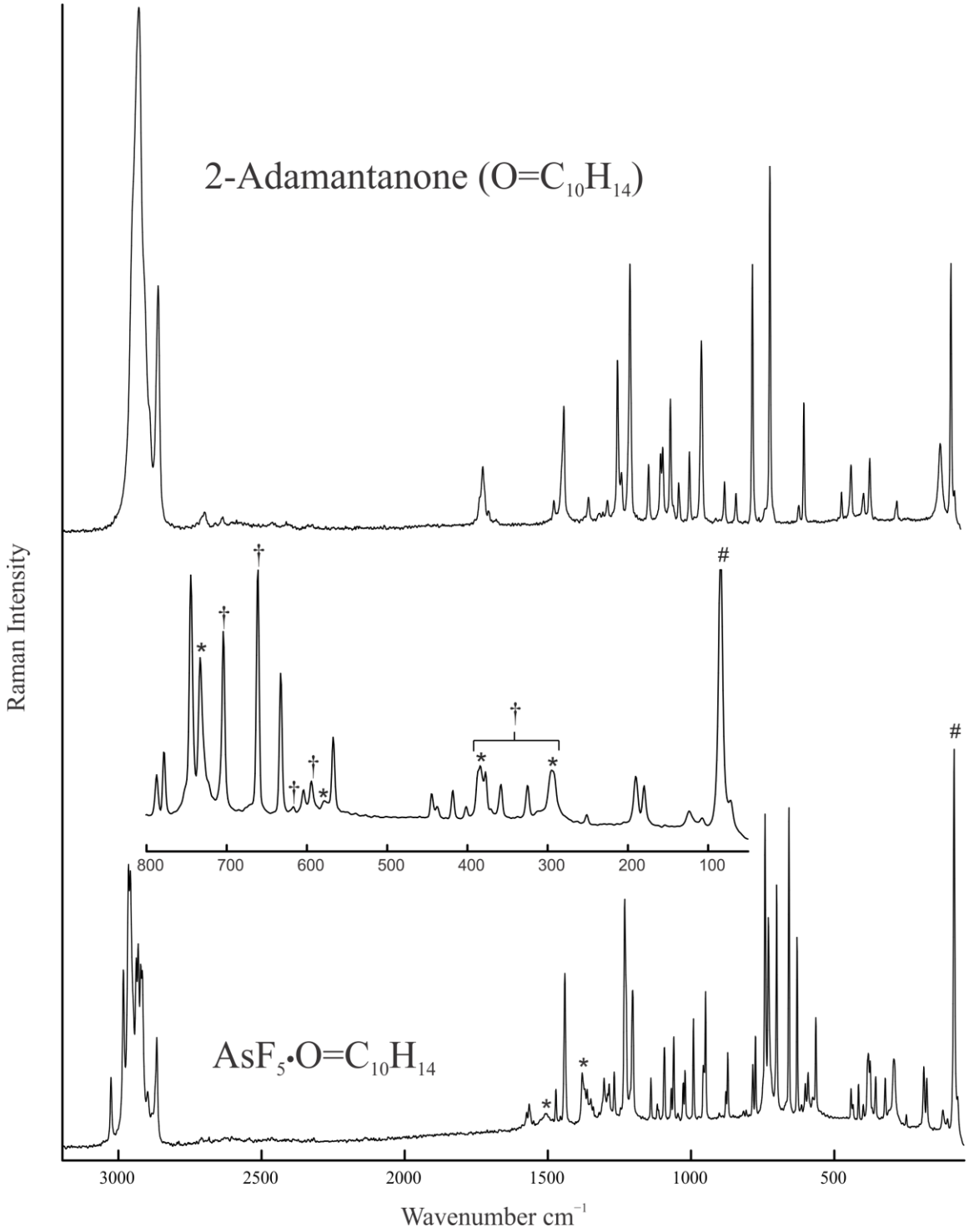

Figure 6.5 Raman spectrum of $O=C_{10}H_{14}$ and $AsF_5 \cdot O=C_{10}H_{14}$ at −100 °C. Symbols denote bands arising from FEP sample tube (*), an instrumental artifact (#), and the AsF_5 vibrations (†).

The interaction of the Lewis acid, AsF_5, with each ketone resulted in changes of vibrational bands associated with the ketones in the Raman spectra, most dramatically for the characteristic ν(CO) frequency. A comparison of the ν(CO) frequencies is found in Table 6.1. Formation of the As---O dative bonds in the $AsF_5{\cdot}O{=}R$ (R = $C(CH_3)_2$, C_5H_8, $C_{10}H_{14}$) adducts or the protonation of ketones (see Chapter 5) both result in a significant weakening of the C=O bond as reflected by a decrease in the ν(CO) stretch. Forming the $AsF_5{\cdot}O{=}C(CH_3)_2$ adduct caused a decrease of 117 cm^{-1} in the C=O stretching frequency compared to neat acetone. The $AsF_5{\cdot}O{=}C_5H_8$ and $AsF_5{\cdot}O{=}C_{10}H_{14}$ compounds showed decreases of 123 and 151 cm^{-1} relative to their parent ketones, respectively. A previous matrix-isolation study of the complimentary SbF_5 adducts, $SbF_5{\cdot}O{=}C(CH_3)_2$ ($\Delta\nu$ = 110 cm^{-1}), $SbF_5{\cdot}O{=}C_5H_8$ ($\Delta\nu$ = 125 cm^{-1}), and $SbF_5{\cdot}O{=}C_{10}H_{14}$ ($\Delta\nu$ = 165 cm^{-1}), used vibrational spectroscopy to show similar decreases in the C=O stretching frequencies. These changes in frequencies are also comparable to salts of the monoprotonated ketones $[HO{=}C(CH_3)_2]^+$ ($\Delta\nu$ = 116 cm^{-1}), $[HO{=}C_5H_8]^+$ ($\Delta\nu$ = 122 cm^{-1}), and $[HO{=}C_{10}H_{14}]^+$ ($\Delta\nu$ = 155 cm^{-1}).[15] Calculated frequencies of the geometry optimized gas-phase structures predicted slightly smaller decreases in C=O frequencies ($AsF_5{\cdot}O{=}C(CH_3)_2$ 99 cm^{-1}; $AsF_5{\cdot}O{=}C_5H_8$ 100 cm^{-1}; and $AsF_5{\cdot}O{=}C_{10}H_{14}$ 111 cm^{-1}). The ring breathing modes of cyclopentanone, 811 cm^{-1}, and 2-adamantanone, 717 cm^{-1}, increased to 841 and 745 cm^{-1}, respectively, for the synthesized $AsF_5{\cdot}O{=}C_5H_8$ and $AsF_5{\cdot}O{=}C_{10}H_{14}$ compounds. The ν_s(CCC) stretching frequency of $AsF_5{\cdot}O{=}C(CH_3)_2$ (838 cm^{-1}) is also increased relative to acetone (788 cm^{-1}). Comparable to similar trends for the monoprotonated ketones, the interaction of AsF_5 with the carbonyl group causes a strengthening of the *cis* and *trans* C−C bonds.

The characteristic As−F stretches of adducted AsF_5 appear as intense bands in the Raman spectra. For $AsF_5{\cdot}O{=}C(CH_3)_2$, the $\nu_s(AsF_{4,eq})$ stretching frequency at 660 cm^{-1} was the most intense Raman band. The second most intense band at 710 cm^{-1} was assigned to the $\nu(AsF_{ax})$ stretching frequency. The frequencies of these bands are rather invariant between the adducts of the three ketones: $AsF_5{\cdot}O{=}C_5H_8$ ($\nu(AsF_{ax})$ 711; $\nu_s(AsF_{4,eq})$ 659 cm^{-1}) and $AsF_5{\cdot}O{=}C_{10}H_{14}$ ($\nu(AsF_{ax})$ 704; $\nu_s(AsF_{4,eq})$ 661 cm^{-1}). The calculated $\nu(AsF_{ax})$ stretches for the adducts were slightly overestimated (by upwards of 25 cm^{-1}) and $\nu_s(AsF_{4,eq})$ stretches were underestimated (by upwards of 9 cm^{-1}) when compared to the experimental values.

6.2.3 NMR Spectroscopy

The ^{19}F and ^{1}H resonances of $AsF_5{\cdot}O{=}C(CH_3)_2$, $AsF_5{\cdot}O{=}C_5H_8$, and $AsF_5{\cdot}O{=}C_{10}H_{14}$ are listed in Table 6.2 and the ^{19}F NMR spectra are depicted in Figure 6.6. The ^{19}F and ^{1}H NMR spectra were collected at −70 °C in liquid SO_2.

The ^{19}F NMR spectra of $AsF_5{\cdot}O{=}C(CH_3)_2$, $AsF_5{\cdot}O{=}C_5H_8$, and $AsF_5{\cdot}O{=}C_{10}H_{14}$ adducts contained two signals: doublets arising from the equatorial fluorine environments of AsF_5 at −48.37 ($\Delta\nu_{1/2}$ = 90 Hz), −50.87 ($\Delta\nu_{1/2}$ = 53 Hz), and −46.72 ($\Delta\nu_{1/2}$ = 61 Hz) ppm; and quintets arising from the axial fluorine atoms of AsF_5 at −73.28 ($\Delta\nu_{1/2}$ = 105 Hz), −73.27 ($\Delta\nu_{1/2}$ = 62 Hz), and −71.59 ($\Delta\nu_{1/2}$ = 49 Hz) ppm, respectively.

Table 6.2 ^{19}F and ^{1}H NMR chemical shifts (δ) for $AsF_5{\cdot}O{=}C(CH_3)_2$, $AsF_5{\cdot}O{=}C_5H_8$, and $AsF_5{\cdot}O{=}C_{10}H_{14}$, as well as their neutral ketones, in SO_2 at −70 °C.

Compounds	^{19}F Chemical Shift (ppm) [a], AsF_5	$\Delta\nu_{1/2}$, Hz	$^{2}J(^{19}F{-}^{19}F)$ (Hz)	^{1}H Chemical Shift (ppm)
$O{=}C(CH_3)_2$	--		--	2.53
$O{=}C_5H_8$	--		--	2.40, 2.16
$O{=}C_{10}H_{14}$	--		--	2.82, 2.45, 2.42, 2.34, 2.31, 2.25, 2.24
$AsF_5{\cdot}SO_2$	−44.71 (s)	88	--	--
$AsF_5{\cdot}O{=}C(CH_3)_2$	−48.37 (F_{eq}, d), −73.28 (F_{ax}, qn)	90 [b] 105 [b]	124	3.05
$AsF_5{\cdot}O{=}C_5H_8$	−50.87 (F_{eq}, d), −73.27 (F_{ax}, qn)	61 62	124	3.44, 3.34, 2.50
$AsF_5{\cdot}O{=}C_{10}H_{14}$	−46.72 (F_{eq}, d), −71.59 (F_{ax}, qn)	53 49	125	2.71, 2,68, 2.55, 2.51, 2.36, 2.27

[a] Abbreviations: (s) singlet; (d) doublet; (qn) quintet; (eq) equatorial; (ax) axial.
[b] Obtained by spectral simulation using Mestre Nova

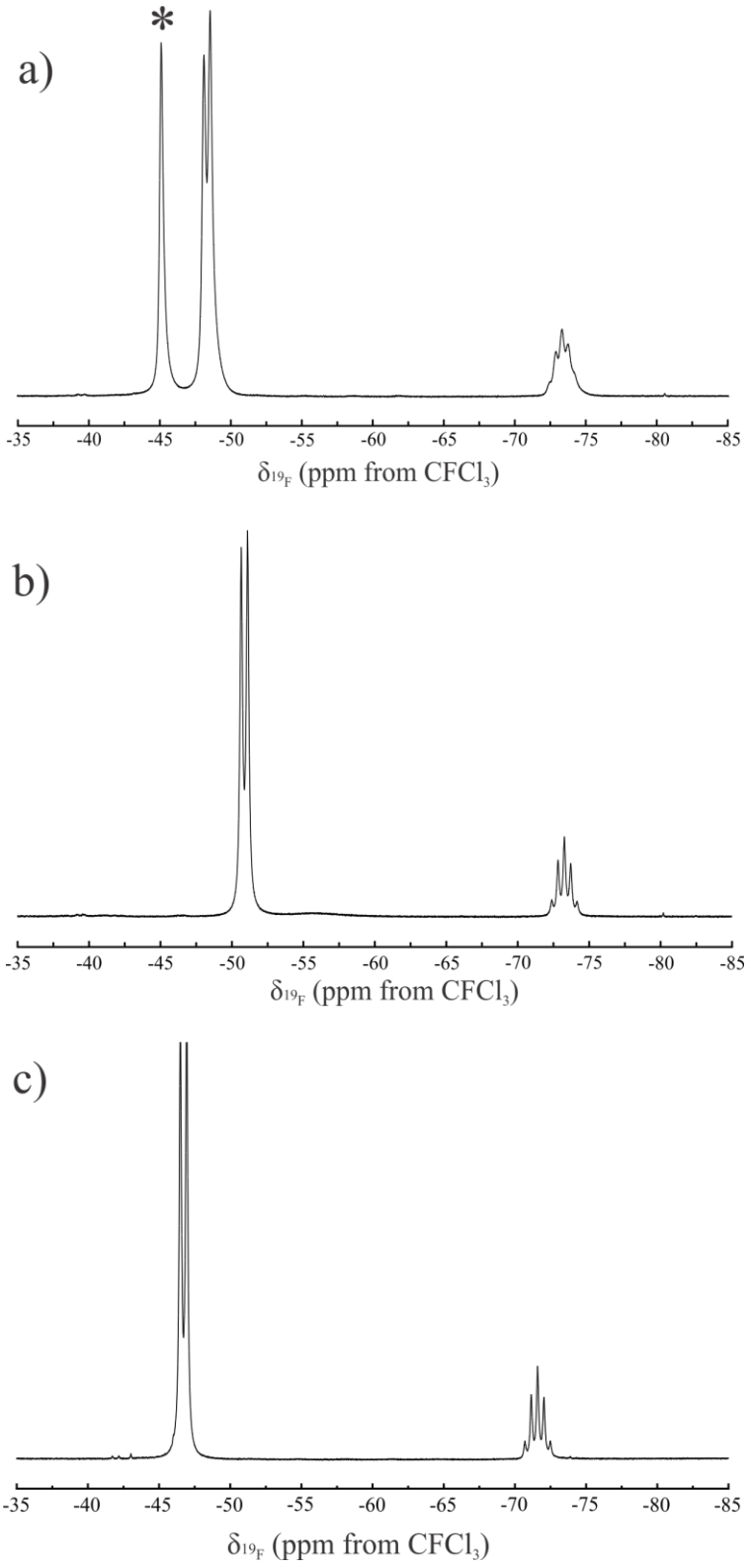

Figure 6.6 ^{19}F NMR spectrum of (a) $AsF_5 \cdot O=C(CH_3)_2$, (b) $AsF_5 \cdot O=C_5H_8$, and (c) $AsF_5 \cdot O=C_{10}H_{14}$ (c) adducts in liquid SO_2 at −70 °C. Externally referenced to $CFCl_3$. The symbol (*) denotes the $AsF_5 \cdot SO_2$ signal.

Upon accepting an electron lone pair from the ketone, the trigonal bipyramidal geometry of free AsF_5 changes and adopts a pseudo octahedral geometry with the C=O---As moiety in the axial position. At −70 °C the exchange between the axial and equatorial ligands is slow enough to observe the two distinct environments on an NMR timescale. The scalar $^2J(^{19}F–^{19}F)$ coupling of 124 or 125 Hz between the equatorial and axial fluorine atoms for AsF_5·O=R is a result of this adopted pseudo octahedral geometry.

When AsF_5 was added to SO_2 in the presence of no ketone, even at −70 °C, only a singlet at −44.71 ppm ($\Delta\nu_{1/2}$ = 88 Hz) corresponding to the AsF_5·SO_2 adduct was observed in the ^{19}F NMR spectrum. In the ^{19}F NMR spectrum of AsF_5·O=C$(CH_3)_2$, the resonance at −45.18 ppm ($\Delta\nu_{1/2}$ = 86 Hz) (Figure 6.6) was attributed to the AsF_5·SO_2 adduct formed due to a slight excess of AsF_5 in solution. This adduct was previously characterized by Raman spectroscopy and ^{19}F NMR spectroscopy.[10,16] Unlike AsF_5·SO_2, the relatively strong As---O interactions in the AsF_5·O=R adducts result in slow exchange between the fluorine environments and observation of scalar $^2J(^{19}F–^{19}F)$ coupling. The electric field gradient about ^{75}As in these adducts causes rapid quadrupolar relaxation of the ^{75}As (I = 3/2, 100%) nucleus with no $^1J(^{75}As–^{19}F)$ coupling being observed. The ^1H resonances of the non-adducted ketones, acetone, cyclopentanone, and 2-adamantanone, are all shifted to higher frequencies upon addition of AsF_5 at −70 °C in SO_2 (Table 6.2). The AsF_5·O=R adducts show increasing peak width at half height values ($\Delta\nu_{1/2}$) from O=$C_{10}H_{14}$ < O=C_5H_8 < O=C$(CH_3)_2$ (Table 6.2). The donor strength of acetone (76.03±0.21 kJ/mol) and cyclopentanone (77.44±0.45 kJ/mol), measured by their affinity to BF_3, are too similar to account for the difference in $\Delta\nu_{1/2}$ values.[17] The calculated As---O distances in the gas-phase adducts are also similar and, therefore, will not account for the broadening observed

in the ^{19}F NMR spectrum of $AsF_5{\cdot}O{=}C(CH_3)_2$. The slight excess of AsF_5 in solution, as noted from the $AsF_5{\cdot}SO_2$ signal in the ^{19}F NMR spectrum of $AsF_5{\cdot}O{=}C(CH_3)_2$ (see Figure 6.6a), could be the cause of the broadening of signals as a result of exchange of AsF_5 between the acetone and SO_2. After warming the reaction to RT for 40 min, the ^{19}F resonance at −45.18 ppm was no longer present and the doublet (−48.3 ppm) and quintet (−73.34 ppm) from $AsF_5{\cdot}O{=}C(CH_3)_2$ became sharper (Figure 6.7). As well, some $[AsF_6]^-$ was formed as shown from the equal intensity quartet at −56.8 with a $^1J(^{19}F{-}^{75}As)$ coupling of 926 Hz. Although the source of the F^- that produces $[AsF_6]^-$ is not conclusively known, it may be formed by reaction of HF, produced by hydrolysis from trace amounts of moisture through the FEP reactor after having been left at RT for 40 min, with AsF_5 to produce $[H_2F][AsF_6]$ in small quantities.

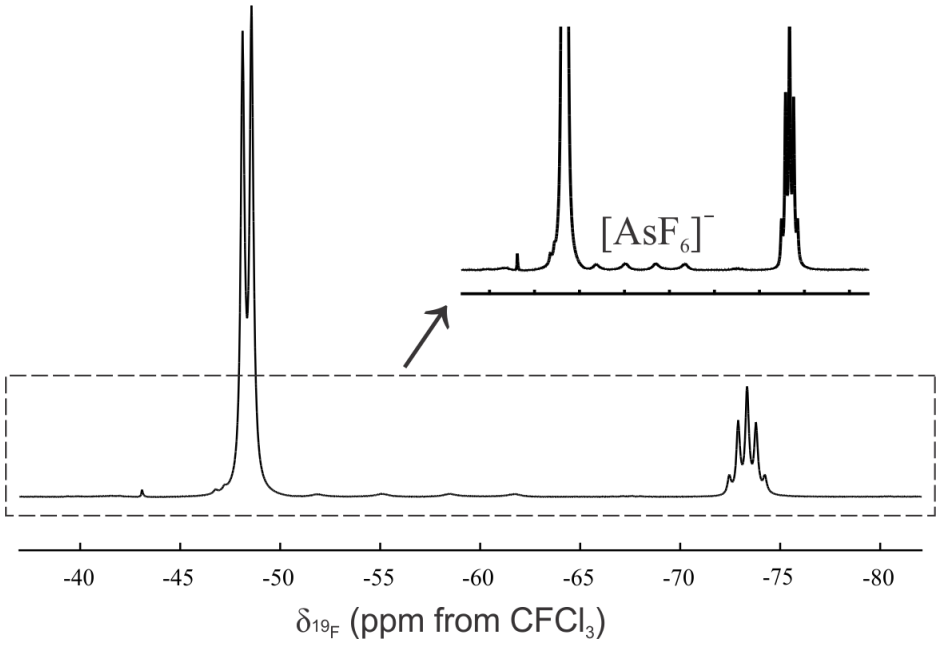

Figure 6.7 ^{19}F NMR spectrum of $AsF_5{\cdot}O{=}C(CH_3)_2$ after warming to RT for 40 min. Externally referenced to $CFCl_3$.

6.2.4 Computational Results

Density functional theory (DFT) calculations were carried out on the $AsF_5{\cdot}O{=}R$ adducts (R = $C(CH_3)_2$, C_5H_8, $C_{10}H_{14}$) along with their parent ketones. The B3LYP functional was chosen along with the aug-cc-pVTZ (used for $AsF_5{\cdot}O{=}C(CH_3)_2$) and cc-pVTZ (used for $AsF_5{\cdot}O{=}C_5H_8$ and $AsF_5{\cdot}O{=}C_{10}H_{14}$) basis sets as it consistently provides reliable structural information (see Chapter 2, Section 2.11 for method validation). The gas-phase geometries of the compounds $AsF_5{\cdot}O{=}C(CH_3)_2$, $AsF_5{\cdot}O{=}C_5H_8$, and $AsF_5{\cdot}O{=}C_{10}H_{14}$, as well as the respective free ketones, were optimized and the geometric parameters can be found in Appendix Tables A.3.1−A.3.3 (Figure 6.8). A summary of selected geometric parameters is given in Table 6.3. These adducts adopt a pseudo octahedral geometry around the As center and the As---O distances range between 2.044 ($AsF_5{\cdot}O{=}C_{10}H_{14}$) and 2.065 Å ($AsF_5{\cdot}O{=}C(CH_3)_2$). The ketones form weak bonds with AsF_5 at As−O−C angles of 133.06, 130.27, and 132.56° for $AsF_5{\cdot}O{=}C(CH_3)_2$, $AsF_5{\cdot}O{=}C_5H_8$, and $AsF_5{\cdot}O{=}C_{10}H_{14}$, respectively. These angles are larger than the reported B−O−C angle of 118.7(3)° in the crystal structure of the $BF_3{\cdot}$benzaldehyde adduct,[3] which is likely a result of the AsF_5 moiety being larger than BF_3 and providing more steric hinderance resulting in a larger angle. The As−O−C−C dihedral angles for each adduct deviate by no more than 1.89° ($AsF_5{\cdot}O{=}C_5H_8$) from 0° resulting in the As−O−CC_2 moiety being essentially planar. These geometries were used to calculate the vibrational frequencies along with IR and Raman intensities and generally showed excellent agreement with the experimental values (*vide supra*), as listed in Appendix A.3.4−A.3.6.

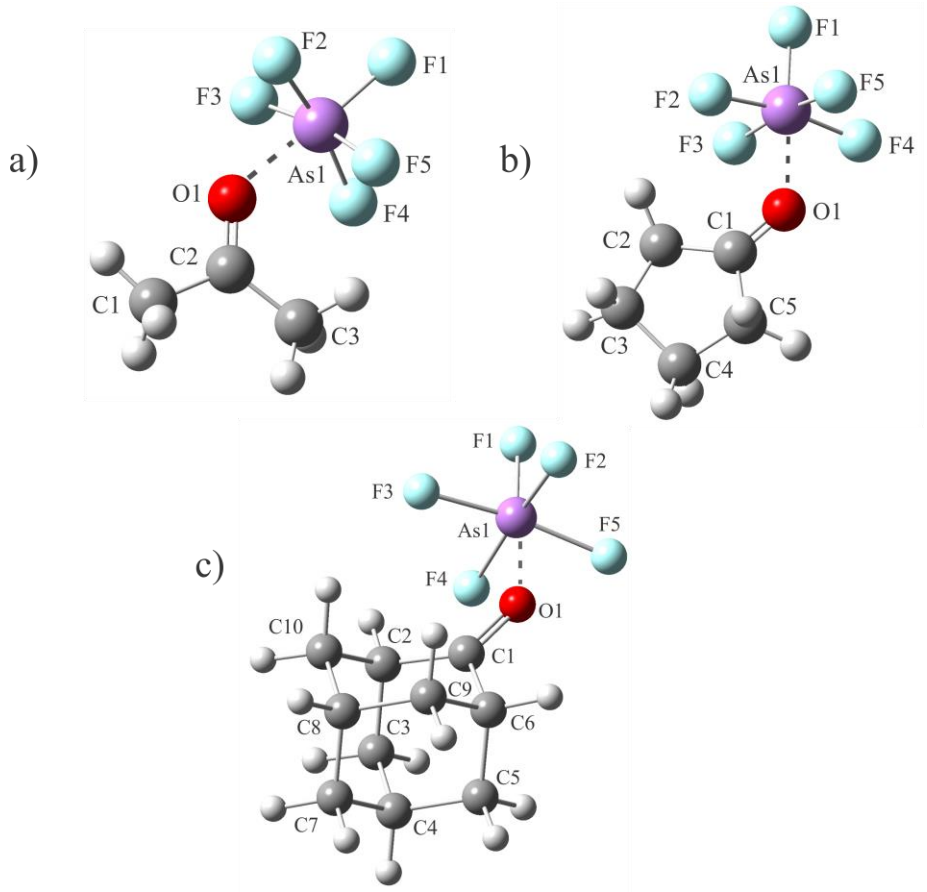

Figure 6.8 Optimized gas-phase geometries of a) $AsF_5 \cdot O{=}C(CH_3)_2$, b) $AsF_5 \cdot O{=}C_5H_8$, and c) $AsF_5 \cdot O{=}C_{10}H_{14}$.

Table 6.3 Selected Calculated Bond Lengths (Å) and Bond Angles (°) of $AsF_5 \cdot O{=}C(CH_3)_2$, $AsF_5 \cdot O{=}C_5H_8$, and $AsF_5 \cdot O{=}C_{10}H_{14}$ Adducts.

	$AsF_5 \cdot O{=}C(CH_3)_2$ [c]	$AsF_5 \cdot O{=}C_5H_8$ [d]	$AsF_5 \cdot O{=}C_{10}H_{14}$ [d]
C=O	1.237	1.232	1.240
$C_{C=O}{-}C^{[a]}$	1.491	1.499	1.497
$C_{C=O}{-}C^{[b]}$	1.493	1.504	1.501
O---As	2.065	2.064	2.044
As−O−C	133.06	130.27	132.56
As−O−C−C	1.30	1.89	0.00

[a] Refers to the carbon *cis* to the As adducted to oxygen; [b] Refers to the carbon *trans* to the As adducted to oxygen; [c] DFT calculations at the B3LYP/aug-cc-pVTZ level of theory; [d] DFT calculations at the B3LYP/cc-pVTZ level of theory.

Natural bond order (NBO) analyses were carried out to investigate the bonding in these $AsF_5{\cdot}O{=}R$ compounds (Appendix Tables A.3.7−A.3.9). A summary of the NBO analyses is found in Table 6.4.

Table 6.4 Selected NPA Charges, Valences and Wiberg Bond Indices of the $AsF_5{\cdot}O{=}R$ (R = $C(CH_3)_2$, C_5H_8, and $C_{10}H_{14}$) Compounds and their Respective Free Ketones.

	NPA Charges (Valences [a])	NPA Charges (Valences [a])	Wiberg Bond Indices	
	O	C	CO	As---O
$O{=}C(CH_3)_2$	−0.55 (2.04)	0.59 (3.87)	1.83	
$AsF_5{\cdot}O{=}C(CH_3)_2$	−0.59 (2.14)	0.69 (3.78)	1.59	0.29
$O{=}C_5H_8$	−0.54 (2.06)	0.60 (3.87)	1.84	
$AsF_5{\cdot}O{=}C_5H_8$	−0.59 (2.15)	0.71 (3.77)	1.60	0.30
$O{=}C_{10}H_{14}$	−0.56 (2.04)	0.61 (3.87)	1.83	
$AsF_5{\cdot}O{=}C_{10}H_{14}$	−0.61 (2.14)	0.73 (3.76)	1.57	0.31

[a] Sum of the Wiberg Bond Indices per atom.

For each of the $AsF_5{\cdot}O{=}R$ adducts, the Natural Population Analysis (NPA) charge on the carbonyl carbon increased by between 0.10 and 0.12. The negative charge on oxygen increased by 0.04, for $AsF_5{\cdot}O{=}C(CH_3)_2$, and 0.05, for $AsF_5{\cdot}O{=}C_5H_8$, and $AsF_5{\cdot}O{=}C_{10}H_{14}$. This is comparable to the monoprotonated ketones $[HO{=}R]^+$ (R = $C_{10}H_{14}$, C_5H_8, or $C(CH_3)_2$) studied where the charge on carbon increased by between 0.13 and 0.14.[15] However, when looking at the calculated C=O Wiberg bond index (WBI), the $AsF_5{\cdot}O{=}R$ adducts did not show as great of a decrease in C=O bond order compared to the monoprotonated ketones. A decrease between 0.24 and 0.26 was calculated for $AsF_5{\cdot}O{=}R$, whereas a decrease between 0.44 and 0.48 was calculated for the $[HO{=}R]^+$ cations, all relative to the free ketones. Comparable to the $[HO{=}R]^+$ cations, the oxonium structure is the dominant resonance over the carbenium structure in the $AsF_5{\cdot}O{=}R$ adducts (Scheme 6.2). The C=O bond in $[HO{=}R]^+$ cations is more polarized than in $AsF_5{\cdot}O{=}R$ adducts,

which is paralleled by the C=O bond in the $[HO{=}R]^+$ cations containing less double-bond character than the $AsF_5{\cdot}O{=}R$ adducts, as shown by the lower bond index. Addition of the acid, whether it is AsF_5 or $[H]^+$, is responsible for the increased positive charge on the carbon of the carbonyl and decreased C=O bond order.

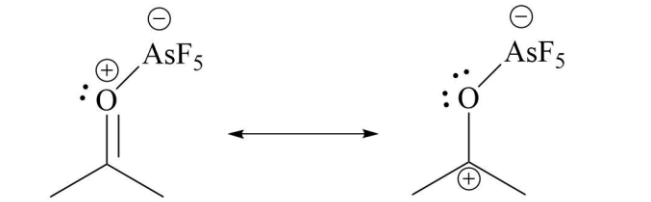

Oxonium Structure Oxocarbenium Structure

Scheme 6.2 Resonance structures for $AsF_5{\cdot}O{=}C(CH_3)_2$.

The As---O bond index in the adducts range from 0.29 to 0.31. The bond order for the As---O bonds is approximately half of that of the As−F bonds in the adducts (WBI = 0.56 to 0.62). For the protonated ketones, the strong polarization of the C=O bond by protonation can be explained by the much higher O−H bond order (0.70) compared to that of the As---O bond.

The molecular orbital energies were calculated for the $AsF_5{\cdot}O{=}R$ compounds (see Appendix Figures A.3.1−A.3.6). Using $AsF_5{\cdot}O{=}C(CH_3)_2$ as a representative example, Figure 6.9 shows the altered shape and energies of the HOMO and LUMO upon addition of AsF_5. A dramatic decrease in energy by 771 kJ/mol is observed for the HOMO, and 241 kJ/mol for the LUMO upon formation of $AsF_5{\cdot}O{=}C(CH_3)_2$.

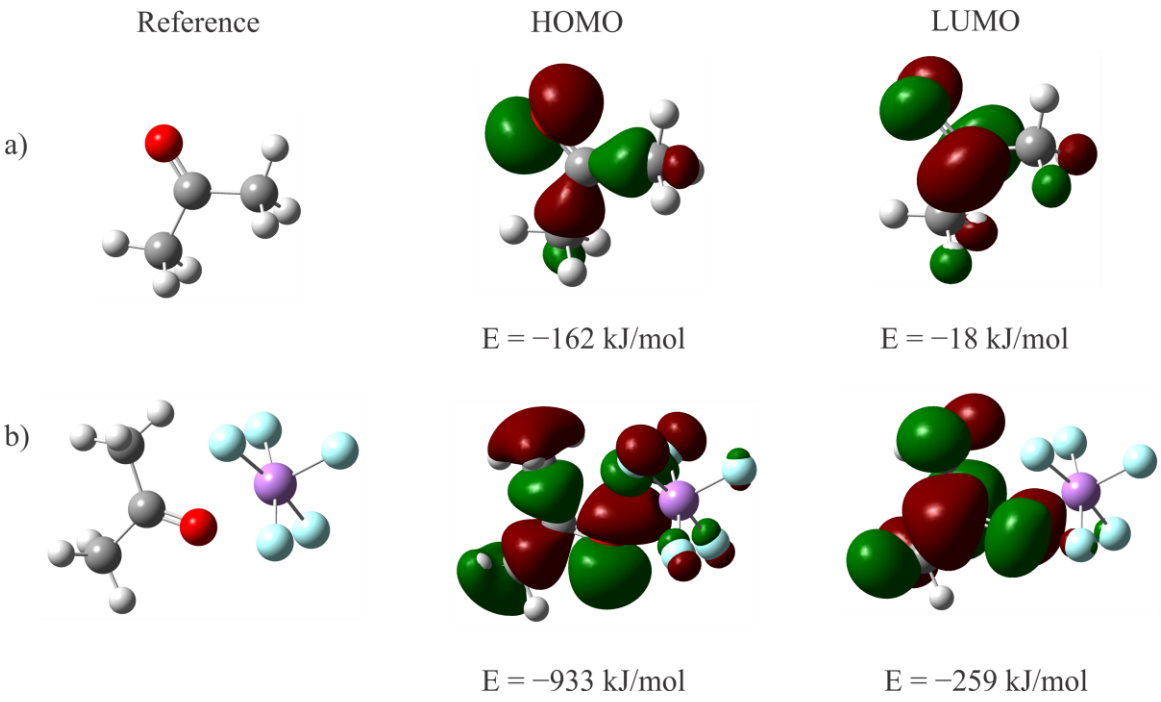

Figure 6.9 Molecular orbitals of a) acetone and b) $AsF_5{\cdot}O{=}C(CH_3)_2$. From left to right are the reference molecules, HOMO diagrams, LUMO diagrams.

The formation of the C=O---As moiety dramatically lowers the LUMO of the ketone creating a much more reactive species towards nucleophilic attack compared to the free ketone. The substantial decrease in energy of the HOMO significantly reduces the reactivity towards electrophilic attack. The HOMO also contains some π orbital contribution from the fluorine atoms of AsF_5 which might contribute to the considerable lowering in energy. These findings are consistent with previous calculations for the $[HO{=}R]^+$ cations. A summary of the HOMO and LUMO energies for the $AsF_5{\cdot}O{=}R$ adducts and $[HO{=}R]^+$ cations is shown in Table 6.5. The LUMO energy of $AsF_5{\cdot}O{=}C(CH_3)_2$ (−259 kJ/mol) is significantly lower than that of $[HO{=}C(CH_3)_2]^+$ (−189 kJ/mol) and will be more prone to nucleophilic attack. This may account for one of the reasons Lewis acids are used over $[H]^+$ to activate specific organic reactions, such as the Diels-Alder reaction. A previous study

investigating the change in energy of the HOMO and LUMO of $BF_3{\cdot}OCHCH_3$ only showed a decrease of 80 kJ/mol in the LUMO and 173 kJ/mol in the HOMO.[3] This can be attributed to the stronger Lewis acidity of AsF_5 compared to BF_3, whereby the C=O---As moiety more heavily influences the reactivity of the ketone.

Table 6.5 Calculated Energies (kJ/mol) of the HOMO and LUMO for the $AsF_5{\cdot}O{=}R$ Adducts and the Protonated Ketones $[H(O{=}R)_x]^+$ (x = 1 or 2; R = $C(CH_3)_2$, C_5H_8, $C_{10}H_{14}$).

Compound	HOMO Energy	LUMO Energy
$O{=}C_{10}H_{14}$	−151	−13
$[HO{=}C_{10}H_{14}]^+$	−286	−163
$AsF_5{\cdot}O{=}C_{10}H_{14}$	−837	−229
$O{=}C_5H_8$	−157	−20
$[HO{=}C_5H_8]^+$	−323	−182
$AsF_5{\cdot}O{=}C_5H_8$	−890	−256
$O{=}C(CH_3)_2$	−162	−18
$[HO{=}C(CH_3)_2]^+$	−376	−189
$[H(O{=}C(CH_3)_2)_2]^+$	−1203	−596
$AsF_5{\cdot}O{=}C(CH_3)_2$	−933	−259

6.3 Summary and Conclusions

For the first time, Lewis acid-base adducts of aliphatic and alicyclic ketones with AsF_5 were synthesized and characterized by Raman, ^1H, and ^{19}F NMR spectroscopies. These $AsF_5{\cdot}O{=}R$ adducts (R = $C(CH_3)_2$, C_5H_8, $C_{10}H_{14}$) adducts were isolated as white powders and found to decompose upon warming to RT. Raman spectroscopy showed characteristic bands of the ketones that are shifted upon addition of AsF_5 and subsequent adduct formation. Specifically, the C=O stretching frequency dramatically decreased by between 107−151 cm^{-1} and ν_s(CCC) stretches and ring breathing modes of the ketones increased to higher frequencies. The ^{19}F NMR spectra of these compounds showed they had developed pseudo octahedral geometries about the ^{75}As metal center. While no

$^{1}J(^{75}As–^{19}F)$ coupling could be distinguished, the $^{2}J(^{19}F–^{19}F)$ coupling between the axial and equatorial fluorine environments of AsF_5 was observed.

NBO analyses of these AsF_5·O=R adducts showed an increase in the charge of the carbon of the carbonyl group, as well as, a decrease in the C=O bond order due to the strong Lewis acid, AsF_5, withdrawing electron density from the C=O group. Decreases in the HOMO and LUMO energies also confirmed the activation and increased reactivity of the ketones in Lewis-acid catalyzed organic reactions. These results are comparable to the oxonium $[HO=R]^+$ cations (R = $C(CH_3)_2$, C_5H_8, $C_{10}H_{14}$) typically observed as intermediates in acid-catalyzed organic reactions. DFT calculations showed the C=O bond of $[HO=R]^+$ cations to contain more single-bond character than the AsF_5·O=R adducts, as indicated by larger decreases in the C=O bond order. While the C=O bond is less polarized by AsF_5 compared to HF, the LUMO of the AsF_5·O=R adduct is lower in energy than the $[HO=R]^+$ cation confirming why the reactivity of carbonyl compounds are enhanced by Lewis acids and sometimes favoured over Brønsted acids.

References

[1] (a) Rueping, M.; Nachtsheim, B. J. *Beilstein J. Org. Chem.* **2010**, *6*, No. 6. (b) Fringuelli, F.; Piermatti, O.; Pizzo, F.; Vaccaro, L. *Eur. J. Org. Chem.* **2001**, 439−455. (c) Lade, J. J.; Pardeshi, S. D.; Vadagaonkar, K. S.; Murugan, K.; Chaskar, A. C. *RSC Adv.* **2017**, *7*, 8011−8033. (d) Kan, S. B. J.; Ng, K. K.-H.; Paterson, I. *Angew. Chem. Int. Ed.* **2013**, *52*, 9097−9108.

[2] Childs, R. F.; Mulholland, L. D.; Nixon, A. *Can. J. Chem.* **1982**, *60*, 801−808.

[3] Reetz, M. T.; Hüllmann, M.; Massa, W.; Berger, S.; Rademacher, P.; Heymanns, P. *J. Am. Chem. Soc.* **1986**, *108*, 2405−2408.

[4] (a) Fleming, I. In *Comprehensive Organic Synthesis*; Trost, B. M.; Fleming, I., Eds.; Pergamon: Oxford, 1991; Vol. *2*, 563−593. (b) Hosomi, A.; Sakurai, H. *Tetrahedron Lett.* **1976**, No. 16, 1295−1298.

[5] Christe, K. O. *Inorg. Chem.* **1967**, *6*, 1706−1710.

[6] Berthold, H.; Boatz, J. A.; Hegge, J.; Christe, K. O. *Inorg. Chem.* **1999**, *38*, 3143−3149.

[7] Shambayati, S.; Schreiber, S. L. In *Comprehensive Organic Synthesis*; Trost, B. M.; Fleming, I., Eds.; Pergamon: Oxford, 1991; Vol. *1*, 283−324.

[8] Hartman, J. S.; Stilbs, P.; Forsén, S. *Tetrahedron Lett.* **1975**, No. 40, 3497−3500.

[9] Bittner, A.; Mannih, D.; Noth, H. *Z. Naturforsch.*, **1986**, *41b*, 587−591.

[10] Chen, G. S. H.; Passmore, J. *J. Chem. Soc. Dalton Trans.* **1979**, 1257−1261.

[11] Vančik, H.; Gabelica, V.; Mihalić, Z.; Sunko, D. E. *J. Chem. Soc. Perkin Trans II* **1992**, 1611−1614.

[12] Minkwitz, R.; Gerhard, V. *Z. Anorg. Allg. Chem.* **1991**, *603*, 95−101.

[13] Minkwitz, R.; Lohmann, U.; Preut, H. *Z. Naturforsch.* **1996**, *51b*, 133−138.

[14] Lunazzi, L.; Brownstein, S. *J. Magn. Reson.* **1969**, *1*, 119−123.

[15] Stuart, D.; Wetmore, S. D.; Gerken, M. *Angew. Chem. Int. Ed.* **2017**, *56*, 16380−16384.

[16] Brownstein, M.; Gillespie, R. J. *J. Am. Chem. Soc.* **1970**, *92*, 2718−2721.

[17] Laurence, C.; Gal, J.-F. *Lewis Basicity and Affinity Scales: Data and Measurement*; John Wiley & Sons: Chichester, 2010; Chapter 3.

7. Summary and Future Work

7.1 Summary

The mechanism of the deoxofluorination reaction of carbonyl compounds involving SF_4 is not well understood and multiple mechanisms have previously been proposed. The results in this thesis have provided a new outlook on possible reactive intermediates involved in deoxofluorination and have expanded upon previous knowledge of proposed mechanisms.

The Lewis acid-base interactions between SF_4 and the ketones acetone and 2-adamantanone have been explored in the solid state. The $[SF_4{\cdot}O{=}C(CH_3)_2]_2$ and $SF_4{\cdot}[O{=}C(CH_3)_2]_2$ adducts were synthesized and characterized at low temperatures using Raman spectroscopy and, in the case of $[SF_4{\cdot}O{=}C(CH_3)_2]_2$, single-crystal X-ray diffraction. The X-ray crystal structure of $[SF_4{\cdot}O{=}C(CH_3)_2]_2$ showed weak S---O chalcogen bonding interactions. This was confirmed using Raman spectroscopy where small decreases (< 10 cm^{-1}) in the C=O stretching frequencies and large decreases (upwards of 24 cm^{-1}) in the axial and equatorial SF_2 stretches of SF_4 were detected. The X-ray crystal structure of $SF_4{\cdot}(O{=}C_{10}H_{14}){\cdot}(HF)$ exhibited a surprising bonding modality where HF bridges a ketone and SF_4. This structure contrasts with what HF is commonly thought to do in such reactions. It is postulated that HF interacts with SF_4 to abstract a fluoride ion and generate the $[SF_3]^+$ cation.

Adducts involving the Lewis acid $[SF_3]^+$ with acetone, the simplest aliphatic ketone, cyclopentanone, a cyclic ketone, and 2-adamantanone, a polycyclic ketone, were explored in solutions using ^{19}F and ^{1}H NMR spectroscopy at low temperatures. It was found that the $[SF_3{\cdot}(O{=}R)_x]^+$ (R = $C(CH_3)_2$, C_5H_8, $C_{10}H_{14}$; x = 1 or 2) adducts exist below −40 °C. In

the reaction where $[SF_3][AsF_6]$ was mixed with an excess of acetone, the proposed $[SF_3{\cdot}\{O{=}C(CH_3)_2\}_3]^+$ cation was observed, as evidenced by the dramatic change in chemical shift (18.43 ppm) compared to non-adducted $[SF_3]^+$ (32.91 ppm). In the reactions where one equivalent of ketone reacted with $[SF_3][AsF_6]$, it was found that $AsF_5{\cdot}O{=}R$ (R = $C(CH_3)_2$, C_5H_8, $C_{10}H_{14}$) adducts were significant by-products. Above −40 °C, SF_4 formation was observed for each of the reactions. The integration of the ^{19}F resonances of SF_4 versus $[AsF_6]^-$ is consistent with a proposed dismutation reaction where a highly reactive, elusive $[SF_2]^{2+}$ cationic species is formed. The nature of the cationic species present in solution after warming these reactions could not be identified, however, the change in colour to a dark red or orange/brown solution that accompanied the SF_4 formation may be indicative of a radical cation which is not observable using NMR spectroscopy.

The reactions of $[SF_3][AsF_6]$ with ketones in different solvents led to the discovery of the superacidic medium $[SF_3][AsF_6]$/aHF which, consequently, resulted in protonation of the ketones. Superacidic media have long been used to synthesize and stabilize highly reactive species, such as the oxonium cation $[HO{=}R]^+$, however, many of these studies are limited to the solution state. In addition, one of the proposed deoxofluorination mechanisms invokes an intermediate which involves HF polarizing the C=O bond allowing for nucleophilic attack of a fluoride. The synthesis of the protonated ketones $[HO{=}C_{10}H_{14}]^+$, $[HO{=}C_5H_8]^+$, and $[HO{=}C(CH_3)_2]^+$, as well as, the protonated aldehydes $[H(O{=}CHC_6H_5)_2]^+$, $[HO{=}CHCH_3]^+$, and $[H(O{=}CHCH_3)_2]^+$ was carried out and these compounds were characterized in the solid state for the first time. The X-ray crystal structure of the hemiprotonated acetone cation was obtained for the first time, as shown in the complex salt of $[H\{O{=}C(CH_3)_2\}_2]_3[HO{=}C(CH_3)_2]_3[SbF_6]_5F$.

The AsF_5·O=R adducts, by-products in the deoxofluorination reactions of $[SF_3][AsF_6]$ with ketones previously discussed, were further studied in targeted reactions to better understand the Lewis acid-base interactions between AsF_5 and ketones. Lewis acids are frequently used as catalysts in organic reactions and the mechanism is well understood. However, there have been no systematic studies examining the interactions of a Lewis acid with ketones in the solid state. The AsF_5·O=R (R = $C(CH_3)_2$, C_5H_8, $C_{10}H_{14}$) adducts have now been synthesized and characterized in the solution and solid states using low-temperature NMR and Raman spectroscopies. The ^{19}F NMR spectra showed the AsF_5·O=R adducts adopting pseudo octahedral geometries about the ^{75}As nucleus allowing for the observation of two resonances for the axial and equatorial fluorine environments about As. Raman spectroscopy showed characteristic bands of the ketones being shifted upon adduct formation.

Density functional theory calculations were used to optimize the gas-phase geometries of the $[SF_3{\cdot}\{O=C(CH_3)_2\}_x]^+$ ($x = 1-3$) cations and previously proposed reaction intermediates of deoxofluorination. The gas-phase geometries were also optimized for the AsF_5·O=R (R = $C(CH_3)_2$, C_5H_8, $C_{10}H_{14}$) adducts and protonated ketones ($[HO=C_{10}H_{14}]^+$, $[HO=C_5H_8]^+$, $[HO=C(CH_3)_2]^+$, $[H\{O=C(CH_3)_2\}_2]^+$), and aldehydes ($[H(O=CHC_6H_5)_2]^+$, $[HO=CHCH_3]^+$, $[H(O=CHCH_3)_2]^+$) and compared with the X-ray crystal structures, where applicable. NBO analyses of the AsF_5·O=R (R = $C(CH_3)_2$, C_5H_8, $C_{10}H_{14}$) adducts, monoprotonated $[HO=R]^+$ (R = $C(CH_3)_2$, C_5H_8, $C_{10}H_{14}$) cations, and hemiprotonated $[H(O=R)_2]^+$ (R = CHC_6H_5, $C(CH_3)_2$, $CHCH_3$) cations were carried out. When a Lewis acid (i.e., AsF_5) or Brønsted acid (i.e., $[H]^+$) is bonded to the oxygen of the carbonyl group, the charge of the carbon of the carbonyl group increases, and the C=O bond order decreases due to electron density being withdrawn from the C=O group.

The HOMO and LUMO energies were also calculated for the $AsF_5{\cdot}O{=}R$, $[HO{=}R]^+$, $[H(O{=}R)_2]^+$, and $[SF_3{\cdot}\{O{=}C(CH_3)_2\}_x]^+$ (x = 1−3) compounds. Using acetone as a model system, the LUMO energies can be compared (Table 7.1). Since $[SF_3]^+$ is more electrophilic than AsF_5 and $[H]^+$, the $[SF_3{\cdot}\{O{=}C(CH_3)_2\}_x]^+$ (x = 1−3) compounds showed the largest decrease in the LUMO energy. The $AsF_5{\cdot}O{=}C(CH_3)_2$ adduct (−259 kJ/mol) had a larger decrease in energy from acetone (−18 kJ/mol) compared to that of $[HO{=}C(CH_3)_2]^+$ (−189 kJ/mol). These values correlate well with the observed reactivity and stability for each of the systems studied.

Table 7.1 Calculated Energies (kJ/mol) of the HOMO and LUMO for Acetone, $[H\{O{=}C(CH_3)_2\}_x]^+$ (x = 1, 2), $AsF_5{\cdot}O{=}C(CH_3)_2$, and $[SF_3{\cdot}\{O{=}C(CH_3)_2\}_x]^+$ (x = 1−3).

Compound	HOMO Energy	LUMO Energy
$O{=}C(CH_3)_2$	−162	−18
$[HO{=}C(CH_3)_2]^+$	−376	−189
$[H\{O{=}C(CH_3)_2\}_2]^+$	−1203	−596
$AsF_5{\cdot}O{=}C(CH_3)_2$	−933	−259
$[SF_3{\cdot}\{O{=}C(CH_3)_2\}_3]^+$	−1035	−500
$[SF_3{\cdot}\{O{=}C(CH_3)_2\}_2]^+$	−1126	−613
$[SF_3{\cdot}O{=}C(CH_3)_2]^+$	−1271	−732

7.2 Directions for Future Work

The reactions involving $[SF_3][AsF_6]$ with various ketones has shed some light on possible reactive intermediates involved in deoxofluorination. The nature of the sulfur species, as well as the cation, in these reactions above −40 °C is still not known and should be further investigated. The use of electron paramagnetic resonance (EPR) spectroscopy could provide valuable information about possible radical species present in solution. As

well, reproducing these low-temperature NMR spectroscopy studies with varying stoichiometries and different solvents (i.e., CH_2Cl_2) aid in characterizing the unknown contents produced in these reactions. Whereas, the $[SF_3]^+$ salts are insoluble in solvents such as CH_2Cl_2, salts with complex cations, i.e., cationic adducts, have been observed to exhibit solubility in such solvents. The characterization of the elusive $[SF_2]^{2+}$ cation should be attempted, which will likely require the use of a stronger base. The $[SF_3][AsF_6]$ salt has proven to be highly reactive towards ketones, even at low temperatures. Reactions utilizing reagents such as Fluolead or DAST might provide a better means to further understanding the interactions of the SF_3 moiety with ketones.

The synthesis and characterization of other hemiprotonated cations should be further explored. The X-ray crystal structure of $[H\{O=C(CH_3)_2\}_2]_3[HO=C(CH_3)_2]_3[SbF_6]_5F$ has shown that hemiprotonated acetone is an isolated cation, unlike the monoprotonated species which contains contacts with the anion. Attempting to further explore the interactions of $[HO=C(CH_3)_2]^+$ with a fluoride anion, similar to the moiety in the X-ray crystal structure of $[H\{O=C(CH_3)_2\}_2]_3[HO=C(CH_3)_2]_3[SbF_6]_5F$, would provide more information about the interaction modalities of these oxonium cations towards Lewis bases. It may also be beneficial to expand the scope of these protonated carbonyl systems to include diketones (i.e., diacetyl) which may lead to the synthesis of novel dicationic compounds.

8. Appendix

Table A.1.1 Observed and Calculated (B3LYP/aug-cc-pVTZ) Raman Frequencies for $[SF_4{\cdot}O{=}C(CH_3)_2]_2$, $SF_4{\cdot}[O{=}C(CH_3)_2]_2$, and $O{=}C(CH_3)_2$.

$[SF_4{\cdot}O{=}C(CH_3)_2]_2$		$SF_4{\cdot}[O{=}C(CH_3)_2]_2$		$O{=}C(CH_3)_2$			Tentative Asignments [a]
exptl [d]	*calcd* [c]	*exptl* [d]	*calcd* [c]	*exptl* [b]	*calcd* [c]		
3018(8)	3151(42)[2]	3011(18)	3151(50)[0]	3005(13)	3139(67)[6]		
	3150(44)[1]		3151(50)[0]		3138(53)[12]		
	3148(42)[6]		3140(40)[11]				
	3145(42)[6]		3140(66)[5]				
2977(12)	3089(134)[8]	2973(22)	3086(105)[12]	2963(14)	3084(95)[17]		
	3089(43)[9]		3086(95)[13]				
2969(12)	3084(45)[4]		3079(26)[2]		3077(12)[0]		$\nu_s + \nu_{as}$ (CH_3)
	3084(47)[5]		3079(24)[2]				
2931(52)	3035(335)[6]	2926(100)	3033(463)[8]	2923(100)	3033(320)[7]		
	3034(298)[6]		3033(205)[13]				
	3029(13)[0]		3027(8)[1]		3025(2)[1]		
	3029(17)[1]		3027(8)[1]				
2846(4)		2850(8)		2848(7)			
2707(3)		2699(4)					
				1751(3)			ν(CO)
1705sh		1702(22)		1709(16)	1782(13)[195]		
1699(35)	1759(30)[199]		1770(32)[80]				
1694(21)	1753(13)[424]		1766(15)[494]				
		1673sh					
	1489(1)[12]		1491(1)[13]				
	1489(0)[21]		1491(0)[18]		1488(0)[19]		
1452(4)	1476(10)[10]		1473(10)[15]				
1429(15)	1475(13)[9]	1426(24)	1473(14)[14]	1428(10)	1470(12)[31]		$\delta(CH_2)$

	1462(2)[3]		1465(13)[9]		1466(8)[0]		
	1461(3)[7]		1465(10)[24]		1460(1)[1]		
	1460(15)[18]		1461(1)[1]				
	1460(6)[29]		1461(1)[2]				
	1395(0)[72]		1394(2)[16]				
	1394(0)[19]		1394(0)[62]				$\delta(CH_2)$
1383(6) [e]	1392(1)[30]	1384(8) [e]	1388(1)[37]		1388(0)[54]		
1362(6)	1391(1)[28]	1358(8)	1388(0)[32]	1358(3)	1388(2)[19]		
		1308(9) [e]					
		1251(3)					
1236(11)	1247(8)[119]	1230(13)	1243(12)[79]	1222(6)	1234(5)[72]		$\nu_{as}(CCC)$
	1247(19)[5]		1242(16)[56]				
	1121(1)[5]		1122(1)[4]				o.o.p.(CCC) def + $\delta(CH_3)$
	1120(0)[4]		1122(0)[2]		1121(0)[3]		
1072(6)	1089(2)[0]	1070(8)	1090(2)[0]	1067(6)	1085(2)[0]		$\rho_r(CH_3)$
	1089(1)[0]	1098(3)	1089(2)[0]				
	913(2)[8]		901(2)[8]		887(0)[0]		$\rho_r(CH_3)$
	910(2)[7]		900(2)[8]				
	890(1)[0]		889(1)[1]	908(2)	887(2)[9]		$\omega(CH_3)$
	890(1)[1]		889(0)[1]				
880sh	828(11)[281]						$\nu_s(SF_{2,\ eq})$
873(100)	839(108)[25]	868(26)	836(95)[158]				
850(6)	805(2)[438]						$\nu_{as}(SF_{2,\ eq})$
837(21)	797(28)[1]	833(9)	803(18)[251]				
798(20)	790(15)[5]	794(45)	788(22)[1]	788(37)	783(16)[2]		$\nu_s(CCC)$
794sh	790(7)[8]	805sh	788(5)[10]				
		778sh					
		712(4)					
662(2)	688(2)[975]						$\nu_{as}(SF_{2,\ ax})$

643(2)	650(2)[23]	n.o.	652(1)[555]				
541sh	543(1)[23]	561(3)	541(1)[10]	531(6)	535(1)[14]		$\delta_{i.p.}(CO)$
534sh	543(1)[1]	537sh	541(0)[12]				
526(36)	516(12)[7]	528(24)	506(10)[1]				$\nu_s(SF_{2,\,ax})$
519(35)	511(4)[8]						
494(4)	495(0)[0]	492(4)	493(0)[1]	494(3)	491(0)[1]		$\delta_{o.o.p.}(CO)$
	495(0)[1]		493(0)[0]				
	494(0)[3]						
	491(0)[12]						$\delta_{sc}(SF_{2,\,ax}) + \delta_{sc}(SF_{2,\,eq})$
452(6)	486(1)[23]	450(3)	486(1)[28]				
	481(1)[24]		486(0)[10]				
	429(1)[0]		423(1)[0]				$\tau(SF_2)$
	425(1)[0]	406sh					
400(5)	390(0)[5]	397(5)	387(1)[2]	396(2)	381(1)[2]		$\delta(CCC)$
	389(0)[6]		387(1)[10]				
	334(0)[24]		332(0)[19]				$\delta_{sc,\,o.o.p.}(SF_{2,\,ax})$
	331(0)[2]						
249(4)	227(1)[1]	250(2)	234(2)[1]				$\delta_{sc}(SF_{2,\,ax}) - \delta_{sc}(SF_{2,\,eq})$
	223(1)[1]						
119(11)	127(0)[2]		132(0)[1]		132(0)[0]		$\tau(CH_3)$
	122(0)[3]		129(0)[0]		28(0)[0]		
	117(1)[2]		113(0)[2]				
	107(1)[0]						
	102(0)[1]						
	94(0)[4]		88(0)[2]				SF_4 + Acetone Combination Modes
	91(0)[2]		84(0)[3]				
	84(1)[3]		81(0)[3]				
	75(0)[0]		74(0)[1]				
	66(1)[1]		64(1)[2]				

	63(0)[0]		64(1)[0]				
	53(0)[0]		61(1)[0]				
	48(0)[1]		47(1)[0]				
	43(0)[1]		44(1)[2]				
	39(0)[0]						
	33(0)[0]						
	33(0)[1]						
	28(0)[0]						
	23(1)[1]		24(0)[2]				
	17(1)[1]		12(2)[2]				
	11(1)[1]		9(1)[1]				
	6(1)[2]		6(1)[2]				

[a] The abbreviations denote symmetric (s), asymmetric (as), stretch (ν), bend (δ), twist (τ), wagging (ω), rock (ρ_r), scissor (sc), in-plane (i.p.), out-of-plane (o.o.p.), equatorial (eq), axial (ax), shoulder (sh), and not observed (n.o.). [b] The Raman spectrum was recorded in a 5-mm glass NMR tube at –100 °C. [c] Unscaled Raman intensities, in $Å^4\ u^{-1}$, are given in parentheses; infrared intensities, in km mol^{-1}, are given in square brackets. [d] The Raman spectrum was recorded in a ¼-in. FEP tube at –110 °C. Signals from the FEP sample tube were observed at 1379sh, 1307(3), 1218(2), 751(2), 733(17), 576(2), 387(6), 381(6), and 294(6) cm^{-1} in the $[SF_4{\cdot}O{=}C(CH_3)_2]_2$ sample. Signals from the FEP sample tube were observed at 1506(3), 1217(4), 751(4), 733(26), 578(3), 387(8), 381(8), and 294(7) cm^{-1} in the $SF_4{\cdot}[O{=}C(CH_3)_2]_2$ sample. [e] Overlap with FEP band. Artifacts from the laser were observed at 85 cm^{-1}.

Table A.2.1 Bond Lengths (Å), Hydrogen Bonds (Å), and Bond Angles (°) of $[HO{=}C_{10}H_{14}][AsF_6]$.

Bond Lengths				
	exptl	*calcd*		*exptl*
H1−O1	0.82(3)	0.98	As1−F1	1.7759(10)
O1=C1	1.274(2)	1.285	As1−F2	1.7251(10)
C1−C6	1.472(2)	1.464	As1−F4	1.7162(10)
C1−C2	1.469(2)	1.468	As1−F5	1.7114(11)
C2−C3	1.568(2)	1.567	As1−F6	1.7114(11)
C2−C10	1.549(2)	1.567	As1−F3	1.7048(10)
C4−C3	1.530(2)	1.533		
C4−C5	1.530(3)	1.533		
C4−C7	1.535(2)	1.538		
C6−C5	1.565(2)	1.567		
C6−C9	1.549(2)	1.567		
C8−C10	1.531(2)	1.533		
C8−C9	1.534(2)	1.533		
C8−C7	1.533(2)	1.538		
F1---O1	2.6233(16)			
Bond Angles				
H1−O1=C1	111.8(18)	113.4		
O1=C1−C6	117.84(15)	118.3	F2−As1−F1	87.78(5)
O1=C1−C2	123.90(15)	123.6	F4−As1−F1	88.38(5)
C2−C1−C6	117.85(15)	118.1	F4−As1−F2	176.13(5)
C10−C8−C9	109.11(14)	109.0	F5−As1−F1	88.19(5)
C10−C8−C7	110.13(14)	110.1	F5−As1−F2	90.07(5)
C7−C8−C9	109.92(14)	110.1	F5−As1−F4	90.25(5)
C1−C6−C5	104.18(13)	107.1	F6−As1−F1	88.95(5)
C1−C6−C9	110.05(13)	107.1	F6−As1−F2	89.42(5)
C9−C6−C5	108.91(14)	108.8	F6−As1−F4	90.06(5)
C8−C10−C2	109.93(13)	109.4	F6−As1−F5	177.11(5)
C5−C4−C3	108.84(15)	109.0	F3−As1−F1	179.20(5)
C5−C4−C7	110.50(15)	110.1	F3−As1−F2	91.65(5)
C3−C4−C7	109.59(15)	110.1	F3−As1−F4	92.21(5)
C4−C5−C6	109.51(14)	109.6	F3−As1−F5	91.26(6)
C1−C2−C10	109.39(14)	107.2	F3−As1−F6	91.59(6)
C1−C2−C3	104.21(13)	107.2	As1−F1---O1	124.88(6)
C10−C2−C3	108.78(14)	108.9		
C8−C9−C6	109.55(13)	109.6		
C4−C3−C2	109.86(14)	109.4		
C8−C7−C4	109.51(14)	109.7		

C1=O1---F1	119.27(11)	
Torsion Angles		
H1−O1=C1−C6	172(2)	180.0
H1−O1=C1−C2	0(2)	0.0

Table A.2.2 Calculated Bond Lengths and Bond Angles of $O=C_{10}H_{14}$.

Bond Lengths (Å)			
C1=O1	1.211	C2−C7	1.546
C1−C2	1.520	C7−C9	1.537
C1−C6	1.520	C4−C8	1.538
C2−C3	1.546	C8−C9	1.538
C3−C4	1.537	C9−C10	1.537
C4−C5	1.537	C6−C10	1.546
C5−C6	1.546		
Bond Angles (°)			
O1=C1−C6	123.7	C5−C4−C3	109.2
O1=C1−C2	123.7	C5−C4−C7	100.0
C2−C1−C6	112.7	C3−C4−C7	58.7
C10−C8−C9	35.2	C4−C5−C6	109.8
C10−C8−C7	59.8	C1−C2−C10	57.2
C7−C8−C9	35.2	C1−C2−C3	108.3
C1−C6−C5	108.3	C10−C2−C3	99.6
C1−C6−C9	88.5	C8−C9−C6	89.9
C9−C6−C5	89.7	C4−C3−C2	109.8
C8−C10−C2	64.8	C8−C7−C4	31.4

Table A.2.3 Bond Lengths (Å), Hydrogen Bonds (Å), and Bond Angles (°) of $[HO{=}C_5H_8][PnF_6]$, Pn = As, Sb.

	exptl		*calcd*		*exptl*	
	Pn = As	Pn = Sb			Pn = As	Pn = Sb
Bond Lengths and Hydrogen Bonds						
H1−O1	0.90(5)	0.75(3)	0.980	Pn1−F1	1.7598(17)	1.9118(10)
O1=C1	1.266(3)	1.267(2)	1.275	Pn1−F2	1.6984(17)	1.8705(10)
C1−C2	1.473(3)	1.481(2)	1.470	Pn1−F3	1.696(2)	1.8690(10)
C1−C5	1.469(3)	1.477(2)	1.476	Pn1−F4	1.7130(18)	1.8808(10)
C2−C3	1.530(4)	1.539(2)	1.542	Pn1−F5	1.7060(17)	1.8736(10)
C3−C4	1.538(3)	1.542(2)	1.541	Pn1−F6	1.6986(19)	1.8680(10)
C4−C5	1.532(3)	1.536(2)	1.544			
O1---F1	2.560(3)	2.6043(17)				
Bond Angles						
H1−O1=C1	113(3)	112.1(19)	114.6	F2−Pn1−F1	87.43(9)	89.76(5)
O1=C1−C5	121.7(2)	120.90(15)	126.6	F3−Pn1−F1	179.55(10)	177.59(5)
O1=C1−C2	126.2(2)	126.83(16)	121.0	F4−Pn1−F1	89.05(10)	87.15(5)
C2−C1−C5	112.0(2)	112.26(14)	112.4	F5−Pn1−F1	88.78(10)	88.92(5)
C1−C5−C4	104.4(2)	103.78(13)	103.7	F6−Pn1−F1	87.67(11)	88.98(5)
C1−C2−C3	103.9(2)	103.10(13)	104.0	F3−Pn1−F2	92.22(11)	92.64(5)
C2−C3−C4	104.0(2)	103.74(13)	103.7	F2−Pn1−F4	176.46(11)	176.49(4)
C3−C4−C5	103.6(2)	103.16(13)	103.6	F2−Pn1−F5	90.83(10)	89.63(5)
C1=O1---F1	112.22(16)	104.68(11)		F2−Pn1−F6	91.00(12)	90.58(5)
				F3−Pn1−F4	91.30(12)	90.44(5)
				F3−Pn1−F5	91.52(11)	91.16(5)
				F3−Pn1−F6	92.05(13)	90.96(5)
				F5−Pn1−F4	88.78(9)	88.64(5)
				F6−Pn1−F4	89.17(11)	91.04(5)

				F6−Pn1−F5	175.93(12)	177.85(5)
				Pn1−F1---O1	139.14(11)	136.97(6)
Torsion Angles						
H1−O1=C1−C5	179(3)	177(2)	178.0			
H1−O1=C1−C2	−2(3)	−2(2)	−2.0			

Table A.2.4 Calculated Bond Lengths and Bond Angles of $O=C_5H_8$.

Bond Lengths (Å)		Bond Angles (°)	
C1=O1	1.205	O1=C1−C5	125.8
C1−C2	1.528	O1=C1−C2	125.8
C2−C3	1.533	C5−C1−C2	108.4
C3−C4	1.543	C1−C5−C4	105.0
C4−C5	1.533	C1−C2−C3	105.0
C5−C1	1.528	C2−C3−C4	104.1
		C5−C4−C3	104.1

Table A.2.5 Bond Lengths (Å), Hydrogen Bonds (Å), and Bond Angles (°) of $[HO=C(CH_3)_2][SbF_6]$.

Bond Lengths (Å)				
	exptl	*calcd*		*exptl*
H1−O1	0.76(4)	0.976	Sb2−F4	1.8670(14)
O1=C2	1.271(3)	1.277	Sb2−F5	1.8666(15)
C1−C2	1.459(4)	1.466	Sb2−F6	1.9176(15)
C2−C3	1.467(3)	1.470	Sb2−F7	1.8754(15)
H2−O2	0.94(4)		Sb2−F8	1.8676(14)
O2−C5	1.273(3)		Sb2−F9	1.8764(14)
C4−C5	1.464(4)		F6---O1	2.597(2)
C5−C6	1.469(4)		Sb3−F10^{ii}	1.9036(14)
Sb1−F1	1.8761(15)		Sb3−F10	1.9036(14)
Sb1−F1^{i}	1.8761(14)		Sb3−F11	1.8666(15)
Sb1−F2^{i}	1.8763(15)		Sb3−F11^{ii}	1.8666(15)
Sb1−F2	1.8763(15)		Sb3−F12^{ii}	1.8645(15)
Sb1−F3^{i}	1.8760(14)		Sb3−F12	1.8646(15)
Sb1−F3	1.8760(14)		F10---O2	2.619(2)
Bond Angles (°)				
C2=O1---F6	114.64(16)		F4−Sb2−F6	179.79(6)
H1−O1=C2	109(3)	115.0	F4−Sb2−F7	90.86(7)
O1=C2−C1	116.7(2)	115.8	F4−Sb2−F8	91.27(7)
O1=C2−C3	121.5(2)	121.4	F4−Sb2−F9	92.27(7)
C1−C2−C3	121.7(2)	122.8	F5−Sb2−F4	91.23(7)
C5=O2---F10	111.66(16)		F5−Sb2−F6	88.69(7)
H1−O2=C5	105(2)		F5−Sb2−F7	177.67(6)
O2=C5−C4	116.8(2)		F5−Sb2−F8	90.73(7)

O2=C5−C6	121.8(2)	F5−Sb2−F9	89.73(7)
C4−C5−C6	121.4(2)	F7−Sb2−F6	89.22(7)
F1−Sb1−F1^{i}	180.00(10)	F7−Sb2−F9	89.16(7)
F1^{i}−Sb1−F2	89.77(7)	F8−Sb2−F6	88.92(7)
F1^{i}−Sb1−F2^{i}	90.22(7)	F8−Sb2−F7	90.25(7)
F1−Sb1−F2	90.23(7)	F8−Sb2−F9	176.42(7)
F1−Sb1−F2^{i}	89.78(7)	F9−Sb2−F6	87.54(7)
F2^{i}−Sb1−F2	180	Sb2−F6---O1	144.21(9)
F3^{i}−Sb1−F1	90.29(7)	F10−Sb3−F10^{ii}	180.00(9)
F3−Sb1−F1	89.71(7)	F11−Sb3−F10	90.21(7)
F3−Sb1−F1^{i}	90.29(7)	F11−Sb3−F10^{ii}	89.79(7)
F3^{i}−Sb1−F1^{i}	89.71(7)	F11^{ii}−Sb3−F10	89.79(7)
F3^{i}−Sb1−F2	89.18(7)	F11^{ii}−Sb3−F10^{ii}	90.21(7)
F3^{i}−Sb1−F2^{i}	90.82(7)	F11^{ii}−Sb3−F11	180.00(10)
F3−Sb1−F2	90.82(7)	F12−Sb3−F10	90.12(7)
F3−Sb1−F2^{i}	89.18(7)	F12^{ii}−Sb3−F10^{ii}	90.12(7)
F3−Sb1−F3^{i}	180	F12−Sb3−F10^{ii}	89.88(7)
		F12^{ii}−Sb3−F10	89.88(7)
		F12^{ii}−Sb3−F11	89.56(7)
		F12−Sb3−F11^{ii}	89.56(7)
		F12−Sb3−F11	90.44(7)
		F12^{ii}−Sb3−F11^{ii}	90.44(7)
		F12^{ii}−Sb3−F12	180.00(10)
		Sb3−F10---O2	143.66(8)

Torsion Angles

H1−O1=C2−C1	179(3)	178.0
H1−O1=C2−C3	1(3)	−2.0

H2−O2=C5−C4	179(2)
H2−O2=C5−C6	−1(2)

Symmetry codes: (i) 2-x ,−y ,2−z; (ii) 1−x, 1−y, 2−z

Table A.2.6 Bond Lengths (Å), Hydrogen Bonds (Å), and Bond Angles (°) of $[H\{O{=}C(CH_3)_2\}_2]_3[HO{=}C(CH_3)_2]_3[SbF_6]_5F$.

Bond Lengths				
	exptl	*calcd*		*exptl*
O1---O2	2.450(3)	2.423	Sb1−F2	1.864(2)
O1−H1	1.13(7)	1.15	Sb1−F3	1.879(2)
O2−H1	1.33(7)	1.27	Sb1−F4	1.875(2)
O1−C2	1.241(4)	1.250	Sb1−F5	1.872(2)
O2−C5	1.242(4)	1.242	Sb1−F6	1.8725(19)
C1−C2	1.482(5)	1.482	Sb1−F7	1.871(2)
C2−C3	1.476(5)	1.486	Sb2−F8	1.868(2)
C4−C5	1.480(5)	1.491	Sb2−F9	1.872(2)
C5−C6	1.477(5)	1.487	Sb2−F10	1.867(2)
O3---O4	2.437(3)		Sb2−F11	1.870(2)
O3−H3	1.04(6)		Sb2−F12	1.869(2)
O4−H3	1.40(6)		Sb2−F13	1.873(2)
O3−C8	1.243(4)		Sb3−F14	1.858(3)
O4−C11	1.236(4)		Sb3−F15	1.883(2)
C7−C8	1.479(5)		Sb3−F16	1.847(3)
C8−C9	1.472(6)		Sb3−F17	1.850(2)
C10−C11	1.487(5)		Sb3−F18	1.855(2)
C11−C12	1.481(5)		Sb3−F19	1.862(3)
O5---O6	2.450(3)		Sb4−F20	1.862(3)
O5−H5	1.09(6)		Sb4−F21	1.863(3)
O6−H5	1.37(6)		Sb4−F22	1.846(3)
O5−C14	1.241(4)		Sb4−F23	1.876(2)
O6−C17	1.243(4)		Sb4−F24	1.851(3)
C13−C14	1.479(5)		Sb4−F25	1.877(2)
C14−C15	1.486(4)		Sb5−F26	1.874(2)
C16−C17	1.477(5)		Sb5−F27	1.874(2)
C17−C18	1.480(5)		Sb5−F28	1.861(2)
O7---F1	2.462(3)		Sb5−F29	1.866(2)
O7−H7	0.84(5)	0.976	Sb5−F30	1.873(2)
O7−C20	1.259(4)	1.277	Sb5−F31	1.873(2)
C19−C20	1.469(5)	1.466		
C20−C21	1.468(5)	1.470		
O8---F1	2.444(3)			
O8−H8	0.91(5)			
O8−C23	1.255(4)			
C22−C23	1.474(5)			
C23−C24	1.468(5)			

O9---F1	2.443(3)
O9−H9	0.89(6)
O9−C26	1.253(4)
C25−C26	1.465(5)
C26−C27	1.479(5)

Bond Angles				
O1−C2−C1	117.8(3)	118.1	F14−Sb3−F15	89.69(13)
O1−C2−C3	122.3(3)	122.0	F14−Sb3−F19	88.26(18)
C3−C2−C1	119.9(3)	119.9	F16−Sb3−F14	178.54(15)
O2−C5−C4	121.1(3)	122.0	F16−Sb3−F15	88.85(14)
O2−C5−C6	119.7(3)	118.9	F16−Sb3−F17	92.98(15)
C6−C5−C4	119.2(3)	119.1	F16−Sb3−F18	89.85(17)
O3−C8−C7	117.3(4)		F16−Sb3−F19	91.63(19)
O3−C8−C9	121.3(4)		F17−Sb3−F14	88.48(14)
C9−C8−C7	121.4(4)		F17−Sb3−F15	178.09(13)
O4−C11−C10	118.6(3)		F17−Sb3−F18	91.03(12)
O4−C11−C12	122.0(3)		F17−Sb3−F19	91.37(12)
C12−C11−C10	119.4(3)		F18−Sb3−F14	90.20(17)
O5−C14−C13	118.7(3)		F18−Sb3−F15	89.52(12)
O5−C14−C15	122.0(3)		F18−Sb3−F19	177.11(16)
C13−C14−C15	119.3(3)		F19−Sb3−F15	88.03(12)
O6−C17−C16	122.3(3)			
O6−C17−C18	117.9(3)		F20−Sb4−F21	89.44(17)
C16−C17−C18	119.8(3)		F20−Sb4−F23	88.58(13)
O7−C20−C19	117.1(3)	115.8	F20−Sb4−F25	88.81(15)
O7−C20−C21	121.5(3)	121.4	F21−Sb4−F23	177.93(15)
C21−C20−C19	121.4(3)	122.8	F21−Sb4−F25	89.94(12)
O8−C23−C22	122.4(3)		F22−Sb4−F20	177.27(19)
O8−C23−C24	117.0(4)		F22−Sb4−F21	92.0(2)
C24−C23−C22	120.7(4)		F22−Sb4−F23	89.92(16)
O9−C26−C25	121.9(3)		F22−Sb4−F24	90.8(2)
O9−C26−C27	117.4(3)		F23−Sb4−F25	88.89(17)
C25−C26−C27	120.7(3)		F24−Sb4−F20	89.42(10)
			F24−Sb4−F21	91.46(19)
F2−Sb1−F3	90.43(10)		F24−Sb4−F23	89.27(12)
F2− Sb1−F4	90.33(12)		F24−Sb4−F25	178.65(13)
F2− Sb1−F5	178.76(11)			
F2− Sb1−F6	90.27(10)		F27−Sb5−F26	88.29(14)
F2− Sb1−F7	90.56(13)		F28−Sb5−F26	179.24(14)
F4− Sb1−F3	89.84(10)		F28−Sb5−F27	90.97(13)

F5− Sb1−F3	90.61(10)	F28−Sb5−F29	90.23(12)
F5− Sb1−F4	90.34(11)	F28−Sb5−F30	89.79(12)
F5− Sb1−F6	88.69(10)	F28−Sb5−F31	90.94(13)
F6− Sb1−F3	179.25(10)	F29−Sb5−F26	90.51(13)
F6− Sb1−F4	89.88(10)	F29−Sb5−F27	178.73(13)
F7− Sb1−F3	89.94(11)	F29−Sb5−F30	90.35(10)
F7− Sb1−F4	179.08(12)	F29−Sb5−F31	89.40(12)
F7− Sb1−F5	88.77(12)	F30−Sb5−F26	90.02(11)
F7− Sb1−F6	90.33(10)	F30−Sb5−F27	89.21(10)
		F30−Sb5−F31	179.23(13)
F8−Sb2−F9	88.74(11)	F31−Sb5−F26	89.26(13)
F8−Sb2−F11	90.14(11)	F31−Sb5−F27	91.02(12)
F8−Sb2−F12	90.62(11)		
F8−Sb2−F13	178.87(10)	O1−H1−O2	169(6)
F9−Sb2−F13	90.18(10)	O3−H3−O4	176(5)
F10−Sb2−F8	89.57(11)	O6−H5−O5	175(5)
F10−Sb2−F9	90.12(13)	O7−H7−F1	171(5)
F10−Sb2−F11	90.33(14)	O8−H8−F1	179(5)
F10−Sb2−F12	179.48(13)	O9−H9−F1	170(7)
F10−Sb2−F13	90.78(11)		
F11−Sb2−F9	178.80(12)		
F11−Sb2−F13	90.93(11)		
F12−Sb2−F9	89.40(13)		
F12−Sb2−F11	90.15(13)		
F12−Sb2−F13	89.02(10)		

Table A.2.7 Calculated Bond Lengths and Bond Angles of $O=C(CH_3)_2$.

Bond Lengths (Å)		Bond Angles (°)	
O1=C2	1.210	O1=C2−C1	121.7
C1−C2	1.514	O1=C2−C3	121.7
C2−C3	1.514	C1−C2−C3	116.6

Table A.2.8 Bond Lengths (Å), Hydrogen Bonds (Å), and Bond Angles (°) of $[H(O{=}CHC_6H_5)_2][SbF_6]$.

Bond Lengths				
	exptl	*calcd*		*exptl*
O1---O1A	2.425(4)	2.415	Sb1−F1^{i}	1.8657(19)
H1−O1	1.213(3)	1.140/1.276	Sb1−F1	1.8657(19)
O1=C1	1.248(3)	1.256/1.246	Sb1−F2^{i}	1.8762(16)
C1−C2	1.441(4)	1.423/1.433	Sb1−F2	1.8762(16)
C2−C3	1.399(4)	1.410/1.407	Sb1−F3	1.8750(16)
C2−C7	1.397(4)	1.408/1.405	Sb1−F3^{i}	1.8750(16)
C3−C4	1.380(4)	1.378/1.380		
C4−C5	1.396(4)	1.398/1.397		
C5−C6	1.384(4)	1.393/1.392		
C6−C7	1.384(4)	1.382/1.382		
Bond Angles				
	exptl	*calcd*		*exptl*
H1−O1=C1	114.1(2)	114.8/118.8	F1^{i}−Sb1−F1	180
O1=C1−C2	122.0(3)	123.7/124.1	F1−Sb1−F2	88.69(10)
C3−C2−C1	120.5(2)	121.7/121.5	F1^{i}−Sb1−F2^{i}	88.69(10)
C7−C2−C1	119.0(2)	118.1/118.4	F1^{i}−Sb1−F2	91.31(10)
C7−C2−C3	120.4(2)	120.2/120.2	F1−Sb1−F2^{i}	91.31(10)
C4−C3−C2	120.1(3)	119.4/119.5	F1^{i}−Sb1−F3	90.65(11)
C3−C4−C5	119.2(3)	119.9/119.9	F1−Sb1−F3^{i}	90.65(11)
C6−C5−C4	120.9(3)	121.1/121.0	F1−Sb1−F3	89.35(11)
C5−C6−C7	120.1(3)	119.5/119.5	F1^{i}−Sb1−F3^{i}	89.35(11)
C6−C7−C2	119.3(2)	119.9/119.9	F2^{i}−Sb1−F2	180
			F3^{i}−Sb1−F2	89.64(8)
			F3−Sb1−F2	90.36(8)
			F3−Sb1−F2^{i}	89.64(8)
			F3^{i}−Sb1−F2^{i}	90.36(8)
			F3−Sb1−F3^{i}	180
Torsion Angles				
H1−O1=C1−C2	178.8(2)	−180.0		

Symmetry codes: (i) 2−x, 1−y, 2−z

Table A.2.9 Calculated Bond Lengths (Å) and Bond Angles (°) of $O{=}CHC_6H_5$.

Bond Lengths (Å)		Bond Angles (°)	
O1=C2	1.208	O1=C1−C2	125.0
C1−C2	1.478	C3−C2−C1	119.5
C2−C3	1.394	C7−C2−C1	120.7
C3−C4	1.389	C7−C2−C3	119.8
C4−C5	1.390	C4−C3−C2	120.3
C5−C6	1.395	C3−C4−C5	119.7
C6−C7	1.385	C6−C5−C4	120.3
C7−C2	1.398	C5−C6−C7	120.0
		C6−C7−C2	119.9

Table A.2.10 Bond Lengths (Å), Hydrogen Bonds (Å), and Bond Angles (°) of $[H(O{=}CHCH_3)_2][SbF_6]$.

Bond Lengths				
	exptl	*calcd*		*exptl*
O1---O2	2.4449(19)	2.419	Sb1−F4	1.8765(12)
H1−O1	0.88(4)	1.170	Sb1−F5	1.8847(11)
O1=C2	1.239(2)	1.240	Sb1−F6	1.8828(11)
H1−O2	1.58(4)	1.250	Sb1−F3	1.8739(11)
O2=C3	1.232(2)	1.233	Sb1−F1	1.8739(11)
C3−C4	1.471(3)	1.472	Sb1−F2	1.8861(11)
C1−C2	1.457(3)	1.464		
Bond Angles				
	exptl	*calcd*		*exptl*
C2=O1---O2	122.57(13)	115.1	F4−Sb1−F6	178.34(5)
C3=O2---O1	123.97(13)	125.2	F4−Sb1−F2	90.77(5)
O2=C3−C4	122.04(18)	126.0	F5−Sb1−F2	89.55(5)
H1−O1=C2	116(2)	117.0	F6−Sb1−F5	89.29(5)
O2---O1−H1	7(2)	2.0	F6−Sb1−F2	87.87(5)
H1---O2---O1	3.9(13)	1.9	F3−Sb1−F4	90.45(5)
O1=C2−C1	125.37(17)	122.6	F3−Sb1−F5	178.84(5)
F1−Sb1−F4	90.15(5)		F3−Sb1−F6	90.49(5)
F1−Sb1−F5	89.35(5)		F3−Sb1−F2	89.30(5)
F1−Sb1−F6	91.20(5)			
F1−Sb1−F3	91.80(5)			
F1−Sb1−F2	178.57(5)			

F4−Sb1−F5	89.75(5)	
	Torsion Angles	
	exptl	*calcd*
H1−O2=C3−C4	−177.1(16)	180.0

Table A.2.11 Calculated Bond Lengths and Bond Angles of $O{=}CHCH_3$.

Bond Lengths (Å)		Bond Angles (°)	
C1=O1	1.205	O1=C1−C2	124.8
C1−C2	1.501		

Table A.2.12 Observed and Calculated (B3LYP/aug-cc-pVTZ) Frequencies for 2-Adamantanone ($O=C_{10}H_{14}$), $[HO=C_{10}H_{14}][AsF_6]$, and $[HO=C_{10}H_{14}][SbF_6]$.

2-Adamantanone ($O=C_{10}H_{14}$)		$[HO=C_{10}H_{14}][AsF_6]$		$[HO=C_{10}H_{14}][SbF_6]$		$[HO=C_{10}H_{14}]^+$	
Exptl [b]	*Calcd* [c]	*Exptl* [d]	*Exptl* [e]	*Calcd* [c]		*Tentative Cation Assignments* [a]
				3647(120)[157]		ν(OH)
	3071(275)[16]	2996(29)	2990(35)	3099(130)[3]		
	3070(79)[42]	2977(29)	2974(30)	3092(128)[7]		
2936sh	3053(178)[49]	2961(54)	2961(49)	3091(114)[7]		
	3051(78)[55]			3091(44)[11]		
	3050(134)[52]			3089(9)[2]		
	3048(0)[0]		2957(42)	3078(45)[12]		
	3043(30)[19]	2947(52)	2940(65)	3063(582)[1]		
2920(100)	3037(515)[70]			3060(54)[23]		
	3032(71)[100]	2925(34)	2931(45)	3051(106)[25]		
	3015(45)[78]	2911(13)	2914(13)	3047(71)[7]		Overtones or combination modes
2907sh	3014(154)[2]			3046(72)[9]		and ν(C−H)
	3013(45)[0]			3045(57)[5]		
	3013(52)[16]			3040(55)[14]		
	3009(59)[17]			3040(48)[2]		
2883sh		2875(9)	2897(9)			
2853(56)		2867(11)	2870(14)			
2691(5)			2860(7)			
2627(3)						
2405(3)						
2329(3)						
1730sh		1578(2)	1578(2)			ν(CO)
1719(13)	1779(17)[280]	1564(11)	1561(11)	1555(8)[184]		

1700sh				1552(2)		1551(3)				
		1518(3)[0]				1529(1)		1520(1)[9]		$\delta(CH_2)$
		1502(0)[9]						1511(0)[53]		
		1500(0)[14]						1504(0)[13]		
1471(5)		1492(10)[6]		1478(5)		1477(4)		1494(11)[37]		$\delta(CH_2)$
1441sh				1463(3)		1456sh				
1436(24)		1486(16)[0]		1446(34)		1446(27)		1487(14)[0]		
				1437(15)		1437(13)		1461(0)[70]		$\delta(C_{C=O}OH) + \delta(CH_2)$
		1395(1)[0]						1393(0)[1]		$\omega(CH_2)$
		1390(0)[0]		1366(5)		1366(4)		1388(2)[1]		$\delta(CH) + \omega(CH_2)$
		1382(0)[1]		1359(4)		1360(3)		1374(1)[63]		
1350(8)		1381(3)[0]		1351(5)		1352(4)		1368(2)[0]		
		1379(1)[1]						1365(1)[9]		$\delta(CH) + \omega(CH_2) + \delta(OH)$
		1356(0)[0]						1354(0)[0]		$\delta(CH) + \omega(CH_2)$
		1352(0)[0]						1346(0)[0]		$\delta(CH) + \omega(CH_2)$
		1339(2)[5]		1337(3)		1337(15)		1337(0)[25]		$\delta(CH) + \delta(OH)$
						1318sh				
		1325(2)[0]		1310(4)		1312(2)		1320(1)[1]		$\delta(CH) + \omega(CH_2)$
		1311(0)[4]								
1284(5)		1310(3)[0]		1290(11)		1290(8)		1302(2)[0]		
		1285(0)[1]		1252(5)		1254(3)		1296(3)[16]		
1249(34)		1271(12)[0]		1240(40)		1240(36)		1253(17)[0]		$\delta(CH) + \tau(CH_2)$
1235(11)		1256(3)[12]		1228(34)		1229(29)		1236(27)[15]		
1205(50)		1228(22)[0]		1207(39)		1206(36)		1228(4)[22]		
				1144(4)		1142(4)		1192(3)[89]		$\delta(OH) + \delta(CH)$
1140(13)		1158(4)[0]		1141(4)				1150(0)[1]		$\delta(CH) + \omega(CH_2)$
		1135(0)[0]						1138(0)[0]		

		1133(0)[0]		1119(4)		1119(3)		1132(0)[0]		
1098(16)		1118(4)[0]		1096(15)		1097(15)		1115(2)[3]		$\delta(CH) + \omega(CH_2)$
1091(16)		1110(4)[0]		1071(6)		1071(6)		1107(2)[4]		
1064(26)		1080(6)[2]		1065(14)		1064(15)		1072(2)[58]		$\delta(OH) + \delta(CH)$
		1064(0)[30]		1044(2)		1044(2)		1067(5)[0]		$\nu(CC) + \omega(CH_2)$
		1055(1)[0]								$\rho(CH_2)$
1035(11)		1047(1)[3]		1027(8)		1027(7)		1034(0)[1]		$\nu(CC) + \omega(CH_2)$
		1036(1)[0]		1021(11)		1020(9)		1033(1)[13]		ring mode
997(16)		1005(4)[1]		989(20)		989(18)		1006(4)[3]		
956(37)		965(6)[2]		960(24)		959(23)		988(7)[0]		ring mode
		959(7)[2]						954(6)[5]		
		906(0)[0]		953(18)		952(15)		952(11)[8]		
		896(0)[0]		887sh		888(2)		895(0)[2]		$\tau(CH_2)$
		893(0)[4]		877(3)		880(3)		893(1)[5]		$\tau(CH_2)$
								885(0)[4]		ring mode
875(10)		876(1)[6]		871(6)		869(6)		871(1)[30]		ring mode (symmetric)
835(8)		837(1)[1]		811(2)		811(2)		820(0)[1]		$\delta_{o.o.p.}(C=O)$
		812(0)[0]						804(0)[4]		ring mode (asymmetric)
		782(0)[0]		790(8)		790(7)		791(2)[1]		ring mode (symmetric)
778(50)		776(13)[0]		777(11)		778(11)		784(1)[4]		ring mode (asymmetric) + $\delta_{o.o.p.}(C_{C=O}OH)$
								744(1)[85]		$\delta(OH)$
717(68)		714(19)[2]		744(100)		743(100)		742(31)[0]		ring mode (breathing mode)
615(5)		626(1)[3]		621(15)		622(22)		627(2)[1]		ring mode
		625(1)[0]						622(0)[4]		ring mode
598(26)		604(5)[0]		593(24)		591(23)		597(9)[1]		ring mode
466(8)		469(0)[11]		467(9)		467(8)		441(0)[4]		$\delta_{i.p.}(C=O) + \rho_r(CH_2)$
433(13)		438(1)[0]		442(8)		443(7)		439(1)[0]		$\rho_r(CH_2)$

		435(1)[0]		435(8)		435(7)		433(1)[10]		$\delta_{i.p.}$(C=O) + ρ_r(CH_2)
						393sh				
389(8)		397(2)[0]		386(16)[f]		388(15) [f]		391(2)[1]		ring mode
368(13)		371(2)[1]		363sh		363(4)		367(4)[0]		ring mode (breathing mode)
		366(0)[0]						363(0)[1]		ρ_r(CH_2)
						306(5)				
				289sh		286sh				
278sh		285(0)[0]		273(2)				270(0)[1]		ρ_r(CH_2)
273(5)		276(0)[1]						266(0)[2]		ρ_r(CH_2)
				139(5)		139(5)				
122(16)		108(1)[4]		121(3)		119(1)		79(0)[3]		$\delta_{o.o.p.}$(C=O)

[a] The abbreviations denote stretch (ν), bend (δ), twist (τ), wagging (ω), rock (ρ_r), in-plane (i.p.), and out-of-plane (o.o.p.). [b] The Raman spectrum was recorded in a 5-mm glass NMR tube at –100 °C. [c] Unscaled Raman intensities, in $Å^4\ u^{-1}$, are given in parentheses; infrared intensities, in km mol^{-1}, are given in square brackets. [d] The Raman spectrum was recorded in a ¼-in. FEP tube at –100 °C. Signals from the FEP sample tube were observed at 1396(6), 1305(5), 750sh, 733(25), 587(17), 381sh, 294(6) cm^{-1}. Signals from $[AsF_6]^-$ were observed at: 709(21), 703(17), 680(4), ν(T_{1u}); 671(63), ν(A_{1g}); 578(2), 536(5), ν(E_g); 406(2), 373(36), 366(20) cm^{-1}, ν(T_{2g}). [e] The Raman spectrum was recorded in a ¼-in. FEP tube at –100 °C. Signals from the FEP sample tube were observed at 1383(4), 1304(4), 1215(8), 750sh, 734(17), 587sh, 381sh, 292(6) cm^{-1}. Signals from $[SbF_6]^-$ were observed at: 674sh, 668(32), 662(17), ν(T_{1u}); 641(62), ν(A_{1g}); 540(6), ν(E_g); 282(18), 275(18), 266(7) cm^{-1}, ν(T_{2g}). [f] Overlap with FEP band. Artifact from laser observed at 84 cm^{-1}.

Table A.2.13 Observed and Calculated (B3LYP/aug-cc-pVTZ) Frequencies for Cyclopentanone ($O=C_5H_8$), $[HO=C_5H_8][AsF_6]$, and $[HO=C_5H_8][SbF_6]$.

Cyclopentanone ($O=C_5H_8$)		$[HO=C_5H_8]$ $[AsF_6]$		$[HO=C_5H_8]$ $[SbF_6]$		$[HO=C_5H_8]^+$		
Exptl [b]	*Calcd* [c]	*Exptl* [d]		*Exptl* [d]		*Calcd* [c]		*Tentative Cation Assignments* [a]
						3648(95)[196]		ν(OH)
				3030sh				
	3099(41)[23]	3020(22)		3023(23)		3138(60)[2]		
	3098(153)[6]	3010(27)		3014(36)		3133(97)[1]		
	3089(52)[31]	3000(15)		2999(36)		3087(116)[5]		
2969(100)	3085(173)[25]	2980(48)		2983(44)		3075(91)[1]		
		2968sh		2979sh				Overtones or
	3036(28)[41]	2947(10)		2959(20)		3070(53)[14]		combination modes
2901(84)	3029(57)[23]	2932(8)		2939(9)		3062(116)[2]		and ν(C−H)
				2910(10)				
2883(95)	3022(336)[1]	2893(31)		2897(23)		2965(200)[17]		
	3022(2)[5]	2877(43)		2882(86)		2962(26)[41]		
2798(7)		2849(5)						
2605(3)		2835(2)						
1743(16)	1806(15)[264]	1605(16)		1611(14)		1591(9)[211]		ν(CO)
1727(23)								
	1512(2)[2]					1514(2)[1]		δ(β-CH_2)
1470(11)	1500(8)[4]	1469(10)		1475(6)		1507(7)[12]		δ(β-CH_2)
						1430(1)[77]		δ($C_{C=O}OH$) + δ(α-CH_2)
1455(26)	1453(10)[0]	1459(17)		1465(15)		1402(18)[15]		δ(α-CH_2)
1409(25)	1452(1)[20]	1378(56)[f]		1378(38)[f]		1393(4)[95]		δ(α-CH_2)
	1346(0)[2]	1371sh		1371(12)		1354(1)[4]		δ(α-CH_2)

				1339(2)						
		1342(1)[0]		1321(4)		1320(4)		1327(1)[40]		$\omega(\alpha\text{-}CH_2) + \omega(\beta\text{-}CH_2)$
1313(5)		1308(2)[1]		1284(11)		1289(8)		1307(3)[4]		$\omega(\alpha\text{-}CH_2)$
1278(11)		1299(3)[5]		1277(11)		1277(5)		1292(2)[7]		$\omega(\alpha\text{-}CH_2)$
1269(11)		1257(3)[1]		1252(31)		1252(19)		1269(5)[15]		$\tau(CH_2)$
1232(13)		1222(1)[0]		1213(4)				1198(1)[2]		$\tau(\alpha\text{-}CH_2)$
1197(6)		1174(2)[1]		1186(5)		1188(3)		1187(1)[5]		$\tau(CH_2)$
		1169(1)[2]		1167(12)		1171(3)		1178(1)[12]		$\tau(CH_2) + \delta(C_{C=O}OH)$
1154(11)		1148(1)[71]				1162(4)				
								1099(1)[100]		$\delta(OH)$
1023(24)		1030(5)[1]		1024(31)		1019(19)		1017(5)[2]		Ring mode
960(11)		968(1)[9]		957(23)		958(13)		952(2)[10]		Ring mode
				943(3)		953sh				
		964(1)[0]						977(0)[8]		$\tau(CH_2)$
		925(0)[1]						904(1)[2]		Ring mode + $\rho(CH_2)$
892(93)		894(15)[0]		908(20)		902(19)		894(11)[2]		Ring mode
811(37)		810(5)[2]		898(13)		898(14)		856(9)[1]		Ring mode
				886(12)		880(7)				
		841(1)[10]		846(24)		843(15)		835(0)[12]		Ring mode
								761(1)[76]		$\delta_{o.o.p.}(OH)$
711(21)		707(6)[1]						663(5)[27]		Ring mode
583(11)		589(1)[3]		600(9)		600(8)		608(1)[1]		Ring mode
566 sh		569(3)[5]		536(13)		548(12)		539(3)[12]		Ring mode
473(16)		473(2)[5]		471(19)		466(8)		445(1)[6]		$\delta_{o.o.p.}(C=O) + \rho_r(\beta\text{-}CH_2)$
451(6)		452(1)[3]		439(3)		430(2)		419(0)[8]		$\delta_{i.p.}(C=O)$
242(3)		230(0)[0]		246(2)				227(1)[1]		$\rho_r(CH_2)$
				165(5)		172(4)				

						150(4)				
						147sh				
		97(0)[5]		115(9)		115(4)		119(0)[1]		
						105(6)				

[a] The abbreviations denote stretch (ν), bend (δ), twist (τ), wagging (ω), rock (ρ_r), in-plane (i.p.), and out-of-plane (o.o.p.). [b] The Raman spectrum was recorded in a 5-mm glass NMR tube at –100 °C. [c] Unscaled Raman intensities, in $Å^4\ u^{-1}$, are given in parentheses; infrared intensities, in km mol^{-1}, are given in square brackets. [d] The Raman spectrum was recorded in a ¼-in. FEP tube at –100 °C. Signals from the FEP sample tube were observed at 1508(4), 1306(7), 1218(4), 751(7), 733(48), 579(5), 386(14), 381(14), 294(12) cm^{-1}. Signals from $[AsF_6]^-$ were observed at: 718sh, 701(100), 684(24), 671(83), ν(T_{1u}), ν(A_{1g}); 592(17), 556(13), ν(E_g); 375(31), 363(29) cm^{-1}, ν(T_{2g}). [e] The Raman spectrum was recorded in a ¼-in. FEP tube at –100 °C. Signals from the FEP sample tube were observed at 1303(3), 1218(1), 751(3), 733(16), 580sh, 387(4), 381(4), 296(7) cm^{-1}. Signals from $[SbF_6]^-$ were observed at: 682(14), 670(6) ν(T_{1u}); 660(100), 641(50), ν(A_{1g}); 586(13), 556(13), ν(E_g); 306(4), 291(7), 282(19), 277(19), 269(9) cm^{-1}, ν(T_{2g}). Artifacts from the laser were observed at 84 cm^{-1}. [f] Overlap with FEP band.

Table A.2.14 Observed and Calculated (B3LYP/aug-cc-pVTZ) Frequencies for Acetone ($O=C(CH_3)_2$) and $[HO=C(CH_3)_2][SbF_6]$.

Acetone ($O=C(CH_3)_2$)		[HO=C(CH$_3$)$_2$][SbF$_6$]		[HO=C(CH$_3$)$_2$]$^+$		
Exptl [b]	*Calcd* [c]	*Exptl* [d]	*Calcd* [c]			*Tentative Cation Assignments* [a]
			3644(73)[183]			ν(OH)
3005(13)	3139(67)[6]	3040(10)	3158(47)[5]			
	3138(53)[12]		3133(41)[3]			
2963(14)	3084(95)[17]	2991(6)	3086(61)[11]			
	3077(12)[0]	2967(11)	3078(88)[8]			$\nu_s + \nu_{as}$ (CH_3)
2923(100)	3033(320)[7]	2928(25)	3008(222)[26]			
	3025(2)[1]	2921sh	2997(55)[61]			
2848(7)						
1751(3)						ν(CO)
1709(16)	1782(13)[195]	1593(10)	1588(4)[97]			
	1488(0)[19]	1487(1)	1490(1)[77]			$\delta(CH_2) + \delta(C_{C=O}OH)$
1428(10)	1470(12)[31]	1424(5)	1468(3)[47]			
	1466(8)[0]	1408(9)	1448(4)[60]			
	1460(1)[1]		1429(1)[64]			δ(CH_2)
			1409(9)[56]			
	1388(0)[54]	1348(22)	1375(16)[92]			
1358(3)	1388(2)[19]	1342sh	1366(7)[30]			
1222(6)	1234(5)[72]					ν_{as}(CCC)
			1160(2)[102]			δ(OH)
	1121(0)[3]		1099(1)[35]			o.o.p.(CCC) def + δ(CH_3)
1067(6)	1085(2)[0]	1074(4)	1080(2)[1]			$\rho_r(CH_3)$
	887(0)[0]		927(1)[21]			$\omega(CH_3) + \delta_{o.o.p.}(OH)$

						722(1)[85]		$\delta_{o.o.p.}$(OH)
908(2)		887(2)[9]				951(0)[15]		$\rho_r(CH_3)$
				840sh			]	
788(37)		783(16)[2]		835(19)		832(11)[8]	├	ν_s(CCC)
				817sh			]	
531(6)		535(1)[14]		539(22)		514(1)[12]		$\delta_{i.p.}$(CO)
494(3)		491(0)[1]		485(1)		485(0)[4]		$\delta_{o.o.p.}$(CO)
396(2)		381(1)[2]		412(6)		396(1)[0]		δ(CCC)
				232(2)				
				200(1)				
		132(0)[0]		134(10)		127(1)[1]		$\tau(CH_3)$
		28(0)[0]		109(7)		105(0)[1]		$\tau(CH_3)$

[a] The abbreviations denote symmetric (s), asymmetric (as), stretch (ν), bend (δ), twist (τ), wagging (ω), rock (ρ_r), in-plane (i.p.), and out-of-plane (o.o.p.). [b] The Raman spectrum was recorded in a 5-mm glass NMR tube at –100 °C. [c] Unscaled Raman intensities, in $Å^4$ u^{-1}, are given in parentheses; infrared intensities, in km mol^{-1}, are given in square brackets. [d] The Raman spectrum was recorded in a ¼-in. FEP tube at –100 °C. Signals from the FEP sample tube were observed at 1509(3), 1384(13), 1307(4), 1215(4), 750(4), 733(28), 387(14), 381(14), 294(16) cm^{-1}. Signals from $[SbF_6]^-$ anions were observed at: 683(9), 671(28), 662(50), 657(56), 645(100), $\nu(T_{1u})$, $\nu(A_{1g})$; 594(7), 582(10), $\nu(E_g)$; 280(51), 270sh cm^{-1}, $\nu(T_{2g})$. Artifacts from the laser were observed at 84 cm^{-1}.

Table A.2.15 Observed and Calculated (B3LYP/cc-pVTZ) Frequencies for Benzaldehyde ($O{=}CHC_6H_5$) and $[H(O{=}CHC_6H_5)_2][SbF_6]$.

Benzaldehyde ($O{=}CHC_6H_5$)				$[H(O{=}CHC_6H_5)_2][SbF_6]$				
Exptl [a]		*Calcd* [c]		*Exptl* [d]		*Calcd* [c]		*Tentative Cation Assignments* [a]
3066(24)		3197(213)[8]		3085(7)		3212(243)[1]	⎫	
						3211(240)[1]	⎪	
3054sh		3191(116)[13]				3208(102)[0]	⎪	
						3206(99)[1]	⎪	
3010(3)		3181(83)[13]		3069(4)		3199(91)[0]	⎪	$\nu(C_{aromatic}{-}H)$
						3197(97)[1]	⎭	
2975(3)		3169(87)[1]		3059(3)		3188(81)[0]	⎪	
						3186(77)[0]	⎪	
2826(4)		3159(45)[4]				3180(37)[0]	⎪	
						3176(42)[1]	⎭	
2743(5)		2877(146)[122]		2943(1)		3073(46)[11]		$\nu(C{-}H)$
						3032(56)[24]		$\nu(C{-}H)$
1698(46)		1776(82)[253]		1657sh		1712(11)[23]		$\nu_{as}(CO) + \delta(OH)$
1653(5)				1639(66)		1678(125)[61]		$\nu_{s}(CO) + \delta(OH)$
				1629sh		1652(12)[106]		$\delta(OH) + \nu(CO)$ + ring mode
1598(55)		1642(84)[30]				1644(3)[23]	⎫	
				1599(100)		1639(428)[13]	⎪	
1585(28)		1625(9)[12]				1611(12)[1]	⎪	
				1579(32)		1604(20)[11]	⎪	Ring modes
1492(2)		1527(1)[0]		1497(3)		1531(9)[0]	⎪	
						1529(2)[17]	⎪	
1457(4)		1492(2)[13]		1460(11)		1491(11)[9]	⎪	
						1488(6)[33]	⎭	
1426(1)		1423(2)[6]		1419(2)		1427(44)[6]		δ_s (C−H)
				1406(17)		1408(7)[92]		δ_{as}(C−H)

1391(2)		1356(1)[6]		1380sh		1376(6)[21]		
				1367(4)		1371(5)[16]		Ring mode
				1359(4)				
1312(2)		1338(1)[17]		1347(1)		1358(1)[0]		Ring mode
				1332(4)		1352(0)[18]		
				1324(2)		1299(0)[48]		$\delta_{o.o.p.}$(OH)
				1301sh				
1204(31)		1226(23)[55]		1266(3)		1278(15)[31]		Ring mode + $\delta_{i.p.}$(C−H)
				1256(2)		1268(8)[15]		
				1236(19)				
1167(15)		1191(10)[26]		1184(15)		1211(6)[235]		
				1174(9)		1205(10)[7]		
1162sh		1186(7)[3]		1168(14)		1200(9)[2]		Ring modes
						1198(8)[2]		
1073(1)		1104(1)[5]		1100(3)		1120(2)[145]		
				1075(3)		1117(1)[10]		
						1055(1)[0]		$\delta_{o.o.p.s.}$(C−H)
						1049(0)[0]		$\delta_{o.o.p.}$($C_{aromatic}$−H)
						1046(0)[0]		
1024(15)		1047(8)[3]		1026(10)		1046(22)[581]		Ring mode
						1042(23)[53]		
		1040(3)[1]				1037(0)[13]		$\delta_{o.o.p.as.}$(C−H)
						1028(20)[1744]		ν(OH) + Ring mode
1001(100)		1022(34)[1]		1015(2)		1019(76)[5]		Ring mode
989(5)		1022(0)[0]				1018(0)[0]		
						1017(0)[0]		Ring mode
		1003(0)[0]				977(0)[0]		
						973(0)[0]		

				999(95)		976(101)[9448]		ν(OH)
				987(2)				
		950(0)[1]		943(2)				
823(20)		871(1)[0]				866(0)[0]		$\delta_{o.o.p.}(C_{aromatic}-H)$
						863(0)[0]		$\delta_{o.o.p.}(C_{aromatic}-H)$
				852(38)		863(55)[217]		Ring mode
814sh		841(11)[33]				842(2)[419]		
		769(0)[43]				788(0)[14]	⎫	
				774(2)		785(0)[51]	⎬	$\delta_{o.o.p.}(C_{aromatic}-H)$
		710(0)[30]				695(0)[35]	⎭	
						690(0)[39]		
650(6)		664(3)[24]		637(18)		689(15)[2063]	⎫	Ring mode + ν(OH)
						645(5)[502]	⎭	
616(12)		633(5)[0]		619sh		628(12)[3]	⎫	Ring mode
				615(19)		626(5)[21]	⎭	
				577(8)		521(32)[1456]		Ring mode + ν(O---H)
447sh		469(0)[6]		465(3)		469(0)[1]	⎫	$\delta_{o.o.p.}(C_{aromatic}-H)$
						464(0)[23]	⎭	
439(14)		443(6)[0]				430(22)[842]		Ring mode + ν(OH)
		420(0)[0]				415(0)[0]	⎫	$\delta_{o.o.p.}(C_{aromatic}-H)$
						412(0)[0]	⎭	
				371(11)		356(1)[794]		$\nu(OH) + \rho_r(CCO)$
				315(3)				
238(5)		238(1)[7]		289(13)		273(0)[10]	⎫	$\delta_{o.o.p..}(C-H)$
						263(0)[16]	⎭	
225(5)		221(1)[8]		180sh		219(2)[178]		$\delta_{i.p.}(CO)$
131(25)		119(2)[4]		174(5)		156(0)[0]		$\delta_{o.o.p.}(CO)$
				137sh		129(0)[2]		$\delta_{o.o.p.}(CO)$ +ring mode

				129(31)		123(1)[131]	⎫	ρ_r(ring)
				120(36)		97(1)[12]	⎪	
				112sh			⎪	
90(46)				92(60)		76(16)[0]	⎬	ρ_r(ring) + ring modes
						25(0)[0]	⎪	
						18(0)[8]	⎪	
						8(0)[2]	⎭	

[a] The abbreviations denote symmetric (s), asymmetric (as), stretch (ν), bend (δ), twist (τ), wagging (ω), rock (ρ_r), in-plane (i.p.), and out-of-plane (o.o.p.). [b] The Raman spectrum was recorded in a 5-mm glass NMR tube at –100 °C. [c] Unscaled Raman intensities, in $Å^4$ u^{-1}, are given in parentheses; infrared intensities, in km mol^{-1}, are given in square brackets. [d] The Raman spectrum was recorded in a ¼-in. FEP tube at –100 °C. Signals from the FEP sample tube were observed at 1509(2), 1383(7), 1305(6), 1216(8), 754(4), 733(28), 386(7), 381(7), 292sh cm^{-1}. Signals from $[SbF_6]^-$ anions were observed at: 719sh, 713sh, ν(T_{1u}); 677sh, 671(43), 653(15), 647(60), 560(4), ν(A_{1g}) and ν(E_g); 280(28), 268sh cm^{-1}, ν(T_{2g}).

Table A.2.16 Observed and Calculated (B3LYP/aug-cc-pVTZ) Frequencies for Acetladehyde ($O{=}CHCH_3$), $[H(O{=}CHCH_3)_2][SbF_6]$, and $[H(O{=}CHCH_3)_2]^+$.

Acetaldehyde ($O{=}CHCH_3$)		$[H(O{=}CHCH_3)_2][SbF_6]$		$[H(O{=}CHCH_3)_2]^+$		
Exptl [b]	*Calcd* [c]	*Exptl* [d]	*Calcd* [c]			*Tentative Cation Assignments* [a]
		3125(3)				
3004(10)	3134(44)[9]	3047(11)	3159(37)[2]			
		3042(13)	3148(24)[2]			
2963(15)	3073(61)[6]		3064(161)[4]			
			3062(72)[4]			
2916(100)	3022(193)[2]	3032(10)	3054(95)[7]			
		3009(6)	3054(77)[5]			ν(C−H), combination modes
		2998sh				and overtones
2850(20)	2869(170)[119]	2984(13)	3019(185)[17]			
		2964(26)	3014(197)[23]			
		2956(26)				
2759(15)		2937(27)				
2740sh		2922(40)				
2681(4)		2914sh				
		1684(7)				splitting/coupling
		1670sh				splitting/coupling
1732sh		1665(15)	1740(7)[117]			ν(CO) of C=O---H
1712(33)	1805(13)[197]	1629(18)	1715(15)[51]			ν(CO) of C=O−H
			1626(1)[121]			$\delta_{i.p.}$(OHO)
		1432sh				
	1469(4)[10]	1419(20)	1462(12)[12]			$\delta_s(CH_3)$ H-bonded acetaldehyde
			1451(3)[20]			$\delta_{as}(CH_3)$ H-bonded acetaldehyde

1432(19)		1460(9)[23]		1406(29)		1448(8)[21]		$\delta_s(CH_3)$ prot acetaldehyde
						1446(4)[13]		$\delta_{as}(CH_3)$ prot acetaldehyde
						1441(2)[169]		$\delta(C_{C=O}{-}H)$ H-bonded acetaldehyde
1399(9)		1422(3)[10]		1393(12)		1416(2)[2]		$\delta(C_{C=O}{-}H)$ prot acetaldehyde
						1383(0)[61]		$\delta_{o.o.p.}(OHO)$
1349(6)		1379(2)[25]		1351(63)		1379(16)[70]		$\delta_s(CH_3)$ H-bonded acetaldehyde
				1347sh		1372(19)[114]		$\delta_s(CH_3)$ prot acetaldehyde
				1153(4)		1176(2)[20]		$\rho_r(CH_3)$
		1136(1)[0]		1142sh				$\delta_{o.o.p.}(C{-}H)$
1118(9)		1129(3)[25]		1137(8)		1166(6)[221]		$\rho_r(CH_3)$
				1118(11)		1150(1)[1]		$\delta_{o.o.p.}(C{-}H)$ prot acetaldehyde
						1144(0)[2]		$\delta_{o.o.p.}(C{-}H)$ H-bonded acetaldehyde
						987(3)[1945]		$\nu(OH) + \nu(CC)$ of prot acetaldehyde
888(7)		886(6)[10]				916(3)[53]		$\nu(CC)$ H-bonded acetaldehyde
						836(5)[3131]		$\nu(OH) + \rho_r(CH_3)$ of prot acetaldehyde
769(6)		775(3)[1]				809(2)[16]		$\delta_{o.o.p.}(C{-}H) + \omega(CH_3)$
						785(1)[1]		$\delta_{o.o.p.}(C{-}H) + \omega(CH_3)$
						591(1)[766]		$\nu(OH) + \delta(CCO)$ H-bonded acetaldehyde
515(16)		510(1)[13]		510(5)		489(2)[738]		$\nu(OH) + \delta(CCO)$
				503sh				
				348(3)		386(4)[117]		$\delta(CCO)$ H-bonded acetaldehyde
						240(1)[2]		$\rho_r(CH_2)$
						166(1)[0]		
107(24)		158(1)[1]		122(9)		150(1)[1]		$\rho_r(CH_2)$
						147(1)[7]		
						104(0)[0]		

						45(0)[19]		$\rho_r(CH_2)$
						44(0)[17]		

[a] The abbreviations denote symmetric (s), asymmetric (as), stretch (ν), bend (δ), twist (τ), wagging (ω), rock (ρ_r), in-plane (i.p.), and out-of-plane (o.o.p.). [b] The Raman spectrum was recorded in a 5-mm glass NMR tube at –100 °C. [c] Unscaled Raman intensities, in $Å^4$ u^{-1}, are given in parentheses; infrared intensities, in km mol^{-1}, are given in square brackets. [d] The Raman spectrum was recorded in a ¼-in. FEP tube at –100 °C. Signals from the FEP sample tube were observed at 1513(6), 1384(24), 1307(12), 1215(7), 750(5), 733(38), 387(9), 381(9), 294sh cm^{-1}. Signals from $[SbF_6]^-$ anions were observed at: 721sh, 712sh, $\nu(T_{1u})$; 657(93), 644(100) $\nu(A_{1g})$; 580(13), 570(16), 552(8), 540(4), 528(3), $\nu(E_g)$; 281(51), 262(4) cm^{-1}, $\nu(T_{2g})$. Some bands can be assigned to [**5**–H][SbF_6] including 2922(40), 1604(14), and 1325(20) for $[\mathbf{5}–H]^+$**,** and 570(16) and 528(3) for the $[SbF_6]^-$ anion. An artifact from the laser was observed at 85 cm^{-1}.

Table A.2.17 Observed and Calculated (B3LYP/aug-cc-pVTZ) Frequencies for Acetaldehyde ($O{=}CHCH_3$), $[HO{=}CHCH_3][SbF_6]$, and $[HO{=}CHCH_3]^+$.

Acetaldehyde ($O{=}CHCH_3$)		[$HO{=}CHCH_3$][SbF_6]		$[HO{=}CHCH_3]^+$		
Exptl [b]	*Calcd* [c]	*Exptl* [d]		*Calcd* [c]		*Tentative Cation Assignments* [a]
				3627(82)[297]		ν(OH)
3004(10)	3134(44)[9]	3125(3)		3162(28)[11]		
2963(15)	3073(61)[6]	3043(4)		3116(78)[0]		
		3030(3)				
		3015(2)				
		2987(3)				ν(C−H) + ν(CH_3)
		2980(3)				
2916(100)	3022(193)[2]	2965(8)		3014(68)[25]		
		2956sh				
		2935(7)				
2850(20)	2869(170)[119]	2921(24)		2986(175)[77]		
2759(15)						
2740sh						
2681(4)						
1732sh		1665(2)				
1712(33)	1805(13)[197]	1604(18)		1644(7)[137]		ν(CO)
	1469(4)[10]	1432sh				δ(CH_2)
1432(19)	1460(9)[23]	1421(8)		1437(3)[0]		δ(CH_3) + δ(C−H)
1399(9)	1422(3)[10]	1406(4)		1433(4)[101]		δ(C−H)
		1392(7)		1421(4)[20]		δ(CH_2)
		1351(8)				
1349(6)	1379(2)[25]	1325(22)		1336(21)[122]		δ(CH_2) + $\delta_{i.p.}$(C−H)
		1311sh		1298(4)[96]		$\delta_{i.p.}$(O−H) + δ(CH_3)

		1136(1)[0]		1134(4)		1143(1)[7]		$\delta_{o.o.p.}$(C−H)
1118(9)		1129(3)[25]						$\rho_r(CH_3)$
				1124(2)		1106(5)[56]		$\delta_{i.p.}$(O−H) + $\rho_r(CH_3)$
						939(1)[27]		$\delta_{o.o.p.}$(OH) + $\tau(CH_3)$ + $\delta_{o.o.p.}$(C−H)
769(6)		775(3)[1]						$\tau(CH_3)$ + $\delta_{o.o.p.}$(C−H)
888(7)		886(6)[10]		937(1)		928(3)[22]		ν(CC)
						657(1)[117]		$\delta_{o.o.p.}$(OH) + $\delta_{o.o.p.}(CH_3)$ + $\delta_{o.o.p.}$(C−H)
515(16)		510(1)[13]				492(1)[15]		$\rho_r(CH_3)$ + δ(CCO)
107(24)		158(1)[1]		117(7)		163(1)[0]		$\tau(CH_3)$

[a] The abbreviations denote symmetric (s), asymmetric (as), stretch (ν), bend (δ), twist (τ), wagging (ω), rock (ρ_r), in-plane (i.p.), and out-of-plane (o.o.p.). [b] The Raman spectrum was recorded in a 5-mm glass NMR tube at –100 °C. [c] Unscaled Raman intensities, in $Å^4$ u^{-1}, are given in parentheses; infrared intensities, in km mol^{-1}, are given in square brackets. [d] The Raman spectrum was recorded in a ¼-in. FEP tube at –100 °C. Signals from the FEP sample tube were observed at 1510(2), 1384(6), 1215(3), 751(3), 733(22), 386(4), 381(4), 292sh cm^{-1}. Signals from $[SbF_6]^-$ anion were observed at: 671(4), 663sh, $\nu(T_{1u})$; 653(100), 644(29), $\nu(A_{1g})$; 587(6), 570(19), 537(4), 527(7), $\nu(E_g)$; 307(7), 281(33), 265sh cm^{-1}, $\nu(T_{2g})$. An artifact from the laser was observed at 85 cm^{-1}.

a)

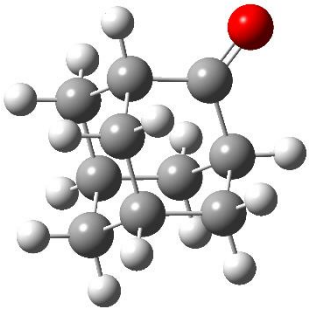

b) E = −195 kJ/mol

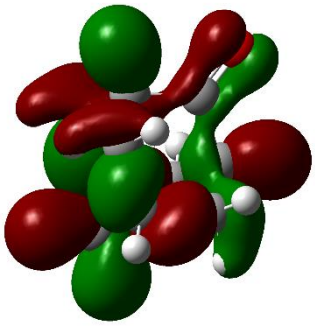

c) E = −151 kJ/mol

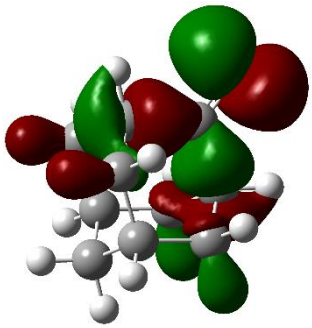

d) E = −13 kJ/mol

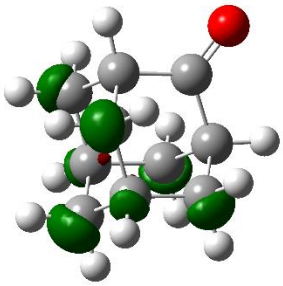

e) E = −12 kJ/mol

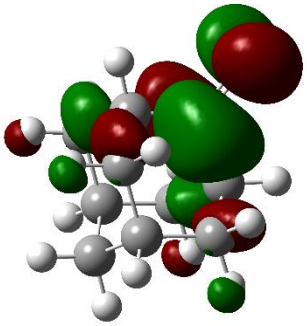

Figure A.2.1 Molecular orbitals and energies of 2-adamantanone: a) neutral 2-adamantanone for reference, b) HOMO−3 (MO 38), c) HOMO (MO 41), d) LUMO (MO 42), e) LUMO+1 (MO 43). Isovalue of 0.030.

a)

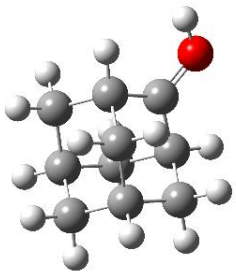

b) E = −410 kJ/mol

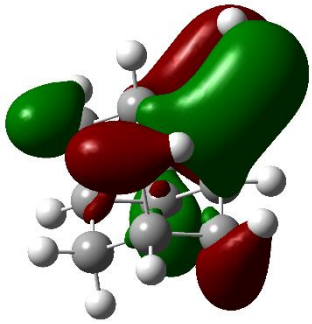

c) E = −287 kJ/mol

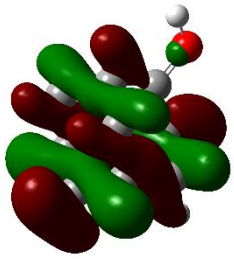

d) E = −286 kJ/mol

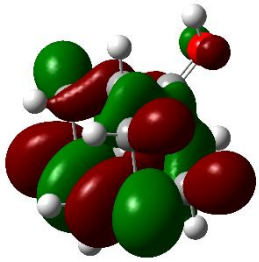

e) E = −163 kJ/mol

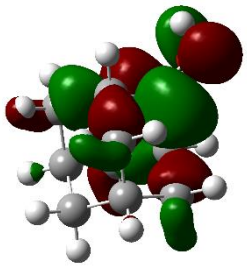

Figure A.2.2 Molecular orbitals and energies of protonated 2-adamantanone: a) protonated 2-adamantanone for reference, b) HOMO−16 (MO 25), c) HOMO−1 (MO 40), d) HOMO (MO 41), e) LUMO (MO 42). Isovalue of 0.030.

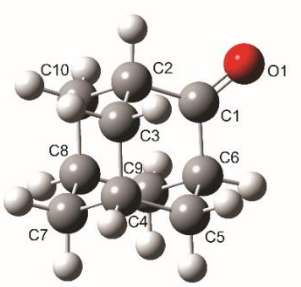

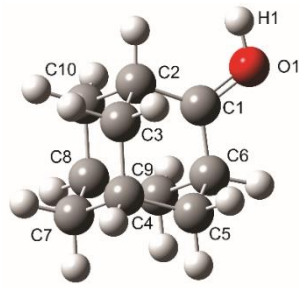

Table A.2.18 Natural Bond Order (NBO) Valences, Bond Orders, and Natural Population Analysis (NPA) Charges[a] for 2-Adamantanone ($O=C_{10}H_{14}$) and Cation $[HO=C_{10}H_{14}]^+$ in $[HO=C_{10}H_{14}][AsF_6]$.

$O=C_{10}H_{14}$			**$[HO=C_{10}H_{14}]^+$**		
	Natural Charges	*Valences*		*Natural Charges*	*Valences*
			H1	0.51	0.74
O1	−0.56	2.04	O1	−0.54	2.21
C1	0.61	3.87	C1	0.74	3.72
C2	−0.31	3.97	C2	−0.33	3.97
C3	−0.37	3.93	C3	−0.36	3.91
C4	−0.21	3.98	C4	−0.23	3.97
C5	−0.37	3.93	C5	−0.36	3.91
C6	−0.31	3.97	C6	−0.32	3.96
C7	−0.38	3.94	C7	−0.39	3.92
C8	−0.21	3.98	C8	−0.23	3.97
C9	−0.37	3.93	C9	−0.36	3.91
C10	−0.37	3.93	C10	−0.36	3.91
	Wiberg Bond Indices			*Wiberg Bond Indices*	
			O1−H1	0.70	
C1=O1	1.83		C1=O1	1.35	
C1−C2	0.97		C1−C2	1.08	
C1−C6	0.97		C1−C6	1.07	
C2−C10	0.98		C2−C10	0.94	
C2−C3	0.98		C2−C3	0.94	
C3−C4	1.00		C3−C4	1.01	
C4−C5	1.00		C4−C5	1.01	
C5−C6	0.98		C5−C6	0.94	
C6−C10	0.98		C6−C10	0.94	
C7−C4	1.00		C7−C4	1.00	
C8−C7	1.00		C8−C7	1.00	
C8−C9	1.00		C8−C9	1.01	
C9−C6	0.98		C9−C6	0.94	
C10−C8	1.00		C10−C8	1.01	

[a]The B3LYP/aug-cc-pVTZ level was used.

a)

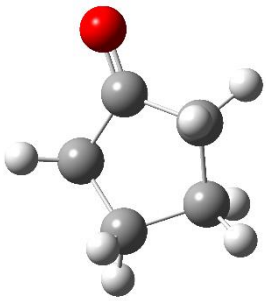

b) E = −218 kJ/mol

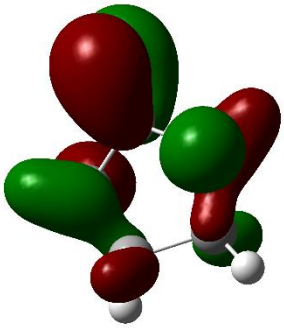

c) E = −216 kJ/mol

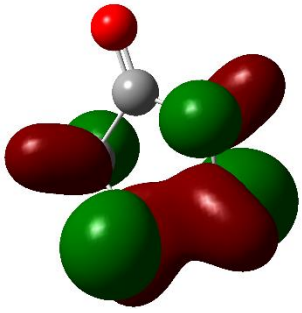

d) E = −157 kJ/mol

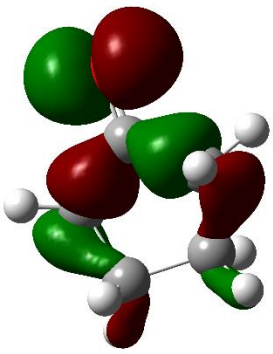

e) E = −20 kJ/mol

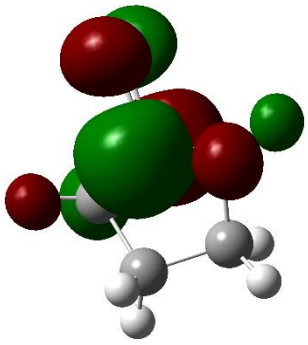

Figure A.2.3 Molecular orbitals and energies of cyclopentanone: a) neutral cyclopentanone for reference, b) HOMO−2 (MO 21), c) HOMO−1 (MO 22), d) HOMO (MO 23), e) LUMO (MO 24). Isovalue of 0.040.

a) E = −431 kJ/mol

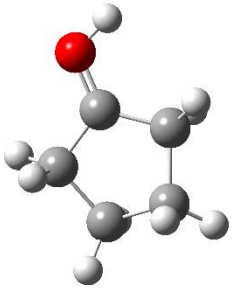

b) E = −403 kJ/mol

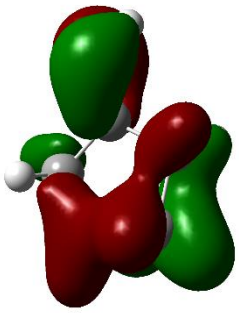

c) E = −323 kJ/mol

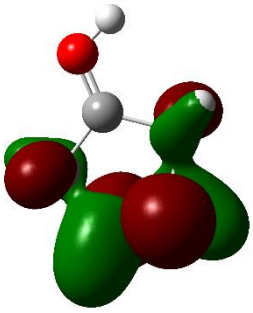

d) E = −181 kJ/mol

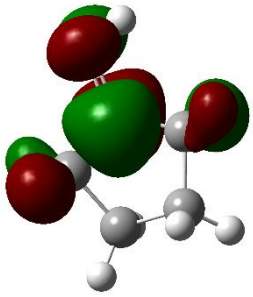

Figure A.2.4 Molecular orbitals and energies of protonated cyclopentanone: a) protonated cyclopentanone for reference, b) HOMO−7 (MO 16), c) HOMO (MO 23), d) LUMO (MO 24). Isovalue of 0.040.

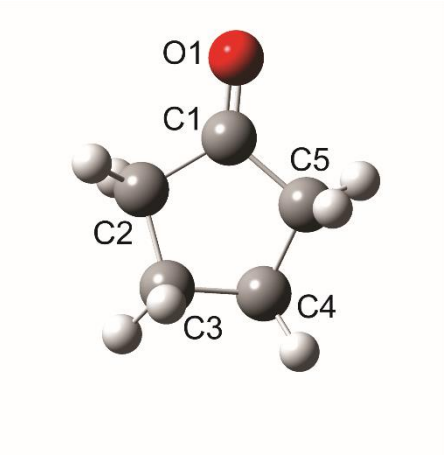

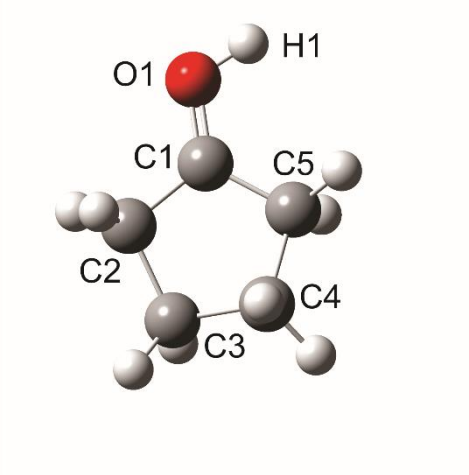

Table A.2.19 Natural Bond Order (NBO) Valences, Bond Orders, and Natural Population Analysis (NPA) Charges[a] for Cyclopentanone ($O{=}C_5H_8$) and Cation $[HO{=}C_5H_8]^+$ in $[HO{=}C_5H_8][AsF_6]$ and $[HO{=}C_5H_8][SbF_6]$.

	$O{=}C_5H_8$			**$[HO{=}C_5H_8]^+$**	
	Natural Charges	*Valences*		*Natural Charges*	*Valences*
			H1	0.52	0.73
O1	−0.54	2.06	O1	−0.52	2.23
C1	0.60	3.87	C1	0.74	3.71
C2	−0.50	3.92	C2	−0.51	3.90
C3	−0.38	3.93	C3	−0.38	3.90
C4	−0.38	3.93	C4	−0.38	3.90
C5	−0.50	3.92	C5	−0.53	3.90

	Wiberg Bond Indices		*Wiberg Bond Indices*
		O1−H1	0.70
C1=O1	1.84	C1=O1	1.39
C1−C2	0.98	C1−C2	1.09
C2−C3	1.02	C2−C3	1.00
C3−C4	1.01	C3−C4	1.01
C4−C5	1.02	C4−C5	0.99
C5−C1	0.98	C5−C1	1.09

[a]The B3LYP/aug-cc-pVTZ level was used.

a)

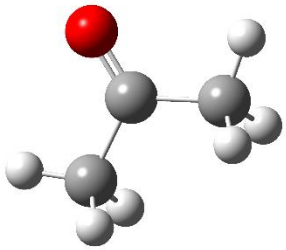

b) E = −226 kJ/mol

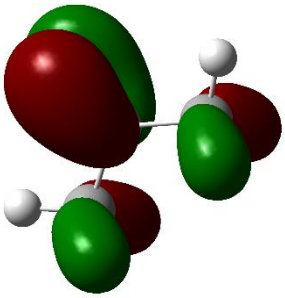

c) E = −162 kJ/mol

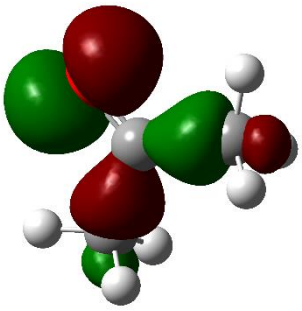

d) E = −18 kJ/mol

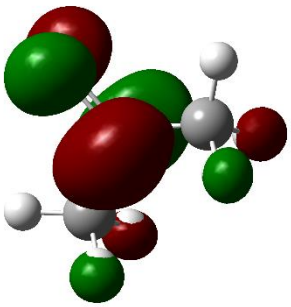

Figure A.2.5 Molecular orbitals of acetone: a) neutral acetone for reference, b) HOMO−1 (MO 15), c) HOMO (MO 16), d) LUMO (MO 17). Isovalue of 0.040.

a)

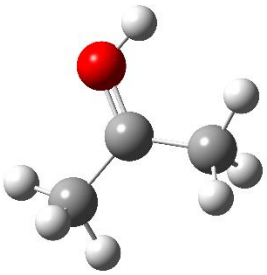

b) E = −447 kJ/mol

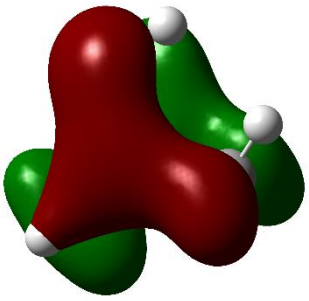

c) E = −384 kJ/mol

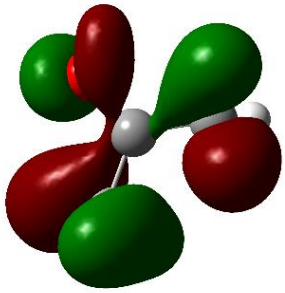

d) E = −376 kJ/mol

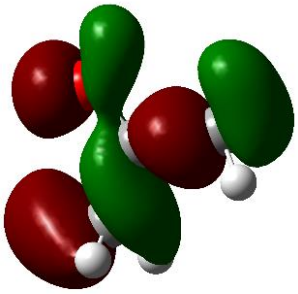

e) E = −189 kJ/mol

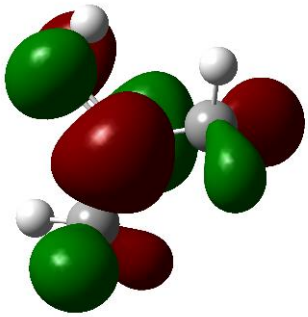

Figure A.2.6 Molecular orbitals of protonated acetone: a) protonated acetone for reference, b) HOMO−5 (MO 11), c) HOMO−1 (MO 15), d) HOMO (MO 16), e) LUMO (MO 17). Isovalue of 0.040.

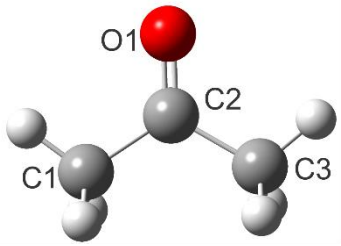

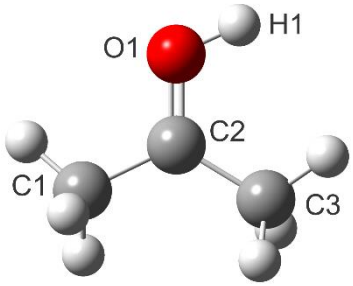

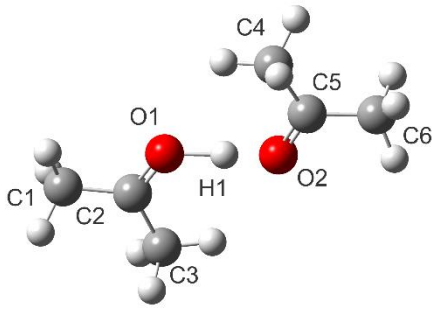

Table A.2.20 Natural Bond Order (NBO) Valences, Bond Orders, and Natural Population Analysis (NPA) Charges[a] for Acetone ($O=C(CH_3)_2$), Cation $[HO=C(CH_3)_2]^+$ in $[HO=C(CH_3)_2][SbF_6]$, and Cation $[H\{O=C(CH_3)_2\}_2]^+$ in $[H\{O=C(CH_3)_2\}_2]_3[HO=C(CH_3)_2]_3[SbF_6]_5F$.

$O=C(CH_3)_2$			**$[HO=C(CH_3)_2]^+$**			**$[H\{O=C(CH_3)_2\}_2]^+$**		
	Natural Charges	*Valences*		*Natural Charges*	*Valences*		*Natural Charges*	*Valences*
			H1	0.52	0.73	H1	0.49	0.77
O1	−0.55	2.04	O1	−0.52	2.23	O1	−0.57	2.18
C2	0.59	3.87	C2	0.73	3.71	C2	0.70	3.76
C1	−0.69	3.87	C1	−0.70	3.83	C1	−0.69	3.85
C3	−0.69	3.87	C3	−0.72	3.83	C3	−0.71	3.84
						O2	−0.59	2.13
						C5	0.68	3.77
						C4	−0.71	3.85
						C6	−0.69	3.85
	Wiberg Bond Indices			*Wiberg Bond Indices*			*Wiberg Bond Indices*	
			O1−H1	0.70		O1−H1	0.42	
C2=O1	1.83		C2=O1	1.39		C2=O1	1.53	

C1−C2	1.01	C1−C2	1.11	C1−C2	1.07
C3−C2	1.01	C3−C2	1.11	C3−C2	1.07
				O2−H1	0.31
				C5=O2	1.58
				C6−C5	1.06
				C4−C5	1.06
				O1---O2	0.06

[a]The B3LYP/aug-cc-pVTZ level was used.

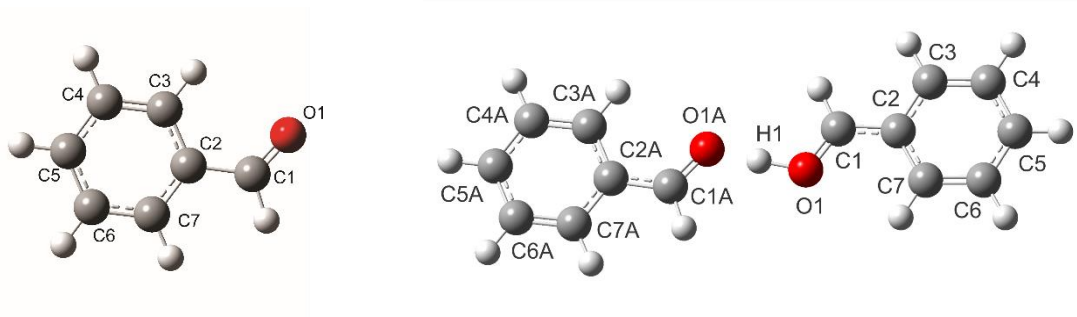

Table A.2.21 Natural Bond Order (NBO) Valences, Bond Orders, and Natural Population Analysis (NPA) Charges[a] for Benzaldehyde ($O{=}CHC_6H_5$) and Cation $[H(O{=}CHC_6H_5)_2]^+$ in $[H(O{=}CHC_6H_5)_2][SbF_6]$.

$O{=}CHC_6H_5$			**$[H(O{=}CHC_6H_5)_2]^+$**		
	Natural Charges	*Valences*		*Natural Charges*	*Valences*
			H1	0.49	0.76
O1	−0.52	2.06	O1/O1A	−0.56/−0.57	2.17/2.11
C1	0.41	3.85	C1/C1A	0.45/0.45	3.77/3.78
C2	−0.15	4.01	C2/C2A	−0.19/−0.19	4.01/4.01
C3	−0.15	3.96	C3/C3A	−0.11/−0.12	3.95/3.96
C4	−0.20	3.97	C4/C4A	−0.19/−0.19	3.96/3.96
C5	−0.17	3.97	C5/C5A	−0.10/−0.11	3.95/3.95
C6	−0.20	3.97	C6/C6A	−0.20/−0.20	3.96/3.96
C7	−0.17	3.97	C7/C7A	−0.11/−0.12	3.96/3.96
	Wiberg Bond Indices			*Wiberg Bond Indices*	
			O1−H1	0.70	
C1=O1	1.82		C1=O1	1.48/1.54	
C1−C2	1.05		C1−C2	1.22/1.18	
C2−C3	1.36		C2−C3	1.29/1.31	
C3−C4	1.47		C3−C4	1.51/1.50	
C4−C5	1.42		C4−C5	1.39/1.40	
C5−C6	1.44		C5−C6	1.42/1.43	
C6−C7	1.44		C6−C7	1.47/1.47	
C7−C2	1.39		C7−C2	1.31/1.33	

[a]The B3LYP/cc-pVTZ level was used.

a)

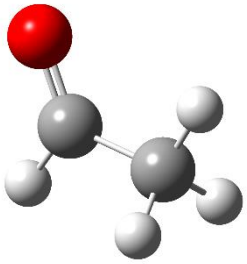

b) E = −218 kJ/mol

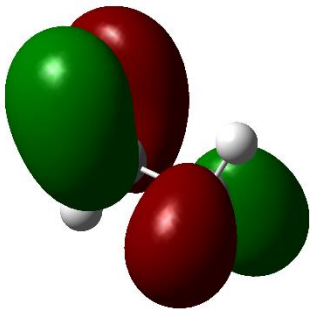

c) E = −216 kJ/mol

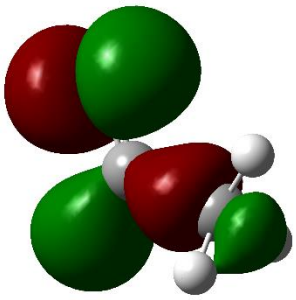

d) E = −157 kJ/mol

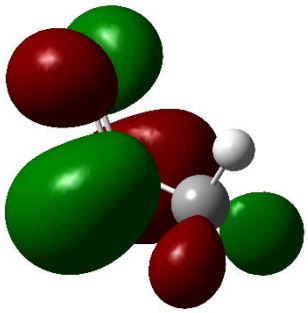

Figure A.2.7 Molecular orbitals and energies of acetaldehyde: a) neutral acetaldehyde for reference, b) HOMO−1 (MO 11), c) HOMO (MO 12), d) LUMO (MO 13). Isovalue of 0.040.

a)

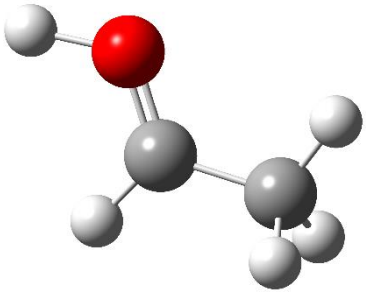

b) E = −451 kJ/mol

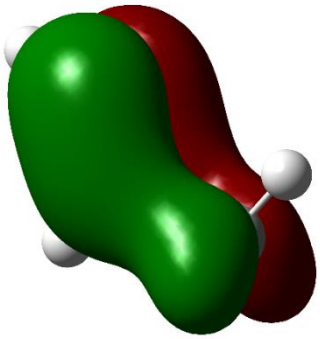

c) E = −382 kJ/mol

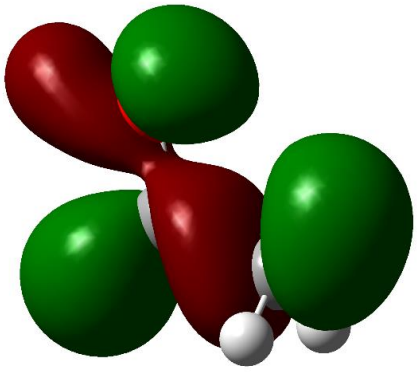

d) E = −201 kJ/mol

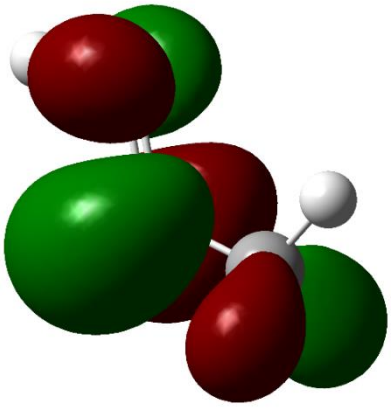

Figure A.2.8 Molecular orbitals and energies of protonated acetaldehyde: a) protonated acetaldehyde for reference, b) HOMO−3 (MO 9), c) HOMO (MO 12), d) LUMO (MO 13). Isovalue of 0.040.

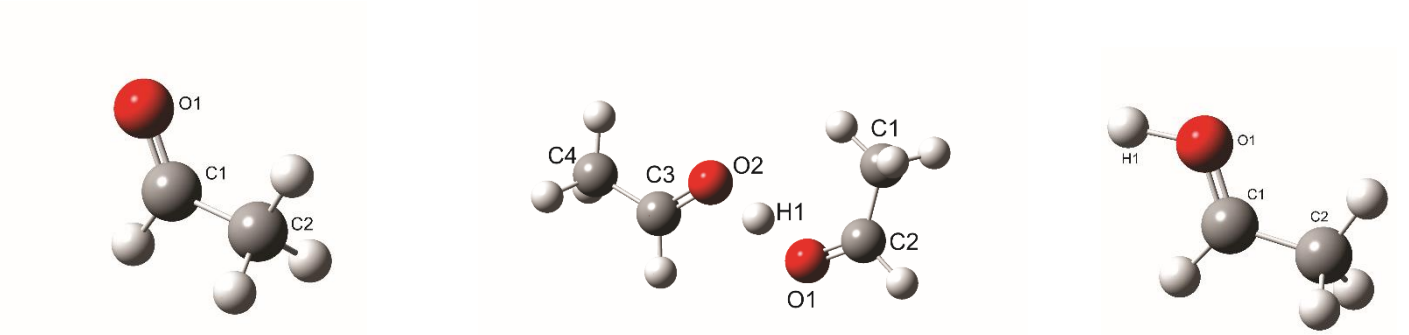

Table A.2.22 Natural Bond Order (NBO) Valences, Bond Orders, and Natural Population Analysis (NPA) Charges[a] for Acetaldehyde ($O{=}CHCH_3$), Cation $[H(O{=}CHCH_3)_2]^+$ in $[H(O{=}CHCH_3)_2][SbF_6]$, and cation $[HO{=}CHCH_3]^+$ in $[HO{=}CHCH_3][SbF_6]$.

$O{=}CHCH_3$			**$[H(O{=}CHCH_3)_2]^+$**			**$[HO{=}CHCH_3]^+$**		
	Natural Charges	*Valences*		*Natural Charges*	*Valences*		*Natural Charges*	*Valences*
			H1	0.49	0.50	H1	0.54	0.71
O1	−0.52	2.06	O1	−0.54	2.20	O1	−0.49	2.26
C1	0.44	3.83	C2	0.54	3.84	C1	0.57	3.61
C2	−0.69	3.87	C1	−0.71	3.69	C2	−0.72	3.82
			O2	−0.55	2.17			
			C3	0.53	3.70			
			C4	−0.72	3.84			
	Wiberg Bond Indices			*Wiberg Bond Indices*			*Wiberg Bond Indices*	
			O1−H1	0.40		O1−H1	0.69	
C1=O1	1.88		C2=O1	1.61		C1=O1	1.47	
C1−C2	1.03		C2−C1	1.11		C1−C2	1.16	
			O2−H1	0.33				
			C3=O2	1.65				
			C3−C4	1.10				

[a]The B3LYP/aug-cc-pVTZ level was used.

Table A.3.1 Calculated Bond Lengths (Å) and Bond Angles (°) of $AsF_5 \cdot O=C_{10}H_{14}$.

Bond Lengths			
O1=C1	1.240	As1−F1	1.706
C1−C6	1.501	As1−F2	1.721
C1−C2	1.497	As1−F3	1.740
C2−C3	1.554	As1−F4	1.740
C2−C10	1.554	As1−F5	1.721
C4−C3	1.534		
C4−C5	1.535	As1---O1	2.044
C4−C7	1.539		
C6−C5	1.551		
C6−C9	1.551		
C8−C10	1.535		
C8−C9	1.535		
C8−C7	1.539		
Bond Angles			
O1=C1−C6	118.08	F2−As1−F1	169.75
O1=C1−C2	127.14	F4−As1−F1	94.30
C2−C1−C6	114.78	F4−As1−F2	170.35
C10−C8−C9	108.84	F5−As1−F1	95.32
C10−C8−C7	109.85	F5−As1−F2	90.64
C7−C8−C9	109.80	F5−As1−F4	89.37
C1−C6−C5	107.99	F3−As1−F1	94.30
C1−C6−C9	107.99	F3−As1−F2	89.37
C9−C6−C5	109.44	F3−As1−F4	89.11
C8−C10−C2	110.17	F3−As1−F5	170.35
C5−C4−C3	108.84		
C5−C4−C7	109.79	As1---O1---C1	132.56
C3−C4−C7	109.85		
C4−C5−C6	109.55		
C1−C2−C10	107.38		
C1−C2−C3	107.38		
C10−C2−C3	109.24		
C8−C9−C6	109.55		
C4−C3−C2	110.17		
C8−C7−C4	109.74		
Torsion Angles			
As1−O1−C1−C2	0.00		
As1−O1−C1−C6	−180.00		

Table A.3.2 Calculated Bond Lengths (Å) and Bond Angles (°) of $AsF_5 \cdot O=C_5H_8$.

Bond Lengths			
O1=C1	1.232	As1−F1	1.704
C1−C2	1.500	As1−F2	1.738
C1−C5	1.504	As1−F3	1.738
C2−C3	1.536	As1−F4	1.720
C3−C4	1.541	As1−F5	1.719
C4−C5	1.535		
		As1---O1	2.064
Bond Angles			
O1=C1−C5	121.09	F2−As1−F1	94.65
O1=C1−C2	128.79	F4−As1−F1	95.66
C2−C1−C5	110.12	F4−As1−F2	169.64
C1−C5−C4	104.59	F5−As1−F1	95.67
C1−C2−C3	104.49	F5−As1−F2	89.40
C2−C3−C4	104.18	F5−As1−F4	90.55
C3−C4−C5	103.64	F3−As1−F1	94.61
		F3−As1−F2	88.84
		F3−As1−F4	89.37
		F3−As1−F5	169.68
		As1---O1---C1	130.27
Torsion Angles			
As1−O1−C1−C2	1.89		
As1−O1−C1−C5	−178.34		

Table A.3.3 Calculated Bond Lengths (Å) and Bond Angles (°) of $AsF_5 \cdot O=C(CH_3)_2$.

Bond Lengths			
O1=C2	1.237	As1−F1	1.706
C1−C2	1.493	As1−F2	1.721
C2−C3	1.491	As1−F3	1.722
		As1−F4	1.738
		As1−F5	1.740
		As1---O1	2.065
Bond Angles			
O1=C2−C1	117.15	F2−As1−F1	95.57
O1=C2−C3	124.25	F4−As1−F1	94.55
C1−C2−C3	118.60	F4−As1−F2	169.86
		F5−As1−F1	94.70
		F5−As1−F2	89.46
		F5−As1−F4	88.94
		F3−As1−F1	95.69
		F3−As1−F2	90.45
		F3−As1−F4	89.33
		F3−As1−F5	169.57
		As1---O1---C1	133.06
Torsion Angles			
As1−O1−C2−C1	179.32		
As1−O1−C2−C3	−1.30		

Table A.3.4 Observed and Calculated (B3LYP/cc-pVTZ) Frequencies for 2-Adamantanone ($O=C_{10}H_{14}$) and $AsF_5 \cdot O=C_{10}H_{14}$.

2-Adamantanone ($O=C_{10}H_{14}$)		$AsF_5 \cdot O=C_{10}H_{14}$		
Exptl [b]	*Calcd* [c]	*Exptl* [d]	*Calcd* [c]	*Tentative Assignments* [a]
	3071(275)[16]	3029(22)	3168(79)[1]	
	3070(79)[42]	2985(58)	3091(124)[12]	
2936sh	3053(178)[49]		3075(120)[24]	
	3051(78)[55]		3074(43)[19]	
	3050(134)[52]		3069(137)[30]	
	3048(0)[0]		3068(19)[8]	
	3043(30)[19]	2967(91)	3055(71)[30]	
2920(100)	3037(515)[70]	2961(89)	3051(553)[38]	
	3032(71)[100]	2953sh	3047(64)[75]	
	3015(45)[78]	2940(61)	3036(41)[33]	
2907sh	3014(154)[2]	2934(65)	3034(52)[0]	Overtones or combination modes
	3013(45)[0]	2925(59)	3031(93)[21]	and ν(C−H)
	3013(52)[16]	2919(57)	3030(58)[5]	
	3009(59)[17]	2901(18)	3020(65)[21]	
		2887(11)		
2883sh		2873sh		
2853(56)		2867(35)		
2691(5)				
2627(3)				
2405(3)				
2329(3)				
1730sh		1577(6)		ν(CO)
1719(13)	1779(17)[280]	1568(9)	1668(7)[513]	
1700sh		1553(3)		
	1518(3)[0]	1508(5)	1523(3)[0]	$\delta(CH_2)$
	1502(0)[9]		1505(0)[12]	
	1500(0)[14]		1503(0)[17]	
1471(5)	1492(10)[6]	1475(13)	1495(14)[13]	
1441sh		1459(4)		
1436(24)	1486(16)[0]	1444(50)	1489(17)[0]	
	1395(1)[0]	1383(18)	1398(2)[2]	$\omega(CH_2)$
	1390(0)[0]		1393(0)[1]	
	1382(0)[1]	1374(12)	1389(1)[6]	
1350(8)	1381(3)[0]	1366(12)	1388(3)[12]	$\delta(CH) + \omega(CH_2)$
	1379(1)[1]	1353(10)	1379(3)[0]	
	1356(0)[0]		1358(0)[0]	

		1352(0)[0]		1344(7)		1354(0)[3]		δ(CH)
		1339(2)[5]				1353(0)[0]		δ(CH) + ω(CH_2)
		1325(2)[0]		1325(4)		1324(1)[0]		δ(CH) + τ(CH_2)
				1311sh		1324(1)[2]		δ(CH) + ω(CH_2)
		1311(0)[4]		1307(16)		1313(1)[3]		δ(CH)
1284(5)		1310(3)[0]		1294(11)		1295(8)[13]		
		1285(0)[1]		1289(14)				ν($CC_{C=O}C$) + δ(CH)
				1271(18)				
1249(34)		1271(12)[0]		1249(6)		1271(7)[3]		
1235(11)		1256(3)[12]		1235(73)		1267(9)[3]		
				1232sh				δ(CH) + τ(CH_2)
				1214sh [e]				
1205(50)		1228(22)[0]		1207(43)		1241(28)[1]		
1140(13)		1158(4)[0]		1143(15)		1156(2)[0]		
		1135(0)[0]		1121(6)		1140(0)[0]		
		1133(0)[0]		1117(4)		1136(0)[0]		δ(CH)
1098(16)		1118(4)[0]		1096(25)		1121(2)[0]		
1091(16)		1110(4)[0]		1072(12)		1116(3)[0]		δ(CH) + ρ(CH_2)
1064(26)		1080(6)[2]		1063(27)		1078(7)[1]		δ(CH) + ω(CH_2)
		1064(0)[30]				1087(0)[29]		ν(CCC) + ω(CH_2)
		1055(1)[0]		1049(3)		1053(0)[0]		
1035(11)		1047(1)[3]		1031(12)		1046(1)[6]		
		1036(1)[0]		1024(17)		1034(3)[0]		
997(16)		1005(4)[1]		995(34)		1005(5)[1]		cage mode
956(37)		965(6)[2]		961(18)		965(7)[2]		
		959(7)[2]		957(15)		963(7)[3]		
				952(42)				
		906(0)[0]				904(0)[0]		
		896(0)[0]		905(2)		899(1)[2]		ρ(CH_2)
		893(0)[4]				899(0)[0]		ρ(CH_2)
				881(9)				
875(10)		876(1)[6]		875(22)		884(3)[5]		cage mode
835(8)		837(1)[1]				838(0)[0]		cage mode
		812(0)[0]				821(0)[0]		ring mode + $\delta_{o.o.p.}$(CO)
		782(0)[0]				787(0)[2]		
778(50)		776(13)[0]		787(18) 778(27)		786(7)[1]		cage mode
717(68)		714(19)[2]		751sh [e] 745(99)		735(11)[50]		cage breathing mode
				733(65) [e]		733(12)[114]		cage breathing mode + $\nu_s(AsF_4)$-out of phase (E)
				725sh		733(0)[139]		$\nu_s(AsF_4)$-out of phase (E)

				704(75)		729(4)[177]		ν(AsF) (A_1)
				669sh				
				661(100)		653(21)[14]		ν_s(AsF_4)-in phase (A_1)
615(5)		626(1)[3]		634(58)		632(3)[1]		cage mode
		625(1)[0]				630(1)[0]		cage mode
598(26)		604(5)[0]		604(11) 595(14)		619(5)[11]		cage mode
				617(4)		591(2)[2]		ν_{as}(AsF_4) (B_1)
				578(6)				
466(8)		469(0)[11]		567(32)		551(3)[16]		$\delta_{i.p.}$(C=O)
433(13)		438(1)[0]		444(11)		442(0)[1]		ρ_r(CH_2)
		435(1)[0]		438(5)		440(0)[1]		$\delta_{i.p.}$(C=O) + ρ_r(CH_2)
389(8)		397(2)[0]				407(1)[4]		cage mode
				418(12)		403(2)[3]		cage mode
				402(6)		384(0)[37]		δ(AsF) + δ(AsF_4)-in plane (E)
368(13)		371(2)[1]		387sh [e]				cage breathing mode
				384(23) 377(20)		373(1)[3]		δ_{sciss}(AsF_4) (B_2)
				371(5)		373(0)[48]		δ(AsF) + δ(AsF_4)-in plane (E)
		366(0)[0]				369(0)[2]		ρ_r(CH_2)
				358(15)		357(0)[187]		$\delta_{umbrella}$(AsF_4) (A_1)
				325(15)		334(1)[0]		δ(AsF) + δ(AsF_4)-out of plane (E)
278sh		285(0)[0]		312br/sh [e]		315(0)[14]		ρ_r(CH_2)
273(5)		276(0)[1]				286(0)[0]		ρ_r(CH_2)
				295(22) [e]		285(1)[2]		δ(AsF) + δ(AsF_4)-out of plane (E) + ρ_r(CH_2)
						240(0)[0]		δ(AsF_5) + $\delta_{o.o.p.}$(C=O)
						208(0)[0]		δ_{pucker}(AsF_4) (B_1)
122(16)		108(1)[4]		251(4)		173(0)[4]		$\delta_{o.o.p.}$(C=O)
				190(21)		146(2)[7]		
				180(17)		107(0)[0]		
				124(9)		88(0)[0]		
				108(6)		46(0)[0]		
						36(0)[0]		

[a] The abbreviations denote stretch (ν), bend (δ), twist (τ), wagging (ω), rock (ρ_r), scissoring (sciss), in-plane (i.p.), out-of-plane (o.o.p.), equatorial (eq), axial (ax), broad (br), and shoulder (sh). The symmetry species of the modes of free AsF_5 (C_{4v} symmetry) is given in parentheses. [b] The Raman spectrum was recorded in a 5-mm glass NMR tube at –100 °C. [c] Unscaled Raman intensities, in $Å^4\ u^{-1}$, are given in parentheses; infrared intensities, in km mol^{-1}, are given in square brackets. [d] The Raman spectrum was recorded in a ¼-in. FEP tube at –100 °C. Signals from the FEP sample tube were observed at 1214sh, 1396(6),

1305(5), 587(17), 381sh, 294(6) cm^{-1}. [e] Overlap with FEP band. Artifacts from laser observed at 84 cm^{-1}.

Table A.3.5 Observed and Calculated Frequencies for Cyclopentanone ($O=C_5H_8$) and $AsF_5 \cdot O=C_5H_8$.

Cyclopentanone ($O=C_5H_8$)			$AsF_5 \cdot O=C_5H_8$			
Exptl [b]	*Calcd* [c]		*Exptl* [d]	*Calcd* [f]		*Tentative Assignments* [a]
	3099(41)[23]			3128(60)[2]		
	3098(153)[6]		2999(43)	3112(92)[17]		
	3089(52)[31]			3106(83)[15]		
2969(100)	3085(173)[25]		2989(40)	3104(150)[5]		
			2978sh			
			2967sh			Overtones or
2901(84)	3036(28)[41]		2960(10)	3052(27)[31]		combination modes
	3029(57)[23]		2940(8)	3044(113)[15]		and ν(C−H)
2883(95)	3022(336)[1]		2905(18)	3027(107)[5]		
	3022(2)[5]		2890(60)	3015(120)[4]		
2798(7)						
2605(3)						
1743(16)	1806(15)[264]		1620(6)	1706(4)[422]		ν(CO)
1727(23)			1604(2)			
1470(11)	1512(2)[2]		1477(5)	1515(3)[1]		δ(β-CH_2)
1455(26)	1500(8)[4]		1464(20)	1504(10)[6]		δ(β-CH_2)
1409(25)	1453(10)[0]		1383(43) [e]	1438(10)[14]		δ(α-CH_2)
	1452(1)[20]			1433(5)[16]		δ(α-CH_2)
	1346(0)[2]		1326(3)	1352(1)[5]		δ(α-CH_2)
	1342(1)[0]			1350(2)[2]		ω(α-CH_2) + ω(β-CH_2)
1313(5)	1308(2)[1]		1320(4) 1304(4)	1320(2)[0]		ω(α-CH_2)
1278(11)	1299(3)[5]		1290(10)	1306(3)[7]		ω(α-CH_2)
1269(11)	1257(3)[1]		1282(11) 1277(5)	1277(7)[0]		τ(CH_2)
1232(13)	1222(1)[0]		1249(12)	1217(1)[2]		τ(α-CH_2)
1197(6)	1174(2)[1]		1207(6)	1187(3)[5]		τ(CH_2)
	1169(1)[2]		1191(5)	1175(1)[21]		τ(CH_2) + $\delta_{o.o.p.}$(CO)
1154(11)	1148(1)[71]		1168(4) 1162(3)	1202(2)[47]		ν_{as}(CCC)
1023(24)	1030(5)[1]		1027sh 1023(17)	1032(7)[0]		Ring mode
				974(1)[1]		τ(CH_2)
960(11)	968(1)[9]		962(8)	970(1)[5]		Ring mode

		964(1)[0]						$\tau(CH_2)$
		925(0)[1]				921(1)[1]		Ring mode + $\rho(CH_2)$
892(93)		894(15)[0]		901(35)		902(12)[1]		Ring mode
		841(1)[10]		853(3)		851(1)[8]		Ring mode
811(37)		810(5)[2]		841(7)		835(6)[1]		Ring mode
						739(1)[128]		$\nu_{as}(AsF_{2,eq})$ (E)
				704sh		737(1)[144]		$\nu_{as}(AsF_{2,eq})$ (E)
				711(39)		735(6)[187]		$\nu(AsF)$ (A_1)
711(21)		707(6)[1]		721(8)		724(0)[14]		ring mode
				659(100)		655(23)[11]		$\nu_s(AsF_4)$ (A_1)
583(11)		589(1)[3]		602(8)		604(1)[4]		Ring mode
				622(2)		594(2)[3]		$\nu_{as}(AsF_4)$ (B_1)
				594(9)		587(1)[23]		Ring mode
566 sh		569(3)[5]		570(12)		554(2)[12]		$\delta_{i.p.}(C=O)$ + ring mode
473(16)		473(2)[5]		455(3)		466(0)[2]		$\delta_{o.o.p.}(C=O)$
451(6)		452(1)[3]						$\delta_{o.o.p.}(C=O) + \rho_r(\beta\text{-}CH_2)$
				391sh		382(0)[44]		$\delta(AsF) + \delta(AsF_4)$-in plane (E)
				386sh [e] 381(22) [e]		375(1)[5]		$\delta_{sciss}(AsF_4)$ (B_2)
				369(3)		374(0)[39]		$\delta(AsF) + \delta(AsF_4)$-in plane (E)
				350(3)		360(0)[167]		$\delta_{umbrella}(AsF_4)$ (A_1)
				314(8)		321(1)[0]		$\delta(FAsF_4)$-out of plane (E)
				266(15)		296(1)[0]		$\delta(FAsF_4)$-out of plane (E)
						237(0)[0]		$\rho_r(CH_2)$
242(3)		230(0)[0]		256(14)		230(0)[1]		$\rho_r(CH_2)$
				208(8)		211(1)[12]		
						204(0)[0]		$\delta_{pucker}(AsF_4)$ (B_1)
				124(6)		172(1)[9]		
		97(0)[5]		112(7)		112(0)[2]		
						103(0)[0]		Rocking modes
						62(0)[0]		
						54(0)[0]		

[a] The abbreviations denote stretch (ν), bend (δ), twist (τ), wagging (ω), rock (ρ_r), scissoring (sciss), in-plane (i.p.), out-of-plane (o.o.p.), equatorial (eq), and axial (ax). The symmetry species of the modes of free AsF_5 (C_{4v} symmetry) is given in parentheses. [b] The Raman spectrum was recorded in a 5-mm glass NMR tube at –100 °C. [c] Calculations done at the B3LYP/aug-cc-pVTZ level of theory. Unscaled Raman intensities, in $Å^4\ u^{-1}$, are given in parentheses; infrared intensities, in km mol^{-1}, are given in square brackets. [d] The Raman spectrum was recorded in a ¼-in. FEP tube at –100 °C. Signals from the FEP sample tube were observed at 1509(2), 1309(4), 1218(3), 751(3), 733(23), 579sh, 294(8) cm^{-1}. Artifacts from the laser were observed at 84 cm^{-1}. [e] Overlap with FEP band. [f] Calculations done at the B3LYP/cc-pVTZ level of theory.

Table A.3.6 Observed and Calculated (B3LYP/aug-cc-pVTZ) Frequencies for Acetone ($O=C(CH_3)_2$) and $AsF_5 \cdot O=C(CH_3)_2$.

Acetone ($O=C(CH_3)_2$)		$AsF_5 \cdot O=C(CH_3)_2$		
Exptl [b]	*Calcd* [c]	*Exptl* [d]	*Calcd* [c]	*Tentative Assignments* [a]
3005(13)	3139(67)[6]	3052(4)	3158(52)[5]	
	3138(53)[12]		3157(33)[1]	
2963(14)	3084(95)[17]	2963sh	3114(58)[9]	
	3077(12)[0]		3085(67)[0]	$\nu_s + \nu_{as}$ (CH_3)
2923(100)	3033(320)[7]	2935(22)	3046(191)[8]	
	3025(2)[1]		3033(134)[4]	
2848(7)				Combination/overtone
1751(3)				ν(CO)
1709(16)	1782(13)[195]	1592(2)	1683(5)[344]	
	1488(0)[19]		1493(2)[13]	$\delta(CH_2)$
1428(10)	1470(12)[31]	1410(4)br	1470(5)[8]	$\delta(CH_2)$
	1466(8)[0]		1457(4)[4]	
	1460(1)[1]		1455(8)[50]	
	1388(0)[54]	1383(2)	1395(3)[38]	
1358(3)	1388(2)[19]	1351(7)	1388(3)[44]	
1222(6)	1234(5)[72]	1279(5)	1272(6)[65]	ν_{as}(CCC)
	1121(0)[3]		1118(1)[10]	$\delta_{o.o.p.}$(CCC) + $\delta(CH_3)$
1067(6)	1085(2)[0]		1091(1)[6]	$\rho_r(CH_3)$
	887(0)[0]		887(1)[2]	$\omega(CH_3)$
908(2)	887(2)[9]		966(1)[5]	$\rho_r(CH_3)$
788(37)	783(16)[2]	838(4)	819(7)[5]	ν_s(CCC)
		729sh	729(1)[156]	$\nu_{as}(AsF_{2,eq})$ (E)
		679(1)	728(1)[154]	$\nu_{as}(AsF_{2,eq})$ (E)
		710(44)	727(7)[163]	ν(AsF) (A_1)
		660(100)	651(26)[9]	$\nu_s(AsF_4)$ (A_1)
		623(6)	586(2)[2]	$\nu_{as}(AsF_4)$ (B_1)
531(6)	535(1)[14]	594(9)	599(2)[17]	$\delta_{i.p.}$(CO)
494(3)	491(0)[1]		514(0)[1]	$\delta_{o.o.p.}$(CO)
396(2)	381(1)[2]	453(3)	427(1)[14]	δ(CCC)
		393sh 390(5) [e]	380(0)[46]	δ(AsF) + $\delta(AsF_4)$-in plane (E)
		379(20) [e]	375(1)[11]	$\delta_{sciss}(AsF_2)_{exo}$ (B_2/E)
		364(2)	371(0)[30]	$\delta_{sciss}(AsF_2)_{endo}$ (B_2/E)
		351(4)	355(0)[148]	$\delta_{umbrella}(AsF_4)$ (A_1)
		318(11)	320(0)[0]	$\delta(FAsF_4)$-out of plane (E)

				277(20)		295(1)[0]		$\delta(FAsF_4)$-out of plane (E)
				252(4)		235(0)[0]		$\rho_r(C{=}O) + \delta(AsF_5)$
				246(5)		230(1)[7]		
						202(0)[0]		$\delta_{pucker}(AsF_4)$ (B_1)
				141(5)		191(2)[16]		
						121(0)[0]		
		132(0)[0]		115(5)		106(0)[0]		$\tau(CH_3)$
						162(0)[1]		$\tau(CH_3)$
						85(1)[2]		
		28(0)[0]				66(1)[0]		

[a] The abbreviations denote symmetric (s), asymmetric (as), stretch (ν), bend (δ), twist (τ), wagging (ω), rock (ρ_r), scissoring (sciss), in-plane (i.p.), out-of-plane (o.o.p.), equatorial (eq), axial (ax), broad (br), and shoulder (sh). The symmetry species of the modes of free AsF_5 (C_{4v} symmetry) is given in parentheses. [b] The Raman spectrum was recorded in a 5-mm glass NMR tube at –100 °C. [c] Unscaled Raman intensities, in $Å^4\ u^{-1}$, are given in parentheses; infrared intensities, in km mol^{-1}, are given in square brackets. [d] The Raman spectrum was recorded in a ¼-in. FEP tube at –100 °C. Signals from the FEP sample tube were observed at 1504(1), 1383(3), 1307(2), 1214(1), 751(2), 733(12), 577(2), 294(4) cm^{-1}. Artifacts from the laser were observed at 84 cm^{-1}. [e] Signals overlap with FEP.

a)

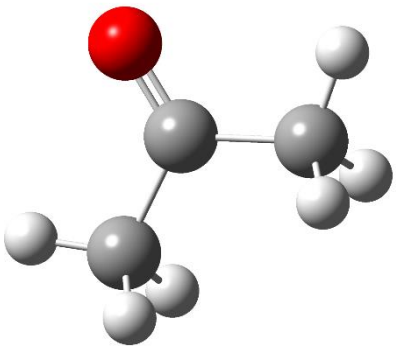

b) E = −162 kJ/mol

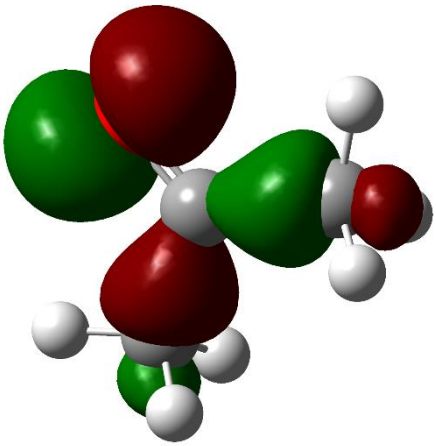

c) E = −18 kJ/mol

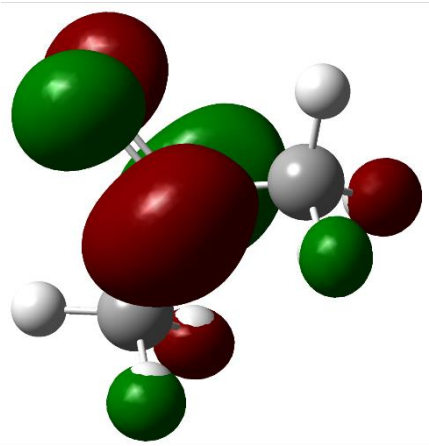

Figure A.3.1 Molecular orbitals and energies of acetone, $O=C(CH_3)_2$: a) neutral acetone for reference, b) HOMO (MO 16), c) LUMO (MO 17). Isovalue of 0.030.

a)

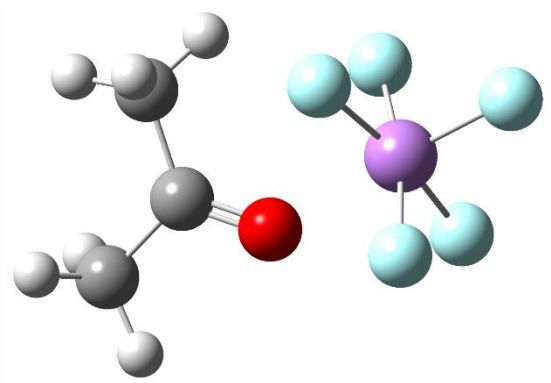

b) E = −933 kJ/mol

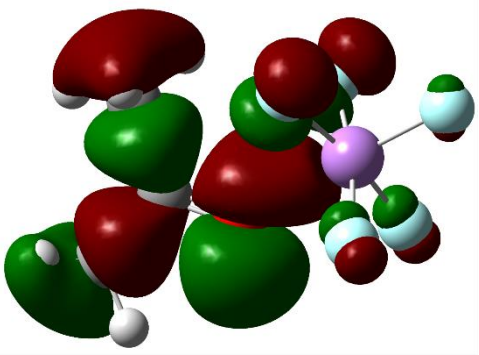

d) E = −259 kJ/mol

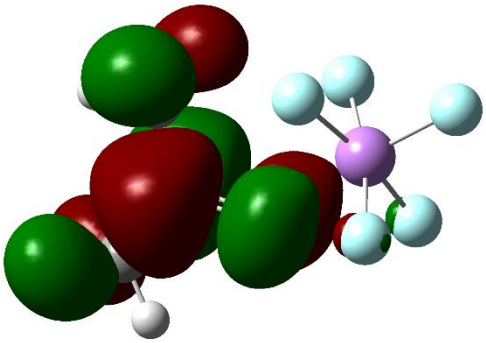

Figure A.3.2 Molecular orbitals and energies of $AsF_5 \cdot O=C(CH_3)_2$: a) $AsF_5 \cdot O=C(CH_3)_2$ adduct for reference, b) HOMO (MO 55), c) LUMO (MO 56). Isovalue of 0.025.

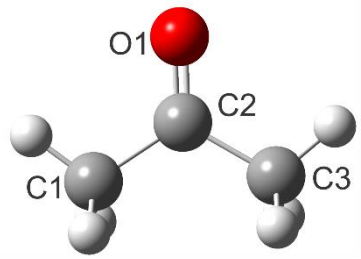

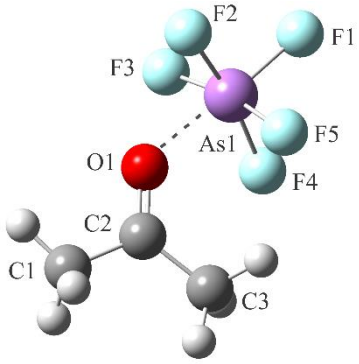

Table A.3.7 Natural Bond Order (NBO) Valences, Bond Orders, and Natural Population Analysis (NPA) Charges[a] for Acetone ($O=C(CH_3)_2$) and $AsF_5 \cdot O=C(CH_3)_2$.

$O=C(CH_3)_2$			**$AsF_5 \cdot O=C(CH_3)_2$**		
	Natural Charges	*Valences*		*Natural Charges*	*Valences*
O1	−0.55	2.04	O1	−0.59	2.14
C2	0.59	3.87	C2	0.69	3.78
C1	−0.69	3.87	C1	−0.68	3.86
C3	−0.69	3.87	C3	−0.71	3.84
			As1	2.71	3.23
			F1	−0.57	0.73
			F2	−0.57	0.73
			F3	−0.58	0.73
			F4	−0.60	0.70
			F5	−0.59	0.70
	Wiberg Bond Indices			*Wiberg Bond Indices*	
C2=O1	1.83		C2=O1	1.59	
C1−C2	1.01		C1−C2	1.05	
C3−C2	1.01		C3−C2	1.06	
			As1---O1	0.29	
			As1−F1	0.61	
			As1−F2	0.59	
			As1−F3	0.59	
			As1−F4	0.56	
			As1−F5	0.56	

[a]The B3LYP/aug-cc-pVTZ level was used.

a)

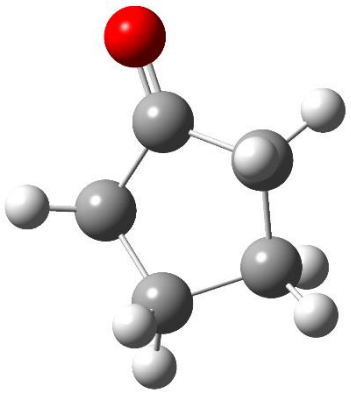

d) E = −157 kJ/mol

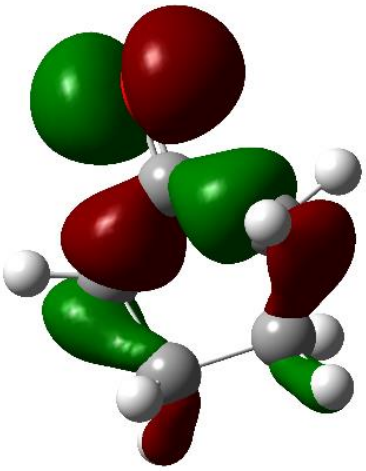

e) E = −20 kJ/mol

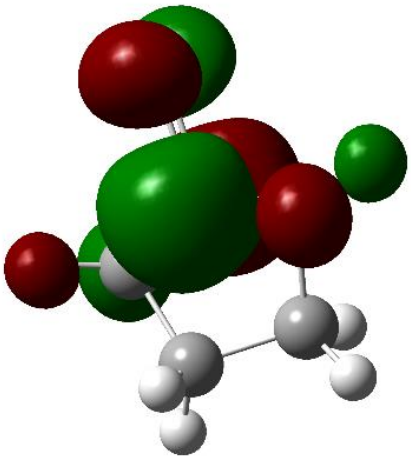

Figure A.3.3 Molecular orbitals and energies of cyclopentanone, $O{=}C_5H_8$: a) neutral cyclopentanone for reference, b) HOMO (MO 23), c) LUMO (MO 24). Isovalue of 0.040.

a)

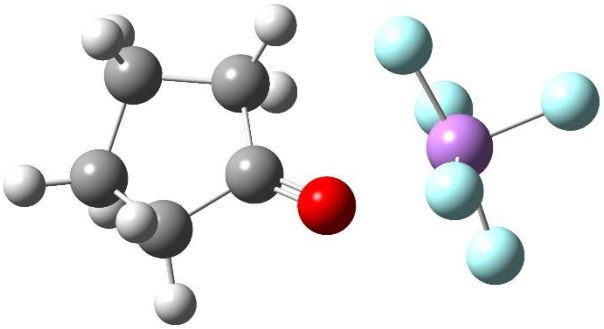

c) E = −890 kJ/mol

d) E = −256 kJ/mol

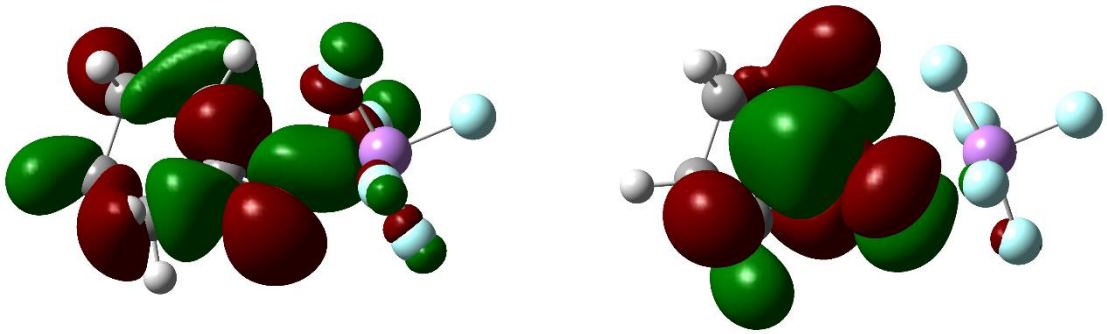

Figure A.3.4 Molecular orbitals and energies of $AsF_5 \cdot O=C_5H_8$: a) $AsF_5 \cdot O=C_5H_8$ adduct for reference, b) HOMO (MO 62), c) LUMO (MO 63). Isovalue of 0.025.

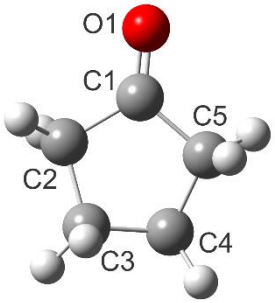

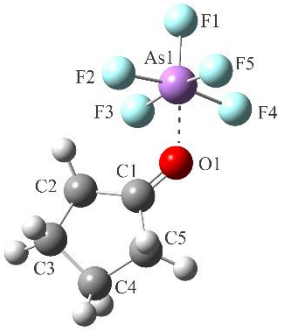

Table A.3.8 Natural Bond Order (NBO) Valences, Bond Orders, and Natural Population Analysis (NPA) Charges[a] for Cyclopentanone ($O{=}C_5H_8$) and $AsF_5{\cdot}O{=}C_5H_8$.

	$O{=}C_5H_8$			**$AsF_5{\cdot}O{=}C_5H_8$**	
	Natural Charges	*Valences*		*Natural Charges*	*Valences*
O1	−0.54	2.06	O1	−0.59	2.15
C1	0.60	3.87	C1	0.71	3.77
C2	−0.50	3.92	C2	−0.52	3.90
C3	−0.38	3.93	C3	−0.38	3.93
C4	−0.38	3.93	C4	−0.37	3.93
C5	−0.50	3.92	C5	−0.50	3.92
			As1	2.68	3.26
			F1	−0.57	0.74
			F2	−0.59	0.71
			F3	−0.59	0.71
			F4	−0.57	0.74
			F5	−0.57	0.74
	Wiberg Bond Indices			*Wiberg Bond Indices*	
C1=O1	1.84		C1=O1	1.60	
C1−C2	0.98		C1−C2	1.04	
C2−C3	1.02		C2−C3	1.01	
C3−C4	1.01		C3−C4	1.01	
C4−C5	1.02		C4−C5	1.01	
C5−C1	0.98		C5−C1	1.02	
			As---O	0.30	
			As1−F1	0.62	
			As1−F2	0.56	
			As1−F3	0.56	
			As1−F4	0.59	
			As1−F5	0.60	

[a]The B3LYP/cc-pVTZ level was used.

a)

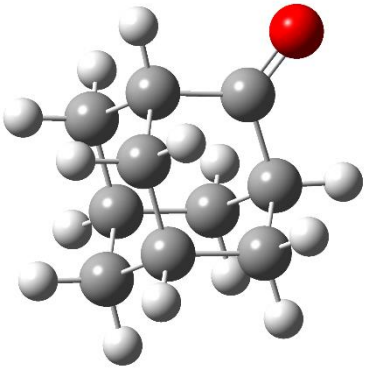

b) E = −151 kJ/mol

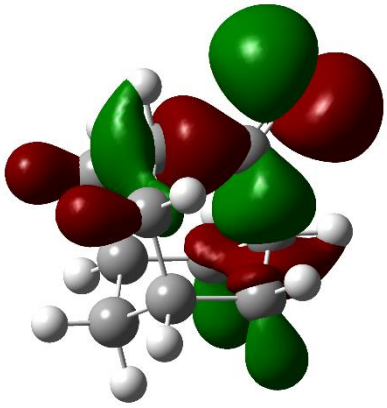

c) E = −13 kJ/mol

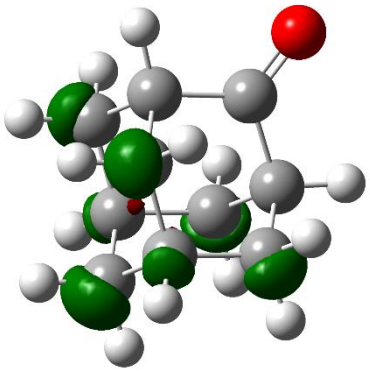

d) E = −12 kJ/mol

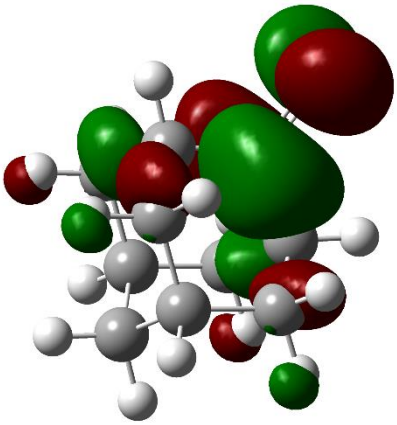

Figure A.3.5 Molecular orbitals of 2-adamantanone, $O=C_{10}H_{14}$: a) neutral 2-adamantanone for reference, b) HOMO (MO 16), c) LUMO (MO 17), d) LUMO+1 (MO 18). Isovalue of 0.040.

a)

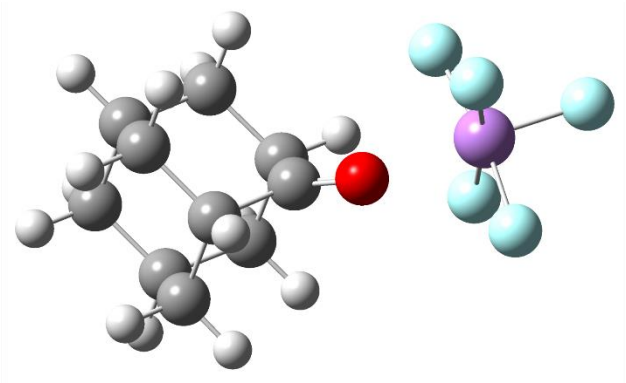

b) E = −837 kJ/mol

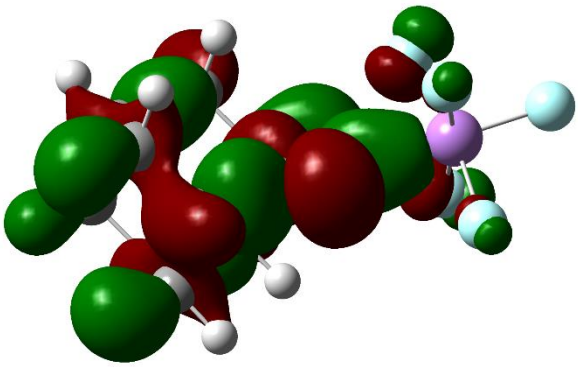

c) E = −229 kJ/mol

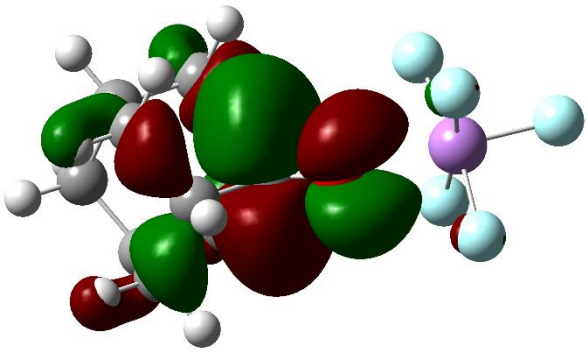

Figure A.3.6 Molecular orbitals and energies of $AsF_5 \cdot O{=}C_{10}H_{14}$: a) $AsF_5 \cdot O{=}C_{10}H_{14}$ adduct for reference, b) HOMO (MO 80), c) LUMO (MO 81). Isovalue of 0.025.

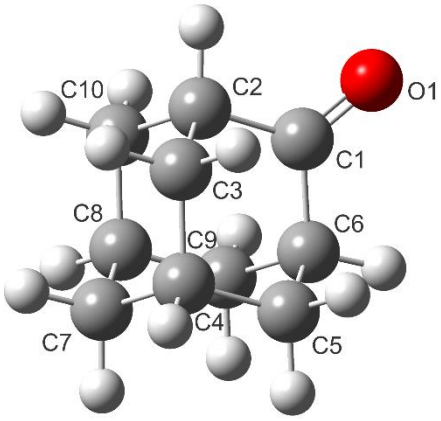

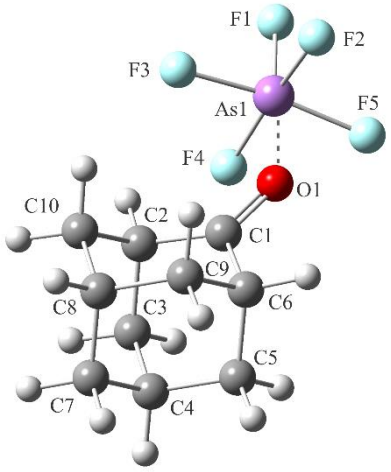

Table A.3.9 Natural Bond Order (NBO) Valences, Bond Orders, and Natural Population Analysis (NPA) Charges[a] for 2-Adamantanone ($O{=}C_{10}H_{14}$) and $AsF_5{\cdot}O{=}C_{10}H_{14}$.

	$O{=}C_{10}H_{14}$			**$AsF_5{\cdot}O{=}C_{10}H_{14}$**	
	Natural Charges	*Valences*		*Natural Charges*	*Valences*
O1	−0.56	2.04	O1	−0.61	2.14
C1	0.61	3.87	C1	0.73	3.76
C2	−0.31	3.97	C2	−0.30	3.97
C3	−0.37	3.93	C3	−0.37	3.93
C4	−0.21	3.98	C4	−0.20	3.97
C5	−0.37	3.93	C5	−0.37	3.93
C6	−0.31	3.97	C6	−0.32	3.95
C7	−0.38	3.94	C7	−0.39	3.94
C8	−0.21	3.98	C8	−0.20	3.97
C9	−0.37	3.93	C9	−0.37	3.93
C10	−0.37	3.93	C10	−0.37	3.93
			As1	2.68	3.26
			F1	−0.57	0.74
			F2	−0.57	0.74
			F3	−0.59	0.71
			F4	−0.59	0.71
			F5	−0.57	0.74
	Wiberg Bond Indices			*Wiberg Bond Indices*	
C1=O1	1.83		C1=O1	1.57	
C1−C2	0.97		C1−C2	1.01	
C1−C6	0.97		C1−C6	1.02	
C2−C10	0.98		C2−C10	0.97	
C2−C3	0.98		C2−C3	0.97	
C3−C4	1.00		C3−C4	1.00	
C4−C5	1.00		C4−C5	1.00	

C5−C6	0.98	C5−C6	0.97
C7−C4	1.00	C7−C4	1.00
C8−C7	1.00	C8−C7	1.00
C8−C9	1.00	C8−C9	1.00
C9−C6	0.98	C9−C6	0.97
C10−C8	1.00	C10−C8	1.00
		As1---O	0.31
		As1−F1	0.61
		As1−F2	0.59
		As1−F3	0.56
		As1−F4	0.56
		As1−F5	0.59

[a]The B3LYP/cc-pVTZ level was used.